MASS TRANSFER IN STRUCTURED PACKING

by

André Brink Erasmus

Dissertation presented for the Degree

of

DOCTOR OF PHILOSOPHY IN ENGINEERING

(Chemical Engineering)

in the Department of Process Engineering

at the University of Stellenbosch

Promotor

Prof. Izak Nieuwoudt

STELLENBOSCH

JANUARY 2004

DECLARATION

I, the undersigned, hereby declare that the work contained in this dissertation is my own original work and that I have not previously, in its entirety or in part, submitted it at any university for a degree.

Signature:.....

Date: .....

ACKNOWLEDGEMENTS

There are quite a few people that contributed directly and indirectly towards the contents and successful completion of this thesis. First and foremost is my study leader, prof. Izak Nieuwoudt. Without his guidance and supervision during the past four years, this thesis would not have been possible. No project is possible without a substantial economic investment. I am grateful for the research sponsorship awarded to me by the NRF during the first three years of the project, and the post graduate departmental bursary from the Department of Process Engineering during the final year. A special word of thanks towards Koch-Glitsch for supplying the structured packing. I enjoyed some of the best times of my life during the past four years in Stellenbosch. This was made possible by all my wonderful friends and colleagues. They celebrated with me during good times and encouraged me through the difficult times. I am grateful towards my family for always being there when I needed them. Without their words of encouragement, especially during the final months, it would indeed have been an uphill battle. Finally, without guidance and strength from Above, this would have been a futile exercise.

SYNOPSIS

Structured packing is a popular column internal for both distillation and absorption unit operations. This is due to the excellent mass transfer characteristics and low pressure drop that it offers compared to random packing or trays. The main disadvantage is the lack in reliable models to describe the mass transfer characteristics of this type of packing. The recent development of the non-equilibrium model or rate based modelling approach has also emphasized the need for accurate hydraulic and efficiency models for sheet metal structured packing.

The main focus of this study was to develop an accurate model for the mass transfer efficiency of Flexipac 350Y using a number of experimental and modelling techniques. Efficiency is however closely related to hydraulic capacity. Before attempting to measure and model the efficiency of Flexipac 350Y, the ability of existing published models to accurately describe the hydraulic capacity of this packing was tested. Holdup and pressure drop were measured using air/water and air/heavy paraffin as test systems. All experiments were performed on pilot plant scale 200mm ID glass columns. Satisfactory results were obtained with most of the models for determining the loading point and pressure drop for the air/water test system. All of the models tested predicted a conservative dependency of capacity on liquid viscosity for the air/paraffin test system. Efficiency and pressure drop were measured using the chlorobenzene/ethylbenzene test systems under conditions of total reflux in a 200mm ID glass column. Widely differing results were however obtained with the different models for the efficiency of Flexipac 350Y. Experiments were subsequently designed and performed to measure and correlate the vapour phase mass transfer coefficient and the effective surface area of Flexipac 350Y independently. The vapour phase mass transfer coefficient was measured and correlated by subliming naphthalene into air from coatings applied to specially fabricated 350Y gauze structured packing. The use of computational fluid dynamics (CFD) to model the vapour phase mass transfer coefficient is also demonstrated. The effective surface area for vapour phase mass transfer was measured with the chemical technique. The specific absorption rate of CO_2 into monoethanolamine (MEA) using n-propanol as solvent was determined in a wetted-wall column and used to determine the effective surface area of Flexipac 350Y on pilot plant scale (200mm ID glass column). The efficiency of Flexipac 350Y could be modelled within an accuracy of 9% when using the correlations developed in this study and ignoring

liquid phase resistance to mass transfer for the chlorobenzene/ethylbenzene test system under conditions of total reflux.

The capacity and efficiency of the new generation high capacity packing Flexipac 350Y HC was also measured and compared with that of the normal capacity packing Flexipac 350Y. An increase in capacity of 20% was observed for the HC packing for the air/water system and 4% for the air/heavy paraffin system compared with the normal packing. For the binary total reflux distillation the increase in capacity varied between 8% and 15% depending on the column pressure. The gain in capacity was at the expense of a loss in efficiency of around 3% in the preloading region.

OPSOMMING

Gestruktureerde pakking is 'n populêre pakkingsmateriaal en word algemeen gebruik in distillasie en absorpsie kolomme. Dit is hoofsaaklik as gevolg van die goeie massa-oordragseienskappe en lae drukval wat dit bied in vergelyking met 'random' pakking en plate. The hoof nadeel is egter die tekort aan akkurate modelle om die massa-oordrags eienskappe te bepaal. Om modelle te kan gebruik waar die massa-oordragstempo direk gebruik word om gepakte hoogte te bepaal, word akkurate kapasiteits- en effektiwiteitsmodelle vir gestruktureerde plaatmetaalpakking benodig.

Die hoof doelwit van hierdie studie was om 'n akkurate model te ontwikkel vir die massa-oordragseffektiwiteit van die plaat metaal pakking Flexipac 350Y deur gebruik te maak van verskillende eksperimentele- en modelleringstegnieke. Effektiwiteit is egter direk gekoppel aan hidroliese kapasiteit. Bestaande modelle in die literatuur is eers getoets om te bepaal of hulle die hidroliese kapasitiet van Flexipac 350Y akkuraat kan voorspel. Vir die doel is vloeistofterughou en drukval gemeet deur gebruik te maak van die sisteme lug/water en lug/swaar parafien. Alle eksperimente is in loodsaanlegskaal 200mm ID glaskolomme uitgevoer. Meeste van die modelle was relatief akkuraat in hulle berekening van die ladingspunt en die drukval vir die lug/water toets sisteem, maar was konsertief in voorspellings van die groothede vir die lug/swaar parafien sisteem. Effektiwiteit en drukval was gemeet deur gebruik te maak van die binêre toetssisteem chlorobenseen/etielbenseen onder totale terugvloei kondisies in 'n 200mm ID glaskolom. Daar is 'n groot verskil in die effektiwiteitsvoorspelling deur die verskillende modelle. Vervolgens is eksperimente ontwerp en uitgevoer om die dampfase massaoordragskoeffisiënt en die effektiewe oppervlakarea vir Flexipac 350Y onafhanklik te meet en te korreleer. Die dampfase massaoordragskoeffisient is gemeet en gekorreleer deur naftaleen te sublimeer vanaf spesiaal vervaardigde 350Y gestruktureerde pakking van metaalgaas. Die gebruik van numeriese vloeimeganika (CFD) om die dampfase massaoordragskoeffisient te bereken word gedemonstreer. Die effektiewe oppervlakarea vir dampfase massaoordrag is bepaal deur van 'n chemiese metode gebruik te maak. Die spesifieke absorpsietempo van CO_2 in monoetanolamien (MEA) met n-propanol as oplosmiddel is gemeet in a benatte wand kolom en gebruik om die effektiewe oppervlakarea van Flexipac 350Y te bepaal op loodsaanlegskaal (200mm ID). Die effektiwiteit van Flexipac 350Y kon met 'n akkuraatheid van binne 9%

gemodelleer word deur vloeistoffaseweerstand te ignoreer en van die korrelasies gebruik te maak wat in hierdie studie ontwikkel is.

Die effektiwiteit en kapasiteit van die nuwe generasie hoë kapasiteit pakking Flexipac 350Y HC is ook gemeet en vergelyk met die normale kapasiteit pakking Flexipac 350Y. 'n Verhoging in kapsiteit van 20% is gemeet vir die HC pakking in vergelyking met die normale kapasiteit pakking vir die lug/water sisteem en 'n 4% verhoging in kapasiteit vir die lug/swaar parafien sisteem. Die verhoging in kapasiteit het gevarieër tussen 8% en 14% in die binêre totale terugvloei distillasie toetse en was afhanklik van die kolom druk. Die verhoging in kapasiteit was ten koste van 'n verlaging in effektiwiteit van ongeveer 3% onderkant die ladingspunt.

CONTENTS

1 Introduction 1

1.1 History of distillation 1

1.2 Distillation and absorption today 2

1.3 Column internals 3

1.3.1 Trays 3

1.3.2 Packing 4

1.3.3 Trays or packing? 6

1.4 Modelling of distillation and absorption 7

1.5 Aims of this study 8

2 Modelling of distillation 10

2.1 Introduction 10

2.2 Mass transfer across interfaces 10

2.2.1 Definition of mass transfer coefficients 10

2.2.2 Models for mass transfer at phase boundaries 12

2.3 The Equilibrium Model 15

2.3.1 Historical perspective 15

2.3.2 Model equations 15

2.3.3 Tray/stage efficiency in tray columns 17

2.3.4 Height equivalent to a theoretical plate (HETP) in packed columns 18

2.4 Modelling distillation in packed columns: The HTU/NTU concept 18

2.4.1 Historical perspective 18

2.4.2 Model equations 18

2.5 The Non-equilibrium Model 21

2.5.1 Historical perspective 21

2.5.2 Model equations 21

2.6 Concluding remarks 25

2.7 Nomenclature 27

3 CFD and Structured Packing 29
3.1 Introduction 29
3.2 Literature review 29
3.2.1 Application of CFD in the structured packing industry 29
3.2.2 Aim of CFD in this study 31
3.3 Theory: Computational fluid dynamics 32
3.3.1 Conservation equations 32
3.3.2 Discretization of the governing equations 38
3.3.3 Solution procedure 41
3.4 CFD code used in this study 43
3.4.1 Pre-processor 43
3.4.2 Solver 44
3.4.3 Post-processor 45
3.5 Implementation of CFD in this study 45
3.6 Nomenclature 49

4 Hydrodynamics 51
4.1 Introduction 51
4.2 Literature survey 51
4.2.1 Basic concepts 51
4.2.2 Capacity charts and empirical correlations 53
4.2.3 Semi-theoretical models 56
4.2.4 Discussion 68
4.3 Experimental 69
4.3.1 Experimental set-up 69
4.3.2 Experimental procedure 72
4.3.3 Physical properties and packing dimensions 73
4.4 Results and discussion 74
4.4.1 Comparison between normal and high capacity packing 74
4.4.2 Comparison with semi-theoretical models 80
4.4.3 Implementation of models in design calculations 87
4.5 Conclusions 88
4.6 Nomenclature 89

5 Mass transfer 92
5.1 Introduction 92
5.2 Literature survey 92
5.2.1 Literature Review 92
5.2.2 Discussion 96
5.3 Theory 98
5.3.1 Naphthalene sublimation in structured packing 100
5.3.2 Evaporation in a wetted wall column 100
5.4 Experimental 101
5.4.1 Experimental set-up 101
5.4.2 Naphthalene coating 101
5.4.3 Experimental procedure 103
5.5 Results and discussion 103
5.5.1 Experimental results 103
5.5.2 Sensitivity analysis 105
5.5.3 Comparison with existing correlations 105
5.5.4 Correlation of experimental results 107
5.6 CFD modelling 110
5.6.1 Wetted-wall CFD simulations 110
5.6.2 CFD modelling of naphthalene sublimation 113
5.7 Conclusions 123
5.8 Nomenclature 127

6 Effective Interfacial Area 129
6.1 Introduction 129
6.2 Literature survey 129
6.2.1 Definitions of effective interfacial area 129
6.2.2 Methods for determining interfacial area 129
6.2.3 Interfacial area in structured packing 130
6.2.4 Chemical systems for determining effective interfacial area 135
6.3 Theory 137
6.3.1 Gas-liquid absorption with chemical reaction 137
6.3.2 Laboratory apparatus for determining absorption rates 142
6.4 Experimental 144

6.4.1 Experimental setup 144
6.4.2 Experimental procedure 150
6.5 Results and discussion 152
6.5.1 Experimental determined absorption rates 153
6.5.2 Effective surface area of Fexipac 350Y 157
6.5.3 Comparison with existing correlations 160
6.5.4 Correlation of experimental results 162
6.6 Conclusions 164
6.7 Nomenclature 165

7 Binary Distillation in Structured Packing 167
7.1 Introduction 167
7.2 Characterization of structured packing 167
7.3 Predicting separation efficiency and pressure drop for Flexipac 350Y 168
7.4 Experimental 172
7.4.1 Setup 172
7.4.2 Procedure 173
7.5 Thermodynamic data and transport properties 175
7.6 Results and discussion 176
7.6.1 Experimental results for Flexipac 350Y and 350Y HC 176
7.6.2 Flexipac 350Y: Model predictions 180
7.6.3 Efficiency 183
7.7 Conclusions 191
7.8 Nomenclature 193

8 Conclusions 195

References 199
Appendix A 214
Appendix B 216
Appendix C 225
Appendix D 239
Appendix E 242

Appendix F 246

LIST OF FIGURES

Figure 2.1 Stage j in equilibrium model 16
Figure 2.2 Packed column with differential element 19
Figure 2.3 Stage j in non-equilibrium model 22
Figure 3.1 Control volume in three-dimensional Cartesian coordinates 38
Figure 3.2 Transformation of grid to curve linear coordinates 41
Figure 3.3 Breakdown of structured packing into re-occurring micro elements 48
Figure 4.1 Pressure drop as a function of superficial vapour velocity 52
Figure 4.2 Liquid hold-up as a function of superficial vapour velocity 52
Figure 4.3 Experimental set-up 71
Figure 4.4 Distributor 72
Figure 4.5 Characteristic dimensions of packing 75
Figure 4.6 Comparison between dry-bed pressure drop for Flexipac 350Y and Flexipac 350Y HC 76
Figure 4.7 Corrugation geometry at top and bottom of packing element 77
Figure 4.8 Comparison of pressure drop over normal and modified packing for the air/water system 78
Figure 4.9 Comparison of hold-up on normal and modified packing for the air/water system 79
Figure 4.10 Comparison of pressure drops over normal and modified packing for the air/Kerosol 200 system 79
Figure 4.11 Comparison of hold-up on normal and modified packing for the air/Kerosol 200 system 80
Figure 4.12 Comparison between pressure drop calculated with semi-theoretical models and experimental values. Flexipac 350Y, air/water system 82
Figure 4.13 Comparison between pressure drop calculated with semi-theoretical models and experimental values. Flexipac 350Y, air/water system 82
Figure 4.14 Comparison between measured and predicted liquid hold-up. Flexipac 350Y, air/water system 83
Figure 4.15 Comparison between measured and predicted liquid hold-up. Flexipac 350Y, air/water system 83

Figure 4.16 Comparison between pressure drop calculated with semi-theoretical models and experimental values. Flexipac 350Y, air/Kerosol 200.....85
Figure 4.17 Comparison between pressure drop calculated with semi-theoretical models and experimental values. Flexipac 350Y, air/Kerosol 200.....85
Figure 4.18 Comparison between measured and predicted liquid hold-up. Flexipac 350Y, air/Kerosol 200 86
Figure 4.19 Comparison between measured and predicted liquid hold-up. Flexipac 350Y, air/Kerosol 200 86
Figure 5.1 Experimental results for naphthalene coated packing. Coating I: coating applied to bottom half of element, Coating II: coating applied to top half of element. Sc_G=2.35. 104
Figure 5.2 Comparison between experimental results and existing k_G correlations. 107
Figure 5.3 Parity plot of mass transfer coefficients predicted with correlation 5.47 and 5.48 against experimental values.....109
Figure 5.4 Geometry of wetted-wall column in 2D axisymmetric CFD model 110
Figure 5.5 CFD results for wetted-wall evaporation 113
Figure 5.6 Computational domain. (a) Top view of cross-corrugated channels. (b) View of inlet- and outlet boundary.....115
Figure 5.7 Mass transfer coefficients calculated at different Re_G with the k-ω and BSL turbulence models 118
Figure 5.8 Mass transfer coefficients calculated at different Re_G for geometry 2 (boundaries next to free shear interface).....119
Figure 5.9 Mass transfer coefficients calculated at different Re_G for geometry 1 (boundaries a distance away from free shear interface).....119
Figure 5.10 Comparison between mass transfer coefficients calculated with the two physical domains used in CFD simulations.....120
Figure 5.11 Comparison of CFD and experimental results for naphthalene sublimation. 122
Figure 6.1 Enhancement factors for second order reactions as a function of Hatta number 139
Figure 6.2 Wetted-wall column 146
Figure 6.3 Wetted-wall flow diagram.....147
Figure 6.4 PFD of pilot plant absorption column 149

Figure 6.5 Verification of pseudo m,nth order reaction.....154
Figure 6.6 Specific absorption rates for different MEA 155
Figure 6.7 Temperature dependence of specific absorption rate 155
Figure 6.8 Comparison between experiemntal and predicted absorption rates ...156
Figure 6.9 Comparison between experiemntal and predicted absorption rates ...157
Figure 6.10 Effective surface area as a function of liquid load for Flexipac 350Y. .158
Figure 6.11 Experimental data plotted with upper and lower confidence limits.....159
Figure 6.12 Comparison between experimental determined effective interfacial area and correlations proposed in literature 160
Figure 6.13 Comparison of experimental results with that predicted by Equation 6.47 163
Figure 7.1 PFD of total reflux distillation column 174
Figure 7.2 Liquid distributor 175
Figure 7.3 Capacity comparison between Flexipac 350Y and 350Y HC at 1.0 bar. 176
Figure 7.4 Efficiency comparison between Flexipac 350Y and 350Y HC at 1.0 bar. 177
Figure 7.5 Capacity comparison between Flexipac 350Y and 350Y HC at 0.6 bar. 177
Figure 7.6 Efficiency comparison between Flexipac 350Y and 350Y HC at 0.6 bar. 178
Figure 7.7 Capacity comparison between Flexipac 350Y and 350Y HC at 0.3 bar. 178
Figure 7.8 Efficiency comparison between Flexipac 350Y and 350Y HC at 0.3 bar. 179
Figure 7.9 Comparison between measured and predicted pressure drop for Flexipac 350Ywith the SRP model. Chlorobenzene/ethylbenzene test system at 1.01 bar, 0.6 bar and 0.3 bar. 181
Figure 7.10 Comparison between measured and predicted pressure drop for Flexipac 350Ywith the Delft model. Chlorobenzene/ethylbenzene test system at 1.01 bar, 0.6 bar and 0.3 bar. 181
Figure 7.11 Comparison between measured and predicted pressure drop for Flexipac 350Ywith the Billet model. Chlorobenzene/ethylbenzene test system at 1.01 bar, 0.6 bar and 0.3 bar. 182

Figure 7.12 Holdup predicted by different models for Flexipac 350Y. Chlorobenzene/ethylbenzene test system at 1.01 bar, 0.6 bar and 0.3 bar. 183
Figure 7.13 Efficiency of Flexipac 350Y predicted by the SRP model. Chlorobenzene/ethylbenzene test system at 1.01 bar, 0.6 bar and 0.3 bar. 184
Figure 7.14 Efficiency of Flexipac 350Y predicted by the Delft model. Chlorobenzene/ethylbenzene test system at 1.01 bar, 0.6 bar and 0.3 bar. 184
Figure 7.15 Efficiency of Flexipac 350Y predicted by the Billet model. Chlorobenzene/ethylbenzene test system at 1.01 bar, 0.6 bar and 0.3 bar. 185
Figure 7.16 Vapour phase mass transfer coefficient predictions by SRP, Delft and Billet models for Flexipac 350Y. Chlorobenzene/ethylbenzene test system at 1.01 bar, 0.6 bar and 0.3 bar.....186
Figure 7.17 Liquid phase mass transfer coefficient predictions by SRP, Delft and Billet models for Flexipac 350Y. Chlorobenzene/ethylbenzene test system at 1.01 bar, 0.6 bar and 0.3 bar.....186
Figure 7.18 Effective surface area predictions by SRP, Delft and Billet models for Flexipac 350Y. Chlorobenzene/ethylbenzene test system at 1.01 bar, 0.6 bar and 0.3 bar. 188
Figure 7.19 Vapour phase mass transfer coefficient predicted with equation 5.48 compared to predictions by SRP, Billet and Delft models. Chlorobenzene/ethylbenzene test system, 1.01 bar.....189
Figure 7.20 Effective surface area predicted with equation 6.47 compared to predictions by SRP, Billet and Delft models. Chlorobenzene/ethylbenzene test system, total reflux, 1.01 bar. 190
Figure 7.21 Efficiency of Flexipac 350Y predicted with k_G and a_e correlations developed in this study. Chlorobenzene/ethylbenzene test system at 1.01 bar, 0.6 bar and 0.3 bar. 191
Figure C.1 Pressure drop as function of F-factor for Flexipac 350Y, air/water system 226
Figure C.2 Holdup as function of F-factor for Flexipac 350Y, air/water system ...226

Figure C.3 Pressure drop as function of F-factor for Flexipac 350Y, air/Kerosol 200 system 227
Figure C.4 Holdup as function of F-factor for Flexipac 350Y, air/Kerosol 200 system 227
Figure C.5 Pressure drop as function of F-factor for Flexipac 350Y HC, air/water system 228
Figure C.6 Holdup as function of F-factor for Flexipac 350Y HC, air/water system 228
Figure C.7 Pressure drop as function of F-factor for Flexipac 350Y HC, air/Kerosol 200 system 229
Figure C.8 Holdup as function of F-factor for Flexipac 350Y HC, air/Kerosol 200 system 229

LIST OF TABLES

Table 1.1 Examples from different generations of random packing 4
Table 1.2 Examples from different generations of structured packing 5
Table 3.1 Formulas for the function f(|P|) 40
Table 4.1 Physical properties of test system 74
Table 4.2 Dimensions of packing 74
Table 5.1 Dimensions of naphthalene coated packing section 103
Table 5.2 Correlations for the gas phase mass transfer coefficient in Figure 5.2 106
Table 5.3 Regression results for naphthalene sublimation data 108
Table 5.4 Boundary conditions: 2D axisymmetric wetted-wall model 111
Table 5.5 Mesh detail for 2D axisymmetric wetted-wall model 112
Table 5.6 Properties of air/naphthalene system 114
Table 5.7 Boundary conditions for micro element 116
Table 5.8 Details of converged grid for packing micro element 117
Table 7.1 Constants for Flexipac 350Y used in the SRP model 170
Table 7.2 Constants for Flexipac 350Y used in the Delft model 171
Table 7.3 Constants for Flexipac 350Y used in the Billet model 171
Table B.1 SRP model equations 216
Table B.2 Delft model equations 218
Table B.3 Billet model equations 220
Table C.1 Experimental data for Flexipac 350Y, air/water system 230
Table C.2 Experimental data for Flexipac 350Y, air/Kerosol 200 system 233
Table C.3 Experimental data for Flexipac 350Y HC, air/water system 234
Table C.4 Experimental data for Flexipac 350Y HC, air/Kerosol 200 system 237
Table D.1 Experimental sublimation data, bottom half of packing coated 240
Table D.2 Experimental sublimation data, top half of packing coated 241
Table E.1 Physical properties of n-propanol 242
Table E.2 Physical properties of monoethanolamine/n-propanol 242
Table E.3 Rate of absorption of CO_2 into n-propanol/monoethanolamine solutions: Wetted-wall column experimental results 243
Table E.4 Experimental results for determination of effective surface area of Flexipac 350Y 245

Table F.1 Total reflux distillation experimental results for Flexipac 350Y, chlorobenzene/ethylbenzene system 247
Table F.2 Total reflux distillation experimental results for Flexipac 350Y HC, chlorobenzene/ethylbenzene system 248

1 INTRODUCTION

1.1 History of distillation

The separation of a liquid mixture into fractions by means of distillation is an age-old process. There is some evidence that suggest that in biblical times crude distillation practices were employed to obtain essential oils and perfume (Song of Solomon 1:3). In these early, crude methods, wool was used to condense and capture the light vapours from a pot of boiling liquid, most probably water containing plant matter. The first distillation apparatus where the vapours were condensed and trapped in a second container dates back to between 100-200 AD and is attributed to the alchemists of Alexandria (Deibele, 1991). Although a variety of natural products, such as perfumes and essential oils, were separated by distillation in the period between 100-200 AD and 1100, the first recipe describing the distillation of wine dates back to around 1100 in Italy. It did, however, spread quite fast across Europe and for the next 700 years distillation was primarily used in the production of alcohol. One of the first books on distillation was published by Porta in 1553. The distillation of various oils, essences, perfumes and wine is described in detail in this book. Some of the principles employed in the design of modern distillation towers were developed by the alchemists of this period. Porta prescribes the use of different lengths for the neck of the still. The function of the different lengths of the neck was to regulate the reflux ratio. The neck served as an air-cooled condenser. Longer necks provided a larger cooling- and condensing area and thus increased the reflux ratio. Porta also describes taking several streams from the still head, with the purest product drawn from the top. Distillation apparatus consisted of only an evaporation and condensing unit up until the end of the 18th century (Deibele, 1994). Various multistage distillation apparatus were invented in the beginning of the 19th century in France, Britain and Germany. These apparatus were almost exclusively used in the production of alcohol from the various starting materials. In France wine was used as starting material, in England grain and in Germany potatoes. With some of these inventions it was possible to obtain alcohol purities in excess of 90 vol%. The distillation column as we know it today was invented in France in 1808 by Jean Baptiste Cellier-Blumenthal (Deibele, 1994). His column was equipped with an early form of the bubble cap tray and was used in the production of alcohol from wine. The first sieve tray column was patented by Aenneas Coffey in England in 1832. Packing were used as far back as 1830 when glass spheres were used in an alcohol still (Kister, 1992). During the

beginning of the twentieth century the application of distillation spread rapidly from almost exclusively being used in the production of alcoholic beverages to the primary separation technique of liquid mixtures in the chemical industries. This rapid expansion was largely due to the invention of petrol and diesel engines and the demand for fuel. Distillation is presently still the primary method used for the separation of liquid mixtures and with no technology set to replace it, will continue to be so in future.

1.2 Distillation and absorption today

The oil and natural gas industry are by far the largest users of distillation and absorption technology today. The size of the refining industry was estimated at 3.7 billion tonnes a year in 1991 and the amount of natural gas consumed in the same year in the order of 2000 billion m^3 (Darton, 1992). The total distillation capacity of refineries is estimated to exceed 5 billion tonnes a year. The natural gas industry is an important market for absorption technology since most of the natural gas is treated in absorption columns to remove water and acid gases. The petrochemicals sector is also a major user of distillation technology. In 1991 the global production of olefins and aromatics were estimated to be around 130 million tonnes a year. Without even mentioning the use of distillation and absorption technology in the chemical and pharmaceutical industry, these figures show that distillation and absorption are indeed a significant business area. Distillation and absorption are by no means a mature technology. Because of the shear size of the industry, small improvements in efficiency will result in large energy savings. It is estimated that by improving the estimation of the height equivalent to a theoretical plate, energy savings in the order of 5% and capital savings in the order of 20% may be possible. Environmental legislation and the global energy crisis in the 1970's and 1980's have stimulated research into cheaper and more energy efficient distillation and absorption technologies. This drive towards cheaper and more efficient processes has also lead to the combination of different unit operations in a single distillation column. Reactive distillation has gained huge popularity in the past decade and a lot of research effort is focussed in this area. Another capital and energy saving development is the combination of two columns in one shell, also referred to as the Petlyuk or divided wall column. With this arrangement it is possible to obtain three product streams of high purity from such a single column.

From the above figures and trends it is evident that distillation and absorption operations still pose huge challenges to the modern engineer. There is a constant

need for improving the efficiency and capacity of column internals. On the other hand there is a need for accurate models in order to be able to confidently design columns that will realize the improvements in efficiency and capacity of new column internals without resorting to huge design safety factors.

1.3 Column internals

Column internals may be classified as either trays or packing. The function of both trays and packing are to provide a large surface area for the vapour- and liquid phases to make contact with one another. When using trays, contact between vapour and liquid is established by bubbling the vapour through the liquid phase. The liquid phase is the continuous phase with the gas the dispersed phase. In packed columns the packing provides a large surface area for the liquid to wet. The area between the vapour and liquid phases is provided by liquid films and drops. The vapour is therefore the continuous phase with the liquid the dispersed phase. Both trays and packing are used extensively in modern distillation towers.

1.3.1 Trays

There are a number of different types of trays commonly used in columns. They may be broadly divided into bubble cap trays, sieve trays and valve trays. Most of the proprietary designs fall into one of these categories.

The bubble cap tray is the oldest design and has been the workhorse in columns prior to 1960 (Kister, 1992). A bubble cap tray is a flat perforated plate with pipes (also called 'gas risers') extending upwards from the perforations (holes). Caps are the placed over the 'gas risers'. These caps are equipped with slots and perforations through which the vapour escapes to bubble through the liquid (hence the naming 'bubble cap'). Compared to other trays they are expensive. They have a high turndown ratio but a low capacity. They are rarely used in modern towers.

The sieve tray is a simple design. It is basically a flat perforated plate without any ‘gas risers’ or bubble caps. They are easy to fabricate and are therefore inexpensive compared to other designs. They do however suffer from weeping (liquid flowing through the holes) and have a low turndown ratio.

A valve tray is also a flat perforated plate, but each perforation is equipped with a movable disk. At low vapour rates, these disks cover most of the open area and prevent the liquid from 'weeping'. At larger vapour rates, the disks move vertically up

and expose more of the hole area. There is an upper limit on the movement of the disks determined by the length of the restrictive legs or the caging structure. There are a variety of proprietary designs for the perforations and the 'valves'. Valve trays are frequently preferred above sieve trays because of their high turndown ratio and relative small increase in cost.

The past decade has seen some major advances in tray design that have lead to an increase in both the hydraulic capacity and tray efficiency. The hydraulic capacity has been increased by using multiple liquid downcomers. An example of such a design is the VGMD tray and VortexTray from Sulzer Chemtech. The efficiency has been increased by using various valve- and aperture designs on valve- and sieve trays to increase vapour/liquid contact and decrease dead volumes on trays.

1.3.2 Packing

Packing may be divided into three classes:

- Random packing
- Structured packing
- Grids

Random packing was first developed followed by structured packing and grids. Random- and structured packing are widely used with grids being restricted to heat transfer applications and wash services (Kister, 1992). The following discussions will focus on the development of random and structured packing

Random packing

With random packing, the packing elements are dumped into a column and form a random structure for the liquid and vapour phases to pass through. These elements are available in a wide variety of designs, sizes and materials. The development of random packing may historically be divided into three distinct phases. The different types of random packing are therefore grouped into three generations. There are a large number of proprietary designs. Some of the well known designs of the different generations are given in table 1.1 (Kister, 1992). Each successive generation improved on both the hydraulic capacity and the efficiency of the packing. The improvement from the second to the third generation was however less than from the first to the second generation of packing (Kister, 1992)

Table 1.1 Examples from different generations of random packing

First generation (1907-1950s)	Second generation (1950s-1970s)	Third generation (1970s-present)
Raschig ring	Intalox saddle	Intalox metal
Lessing ring	Super Intalox packing	Cascade Mini-rings
Berl saddle	Pall ring	Levapak
	Hy-Pak packing	Nutter rings
		Fleximax
		Hiflow ring
		Intalox Snowflake

Structured packing

The need for packing with a high efficiency combined with an extremely low pressure drop per theoretical stage lead to the development of packing with a regular or structured geometry (Billet, 1995). Kister (Kister, 1992) describes the evolution of structured packing analogous to the evolution of random packing by classifying it into different generations. The first two generations of structured packing were manufactured from wire gauze. This type of packing was quite expensive compared to random packing. They were mainly used in vacuum distillation applications where a high number of theoretical stages were required combined with an extremely low pressure drop. The development of sheet metal structured packing (3rd generation of structured packing) by Sulzer in the late 1970's revolutionized the packing industry. It made structured packing more affordable and it became competitive with conventional internals (trays, random packing). The use of structured packing rose in popularity to the point where it became the most popular column internal in use by the end of the 1980's and early 1990's. The constant drive towards an increase in capacity has lead to some modifications being made to the third generation of packing in the late 1990's. These modifications have lead to an increase in capacity with the same efficiency as the conventional third generation structured packing. Table 1.2 lists some of the well-known structured packing of the different generations. A fourth generation of packing is included in the table. With two of these packing, namely Rombopak and Optiflow, there has been a move away from the corrugated sheet structure towards a more open lamella structure. There has been mixed success obtained with this generation of packing. While an increase in efficiency has been realized, this has been at the expense of capacity in some instances.

Table 1.2 Examples from different generations of structured packing

First generation (1940's-1950's)	Second generation (1950's-1970's)	Third generation (1970's-1990's)	Fourth generation (1990's-present)
Panapak	Goodloe	Sulzer Mellapak	Kuhni Rombopak
	Hyperfil	Koch Flexipac	Sulzer Optiflow
	Sulzer, Koch BX	Montzpak-B1	High Capacity
		Gempak	modifications

1.3.3 Trays or packing?

While both trays and packing may be used to perform a given separation, there are factors that would favour either trays or packing. There are also factors that would influence the choice between random- and structured packing. Kister (Kister, 1992) lists the following factors favouring the use of packing (random or structured) above trays:

- Vacuum systems
- Low-pressure-drop applications
- Vacuum column revamps
- Small-diameter columns
- Foaming systems
- Low liquid hold-up required

Because of the high efficiency and low pressure drop of structured packing, it would be favoured above random packing in most applications where packing is preferred above trays. It is however much more expensive than random packing (between 3 and 10 times). Economic considerations therefore play a large role in the choice between random and structured packing. There are however also some exceptions where random packing is preferred above structured packing. Structured packing performs poorly at high operating pressures, in systems with high viscosity and in systems with high surface tensions. The reasons for the poor performance in high-pressure systems are not clearly understood. There are however conflicting views in literature regarding the use of structured packing at high pressure. Structured packing is known to perform poorly in aqueous systems. The poor performance is attributed to poor wetting due to a high surface tension. This problem seems to be most serious when stainless steel is used. The poor performance in systems with high viscosity is not fully understood yet. The older generations of structured packing also performs poorly at high liquid loads, although it would seem that the modifications made to the third generation has improved this situation.

There are situations where trays are favoured over packing. Kister, 1992, lists some of these situations as:

- Solids present in feed
- High liquid rates
- Large diameter columns
- Complex columns
- Uncertainty in performance prediction

Most of the arguments favouring the use of trays over packing presented by Kister (Kister, 1992) stem from practical considerations. Packing tends to become blocked when there is a large percentage of solids present in the feed or when coking or polymerisation occurs. Trays are favoured because they are easier to clean compared to packing. In large diameter columns, good liquid and vapour distribution becomes essential to the efficient operation of both random and structured packing. Although efficient distributors are available for large diameter columns, it is often more economical to use a tray column where mal-distribution of the phases is much less of a problem. It is easier to accommodate heaters and coolers inside the column shell when using trays compared to when using packing (complex columns). High liquid rates may be accommodated in tray columns with the use of multi pass trays. These are all valid considerations favouring the use of trays over packing. What is of concern though is when trays are favoured above packing because of the uncertainty in predicting the performance of packing. The state of the art in predicting packing performance is such that the same author (Kister, 1992) prefers rules of thumb and data interpolation above semi theoretical models in predicting packing efficiency. The problem is also more severe with structured packing. This is probably because it has not been in use for as long a period as random packing. There have only been relatively few studies concerned with predicting structured packing efficiency.

1.4 Modelling of distillation and absorption

In order to utilize the advantages that modern column internals offer, accurate mathematical models are needed to predict their efficiency and capacity.

For more than a century the equilibrium stage model has been used to model distillation and absorption equipment. The equilibrium stage model divides a column into a number of stages where the liquid and vapour leaving such a stage are in thermodynamic equilibrium. In order to link these theoretical stages to real trays or

beds of packing in columns, concepts like tray efficiencies and height equivalent to a theoretical plate (HETP) are introduced. While these concepts are adequate for describing binary systems, they are extremely confusing in multi component systems. In some circles it is believed that these concepts have severely retarded the development of distillation and absorption (Wesselingh, 1997).

The limitations of the equilibrium model in multi component and non-ideal systems, has lead to the development of the non-equilibrium model or rate-based approach (Krishnamurthy, 1985). With this modelling technique, thermodynamic equilibrium is only assumed at the interface between the vapour and liquid phases. Rate equations govern the rate at which mass and heat are transferred from the interface to the bulk of the liquid and vapour phases leaving a non-equilibrium stage. Although this is an improvement on the equilibrium model, it is still not the exact model that engineers dream of.

The ideal 'exact' model (Wesselingh, 1997) would be to subdivide the column into a large number of sub domains (or grid) and solve the difference forms of the equations of fluid motion, diffusion and energy transfer on this computational grid. There are, however, still a few problems associated with doing this. The extremely large number of sub domains that would be necessary to adequately capture all the flow phenomena can not be accommodated by even the most advanced computer available at present. Even if this was the case, there is still a long way to go in understanding the physics governing multiphase, turbulent flow.

Since it is at present not possible to obtain an 'exact' model, simplified hydraulic- and mass transfer models are needed in the equilibrium and non-equilibrium modelling approaches in order to predict the capacity and efficiency of column internals. There are a large number of correlations and semi-empirical models available in literature on the capacity and efficiency of trays and random packing. Although structured packing offers significant capacity and efficiency advantages in some applications, there seems to be a lack of accurate efficiency models. It will also be shown that some rather disturbing results are obtained with some of the efficiency models published in the literature.

1.5 Aims of this study

This study focuses on the modelling of the capacity and efficiency of the sheet metal structured packing Flexipac 350Y, manufactured and marketed by Koch-Glitsch. It is

a typical third generation structured packing. A modification has recently been made to this packing that has lead to an increase in its capacity. At present this packing enjoys a fair portion of the market share with Koch-Glitsch performing at least one installation per week of the new high capacity version of Flexipac (Nieuwoudt, December 2003). There are, however, only a few mass transfer models available in literature to model the efficiency and capacity of sheet metal structured packing. Design engineers rarely trust these models and often resort to expensive pilot plant testing when designing a column containing structured packing. A major cause of concern in these mass transfer models is the accurate correlation of the vapour phase mass transfer coefficient and effective surface area. Correlations for these quantities are often fitted on distillation data rather than measuring and correlating them independently. The primary objective of this study is therefore to develop accurate correlations for the vapour phase mass transfer coefficient and effective surface area. Accurate correlations will allow design engineers to use mass transfer models with greater confidence and therefore save on time and money spent on pilot plant testing. The aims of this study may be summarized as follows:

- Comparing results obtained with existing models in modelling the capacity of Flexipac 350Y and identifying those more suitable.
- Measuring and correlating the vapour phase mass transfer coefficient for Flexipac 350Y independently from the effective surface area.
- Assessing the suitability of Computational Fluid Dynamics (CFD) in modelling the vapour phase mass transfer coefficient in sheet metal structured packing.
- Measuring and correlating the effective interfacial area for vapour phase mass transfer for Flexipac 350Y independently from the vapour phase mass transfer coefficient.
- Comparing the results with existing efficiency and capacity models.
- Quantifying the performance of the high capacity packing in terms of capacity and efficiency and comparing it with the standard packing.

2 MODELLING OF DISTILLATION

2.1 Introduction

The equilibrium or stage based model has been used to model distillation columns for more than a century. The limitations of this approach have been recognized from an early stage. But, this approach is so simple and elegant from a mathematical point of view that it continues to be the primary method used in designing new distillation columns. The recent advances made in the field of multicomponent mass transfer coupled with modern computing power and speed, have triggered the development of the so-called 'non-equilibrium' or 'rate-based' approach. It is fundamentally more correct than the equilibrium model. There is, however, a price to pay in terms of complexity and computing resources. This chapter aims to introduce the different modelling approaches, and to highlight their strengths and weaknesses. Before discussing the different approaches, it is necessary to introduce basic concepts regarding mass transfer across phase boundaries.

2.2 Mass transfer across interfaces

The physical process that occurs inside a packed column is that of mass transfer across a vapour/liquid interface. The theory describing diffusional mass transfer in binary systems is well developed (Cussler, 1984). Fick's Law is often used because of its simplicity and similarity to Fourier's Law for heat transfer (Incropera and De Witt, 1990). In multicomponent mass transfer the Maxwell-Stefan relation for diffusional mass transfer is used because it is generally less composition dependent compared to the Fick diffusion coefficient (Taylor and Krishna, 1993). In the following discussion on mass transfer across a phase boundary, the Maxwell-Stefan approach will be used. Only a brief review will be given. The literature should be consulted for a more complete discussion (Taylor and Krishna, 1993).

2.2.1 Definition of mass transfer coefficients

It is customary to define a mass transfer coefficient when estimating mass transfer rates across a phase boundary. In order to avoid confusion, the mass transfer coefficient in a binary system is defined in the same way as suggested by (Bird et al., 1960) and used by (Taylor and Krishna, 1993):

$$k_b = \lim_{N_1 \to 0} \frac{N_{1,b} - x_{1,b}N_t}{\left(x_{1,b} - x_{1,I}\right)} = \frac{J_{1,b}}{c_t \Delta x_1} \qquad (2.1)]$$

The driving force is taken as the difference between the mole fraction of the component in the bulk phase ($x_{1,b}$) and the interface ($x_{1,I}$). k_b is expressed in units of [m/s]. The mass transfer coefficient defined by Equation 2.1 is the zero flux mass transfer coefficient in terms of the bulk phase. For finite mass transfer rates, the mass transfer coefficient is defined by:

$$k_b^* = \frac{N_{1,b} - x_{1,b}N_t}{\left(x_{1,b} - x_{1,I}\right)} = \frac{J_{1,b}}{c_t \Delta x_1} \tag{2.2}$$

The finite- (or high-) and zero flux coefficient are related through:

$$k_b^* = k_b \Xi_b \tag{2.3}$$

where Ξ_b is the high flux correction factor. The mass transfer coefficient defined in Equation 2.1 (k_b) corresponds to conditions of vanishing small mass transfer rates. In reality, the velocity and composition profiles are distorted by the diffusion of the species across the interface. The high flux correction factor (Ξ_b) accounts for this distortion when calculating the high flux coefficient (k_b*) from the zero flux coefficient (k_b). Most mass transfer correlations are fitted on experimental data where the mass transfer rates are low. The zero flux coefficient is therefore obtained from these correlations and should be corrected according to Equation 2.3 when used in situations where the mass transfer rate across an interface is high.

For a multicomponent system the diffusional flux is given by:

$$\begin{aligned}\left(J_b\right) &= \left(N\right) - \left(x_b\right)N_t \\ &= c_t\left[k_b^*\right]\left(\Delta x\right)\end{aligned} \tag{2.4}$$

The high flux mass transfer coefficient is needed to determine the diffusional fluxes J_i that in turn are needed to determine the molar fluxes N_i. In order to determine the diffusional fluxes and therefore the molar fluxes, we need to have methods for determining the low flux mass transfer coefficients and the high flux correction factors. A few models have been proposed to model the mass transfer across a phase boundary. The film model will be discussed in detail. A brief overview of the remaining models will follow.

2.2.2 Models for mass transfer at phase boundaries

The Film model

The most common (and simplest) approach to modelling mass transfer across interfaces is the well-known film theory proposed by Whitman (Whitman, 1923). From a mass transfer point of view the film model is attractive because of its simplicity. It is used more often than any of the other models. According to this model there exists a stagnant layer of fluid next to the phase boundary through which mass transfer occurs by molecular diffusion alone. It is assumed that the level of turbulence in the bulk phase is high and will eliminate any concentration gradients. The concentration gradient is confined to the stagnant layer next to the phase boundary. Krishna and Standart (Krishna and Standart, 1976) developed an exact solution to the Maxwell-Stefan relations for the film model for an ideal gas mixture. For an ideal gas mixture the Fick diffusion coefficient is constant and this is also a fair approximation for nonideal fluid mixtures where the change in concentration is small. The matrix of low flux mass transfer coefficients is given by:

$$[k] = [R]^{-1} \tag{2.5}$$

where

$$R_{ii} = \frac{y_i}{\kappa_{in}} + \sum_{\substack{k=1 \\ k\neq i}}^{n} \frac{y_k}{\kappa_{ik}}$$

$$R_{ij} = -y_i \left(\frac{1}{\kappa_{ij}} - \frac{1}{\kappa_{in}} \right) \tag{2.6}$$

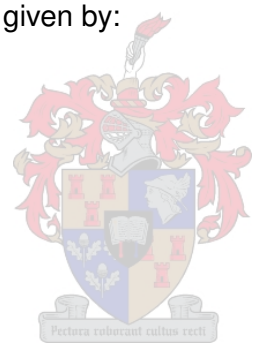

κ_{ij} is the low flux mass transfer coefficient for the i-j binary pair and is defined by:

$$\kappa_{ij} = \frac{D'_{ij}}{\ell} \tag{2.7}$$

If the diffusion fluxes are calculated at edge of the 'film', the molar fractions used in Equation 2.4 are the bulk phase molar fractions. When the diffusion fluxes are calculated at the interface the interface molar fractions are used. The high flux correction factors at the edge of the 'film' and at the interface are given respectively by:

$$[\Xi_0] = [\Phi]\left[\exp[\Phi] - [I]\right]^{-1} \tag{2.8}$$

and

$$[\Xi_\delta] = [\Xi_0]\exp[\Phi] \tag{2.9}$$

[I] is the identy matrix and [Φ] is the rate factor matrix. The elements of the rate factor matrix are calculated with:

$$\Phi_{ii} = \frac{N_i}{c_t \kappa_{in}} + \sum_{\substack{k=1 \\ k \neq i}}^{n} \frac{N_k}{c_t \kappa_{ik}}$$
$$\Phi_{ij} = -N_i \left(\frac{1}{c_t \kappa_{ij}} - \frac{1}{c_t \kappa_{in}} \right) \qquad (2.10)$$

Assuming a constant D' along the diffusion path does not influence the molar flux to a significant extent (Taylor and Krishna, 1993). This assumption would lead to the use of average mole fractions in calculating [k] rather than boundary mole fractions. The rate factor matrix [Φ] simplifies to [Ψ] with elements:

$$\Psi_{ii} = \frac{y_{i,av} N_t}{c_t \kappa_{in}} + \sum_{\substack{k=1 \\ k \neq i}}^{n} \frac{y_{k,av} N_t}{c_t \kappa_{ik}}$$
$$\Psi_{ij} = -y_{i,av} N_t \left(\frac{1}{c_t \kappa_{ij}} - \frac{1}{c_t \kappa_{in}} \right) \qquad (2.11)$$

For a non-ideal fluid system Krishna (Krishna, 1977) developed an approximate solution by assuming that the thermodynamic rate factors Γ_{ik} and Maxwell-Stefan diffusivity D'_{ik} are constant along the diffusion path. The low flux mass transfer coefficients are calculated with (using the appropriate molar fraction):

$$[k] = [R]^{-1} [\Gamma_{av}] \qquad (2.12)$$

The elements of the matrix [R] are the same as in the ideal solution (Equation 2.6). The high flux correction factors are given by:

$$[\Xi_0] = [\Theta] \left[\exp[\Theta] - [I] \right]^{-1} \qquad (2.13)$$

and

$$[\Xi_\delta] = [\Xi_0] \exp[\Theta] \qquad (2.14)$$

where

$$[\Theta] = [\Gamma_{av}]^{-1} [\Phi] \qquad (2.15)$$

[Φ] is the same as defined before.

The binary low flux mass transfer coefficients are usually calculated from a mass transfer correlation with the appropriate diffusivity. The molar fluxes (N_i) are needed in calculating the multi component low flux mass transfer coefficients and high flux correction factors. An iterative scheme is therefore required in solving for N_i. A number of algorithms are given by Taylor and Krishna (Taylor and Krishna, 1993).

Penetration theory

According to the penetration theory of Higbie the film next to the interface is constantly replenished by eddies from the bulk of the fluid. These eddies stay at the interface for a period of time. During this time mass transfer takes place normal to the interface due to molecular diffusion (the eddies are static next to the interface). The eddies then leave the interface to mix again with the bulk fluid. All eddies are assumed to stay at the interface for the same period of time. Equations for the low flux mass transfer coefficients and high flux correction factors are presented by Bird et al. (Bird et al., 1960) for binary systems and by Taylor and Krishna (Taylor and Krishna, 1993) for multicomponent systems. The penetration theory predicts the mass transfer coefficient to be proportional to the square root of the diffusivity.

Random surface renewal theory

Danckwerts (Danckwerts, 1951) refined the penetration theory by enforcing a residence time distribution on the eddies at the interface. Mass transfer coefficients and high flux correction factors for binary and multicomponent systems are given by Taylor and Krishna (Taylor and Krishna, 1993). This theory predicts the same dependence of the mass transfer coefficients on the diffusivity as the penetration theory.

Film penetration theory

Toor and Marchello (Toor and Marchello, 1958) showed that the film model and the penetration- and surface renewal models are complementary to each other and are limiting cases of a more general solution. According to this general solution the penetration- and surface renewal models will predominate in a developing boundary layer while the film model will predominate in a fully developed boundary layer. Between the two regions both mechanisms will contribute to the transfer process.

Boundary layer theory

In the boundary layer theory (Bird et al., 1960) allowance is made for a two-dimensional velocity profile. Transfer therefore occurs due to molecular diffusion in a direction normal to the interface and by convection parallel to the interface. Mass transfer coefficients and high flux correction factors are given by Bird et al. (Bird et al., 1960) in the form of plots for transfer from a flat surface to a laminar boundary layer.

Turbulent mass transfer

In turbulent flows there will be an extra contribution to the overall transfer process in the form of turbulent eddies. A more detailed discussion of turbulence is given in chapter 3.

2.3 The Equilibrium Model

2.3.1 Historical perspective

The first theoretical equations for continuous, steady state distillation were developed by Sorel in 1893. It was based on the concept of an equilibrium stage. These equations formed the basis of the well known graphical solution methods: The Ponchon-Savarit method and the McCabe-Thiele construction. These methods were replaced by rigorous computational methods when digital computers became available. Numerous solution algorithms have been developed over the years (Naphtali and Sandholm, 1971) (Boston and Sullivan, 1972) (Tomich, 1970) (Wang and Henke, 1966) which have been implemented into commercially available process simulation software. It has been the subject of quite a few books (Henley and Seader, 1981, King, 1980, Holland, 1975).

2.3.2 Model equations

In the equilibrium model the column is split up into a number of equilibrium stages (1 to N stages). Figure 2.1 is a representation of an equilibrium stage (stage j). The vapour and liquid leaving an equilibrium stage are assumed to be in thermodynamic equilibrium, i.e. there are no temperature difference and the mole fractions of the components in both phases correspond to their equilibrium values. Material and energy balances are performed around each stage. These balances are collectively known as the '*MESH*' equations: *M* for material balances, *E* for equilibrium relations, *S* for summation equations and *H* for enthalpy balances (Henley and Seader, 1981, Holland, 1975, Foust et al., 1980).

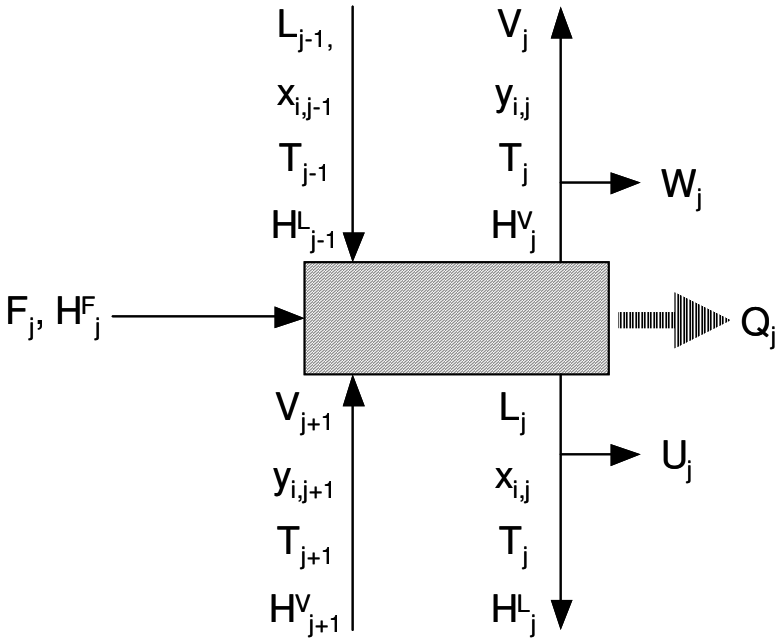

Figure 2.1 Stage j in equilibrium model

Overall material balance:

$$M_{t,j} = L_{j-1} + V_{j+1} + F_j - \left(L_j + U_j\right) - \left(V_j + W_j\right) = 0 \qquad (2.16)$$

Component balance:

$$M_{i,j} = L_{j-1}x_{i,j-1} + V_{j+1}y_{i,j+1} + F_j z_{i,j} - \left(L_j + U_j\right)x_{i,j} - \left(V_j + W_j\right)y_{i,j} = 0 \qquad (2.17)$$

Equilibrium relations:

$$E_{i,j} = y_{i,j} - K_{i,j}x_{i,j} = 0 \qquad (2.18)$$

Summation equations:

$$S_j = \sum_{i=1}^{c}\left(x_{ij} - y_{ij}\right) = 0 \qquad (2.19)$$

Enthalpy balances:

$$H_j = L_{j-1}H_{j-1}^{L} + V_{j+1}H_{j+1}^{V} + F_j H_j^{F} - \left(L_j + U_j\right)H_j^{L} - \left(V_j + W_j\right)H_j^{V} - Q_j = 0 \qquad (2.20)$$

Solution procedure

If there are c components in the system, 2c+3 equations have to be solved for each stage. The 2c+3 variables are represented by a vector as:

$$\left(x_j\right)^T = \left(V_j, y_{1,j}, y_{2,j}, .., y_{c,j}, T_j, x_{1,j}, x_{2,j}, .., x_{c,j}, L_j\right) \qquad (2.21)$$

The corresponding 2c+3 equations are represented by a vector as:

$$\left(F_j\right)^T = \left(M_{t,j}, M_{1,j}, M_{2,j}, .., M_{c,j}, H_j, E_{1,j}, E_{2,j}, .., E_{c,j}, S_j\right) \qquad (2.22)$$

There are a vast number of iterative numerical methods and techniques used to solve these equations. The most common methods are equation tearing procedures and simultaneous correction procedures. The bubble point method (Wang and Henke, 1966) and sum-rates method are examples of the former class of methods. The Naphtali-Sandholm simultaneous correction method (Naphtali and Sandholm, 1971) and the inside out method (Boston and Sullivan, 1972) are examples of the latter class of procedures. In all the methods the well-known Thomas algorithm is widely used because of the tridiagonal matrix form of the equations. The simultaneous correction procedures use a Newton Raphson method in conjunction with a matrix generalization of the Thomas algorithm. A detailed discussion of the methods and algorithms are beyond the scope of this text and can be found elsewhere (Seader and Henley, 1998).

2.3.3 Tray/stage efficiency in tray columns

The method discussed above assumes that thermodynamic equilibrium is achieved between the liquid and vapour leaving a stage, with respect to both temperature and composition. This assumption is acceptable for heat transfer in systems where the temperature differences between stages are small. In most cases the assumption of equilibrium between vapour- and liquid compositions are not reasonable. This limitation is overcome in tray columns by introducing stage- or tray efficiencies. The method proposed by Murphree is widely used. According to this method the component K-value in equation 2.3, defined as

$$K_{i,j} = \frac{y_{i,j}}{x_{i,j}} \tag{2.23}$$

are replaced with the Murphree vapour phase tray efficiency:

$$(E_{MV})_{i,j} = \frac{y_{i,j} - y_{i,j+1}}{y^{*}_{i,j} - y_{i,j+1}} \tag{2.24}$$

The equilibrium composition $y_{i,j}^*$ is obtained from equation 2.6. The Murphree efficiency is thus the ratio of the actual change in vapour phase composition to the change that would have occurred if equilibrium were achieved. A measure of success was achieved in developing correlations for the Murphree efficiency and using it in binary and ideal or near-ideal multicomponent systems. It has been demonstrated that the Murphree efficiency varies widely from component to component and tray to tray in non-ideal multicomponent mixtures, even becoming negative.

2.3.4 Height equivalent to a theoretical plate (HETP) in packed columns

The most common approach in evaluating the performance of packed columns in distillation is in terms of the height equivalent to a theoretical plate, or HETP. This method does not have any theoretical basis and is only used out of convenience. It is related to the height of packing needed for a specific separation by:

$$HETP = \frac{z}{N_{eq}} \tag{2.25}$$

N_{eq} is the number of equilibrium stages needed to model the separation performed in a real column with a packed height z.

2.4 Modelling distillation in packed columns: The HTU/NTU concept

2.4.1 Historical perspective

The packing in a packed column provides surface area for the continuous contact between the liquid and vapour phases. This is quite different from the stage concept that has been discussed up to this point. A method was proposed by Chilton and Colburn (Chilton and Colburn, 1935) whereby the 'HETP' concept is replaced by the 'HTU' method. With this new method differential equations are integrated between the top and bottom compositions of the column to determine the height of packing needed for a specific separation. At first it was assumed that the resistance to mass transfer is entirely in the vapour phase. The method was extended to account for resistance in both phases (Colburn, 1941). This method is still used extensively today, especially in the design of packed absorption columns (Sherwood et al., 1975, Seader and Henley, 1998, Foust et al., 1980, Henley and Seader, 1981, Holland, 1975).

2.4.2 Model equations

A mass balance is performed around a differential section of the tower (Foust et al., 1980) (Figure 2.2):

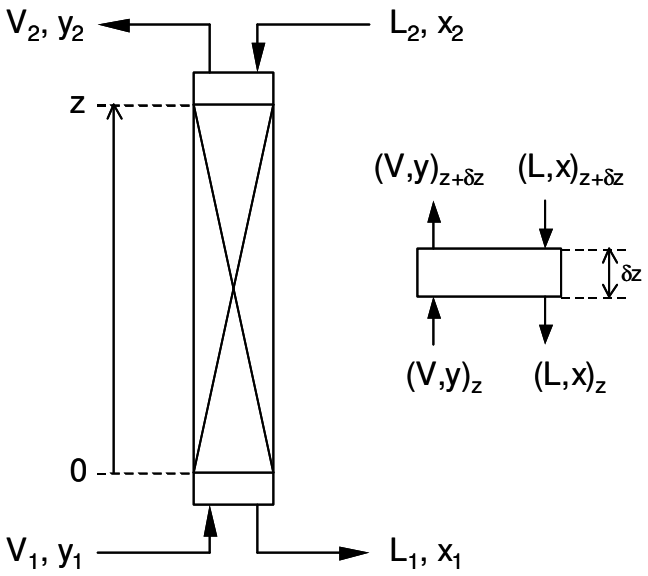

Figure 2.2 Packed column with differential element

$$dV = dL \tag{2.26}$$

with the corresponding component balance given by:

$$d(Vy) = d(Lx) \tag{2.27}$$

The rate of change of a component in a phase is equal to the rate at which that component is transferred to the phase. For equimolar counter diffusion the mass transfer rate for a component in the vapour phase can be expressed in terms of the vapour phase mass transfer coefficient and the driving force:

$$d(Vy) = c_t^G k_G (y_i - y) aSdz \tag{2.28}$$

where a is the interfacial area per unit volume of packing and S the cross section area of the empty column. In this equation the flux correction factor has been ignored.

It is more convenient to express the mass transfer rate in terms of the overall gas phase mass transfer coefficient:

$$d(Vy) = c_t^G k_{OG} (y^* - y) aSdz \tag{2.29}$$

y* is the mole fraction of the component corresponding to the concentration in equilibrium with the bulk liquid phase concentration. The vapour phase mass transfer coefficient (k_G) and overall vapour phase mass transfer coefficient (k_{OG}) is related through (Taylor and Krishna, 1993):

$$k_{OG} = \frac{c_t^G}{c_t^L}\frac{m}{k_L} + \frac{1}{k_V} \tag{2.30}$$

where m is the slope of the equilibrium curve.

Equation 2.12 may be used to solve the column height required by integrating between bottom and top compositions:

$$\int_0^z dz = \int_{y_1}^{y_2} \frac{1}{aS} \frac{d(Vy)}{c_t^V k_{OG}(y^* - y)} \tag{2.31}$$

If L and V are assumed constant over the length of the column and the physical properties do not vary appreciably so that a, c_t^V and k_{OG} stay constant, equation 2.14 simplifies to:

$$z = \frac{V}{aSc_t^G k_{OG}} \int_{y_1}^{y_2} \frac{d(y)}{(y^* - y)} \tag{2.32}$$
$$= H_{T,OG} N_{T,OG}$$

The quantity outside the integral is called the 'height of a transfer unit' (H_T) while the integral term is called the 'number of transfer units' (N_T). The driving force and mass transfer coefficients used in this equation are based on the bulk vapour phase and are indicated by the subscript (OG). An approximation of the integral term, or number of transfer units ($N_{T,OG}$) is given by:

$$N_{T,OG} = \frac{(y_2 - y_1)}{(y^* - y)_{LM}} \tag{2.33}$$

where

$$(y^* - y)_{LM} = \frac{(y_2^* - y_2) - (y_1^* - y_1)}{\ln \frac{(y_2^* - y_2)}{(y_1^* - y_1)}} \tag{2.34}$$

If the slope of the equilibrium line is constant, then this approximation simplifies to:

$$N_{T,OG} = \frac{\ln\left(K \,{}^{V}\!/_{L}\right)}{\left(K \,{}^{V}\!/_{L} - 1\right)} \tag{2.35}$$

In distillation the assumption of constant L and V is only true for equimolar transfer and for columns operated under conditions of total reflux. If the method is to be used for packed distillation columns in general, then the simplifications introduced by assuming constant L and V and constant properties cannot be made and equation 2.29 has to be integrated over the height of the column, or at least separately for the rectification- and stripping sections. The method is, however, widely applied to an equilibrium stage where the assumptions do apply (Sherwood et al., 1975). The

height of packing determined in this way is simply the HETP. A summation of the HETP's over all the equilibrium stages give the total height of packing. An extension of the method using multicomponent mass transfer theory is giving by Taylor and Krishna (Taylor and Krishna, 1993).

2.5 The Non-equilibrium Model

2.5.1 Historical perspective

Real stages in a distillation column rarely operate at equilibrium conditions. Stage- or tray efficiencies were introduced into the equilibrium model to account for this departure from equilibrium. The Murphree efficiency described previously is one of many such definitions. For a multicomponent mixture containing c components, there are c-1 independent component efficiencies. These efficiencies are usually taken to be equal to one another. A wide body of evidence suggested that this is not true (Krishna et al., 1977, Vogelpohl, 1979). This is because in multicomponent mixtures the diffusion of different species is coupled with one another. Models that account for these interaction effects became available (Krishna and Standart, 1979). At first these models were used to estimate efficiencies in multicomponent systems (Vogelpohl, 1979). These models were, however, quite complicated. A new modelling approach was suggested (Krishnamurthy and Taylor, 1985a) where the multicomponent mass transfer models are used directly instead of in the form of tray efficiencies. The model was tested against binary and multicomponent distillation data, and found to yield satisfactory results (Krishnamurthy and Taylor, 1985b). It was also compared with the equilibrium stage model (with tray efficiencies) and found to be superior (Krishnamurthy and Taylor, 1985c). This model is called the non-equilibrium model or rate-based approach and will be discussed in more detail in the next paragraph. Since its inception there has been various modifications and extensions. The solution algorithm was improved (Powers et al., 1988) and the model was extended to include pressure as a variable and to account for weeping and entrainment in plate columns (Taylor et al., 1994). It has also been used to model reactive separation processes (Higler et al., 1998, Higler et al., 1999a, Higler et al., 1999b).

2.5.2 Model equations

In the non-equilibrium model the column is again split up into a number of stages (1 to N). Phase equilibrium is only assumed at the interface between two adjoining phases. This is fundamentally different from the equilibrium approach where

thermodynamic equilibrium is assumed between the liquid and vapour leaving a stage. In the non-equilibrium model, separate material- and energy balances are performed for each phase. These balances are linked by mass- and energy transfer across the interface. Collectively the equations for the non-equilibrium model are known as the '*MERSHQ'* equations: *M* for material balances, *E* for energy balances, *R* for transfer rate equations, *S* for summation equations, *H* for hydraulic equations and *Q* for equilibrium equations. Figure 2.3 represents stage j in the non-equilibrium model

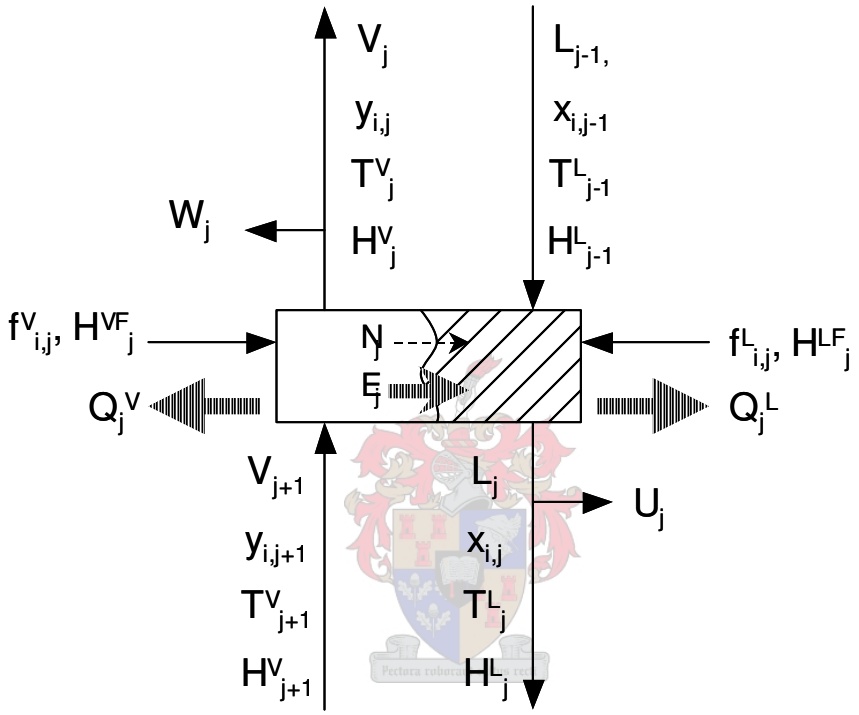

Figure 2.3 Stage j in non-equilibrium model

Conservation equations for the vapour phase:

Component material balance for species i in the vapour phase:

$$M_{i,j}^{V} = \left(V_j + W_j\right) y_{i,j} - V_{j+1} y_{i,j+1} - f_{i,j}^{V} + N_{i,j}^{V} = 0 \qquad (2.36)$$

where $f_{i,j}^{V}$ is the vapour feed flow rate of component i on stage j.

Overall material balance for the vapour phase:

$$M_{t,j}^{V} = V_j - V_{j+1} - F_j^{V} + W_j + N_{t,j}^{V} = 0 \qquad (2.37)$$

where F_j^{V} is the total vapour feed flow rate to stage j.

Energy balance for the vapour phase:

$$E_j^{V} = \left(V_j + W_j\right) H_j^{V} - V_{j+1} H_{j+1}^{V} - F_j^{V} H_j^{VF} + Q_j^{V} + E_j^{V} = 0 \qquad (2.38)$$

Conservation equations for the liquid phase:

Component material balance for species i in the liquid phase:

$$M_{i,j}^{L} = \left(L_j + U_j\right) x_{i,j} - L_{j+1} x_{i,j+1} - f_{i,j}^{L} - N_{i,j}^{L} = 0 \tag{2.39}$$

where $f_{i,j}{}^{L}$ is the liquid feed flow rate of component i on stage j.

Overall material balance for the liquid phase:

$$M_{t,j}^{L} = L_j - L_{j+1} - F_j^{L} + U_j - N_{t,j}^{L} = 0 \tag{2.40}$$

where $F_j{}^{L}$ is the total liquid feed flow rate to stage j.

Energy balance for the liquid phase:

$$E_j^{L} = \left(L_j + U_j\right) H_j^{L} - L_{j+1} H_{j+1}^{L} - F_j^{L} H_j^{LF} Q_j^{L} - E_j^{L} = 0 \tag{2.41}$$

Conservation equations for the interface:

There is no accumulation of material at the interface:

$$M_{i,j}^{I} = N_{i,j}^{V} - N_{i,j}^{L} = 0 \tag{2.42}$$

An energy balance performed around the interface yields:

$$E_j^{I} = E_j^{V} - E_j^{L} = 0 \tag{2.43}$$

Equilibrium equations

Equilibrium between vapour and liquid is assumed at the interface:

$$Q_{i,j}^{I} = K_{i,j} x_{i,j}^{I} - y_{i,j}^{I} = 0 \tag{2.44}$$

In addition the mole fractions at the interface should sum to unity:

$$S_j^{VI} = \sum_{i=1}^{c} y_{i,j}^{I} - 1 = 0 \tag{2.45}$$

$$S_j^{LI} = \sum_{i=1}^{c} x_{i,j}^{I} - 1 = 0 \tag{2.46}$$

Hydraulic equation

With the pressure on the first (top) stage specified, the pressure across the column could be calculated from a suitable model. The pressure on stage j is calculated from:

$$P_j = P_j - P_{j-1} - \left(\Delta P_{j-1}\right) = 0 \tag{2.47}$$

Rate equations

The total mass transfer rate for the vapour phase is given by:

$$\left(N_j^{V}\right) = c_{t,j}^{V} \left[k_j^{V}\right] \left[\Xi_j^{V}\right] a_j \left(y_j - y_j^{I}\right) + N_{t,j}^{V} \left(y_j\right) \tag{2.48}$$

and for the liquid phase:

$$\left(N_j^L\right) = c_{t,j}^L \left[k_j^L\right]\left[\Xi_j^L\right] a_j \left(x_j^I - x_j\right) + N_{t,j}^L \left(x_j\right) \tag{2.49}$$

$[k_j^V]$ and $[k_j^L]$ are the matrices of multicomponent low flux mass transfer equations.

The energy transfer rate for the vapour phase is obtained from:

$$E_j^V = h_j^V a_j \left(T_j^V - T_j^I\right) + \sum_{i=1}^{c} N_{i,j} \bar{H}_{i,j}^V \tag{2.50}$$

The energy transfer rate for the liquid phase is obtained from:

$$E_j^L = h_j^L a_j \left(T_j^I - T_j^L\right) + \sum_{i=1}^{c} N_{i,j} \bar{H}_{i,j}^L \tag{2.51}$$

Reduction in number of variables

A reduction in the total number of unknown variables is possible because only one set of mass transfer rates is independent:

$$N_{i,j} = N_{i,j}^V = N_{i,j}^L \tag{2.52}$$

The mass transfer rates for the vapour and liquid phases in Equations 2.36 and 2.39 are replaced with $N_{i,j}$ and the mass transfer rates (Equations 2.48 and 2.49) are combined with the interface material balances (Equation 2.42) to give:

$$R_{i,j}^V = N_{i,j} - N_{i,j}^V = 0 \tag{2.53}$$

where $$N_{i,j}^V = f\left(k_{ik,j}^V, a_j, y_{k,j}, y_{k,j}^I, N_{k,j}^V\right)_{k=1,2,..,c} \tag{2.54}$$

and

$$R_{i,j}^L = N_{i,j} - N_{i,j}^L = 0 \tag{2.55}$$

where $$N_{i,j}^L = f\left(k_{ik,j}^L, a_j, x_{k,j}, x_{k,j}^I, N_{k,j}^L\right)_{k=1,2,..,c} \tag{2.56}$$

Only c-1 of these equations are independent. The mass transfer rate for the last component is implicit in the energy balances. The energy transfer rates (Equations 2.50 and 2.51) are combined with the interface energy balance (Equation 2.43) to give:

$$E_j^I = h_j^V a_j \left(T_j^V - T_j^I\right) - h_j^L a_j \left(T_j^I - T_j^L\right) + \sum_{i=1}^{c} N_{i,j} \left(\bar{H}_{i,j}^V - \bar{H}_{i,j}^L\right) = 0 \tag{2.57}$$

Solution procedure

The 5c+6 variables for each stage are represented by a vector as:

$$\left(x_j\right)^T = \left(V_j, y_{1,j}, y_{2,j}, .., y_{c,j}, T_j^V, y_{1,j}^I, y_{2,j}^I, .., y_{c,j}^I, x_{1,j}^I, x_{2,j}^I, .., x_{c,j}^I, T_j^I, L_j, x_{1,j}, x_{2,j}, .., x_{c,j}, T_j^L, N_{1,j}, N_{2,j}, .., N_{c,j}, P_j\right) \quad (2.58)$$

The corresponding 5c+6 equations are represented by a vector as:

$$\left(F_j\right)^T = \left(M_{t,j}^V, M_{1,j}^V, M_{2,j}^V, .., M_{c,j}^V, E_j^V, R_{1,j}^V, R_{2,j}^V, .., R_{c-1,j}^V, S_j^{VI}, Q_{1,j}^I, Q_{2,j}^I, .., Q_{c,j}^I, E_j^I, M_{t,j}^L, M_{1,j}^L, M_{2,j}^L, .., M_{c,j}^L, E_j^L, R_{1,j}^L, R_{2,j}^L, .., R_{c-1,j}^L, S_j^{LI}, P_j\right) \quad (2.59)$$

The condenser and reboiler in a non-equilibrium model are modelled as equilibrium stages. Simultaneous correction methods are widely used to solve the set of non-linear equations (Taylor and Krishna, 1993, Krishnamurthy and Taylor, 1985a). When using a simultaneous correction method, it is necessary to supply an initial estimate for all the variables. It is important that these initial estimates are sensible in the case of the non-equilibrium model. Incorporated into the model are models (empirical and fundamental) for mass transfer coefficients and pressure drop. Initial estimates outside the physical bounds of these 'closure' models will cause the non-equilibrium model to diverge. Because of pressure being included as a variable, a computational penalty is added in the evaluation of partial derivatives of all the equations with respect to pressure (especially the thermodynamic properties). Although there are quite a few more equations per stage to solve, and the added complexity of obtaining partial derivatives of equations with respect to pressure, a non-equilibrium model is about as difficult to converge as its equilibrium counterpart (Krishnamurthy and Taylor, 1985a) The computational effort is further reduced if the high flux correction factors are omitted. They were found not to be important in distillation (Powers et al., 1988).

2.6 Concluding remarks

Despite its weaknesses and lack of any theoretical basis, the HETP concept is still widely used in the design of columns containing structured packing. When using this concept one often has to resort to expensive and time consuming pilot plant testing. This could impact the economics of a process negatively. In this chapter the alternative modelling approaches have been introduced and discussed. These modelling approaches are not new and have been around for some time. The HTU/NTU method were introduced in the 1930's and the rate-based approach in the 1980's. In order to use the advantages that these modelling approaches offer, accurate hydrodynamic- and mass transfer models are needed. The current state of

affairs is such that a leading authority on distillation still views the use of mass transfer models as the least accurate method to determine the height of packing for a given separation (Kister, 1992).

The chapters that follow aim to introduce and critically assess the hydrodynamic- and mass transfer models available in literature. Inaccurate correlations for the vapour phase mass transfer coefficient and effective surface area were identified as weaknesses in current available mass transfer models. Experimental- and modelling techniques are employed to develop more accurate correlations for these quantities.

2.7 Nomenclature

a	Effective surface area of packing [m^2/m^3]
c	Molar density [mol/m^3]
D	Fick diffusion coefficient [m^2/s]
D'	Maxwell-Stefan diffusion coefficient [m^2/s]
E	Energy transfer rate [W]
F	Feed molar flow rate [mol/s]
H	Enthalpy [J/mol]
h	Heat transfer coefficient [$W/(m^2\ K)$]
$\bar{H}$	Partial specific enthalpy [J/mol]
HETP	Height equivalent to a theoretical plate [m]
H_T	Height of a transfer unit [m]
J	Diffusional flux [$mol/(m^2\ s)$]
K	Equilibrium constant [--]
k	Low flux mass transfer coefficient [m/s]
k*	Finite flux mass transfer coefficient [m/s]
L	Liquid molar flow rate [mol/s]
ℓ	Film thickness [m]
N	Molar flux [$mol/(m^2\ s)$]
N	Molar transfer rate [mol/s]
N_{eq}	Number of equilibrium stages [-]
N_T	Number of transfer units [-]
P	Pressure [Pa]
Q	Heat duty [W]
S	Column cross sectional area [m^2]
T	Temperature [K]
U	Liquid side draw molar flow rate [mol/s]
V	Vapour molar flow rate [mol/s]
W	Vapour side draw molar flow rate [mol/s]
x	Mole fraction, liquid phase [-]
y	Mole fraction, vapour phase [-]
z	Height of packing [m]

Greek

Γ	Thermodynamic rate factors [-]

δ	Kronecker delta [-]
δ	Distance from interface [m]
γ	Liquid activity coefficient [-]
Ξ	High flux correction factor [-]
κ_{ij}	Low flux i-j pair binary mass transfer coefficient [m/s]
Φ	Rate factors [-]
Ψ	Rate factors assuming constant D' [-]
Θ	Rate factors for mass transfer in non-ideal fluids [-]

Subscripts

av	Average property
i,j,k	Component indices
L	Liquid phase property
OL	Overall liquid phase property
OG	Overall vapour phase property
t	Refers to the total mixture
G	Vapour phase property

Superscript

F	Feed property
I	Interface property
L	Liquid phase property
V	Vapour phase property

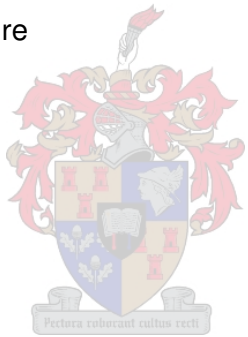

3 CFD AND STRUCTURED PACKING

3.1 Introduction

Computational Fluid Dynamics (CFD) is now an established modelling tool in the chemical process industry. This is to a large extent due to the advances made in computational speed and improvements in physical models implemented into CFD. There are already plans to combine CFD with traditional process simulation software in order to make it accessible to the average chemical engineer (Shanley, 2000). The major advantage of CFD is that it reduces the amount of physical testing that has to be performed and therefore reduces overall development costs. There are however limitations to what CFD can do and this should always be kept in mind. These limitations usually manifest itself in two ways. The first is that current models available in CFD may not be able to accurately model the physical process. Secondly the physical domain may be too large and complex to be represented by a CFD model. In the current study both these limitations are encountered. In a packed distillation column one is faced with stratified counter current two phase flow through a complex geometry. Only elementary physical models are available for this type of flow. It would also be impossible to model a whole segment of packing, let alone the whole column. In order to use the advantages that CFD offers, some simplifications have to be made. This chapter will look at how CFD has been used in the past in the structured packing industry and how it was implemented in this study.

3.2 Literature review

3.2.1 Application of CFD in the structured packing industry

CFD technology has been used in the past in the optimisation of structured packing designs. Mention is sometimes made of the use of CFD in optimising designs in some packing vendor brochures. These results are certainly of a proprietary nature and therefore not published in the open literature. There are however a few studies that have been conducted at universities for which results are available. In most of these studies only single-phase flow is assumed. Some of the studies were specifically on structured packing while others focussed on applications where geometries similar to that of structured packing are employed. These applications generally involve heat transfer. A short review of these follows.

Probably the first published CFD study on a geometry quite similar to that found in corrugated structured packing, is the study by Ciofalo and co-workers (Ciofalo et al., 1996), (Ciofalo, 1996). The study was performed on a type of compact heat exchanger called a rotary regenerator. This heat exchanger is made of a matrix of closely packed corrugated steel plates, quite similar to the corrugated geometry of most commercial structured packing (Mellapak, Flexipac). The heat transfer and pressure drop occurring in a unitary cell in the corrugated matrix were modelled using an early release of the software used in this study (FLOW3D). The results obtained with different turbulence models were compared with experimental data. The low Reynolds number formulation of the k-ε model and LES (large eddy simulation) gave the best overall agreement compared to experimental data.

The motivation behind the study of Hodson (Hodson, 1997) (Hodson et al., 1997) was to modify the existing geometry of corrugated sheet structured packing in order to maximize the gas phase mass transfer rate. The study was not concerned with predicting the gas phase mass transfer rate, but rather to compare qualitatively different modifications to the standard design. The standard k-ε model was used with a wall function to bridge the laminar sublayer. A single unitary cell was modelled and the outflow used as inflow to a next cell. A layer of packing was modelled by staggering a number of these cells. Heat transfer from the wall as well as pressure drop was modelled. A modification to the standard design was proposed. This modification involved punching slots into the corrugated sheets with the punched out tabs protruding into neighbouring channels. A sample of the modified packing was produced and tested. The separation efficiency of the packing was marginally increased. This was however at the expense of capacity.

The dry pressure drop over structured packing is used in most of the proposed pressure drop models. CFD has recently been successfully used to predict the dry pressure drop of most commercially available structured packing (Petre et al., 2003). The study was also extended to the dry pressure drop through the modern 'high capacity' structured packing (Larachi et al., 2003). In the study, the total pressure drop is divided into different contributing mechanism. Each mechanism is modelled separately and then combined according to the model proposed by Olujic (Olujic, 1997). The k-ε turbulence model with a wall function was used in the study.

A successful attempt has been made at using CFD to model binary distillation in a bed of random packing (Yin et al., 2000). The packed bed is modelled as a two dimensional porous region and existing correlations are used for quantities like pressure drop, hold-up and mass transfer coefficients. The results compared favourably with experimental results obtained from the FRI.

The radial and axial dispersion of the liquid phase in structured packing developed for catalytic distillation (KATAPAK-S) (Van Baten et al., 2001) has been modelled with CFD. Good agreement was obtained with experimental data.

Vapour flow around some of the other internals found in packed columns has also been the subject of a few CFD studies. These include the modelling of reboiler vapour return lines (Wehrli et al., 2002) and the maldistribution of the vapour phase caused by liquid redistributors (Mohamed Ali et al., 2002). In these studies the k-ε turbulence model with a wall function were used. CFD has also been used in a study on liquid film flow on inclined plates (Ataki and Bart, 2002).

The use of CFD is not only confined to structured packing. It has also been used to model sieve tray hydrodynamics (Krishna et al., 1999) and the flow inside liquid-liquid extractors (Rieger et al., 1996).

3.2.2 Aim of CFD in this study

CFD has previously successfully been used to model mass transfer rates in complex wall bounded flows (Nesic and Postlethwaite, 1992, Nesic et al., 1993, Wang and Shirazi, 2001). It has also been demonstrated that CFD can be successfully used to model the vapour phase flow in structured packing (Larachi et al., 2003, Petre et al., 2003, Hodson, 1997). A natural extension of these ideas would be to use CFD to model the vapour phase mass transfer in structured packing. This was the main focus of the CFD work in this study. In the remainder of this chapter the general modelling philosophy will be presented. It will start with an overview of the governing equations of fluid flow and how these equations are approximated with the use of computational fluid dynamics. The main features of the CFD code used in this study will be introduced. Finally some details will be given on how CFD was implemented in this study. Chapter 5 should be consulted for a more detailed description of the geometry and boundary conditions used in implementing CFD in this study.

3.3 Theory: Computational fluid dynamics

The governing equations describing the motion of a fluid are complex and highly non-linear. Analytical methods for solving these equations are limited to only the most elementary problems. In computational fluid dynamics (or CFD in short) the governing equations are approximated with a suitable discretization method. The equations are expressed in terms of a set of algebraic equations for the discrete variables at a set of discrete locations in the computational space. Various discretization methods have been developed over the years. Methods that are frequently used are the finite element method, the finite difference method and the finite volume method. Most CFD codes use the finite volume method. This is also the case with CFX-4, the commercial package used in this study. In the paragraphs that follow the conservation equations will be discussed, followed by the discretization method and finally the solution procedure. The discretization method that will be discussed is the finite volume method. Discretization methods for the finite difference and finite element methods can be found elsewhere.(Patankar, 1980)

3.3.1 Conservation equations

The Navier-Stokes equations

The conservation equation for mass over a stationary volume element through which a fluid flows is known as the continuity equation. In a three dimensional cartesian coordinate frame it is represented by (Schlichting, 1979):

$$\frac{\partial \rho}{\partial t}+\left(\frac{\partial}{\partial x}\rho U_x+\frac{\partial}{\partial y}\rho U_y+\frac{\partial}{\partial z}\rho U_z\right)=0 \tag{3.1}$$

The conservation equations for momentum in Newtonian fluids in a three dimensional cartesian coordinate frame are given by (Schlichting, 1979):

$$\begin{aligned}\frac{\partial}{\partial t}(\rho U_x)+\left(\frac{\partial}{\partial x}\rho U_x U_x+\frac{\partial}{\partial y}\rho U_y U_x+\frac{\partial}{\partial z}\rho U_z U_x\right)\\ =-\frac{\partial p}{\partial x}-\left(\frac{\partial}{\partial x}\tau_{xx}+\frac{\partial}{\partial y}\tau_{yx}+\frac{\partial}{\partial z}\tau_{zx}\right)+\rho g_x\end{aligned} \tag{3.2}$$

$$\begin{aligned}\frac{\partial}{\partial t}(\rho U_y)+\left(\frac{\partial}{\partial x}\rho U_x U_y+\frac{\partial}{\partial y}\rho U_y U_y+\frac{\partial}{\partial z}\rho U_z U_y\right)\\ =-\frac{\partial p}{\partial y}-\left(\frac{\partial}{\partial x}\tau_{xy}+\frac{\partial}{\partial y}\tau_{yy}+\frac{\partial}{\partial z}\tau_{zy}\right)+\rho g_y\end{aligned} \tag{3.3}$$

$$\frac{\partial}{\partial t}(\rho U_z)+\left(\frac{\partial}{\partial x}\rho U_x U_z+\frac{\partial}{\partial y}\rho U_y U_z+\frac{\partial}{\partial z}\rho U_z U_z\right) = -\frac{\partial p}{\partial z}-\left(\frac{\partial}{\partial x}\tau_{xz}+\frac{\partial}{\partial y}\tau_{yz}+\frac{\partial}{\partial z}\tau_{zz}\right)+\rho g_z \tag{3.4}$$

The expressions for the stress terms are:

$$\tau_{xx} = -2\mu\frac{\partial U_x}{\partial x}+\frac{2}{3}(\nabla \bullet \mathbf{U}) \tag{3.5}$$

$$\tau_{yy} = -2\mu\frac{\partial U_y}{\partial y}+\frac{2}{3}(\nabla \bullet \mathbf{U}) \tag{3.6}$$

$$\tau_{zz} = -2\mu\frac{\partial U_z}{\partial z}+\frac{2}{3}(\nabla \bullet \mathbf{U}) \tag{3.7}$$

$$\tau_{xy} = \tau_{yx} = -\mu\left(\frac{\partial U_x}{\partial y}+\frac{\partial U_y}{\partial x}\right) \tag{3.8}$$

$$\tau_{yz} = \tau_{zy} = -\mu\left(\frac{\partial U_y}{\partial z}+\frac{\partial U_z}{\partial y}\right) \tag{3.9}$$

$$\tau_{zx} = \tau_{xz} = -\mu\left(\frac{\partial U_z}{\partial x}+\frac{\partial U_x}{\partial z}\right) \tag{3.10}$$

It is convenient to write the continuity equation in vector notation:

$$\frac{\partial \rho}{\partial t}+(\nabla \bullet \rho\mathbf{U}) = 0 \tag{3.11}$$

In vector notation the momentum balances are represented by:

$$\frac{\partial}{\partial t}\rho\mathbf{U}+(\nabla \bullet \rho\mathbf{U}\otimes\mathbf{U}) = -\nabla p-(\nabla \bullet \tau)+\rho\mathbf{g} \tag{3.12}$$

The above equations are known as the 'Navier-Stokes' equations. They completely describe the flow of an isothermal Newtonian fluid.

General conservation equation

A general convection-diffusion conservation equation may by written that governs momentum, mass and heat transfer (Patankar, 1980):

$$\frac{\partial}{\partial t}(\rho\phi)+\nabla \bullet (\rho\mathbf{U}\phi) = \nabla \bullet (\Gamma^{\phi}\nabla\phi)+S^{\phi} \tag{3.13}$$

In this equation ϕ is the dependent variable, Γ^{ϕ} is the diffusion coefficient and S^{ϕ} is the source term. The source term represents the creation or destruction of the dependent variable. For the simple example of conduction, ϕ would represent temperature, Γ^{ϕ} the thermal conductivity and S^{ϕ} some external heat source. For the

momentum equation (Equation 3.12), ϕ represents the velocity vector and Γ^{ϕ} represents viscosity. A number of quantities are lumped into the source term, S^{ϕ}. It contains the pressure gradient, body forces such as gravitation and a part of the stress term.

Turbulence

In most engineering problems turbulent flows are encountered. Turbulence is still an active area of research and there is a large amount of literature devoted to it. Fundamentally, the Navier-Stokes equations also apply to turbulent flows. It is possible to use these equations directly to simulate turbulent flow. This is called 'Direct Numerical Simulation'. It is currently possible to model only simple turbulent flows with this method and even then extensive computational resources are needed (Hirsch, 1988). Most of the models in use today rely on the Reynolds averaged Navier Stokes equations. With this method the turbulent fluctuations are averaged out. This gives rise to mean or time averaged turbulence quantities. The time over which this averaging is carried out must be sufficiently large compared to the time scale of the turbulent fluctuations but sufficiently small compared to the time scale of other time dependent phenomena. The time-averaged component of velocity in the x direction is given by (Schlichting, 1979):

$$\bar{U}_x = \frac{1}{t_0}\int_t^{t+t_0} U_x dt \tag{3.14}$$

The instantaneous velocity is then the sum of the time averaged velocity and a velocity fluctuation:

$$U_x = \bar{U}_x + U_x^{\bullet} \tag{3.15}$$

Similar expressions apply to the other components of velocity and any other transported quantity in general. The Navier-Stokes equations are rewritten in terms of these quantities. In Cartesian coordinates the continuity equation is given by:

$$\frac{\partial \rho}{\partial t} + \left(\frac{\partial}{\partial x}\rho\bar{U}_x + \frac{\partial}{\partial y}\rho\bar{U}_y + \frac{\partial}{\partial z}\rho\bar{U}_z \right) = 0 \tag{3.16}$$

The momentum equation in the x direction is represented by:

$$\begin{aligned} &\frac{\partial}{\partial t}\left(\rho\bar{U}_x\right) + \left(\frac{\partial}{\partial x}\rho\bar{U}_x\bar{U}_x + \frac{\partial}{\partial y}\rho\bar{U}_y\bar{U}_x + \frac{\partial}{\partial z}\rho\bar{U}_z\bar{U}_x \right) \\ &= -\frac{\partial \bar{p}}{\partial x} - \left(\frac{\partial}{\partial x}\rho\overline{U_x^{\bullet}U_x^{\bullet}} + \frac{\partial}{\partial y}\rho\overline{U_y^{\bullet}U_x^{\bullet}} + \frac{\partial}{\partial z}\rho\overline{U_z^{\bullet}U_x^{\bullet}} \right) + \mu\nabla^2\bar{U}_x + \rho g_x \end{aligned} \tag{3.17}$$

Similar expressions can be written for the y and z components of the momentum equation. The terms

$$\tau_{xx}^{t} = \rho\overline{U_x^{\bullet}U_x^{\bullet}} \qquad \tau_{yx}^{t} = \rho\overline{U_y^{\bullet}U_x^{\bullet}} \qquad \tau_{zx}^{t} = \rho\overline{U_z^{\bullet}U_x^{\bullet}} \tag{3.18}$$

are known as the Reynolds stresses. Various models have been proposed to calculate these stresses. Most models rely on Boussinesq's eddy viscosity hypothesis, analogous to Newton's law of viscosity:

$$\tau_{yx}^{t} = -\mu_t \frac{d\bar{U}_x}{dy} \tag{3.19}$$

were μ_t is the turbulent- or eddy viscosity. Similar averaging may be performed on the general convection-diffusion equation. The eddy diffusivity hypothesis is the result. The turbulent transport of quantities like heat and mass are due to the same mechanism as momentum transport. It is therefore expected that the value of the eddy diffusivity will be close or equal to that of the eddy viscosity. This has resulted in the definition of turbulent Prandtl/Schmidt numbers:

$$\sigma_t^{\phi} = \frac{\mu_t}{\Gamma_t^{\phi}} \tag{3.20}$$

Quite a few turbulence models have been proposed that rely on the eddy viscosity concept. These models can be divided into one- and two equation models. The k-ε model by Jones and Launder (Jones and Launder, 1972) and the k-ω model due to Wilcox (Wilcox, 1993b) are examples of two equation eddy viscosity models. In some of the more complex models the eddy viscosity hypothesis is not invoked. Separate transport equations are developed for the different Reynolds stresses. These models are generally referred to as 'Second Moment Closure' models. In most engineering calculations for turbulent flows the so-called 'two equation eddy viscosity' models are used (Menter and Grotjans, 2000). They are more robust than the SMC models and because they have been in use for quite a number of years, they can be applied with a certain amount of confidence. There are however also known limitations to these models (Menter and Grotjans, 2000).

The k-ε model by Jones and Launder (Jones and Launder, 1972) solves an equation for the turbulent kinetic energy (k) and one equation for the turbulent kinetic energy dissipation rate (ε). The equations for the turbulent kinetic energy and the dissipation rate can be written in the following form:

Turbulent kinetic energy (k):

$$\frac{\partial}{\partial t}(\rho k) + \nabla \bullet \left(\rho \bar{\mathbf{U}} k\right) = \nabla \bullet \left(\left(\mu + \frac{\mu_t}{\sigma_t^k}\right)\nabla k\right) + P_k - \rho\varepsilon \tag{3.21}$$

Turbulent kinetic energy dissipation rate (ε):

$$\frac{\partial}{\partial t}(\rho\varepsilon)+\nabla\bullet\left(\rho\bar{\mathbf{U}}\varepsilon\right)=\nabla\bullet\left(\left(\mu+\frac{\mu_t}{\sigma_t^{\varepsilon}}\right)\nabla\varepsilon\right)+\frac{\varepsilon}{k}\left(C_{\varepsilon 1}P_k-C_{\varepsilon 2}\rho\varepsilon\right) \tag{3.22}$$

The eddy viscosity (μ_t) is given by:

$$\mu_t=\rho C_{\mu}\frac{k^2}{\varepsilon} \tag{3.23}$$

The production term for turbulent kinetic energy (P_k) and the model constants are given in Appendix A.

In the k-ω model of Wilcox (Wilcox, 1988) the dissipation rate (ε) is replaced with the 'pseudovorticity' ω. The equation for the turbulent kinetic energy (k) is given by:

$$\frac{\partial}{\partial t}(\rho k)+\nabla\bullet\left(\rho\bar{\mathbf{U}}k\right)=\nabla\bullet\left(\left(\mu+\sigma_t^{k}\mu_t\right)\nabla k\right)+P_k-\beta^{*}\rho k\omega \tag{3.24}$$

The equation for the pseudovorticity ω is given by:

$$\frac{\partial}{\partial t}(\rho\omega)+\nabla\bullet\left(\rho\bar{\mathbf{U}}\omega\right)=\nabla\bullet\left(\left(\mu+\sigma_t^{\omega}\mu_t\right)\nabla\omega\right)+\alpha\frac{\omega}{k}P_k-\beta^{*}\rho\omega^2 \tag{3.25}$$

The eddy viscosity (μ_t) is given by:

$$\mu_t=\alpha^{*}\rho\frac{k}{\omega} \tag{3.26}$$

The production term (P_k) and closure coefficients are given in Appendix A.

An extensive review of these models is given by a number of investigators (Wilcox, 1993a) (Patel et al., 1985) (Menter, 1994). It is known that both models suffer from disadvantages in certain types of flow. The k-ε model is problematic in the viscous sublayer. In order to integrate the equations through this layer complicated viscous damping functions have to introduced. This makes the equations numerically 'stiff' and difficult to solve (Wilcox, 1993a). The k-ω also suffers from certain drawbacks in free shear flows (Menter, 1992). It does have an advantage over the k-ε model in that it does not require complicated damping functions in the viscous sublayer. Menter (Menter, 1994) proposed a turbulence model that combines the advantages of the k-ε and k-ω models. Close to the wall the k-ω model is used while the k-ε model is used near the boundary layer edge and in regions away from the wall (free stream). There are two versions of this hybrid model. The first is known as the Baseline (BSL) model and the second as the Shear-Stress-Transport (SST) model. The BSL model is used in this study and will be discussed next.

In the BSL model the k-e model is transformed into a k-ω formulation. The original k-ω model is multiplied with a function F_1 and added to the transformed model that is multiplied by $(1-F_1)$. The resulting equation for k is:

$$\frac{\partial}{\partial t}(\rho k)+\nabla\bullet\left(\rho\bar{\mathbf{U}}k\right)=\nabla\bullet\left(\left(\mu+\sigma_t^k\mu_t\right)\nabla k\right)+P_k-\beta^*\rho k\omega \tag{3.27}$$

The pseudovorticity ω is given by:

$$\frac{\partial}{\partial t}(\rho\omega)+\nabla\bullet\left(\rho\bar{\mathbf{U}}\omega\right)=\nabla\bullet\left(\left(\mu+\sigma_t^\omega\mu_t\right)\nabla\omega\right)+\frac{\gamma}{\nu_t}P_k-\beta^*\rho\omega^2 + 2(1-F_1)\rho\sigma_{\omega2}\frac{1}{\omega}\nabla k\nabla\omega \tag{3.28}$$

The constants for the BSL model are calculated from:

$$C=F_1C_1+(1-F_1)C_2 \tag{3.29}$$

The production term and constants for the model are given in Appendix A.

The turbulence models discussed above are the so-called 'low-Reynolds number' formulations. The turbulence equations are integrated through the viscous sublayer. A popular way of treating the viscous sublayer is by bridging it with a 'wall function'. This study will focus on mass transport from the wall and it is for this reason that a 'low-Reynolds number' turbulence model was used. Such a treatment is known to give better results for wall quantities like wall shear stress and heat transfer coefficients (Menter and Grotjans, 2000) It is therefore expected to give superior results for mass transfer as well. There are also some serious disadvantages when using wall functions. Menter (Menter and Grotjans, 2000) gives a comprehensive review of these disadvantages.

Boundary Conditions

In order to obtain a unique solution to the governing equations, boundary conditions have to imposed. There are basically three types of boundary conditions (written in terms of a dependent variable ϕ):

1. Dirichlet boundary condition:

   $$\phi=\text{value} \tag{3.30}$$

2. Neumann boundary conditions: The gradient of ϕ is specified in a direction normal to the boundary:

   $$\frac{\partial\phi}{\partial n}=\text{value} \tag{3.31}$$

n is in a direction normal to the boundary.

3. Combination of Dirichlet and Neumann type boundary conditions:

$$\frac{\partial \phi}{\partial n} + \varepsilon\phi = \text{value} \tag{3.32}$$

3.3.2 Discretization of the governing equations

Cartesian coordinates

In the following paragraphs the discretization of the governing equations on a rectangular grid will be discussed. A rectangular control volume in three-dimensional Cartesian coordinates is shown in Figure 3.1. The governing equations for all the dependant variables are written in the following general form (Patankar, 1980):

$$\frac{\partial}{\partial t}(\rho\phi) + \nabla \bullet (\rho \mathbf{U}\phi) = \nabla \bullet (\Gamma^{\phi}\nabla\phi) + S^{\phi} \tag{3.33}$$

were Γ^{ϕ} is the diffusion coefficient and S^{ϕ} is the source term, as discussed previously.

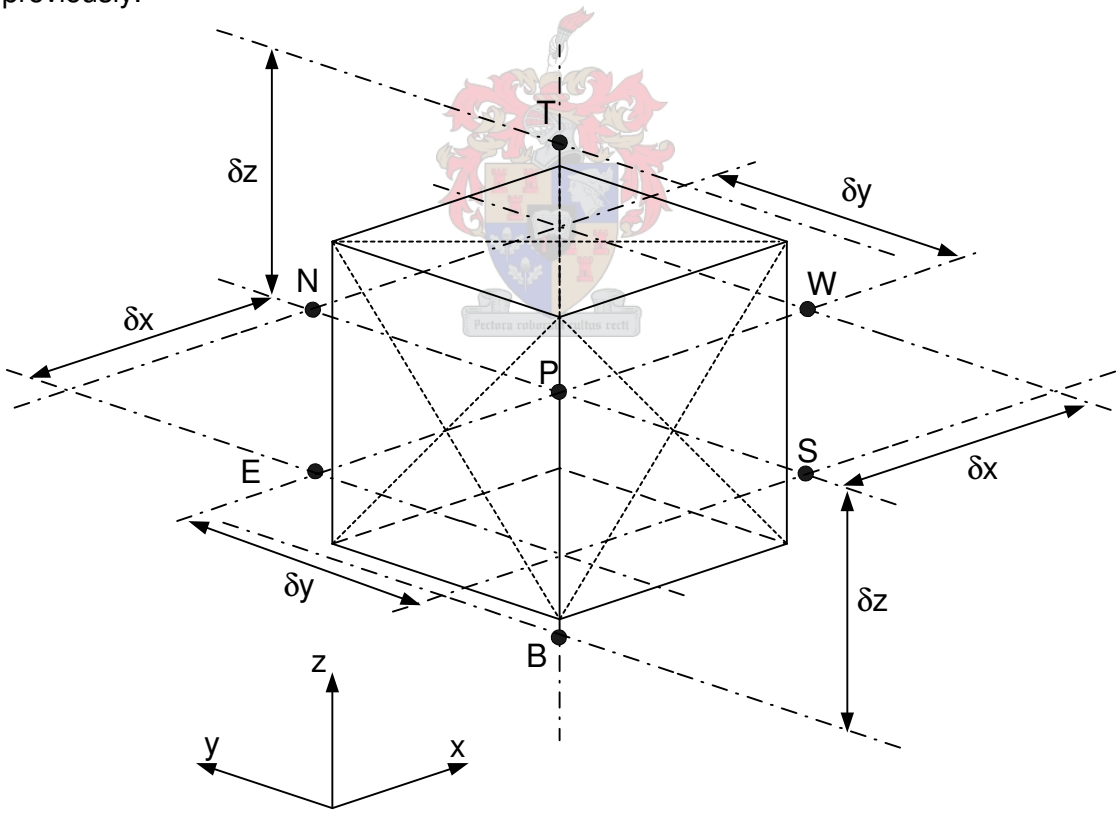

Figure 3.1 Control volume in three-dimensional Cartesian coordinates

The solution to this equation is obtained at a finite number of discreet points in the computational domain. Some analytical function for the variation of the dependent variable between the discreet points is assumed. This is known as interpolation or

differencing schemes. The most common schemes are the central difference scheme and the upwind difference scheme. For this control volume, the general discretization equation for Equation 3.33 is represented by:

$$a_P\phi_P = a_E\phi_E + a_W\phi_W + a_N\phi_N + a_S\phi_S + a_T\phi_T + a_B\phi_B + b \tag{3.34}$$

Subscripts N,S,T and B refer to the discreet points to the North, South, Top and Bottom of the discreet point under consideration. The 'influence coefficients' are:

$$a_E = \left(\frac{\Gamma^\phi A}{\delta x}\right)_e f\left(|P_e|\right) + \max\left[-(\rho u A)_e, 0\right] \tag{3.35}$$

$$a_W = \left(\frac{\Gamma^\phi A}{\delta x}\right)_w f\left(|P_w|\right) + \max\left[(\rho u A)_w, 0\right] \tag{3.36}$$

$$a_N = \left(\frac{\Gamma^\phi A}{\delta y}\right)_n f\left(|P_n|\right) + \max\left[-(\rho u A)_n, 0\right] \tag{3.37}$$

$$a_S = \left(\frac{\Gamma^\phi A}{\delta y}\right)_s f\left(|P_s|\right) + \max\left[(\rho u A)_s, 0\right] \tag{3.38}$$

$$a_T = \left(\frac{\Gamma^\phi A}{\delta z}\right)_t f\left(|P_t|\right) + \max\left[-(\rho u A)_t, 0\right] \tag{3.39}$$

$$a_B = \left(\frac{\Gamma^\phi A}{\delta z}\right)_b f\left(|P_b|\right) + \max\left[(\rho u A)_b, 0\right] \tag{3.40}$$

$$b = S_C^\phi V + a_P^0\phi_P^0 \tag{3.41}$$

$$a_P^0 = \frac{\rho_P^0 V}{\Delta t} \tag{3.42}$$

$$a_P = a_E + a_W + a_N + a_S + a_T + a_B + a_P^0 - S_P^\phi V \tag{3.43}$$

In equations 3.35 to 3.40 A represents the area of the boundary face under consideration and V represents the total volume of the control volume. $\phi_P{}^0$ and $\rho_P{}^0$ refer to the known values at time t, while all the other values are the unknown values at time t+Δt. The variables $S^\phi{}_C$ and $S^\phi{}_P$ result from the linearization of the source term:

$$S^\phi = S_C^\phi + S_P^\phi\phi_P \tag{3.44}$$

Formulas for the function f(|P|) for the different differencing schemes are given in Table 3.1 (Patankar, 1980):

Table 3.1 Formulas for the function f(|P|)

Differencing Scheme	Formula for f(|P|)	
Central	$1-0.5\|P\|$	(3.45)
Upwind	1	(3.46)
Hybrid	$\max\left[0,\left(1-0.5\|P\|\right)\right]$	(3.47)

In Table 3.1 P is the mesh Peclet number. For the west face of the control, the Peclet number is defined by:

$$P_w = \left(\frac{\rho u \delta x}{\Gamma^{\phi}}\right)_w \tag{3.48}$$

Similar expressions are valid for the other control volume faces. The discretization of the momentum equations is performed in the same manner.

Curve-linear coordinates

In order to model the flow in complex geometries using a Cartesian coordinate system, boundaries have to be generated by 'blocking-off' some of the control volumes. This results in irregular or stepwise boundaries. There are some disadvantages associated with this. Most modern CFD codes use a so-called boundary fitted- or curve-linear coordinate system. This is illustrated in Figure 3.2. The curved surfaces in the physical domain are transformed to regular surfaces in the computational domain with a transformation so that the boundary or wall coincide with lines of constant ξ in the computational domain. The governing equations are now written in terms of these new transformed coordinates and solved using the discretization techniques discussed. These transformations can range from being quite simple to rather complex (Ferzigier and Peric, 1996).

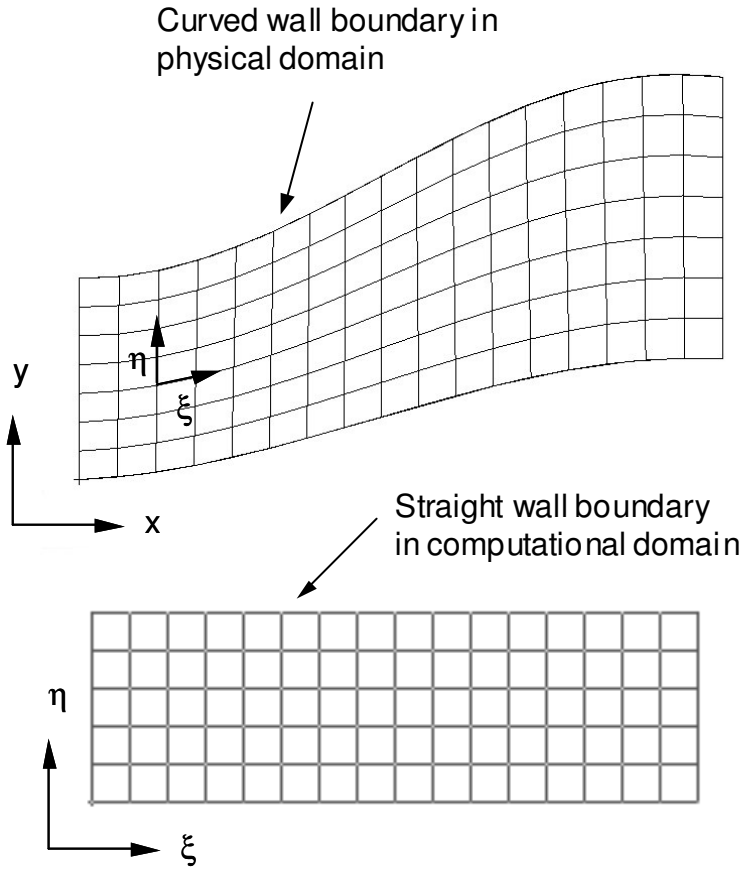

Figure 3.2 Transformation of grid to curve-linear coordinates

3.3.3 Solution procedure

It would seem that it is rather straightforward to obtain the flow field from the discretized governing equations. They form a set of analytical equations that could be solved with standard techniques. The major difficulty however lies in obtaining the unknown pressure field. Only the correct pressure field substituted into the momentum equation will result in the continuity equation being satisfied. This is known as the pressure-velocity coupling in the governing equations. There is also no direct way to obtain the correct pressure.

A further complication is that of checkerboard pressure fields and wavy velocity fields (Patankar, 1980)]. When discretization is performed on the momentum equations, the resulting equation contains the pressure difference between two alternate grid points and not between adjacent grid points. This results in a so-called checkerboard

pressure field satisfying the momentum equation and leading to unrealistic solutions. A similar difficulty arises with discretization of the continuity equation, resulting in wavy velocity fields satisfying the continuity equation. Two popular methods are used to counteract this phenomenon. The first of these is to use a staggered grid. According to this method all the variables except velocity are computed at the central grid points (point P in Figure 3.2). The components of velocity are calculated at the points that lie on the face of a control volume. For the control volume shown in Figure 3.2 these points would lie halfway between point P and all the other points in surrounding control volumes, i.e. on the six faces of the control volume. The discretized continuity equation would then contain differences between velocity components at adjacent grid points. Similarly the discretized momentum equations would contain the pressure difference between adjacent grid points. There are some problems associated with this method applied to non-orthogonal grids (Rhie and Chow, 1983). Rhie and Chow (Rhie and Chow, 1983) proposed a method where a single grid is used. The momentum equations are used to interpolate grid point velocities onto control volume faces in such a way as to avoid the use of pressure differences over alternating grid points.

An extra equation is however still needed to determine the unknown pressure field. This equation is known as the pressure correction equation.

The pressure correction equation

This equation is derived by assuming that the correct pressure field is obtained by adding a pressure correction (p') to the guessed pressure (p*):

$$p = p^* + p' \tag{3.49}$$

This also gives rise to corresponding velocity corrections:

$$U_x = U_x^* + U_x' \qquad U_y = U_y^* + U_y' \qquad U_z = U_z^* + U_z' \tag{3.50}$$

Discretization equations are obtained for the guessed velocity field (U*) using the guessed pressure field (p*). A discretization equation for the velocity correction field (U') is also obtained (in terms of U' and p'). These equations (one for each component of velocity) are then used for the velocity corrections U' in Equation 3.50. The pressure correction equation is now obtained by discretizing the continuity equation and substituting the velocity components with the corresponding velocity correction formula. A complete description of this method is beyond the scope of this text and is given by Patankar (Patankar, 1980) and also by Rhie and Chow (Rhie and Chow, 1983).

Solution algorithm

The solution algorithm that forms the basis for most commercial codes is the well-known SIMPLE algorithm (Patankar, 1980). The acronym SIMPLE stands for Semi-Implicit Method for Pressure Linked Equations. The sequence of operations is:

1. Guess the pressure field p* and the velocity field U*.
2. Solve the momentum equations to obtain new values for U*.
3. Solve the pressure correction equation to obtain p'.
4. Correct the pressure field by adding p' to p*.
5. Calculate U from the velocity correction formulas.
6. Solve the discretization equations for the other variables (f's) if they influence the flow field.
7. Treat the corrected pressure as the new guessed pressure and repeat the procedure until a converged solution is obtained.

There are a number of algorithms based on the original SIMPLE algorithm. The main difference is the way in which the pressure correction equation is derived. The words 'semi-implicit' refer to the omission of the influence of pressure correction on velocity. In the derivation of the pressure correction dicretization equation, the velocity correction terms are omitted. The converged solution obtained from using the SIMPLE algorithm does not contain errors resulting from this omission. Convergence difficulties could however result from this. In algorithms like the SIMPLEC (Van Doormal and Raithby, 1984) the velocity correction equations are modified. This also causes a modification in the pressure correction equation and ultimately results in a more consistent correction field. This results in an overall faster convergence rate.

3.4 CFD code used in this study

CFX-4.4 from AEA technology (Technology, 1999) was used in this study. Like most CFD codes, it is divided into three functional units: Pre-processor, Solver and Post-processor. The pre-processor is used to construct the physical domain, specify boundary surfaces and to create a grid. The solver transforms the grid from the physical domain to the computational domain and solves the discretised equations. The post-processor is used for flow visualization. The main features of each of these units will be briefly discussed next. For a complete discussion the CFX-4.4 user manual should be consulted (Technology, 1999).

3.4.1 Pre-processor

The pre-processor is called CFX-4.4 Build. It contains a lot of the functionalities of a conventional computer aided design package (CAD). The boundaries of the physical

domain can therefore be created with this unit or alternatively imported from other CAD design software. The major steps that have to be followed are:

1. Create (or subdivide imported) geometry with a number of sub regions or blocks. Each of these blocks has to be a hexadron (contain six faces, eight vertices).
2. Label boundaries according to type of condition imposed (inflow, outflow, pressure, periodic, wall etc.)
3. Create structured surface mesh on all 2 dimensional surfaces.
4. Generate hexahedral volume elements using 2D surface mesh.

The output of this unit contains all the geometric data of the multiblock grid (or body-fitted grid) in physical space and the location and type of boundaries imposed.

3.4.2 Solver

In the solver part of the software the grid is transformed from the physical domain to the computational domain. The governing equations are then discretised and solved. The major steps are:

1. Transformation of the grid to the computational domain.
2. Discretization of governing equations
3. Solving the discretised equations

These steps will be discussed in turn next. Some comments regarding closure models will also be made.

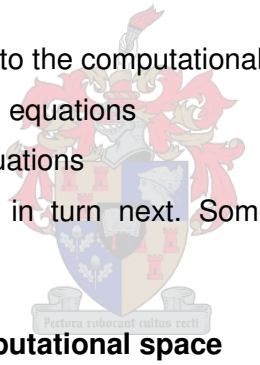

Transformation of grid to computational space

The grid in physical space is transformed to a grid in computational space. For simple rectangular geometries, the grid may be specified in this unit without importing it from the pre-processor. For a 'body fitted' grid each 'block' in the physical domain are transformed to a rectangular grid in the computational domain. This means that the coordinates are transformed (as discussed in curve linear coordinates) so that the boundaries in the physical domain coincide with one of the coordinate directions in the computational domain. This results in a topological rectangular grid for each block in the computational domain. The different blocks with their rectangular grids in the computational domain are then 'glued' together to form the computational grid.

Discretization of governing equations

The next step is to discretise the governing equations. The governing equations are transformed to the computational domain coordinate system and discretised. A non-staggered grid is employed in the discretization. The velocity-pressure coupling in the

governing equations is treated according to the Rhie-Chow method (Rhie and Chow, 1983), as discussed in the section on the pressure correction equation. A number of different pressure-velocity coupling solution algorithms are available in the program with the default being the SIMPLEC algorithm (Van Doormal and Raithby, 1984).

Solving the discretised equations

The linearized (discretised) equations are not solved simultaneously, but rather by an iterative procedure. There are two steps employed in the method used by CFX-4.4. In the 'inner iteration' the spatial coupling for a single variable is solved while in the 'outer iteration' the coupling between variables is solved. In the 'inner iteration' the value for each variable is updated while regarding all the other variables as being constant. The non-linearity of the governing equations is simulated by updating the coefficients in the discrete equations with the most recent calculated value for a variable before the 'outer iteration' is performed. The pressure corrections are performed according to the velocity-pressure method and algorithm described previously. A number of different convergence criteria may be specified for the 'outer iteration' or for global convergence. These range from specifying a global mass source residual to specifying residuals for specific variables There are also a number of ways in which damping may be employed. Full details are provided with the software (Technology, 1999).

'Closure models'

In this study turbulence modelling, and more specifically low Reynolds number formulations of the eddy-viscosity two-equation models, was of high importance. CFX-4.4 contains the low Reynolds number BSL eddy-viscosity model of Menter, which is discussed in more detail in the paragraphs dealing with turbulence modelling. In this regard CFX-4.4 was thought to be superior compared to other available CFD codes.

3.4.3 Post-processor

The post processor is known as CFX-Analyse. A variety of plots may be generated with this software. These include vector plots, fringe plots and particle track lines. It may also be used for animated flow visualization.

3.5 Implementation of CFD in this study

The ideal model for mass transfer inside structured packing would be to divide the column into a large number of small control volumes. The discretised equations of

fluid motion, mass- and heat transfer may then be simultaneously solved for all the control volumes, subject to some specified boundary conditions. At present such a model is not possible. Only elementary physical models are available to model counter current stratified two phase flow. Even if more accurate and robust models were available, then the sheer number of control volumes needed to capture all the details of the multi phase flow field in a bed of structured packing would make such a model impossible. With the elementary physical models currently available it is possible to model the vapour/liquid interface in flow fields where there is no large shear force at the interface between the two phases. Extremely fine grids are then necessary in regions where the interface is expected to be. Since it is usually not known where the interface between the phases will be, a fine grid has to be created over the entire physical domain.

At present it is therefore possible to model only the vapour phase flow inside structured packing with some degree of accuracy. The vapour phase mass transfer rate may be modelled by assuming that the boundary of the physical domain coincides with the interface between the vapour and liquid phases. If it is further assumed that equilibrium is maintained at the interface between the two phases, then the equilibrium concentration of the species transferring into the physical domain may be specified as a wall boundary. The vapour phase mass transfer coefficient may be calculated by performing a mass balance for this species between the inlet and outlet boundaries. This approach was tested in this study by modelling the mass transfer rate for a species evaporating in a short counter current wetted-wall column. The values for the mass transfer coefficient obtained in this manner compared favourably with experimental results. Full details are provided in Chapter 5.

As mentioned before, despite recent advances in computing power, it is at present not possible to model a complete bed of structured packing. This is even more true when a low Reynolds number formulation of a two-equation eddy-viscosity type turbulence model (like the k-ε or k-ω turbulence models) is used. The grid has to be refined to such an extent near the wall that extremely fine grids are necessary to obtain convergence compared to when using the same model with a wall function. The use of the low Reynolds number formulation of these turbulence models was deemed necessary in order to model mass transfer from a wall boundary.

The bed may, however, be broken down into smaller re-occurring sub-domains. A CFD model is set up for each of these sub-domains. The bed is then reconstructed

by adding the contribution from each sub-domain. The contributions are calculated from the number of times that such a sub-domain re-occurs in the bed. A number of previous investigators have followed this approach (Ciofalo et al., 1996, Hodson, 1997, Hodson et al., 1997, Larachi et al., 2003, Petre et al., 2003). From a mass transfer point of view, the most important sub-domain or micro element, is the junction between two cross-corrugated channels. There are three other sub-domains or micro elements also occurring in a bed of packing. These may be visualized by tracing the path that the vapour follows when flowing through a bed of structured packing and are explained by referring to Figure 3.3. Micro element 1 is found at the base of the bed where the vapour phase enters the bed of packing. Micro element 2 is the junction between two cross-corrugated channels. A number of these elements are found before a channel either ends up at the column wall, or reach the horizontal plane where two packing segments meet. At the column wall micro element 3 is found. The vapour is deflected from the wall and switch from the channel of the parent sheet to a channel starting at the wall on the sheet facing the parent sheet. At the horizontal plane where two packing segments meet, the vapour phase undergo a sharp change in direction (total direction change not shown in Figure 3.3. The micro element that re-occurs the most is the junction between corrugated passages (micro element 2). It has been shown that it causes between 65% and 72% of the dry bed pressure drop over the packing (Petre et al., 2003, Larachi et al., 2003). In this study the focus has been on the CFD modelling of micro element 2. The bulk of the packing may be reconstructed by arranging a number of these micro elements in series. The outlets of one element are used as the inlets to the next element and the process is repeated for the whole length of a corrugated channel.

The approach outlined above for modelling the vapour phase mass transfer rate inside structured packing was followed in obtaining the CFD results shown in Chapter 5. Since the aim of this chapter is to introduce the general modelling approach, more details on the physical domain, computational grid and boundary conditions may be found in Chapter 5.

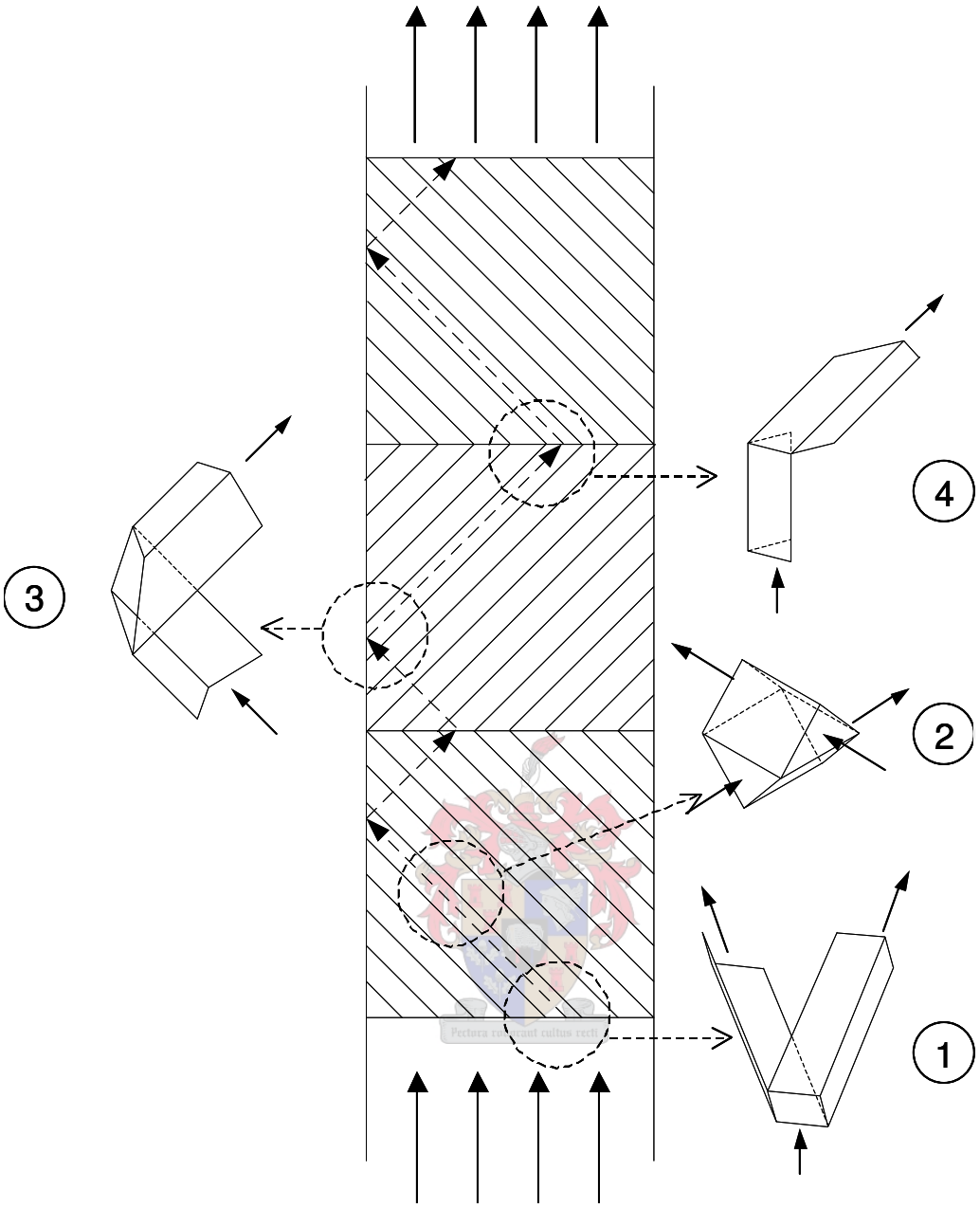

Figure 3.3 Breakdown of structured packing into re-occurring micro elements.

3.6 Nomenclature

A	Area [m^2]
a	Influence coefficients [-]
g	Gravitational acceleration [m/s^2]
k	Turbulent kinetic energy [m^2/s^2]
P	Peclet number [-]
p	Pressure [Pa]
P_k	Production of turbulent kinetic energy [$kg/(m^3s^2$]
S	Source term [-]
u	Component of velocity [m/s]
U	Velocity vector [m/s]
$\mathbf{U}^\bullet$	Velocity fluctuation vector [m/s]
$\bar{\mathbf{U}}$	Time averaged velocity vector [m/s]
V	Volume [m^3]
x,y,z	Cartesian coordinates [m]

Greek

∇	Del operator
μ	Molecular (dynamic) viscosity [kg/(m.s)]
μ_t	Turbulent (eddy) viscosity [kg/(m.s)]
η,ξ	Curve linear coordinates [m]
Γ	Diffusion coefficient (diffusivity) [kg/(m.s)]
Γ_t	Turbulent (eddy) diffusivity [kg/(m.s)]
δ	distance from point to control volume face [m]
ε	Turbulent kinetic energy dissipation rate [m^2/s^3]
ϕ	Variable [-]
ρ	Density [kg/m^3]
σ_t	Turbulent Prandtl/Schmidt number [-]
τ	Stress [Pa]
ω	Pseudo vorticity [1/s]

Subscripts

b	Refers to control face beneath point P
B	Refers to grid point beneath
e	Refers to control face to the east of point P

E	Refers to grid point to the east
n	Refers to control face to the north of point P
N	Refers to grid point to the north
P	Centre point of control volume
s	Refers to control face to the south of point P
S	Refers to grid point to the south
t	Refers to control face above point P
T	Refers to grid point above
w	Refers to control face to the west of point P
W	Refers to grid point to the west

Superscript

0	Values at time t
ϕ	Refers to property of general variable

4 HYDRODYNAMICS

4.1 Introduction

For both equilibrium and rate-based simulations it is important to know the hydraulic capacity of packing, since it determines the diameter of the column. With an equilibrium simulation the column diameter is determined after determining the flow rates and compositions in the column. With a rate-based simulation, the diameter of the column is an input parameter into the model. The modelling of the hydraulic capacity is therefore important if an accurate rate-based simulation is to be performed. The lack in reliable hydraulic models has lead to limited use of rate-based simulations. A few new hydrodynamic models have recently been developed (Olujic et al., 1999, Olujic, 1997, Brunazzi and Pagliante, 1997) and there have also been refinements to existing models (Fair et al., 2000, Billet, 1995). In this chapter these hydrodynamic models are discussed and compared with measured experimental data. The recent improvements in the hydraulic capacity of structured packing are also investigated (Billingham and Lockett, 1999).

4.2 Literature survey

4.2.1 Basic concepts

Before discussing the methods and correlations used to predict the hydraulic capacity of structured packing, it is first necessary to introduce a few basic concepts. These concepts are discussed with relation to Figure 4.1 and Figure 4.2. Figure 4.1 represents the pressure drop over a packed bed and Figure 4.2 shows the hold-up. On both graphs these quantities are plotted against the superficial vapour velocity. Figure 4.1 shows that the pressure drop curve at a specific liquid load is parallel to the pressure drop curve for the dry packing up to a certain point. Beyond this point the pressure drop increases rapidly with an increase in the superficial vapour velocity (the slope of the curve increases). In Figure 4.2 this point coincides with the liquid hold-up starting to be influenced by the vapour velocity. Up to this point the hold-up is independent of the superficial vapour velocity and only dependent on the liquid load and liquid properties. This point shifts to lower superficial vapour velocities with an increase in liquid load. In Figures 4.1 and 4.2 these points are represented with line A-A. Beyond this point the slope of the hold-up curve increases rapidly up to the point were it goes to infinity.

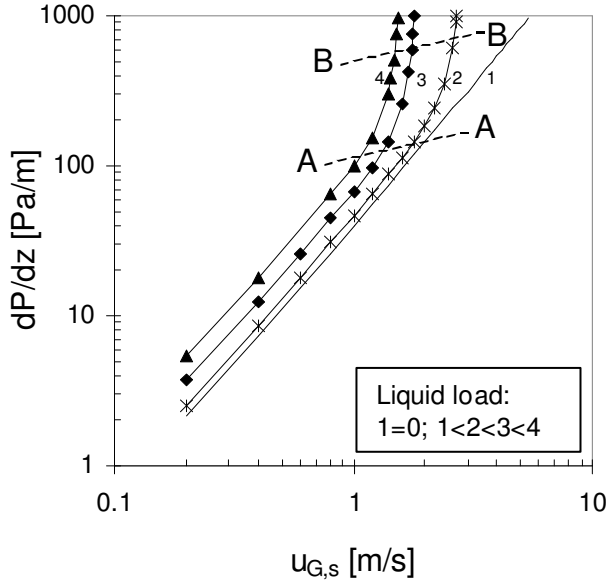

Figure 4.1 Pressure drop as a function of superficial vapour velocity

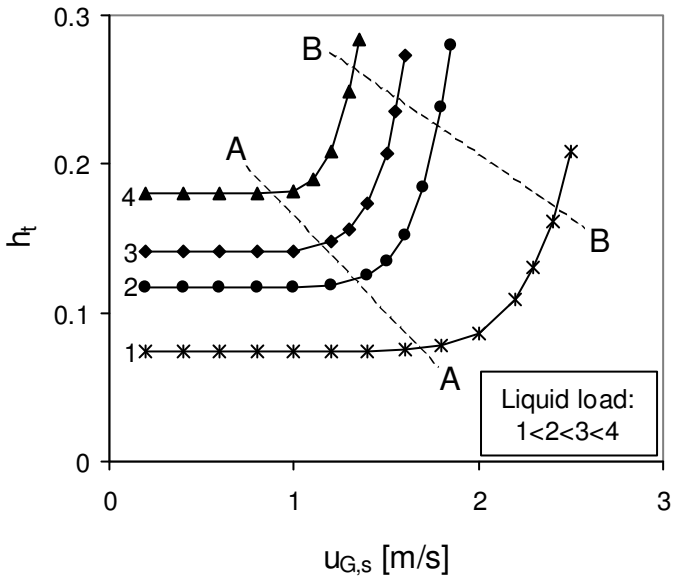

Figure 4.2 Liquid hold-up as a function of superficial vapour velocity

The point where the slope of the pressure drop curve starts to increase is known as the loading point. Line A-A in Figures 4.1 and 4.2 is known as the loading line. The operating region before this line is known as the preloading region. The point where the slope of the pressure drop curve goes to infinity is known as the flood point. This coincides with the point where the slope of the hold-up curve goes to infinity. In Figures 4.1 and 4.2 these points are represented by line B-B. The region between

the loading point (line A-A) and the flood point (line B-B) is known as the loading region. There are a number of other definitions for the flood point (Kister, 1992). The definition here is the same as given by Billet (Billet, 1995) and is used in most theoretical models. The mass transfer efficiency of structured packing is closely related to the hydraulic operating regime. With corrugated sheet structured packing there is a gradual increase in the efficiency with an increase in the liquid- and vapour rates. In the loading region there is a sharp increase in the efficiency, followed by a sharp decrease in the efficiency as the flood point is approached and liquid starts to be entrained. It is therefore important to be able to predict the flood point and also the loading point. There are two methods used to predict the hydraulic capacity of structured packing. The first is capacity charts and empirical correlations, which includes the well-known GDPC charts (Generalized Pressure Drop Correlation), and the second is semi-theoretical models. Capacity charts and empirical correlations are grouped together because they are essentially the same. Both of these approaches are discussed.

4.2.2 Capacity charts and empirical correlations

Capacity charts and empirical correlations have the advantage of being simple. The drawback is that they supply only the vapour- and liquid flow rates for a specific design pressure drop and do not give information about the liquid hold-up.

The well known GPDC charts (Generalized Pressure Drop Correlation) have been used to design columns with random packing for decades. The chart is made up of a number of pressure drop curves that may be used to determine the liquid and vapour flow rates for a specific pressure drop when designing a column. The charts are universal, with only a packing factor characterizing individual packing. There have been quite a number of modifications to these charts. Kister (Kister, 1992) discusses these in detail. There are results from a few studies that are presented in the form of similar capacity charts.

The first published comprehensive study was by McNulty and Hsieh (McNulty and Hsieh, 1982). They measured and characterized the hydraulic performance and efficiency of the Flexipac range of structured packing from Koch in a 3 foot diameter column. Air and water was used at ambient conditions to perform the experimental work. The GPDC method for predicting pressure drop and capacity was found to be inadequate for Flexipac structured packing. Over the liquid loads investigated, the packing factor had to be varied by a factor of two for the GPDC curves to fit the

experimental data. The so-called 'CGCL' method is proposed to correlate the flooding point for the different packing investigated. The 'CGCL' model uses the capacity factors C_G and C_L to correlate the velocity and density dependence of pressure drop and flooding. The correlation suggests a linear relationship for the flooding points in terms of $C_G^{½}$ and $C_L^{½}$. Experimental data confirmed this trend. The influence of liquid viscosity and surface tension was not investigated experimentally. The 'CGCL' model was modified to include viscosity effects by incorporating the same viscosity dependence as has been used in the GPDC model. Surface tension effects were neglected because the surface tension varies within a narrow band for most applications. Efficiency tests were also performed by doing heat transfer experiments. These tests showed that the efficiency increased with an increase in liquid flow rate and this was attributed to better spreading and wetting behaviour of the packing at higher liquid flow rates. Efficiency was found to be 'reasonably independent' of vapour flow rate up to a certain point. An increase in vapour flow rate beyond this point caused a sharp decrease in efficiency. This point is called the maximum design vapour velocity and was found to be at approximately 80% of flooding for a given liquid flow rate. The capacity factor for the vapour- and liquid phases are given by:

$$C_G = u_{G,s}\sqrt{\frac{\rho_G}{\rho_L - \rho_G}} \tag{4.1}$$

$$C_L = u_{L,s}\sqrt{\frac{\rho_L}{\rho_L - \rho_G}} \tag{4.2}$$

The correlation to determine the flood point (or any percentage there of) is:

$$\left(\frac{C_G}{f}\right)^{1/2} + mC_L^{1/2} = \frac{c}{\mu^{0.03}} \tag{4.3}$$

m is the viscosity of the fluid relative to that of water at 70°F (1cP) and f is the fraction of flooding. For design purposes, a value of f=0.8 is recommended. Values for m and c are given for the different types of Flexipac (McNulty and Hsieh, 1982).

Spiegel and Meier (Spiegel and Meier, 1987) characterized the Mellapak range of structured packing using chloro-/ethylbenzene and trans-/cis-decalin test mixtures at total reflux in a column with an internal diameter of 1m. The capacity results are plotted on both a Souders and a Wallis diagram. The results are correlated with an equation of the form:

$$C_G^{1/2} + mC_L^{1/2} = c \tag{4.4}$$

where m and c are adjustable constants. The exact values of these constants are not given but the correlation are reported to predict the capacity with an accuracy of 6%.

The attempts by McNulty and Hsieh (McNulty and Hsieh, 1982) to apply the GDPC charts to structured packing were one of several attempts that were only partially successful. Kister and Gill (Kister and Gill, 1992) identified the limitations of the GDPC charts and proposed the following modifications. The abscissa is the flow parameter and is defined as:

$$X = \frac{L}{G}\left(\frac{\rho_G}{\rho_L}\right)^{0.5} \tag{4.5}$$

The ordinate is the capacity parameter:

$$Y = C_S F_P^{0.5} \nu^{0.05} \tag{4.6}$$

F_P is an empirical factor that characterizes the packing shape and size. C_S is the superficial vapour velocity corrected for density:

$$C_S = u_{G,s}\sqrt{\frac{\rho_G}{\rho_L - \rho_G}} \tag{4.7}$$

A list of packing factors for well known commercial packing is provided (Kister and Gill, 1992). The proposed chart is called the GPDC (SP) interpolation chart. The available experimental data for each type and size of packing is also plotted on the chart. This makes it possible to interpolate between experimental values in operating regions where data are available. Kister (Kister, 1992) provides charts for most of the available commercial structured packing. They also found that the pressure drop at which flooding occurs is accurately correlated by:

$$\Delta P_{flood} = 0.115 F_P^{0.7} \tag{4.8}$$

with dimensions [in H2O/ft].

Robbins (Robbins, 1991) proposed a correlation to predict pressure drop and flooding for random and structured packing. At low liquid loadings, the pressure drop depends only on the vapour flow rate and the geometry of the packing. The packing factors are calculated from dry bed pressure drop data. The correlation is plotted on a chart with the pressure drop as a function of a vapour capacity factor. Pressure drop curves are provided on the chart for different liquid-to-vapour capacity factor ratios. It is generally not recommended for operation at elevated pressures (Kister, 1992).

4.2.3 Semi-theoretical models

There are quite a few semi-theoretical models published for random- and structured packing. These models are in the form of equations and correlations that can be implemented into numerical algorithms. They can be divided into two categories: channel models and porous bed or particle models. In the channel type models the packed bed is modelled as a series of inclined wetted-wall channels. The liquid and vapour is split up, uniformly or non-uniformly, between the different channels. Pressure drop is due to skin friction, form drag and abrupt changes in the flow path. Hold-up in the bed causes the liquid films to become thicker and decrease the total area available for the vapour flow. Examples of channel models are those due to Bravo et al. (Bravo et al., 1985, Bravo et al., 1986), Rocha et al. (Rocha et al., 1993), Billet et al. (Billet, 1995), Brunazzi et al. (Brunazzi and Pagliante, 1997) and Olujic et al. (Olujic, 1997, Olujic et al., 1999). In the particle model the column is modelled as a packed bed using the classic Ergun equation. Pressure drop is due to form drag associated with the particles. The liquid hold-up in the bed reduces the void fraction of the bed and increases the dimension of the particles. Because of the well ordered nature of structure packing and its close resemblance to a series of inclined wetted-walls, there are only a few porous bed (or particle) type models developed for structured packing. A well known particle model is that of Stichlmair et al. (Stichlmair et al., 1989). A more detailed discussion of some of the models will follow.

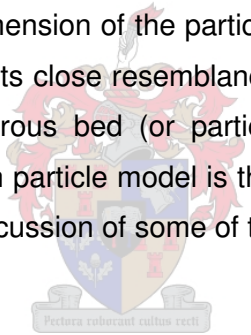

Channel models

The SRP model was developed at the University of Texas over several years (Bravo et al., 1985, Bravo et al., 1986, Fair et al., 2000, Rocha et al., 1993, Rocha and Bravo, 1996). The first model (Bravo et al., 1986) was fitted on air-water pressure drop data for two types of packing, the Flexipac range of packing (McNulty and Hsieh, 1982) and the Gempak range of packing. The dry pressure drop over the bed is correlated with a Darcy type equation:

$$\left(\frac{dP}{dz}\right)_d = f\rho_G \frac{u_{G,e}{}^2}{d_{hG}} \tag{4.9}$$

The friction factor is given by:

$$f = C_1 + \frac{C_2}{Re_{G,e}} \tag{4.10}$$

where C_1 and C_2 are packing specific constants. The pressure drop over an irrigated bed is correlated with an expression similar to that developed for random packing:

$$\frac{dP}{dz} = \left(\frac{dP}{dz}\right)_d \left[\frac{1}{1-h_t}\right]^5 \tag{4.11}$$

The liquid hold-up is correlated with the Froude number:

$$h_t = C_3 Fr_L^{0.5} \tag{4.12}$$

In total three packing specific constants are needed. These constants are published for the Flexipac and Gempak range of packing (Bravo et al., 1986). The model does not apply to conditions where the loading causes significant liquid hold-up.

The model was extended by Rocha et al. (Rocha et al., 1993) in order to predict pressure drop and hold-up in the loading region. The correlations for the dry pressure drop and friction factor are the same as previously (Equation 4.9 and 4.10). The irrigated pressure drop is calculated with an expression similar to Equation 4.11, with the addition of an extra constant:

$$\frac{dP}{dz} = \left(\frac{dP}{dz}\right)_d \left[\frac{1}{1-K_2 h_t}\right]^5 \tag{4.13}$$

where

$$K_2 = 0.614 + 71.35S \tag{4.14}$$

with S the side dimension of a corrugated passage.

In order to calculate the liquid hold-up an effective gravity is used. It is derived by performing a force balance on a fluid element. The final form of the equation is:

$$g_{eff} = g\left[\left(\frac{\rho_L - \rho_G}{\rho_L}\right)\left(1 - \frac{dP/dz}{(dP/dz)_{flood}}\right)\right] \tag{4.15}$$

The pressure drop at flooding needs to be prescribed and in the model it is assumed to be constant at 1025 Pa/m. The film thickness and wetted area is used to calculate the liquid hold-up. The film thickness is calculated according to the classic equation for a laminar falling film, utilizing the effective gravity. A The final form of the equation for liquid hold-up is:

$$h_t = \left(4\frac{F_t}{S}\right)^{\frac{2}{3}} \left(\frac{3\mu_L u_{L,s}}{\rho_L (\sin\theta)\varepsilon g_{eff}}\right)^{\frac{1}{3}} \tag{4.16}$$

The term F_t is a correction factor to account for under wetting of the packing and is based on the Shi and Mersmann (Shi and Mersmann, 1985) correlation for effective interfacial area in random packing:

$$F_t = \frac{29.12\left(We_L Fr_L\right)^{0.15} S^{0.359}}{Re_L{}^{0.2}\,\varepsilon^{0.6}\left(1-0.93\cos\gamma\right)\left(\sin\theta\right)^{0.3}} \tag{4.17}$$

Expressions were developed for the constants in the model based on the characteristic dimensions of seven types of common commercial structured packing. Information needed in the model is the pressure drop at which flooding occurs and the dry pressure drop over the packing.

More recently (Fair et al., 2000) the model was changed by implementing the loading point correlation by Verschoof et al (Verschoof et al., 1999) and renamed the SRP model. The pressure drop in the loading region is calculated with:

$$\frac{dP}{dz} = \left(\frac{dP}{dz}\right)_{preload} F_{load} \tag{4.18}$$

The pressure enhancement factor for the loading region is given by:

$$F_{load} = 3.8\left(\frac{F_G}{F_{G,lp}}\right)^{2/\sin\theta}\left(\frac{u_{L,s}{}^2}{\varepsilon^2 g d_{hG}}\right)^{0.13} \tag{4.19}$$

The loading point F-factor is calculated with:

$$F_{G,lp} = \left(0.053\varepsilon^2 g d_{hG}\left(\rho_L-\rho_G\right)\left(\frac{u_{L,s}}{u_{G,s}\sqrt{\frac{\rho_L}{\rho_G}}}\right)^{-0.25}\left(\sin\theta\right)^{1.15}\right)^{0.5} \tag{4.20}$$

Billet (Billet, 1995) developed a model for both random and structured packing. Most of the experimental data on which the model was fitted were for random packing. There are quite a number of packing specific constants in the model. This makes the model less applicable to structured packing, as only a few types of structured packing were characterized in the study. A broad range of random packing was used and all the necessary packing specific constants in the model for these packing are published (Billet, 1995). Some structured packing data are also included. Although most of the quantities are calculated with correlations, a fundamental approach was followed in deriving the specific form of these correlations. An equation describing the counter current two-phase flow was developed and then used as the basis for developing the different correlations. The dry pressure drop is calculated with:

$$\left(\frac{dP}{dz}\right)_d = \xi_d \frac{a_p}{\varepsilon^3}\frac{u_{G,s}{}^2}{2}\rho_G f_s \tag{4.21}$$

where

$$\xi_d = C_p\left(\frac{64}{Re_{G,s}} + \frac{1.8}{Re_{G,s}^{0.08}}\right) \tag{4.22}$$

and

$$\frac{1}{f_s} = 1 + \frac{4}{a_p d_c} \tag{4.23}$$

The irrigated pressure drop is calculated from:

$$\frac{dP}{dz} = \left(\frac{dP}{dz}\right)_d \frac{\xi_w}{\xi_d}\left(\frac{\varepsilon}{\varepsilon - h_t}\right)^3 \tag{4.24}$$

where

$$\xi_w = C_p W\left(\frac{64}{Re_{G,s}} + \frac{1.8}{Re_{G,s}^{0.08}}\right)\left(\frac{\varepsilon - h_t}{\varepsilon}\right)^{(1.5)} \tag{4.25}$$

and

$$W = \left[\exp\left(\frac{Re_{L,s}}{200}\right)\right]\left(\frac{h_t}{h_{t,lp}}\right)^{0.3} \tag{4.26}$$

In order to determine the pressure drop, values for the hold-up are needed. There are two different types of hold-up calculated with the model. The first hold-up is used to calculate the pressure drop over the packing. Complete wetting is assumed in calculating this hold-up. The hold-up at the loading point is calculated from:

$$h_{t,lp} = 12^{\frac{1}{3}}\left(\frac{u_{L,s}\rho_L}{a_p\mu_L}\right)^{-\frac{1}{3}}\left(\frac{u_{L,s}^2 a_p}{g}\right)^{\frac{1}{3}} \tag{4.27}$$

The hold-up at the flood point is correlated from experimental data as:

$$h_{t,fp} = 0.3741\varepsilon\left(\frac{\mu_L}{\rho_L}\frac{\rho_W}{\mu_W}\right)^{0.05} \quad \mu_L > 1\times10^{-4}\,kg/ms \tag{4.28}$$

Subscript W refers to the properties of water. The hold-up above the loading point is calculated from:

$$(h_t)_{u_{G,s} > (u_{G,s})_{lp}} = h_{t,lp} + (h_{t,fp} - h_{t,lp})\left(\frac{u_{G,s}}{(u_{G,s})_{fp}}\right)^{13} \tag{4.29}$$

In the second approach non-uniform wetting is assumed. The hold-up at the loading point is determined from:

$$\left(h_t\right)_{u_{G,s}\le\left(u_{G,s}\right)_{lp}} = h_{t,lp} = \left(12\frac{\mu_L a^2 u_{L,s}}{\rho_L g}\right)^{\frac{1}{3}}\left(\frac{a_h}{a_p}\right)^{\frac{2}{3}} \tag{4.30}$$

The ratio of the hydraulic area to the wetted area (a_h/a_p) is calculated with:

$$\left(\frac{a_h}{a_p}\right)_{Re_L<5} = C_h\, Re_{L,s}^{\;0.15}\, Fr_{L,s}^{\;0.1} \tag{4.31}$$

$$\left(\frac{a_h}{a_p}\right)_{Re_L\ge5} = 0.85C_h\, Re_{L,s}^{\;0.25}\, Fr_{L,s}^{\;0.1} \tag{4.32}$$

The liquid hold-up at the flood point was found to be approximately 2.2 times higher than the hold-up below the loading point:

$$h_{t,fp} \cong 2.2h_{t,lp} \tag{4.33}$$

The hold-up between the loading- and flood points is calculated with Equation 4.29. In order to calculate hold-up and pressure drop, the superficial vapour velocities at the load- and flood points have to be determined. The superficial vapour velocity at the loading point is calculated from:

$$\left(u_{G,s}\right)_{lp} = \sqrt{\frac{g}{\xi_{lp}}}\left(\varepsilon - h_{t,lp}\right)\sqrt{\frac{h_{t,lp}}{a_p}}\sqrt{\frac{\rho_L}{\rho_G}} \tag{4.34}$$

where the resistance factor is defined as:

$$\xi_{lp} = \frac{g}{C_{lp}^{\;2}\left[\psi\left(\frac{\mu_L}{\mu_G}\right)^{0.4}\right]^{2n_{lp}}} \tag{4.35}$$

The superficial vapour velocity at the flood point is given by:

$$\left(u_{G,s}\right)_{fp} = \sqrt{\frac{2g}{\xi_{fp}}}\frac{\left(\varepsilon - h_{t,fp}\right)^{3/2}}{\varepsilon^{1/2}}\sqrt{\frac{h_{t,fp}}{a_p}}\sqrt{\frac{\rho_L}{\rho_G}} \tag{4.36}$$

The resistance factor differs slightly from the definition in Equation 4.35:

$$\xi_{fp} = \frac{g}{C_{fp}^{\;2}\left[\psi\left(\frac{\mu_L}{\mu_G}\right)^{0.2}\right]^{2n_{fp}}} \tag{4.37}$$

In order to use the model, four packing specific constants are needed: C_p, C_h, C_{lp} and C_{fp}. As mentioned before, a large number of these constants are available for

random packing (Billet, 1995). The number of constants available for structured packing limits the use of the model.

In the pressure drop model by Brunazzi et al. (Brunazzi and Pagliante, 1997), the total pressure drop is calculated as the sum of friction, gravitation and acceleration terms:

$$\left(\frac{dP}{dz}\right)_{TOT} = \left(\frac{dP}{dz}\right)_{F} + \left(\frac{dP}{dz}\right)_{G} + \left(\frac{dP}{dz}\right)_{A} \tag{4.38}$$

The friction term is split up into contributions from losses at the channel walls and at the vapour-liquid interface (distributed losses), and losses from changes in the flow direction (concentrated losses):

$$\left(\frac{dP}{dz}\right)_{F} = \left(\frac{dP}{dz}\right)_{F,d} + \left(\frac{dP}{dz}\right)_{F,c} \tag{4.39}$$

For the dry pressure drop the different terms are:

Acceleration term:

$$\left(\frac{dP}{dz}\right)_{A} = \rho_G u_{G,s} \frac{du_{G,e}}{dz} \tag{4.40}$$

Gravitational term:

$$\left(\frac{dP}{dz}\right)_{G} = -\rho_G g \tag{4.41}$$

Distributed frictional term:

$$\left(\frac{dP}{dz}\right)_{F,d} = \frac{1}{A_G \sin\theta}\left(\tau_{wG} S_G\right) \tag{4.42}$$

A_G is the channel area and S_G is the channel perimeter (defined using the equivalent diameter). The shear stress at the channel wall is calculated from:

$$\tau_{wG} = \frac{1}{2} f_G \rho_G u_{G,e}^{\ 2} \tag{4.43}$$

The friction factor is calculated with:

$$f_G = B_1 + \frac{B_2}{Re_G} \tag{4.44}$$

B_1 and B_2 are packing specific constants. The 'concentrated' frictional term is calculated from:

$$\left(\frac{dP}{dz}\right)_{F,c} = 4 f_G N_c \left(\frac{L_{eq}}{d_{hG}}\right) \frac{\rho_G u_{G,e}^{\ 2}}{2} \tag{4.45}$$

N_c is the number of bends per unit height of packing and L_{eq} is the equivalent length of a channel. The values of these constants are dependent on the height of a packing element and the corrugation angle and are given by Brunazzi et al. (Brunazzi and Pagliante, 1997). In order to calculate the irrigated pressure drop, the wetted area has to be known to calculate frictional losses at the vapour-liquid and vapour-solid interfaces respectively. From the equation for the film thickness of a laminar falling film the following equation is derived:

$$\frac{a_e}{a_p} = \left(\frac{d_{hG}\sin\theta}{4\varepsilon}\right) h_t^{1.5} \left(\frac{\rho_L g}{3\mu_L u_{L,s}}\right)^{0.5} \tag{4.46}$$

For the irrigated pressure drop the gravitational term is the same as for the dry pressure drop. The distributed frictional term is given by:

$$\left(\frac{dP}{dz}\right)_{F,d} = \frac{1}{A_G}\left(\tau_{wG} S_G + \tau_i S_i\right)\frac{1}{\sin\theta} \tag{4.47}$$

S_G and S_i are the dry and wet channel perimeters respectively and A_G is the available area for the vapour phase. In calculating these quantities allowance are made for the liquid hold-up (Brunazzi and Pagliante, 1997). The shear stress at the vapour-liquid interface is calculated from:

$$\tau_i = \frac{1}{2} f_i \rho_G \left(u_{G,e} + u_{L,e}\right)^2 \tag{4.48}$$

The friction factor is calculated using an equation similar to that proposed for counter current annular two-phase flow:

$$f_i = f_G\left[1 + B_3 Bo^{0.3} + B_4\left(\frac{\delta - \delta_0}{d_{hG}}\right)\left(\frac{\mu_L}{\mu_{W,20^oC}}\right)^{0.1} We_L^{B_5}\right] \tag{4.49}$$

The concentrated frictional term is given by:

$$\left(\frac{dP}{dz}\right)_{F,c} = 4 f_m N_c \left(\frac{L_{eq}}{d_{hG}}\right)\frac{\rho_G u_{G,e}^2}{2} \tag{4.50}$$

f_m is a mean friction factor, weighed on the wetted area and calculated from the wall- and interfacial friction factors. The film thickness is calculated from:

$$\delta = \frac{\frac{\tau_i}{2\mu_L} + \sqrt{\left(\pm\frac{\tau_i}{2\mu_L}\right)^2 + 4\left[\rho_L g\sin\theta - \left(\frac{dP}{dz}\right)_{chan}\right]\frac{u_{L,e}}{3\mu_L}}}{\frac{2}{3\mu_L}\left[\rho_L g\sin\theta - \left(\frac{dP}{dz}\right)_{chan}\right]} \tag{4.51}$$

where

$$\left(\frac{dP}{dz}\right)_{chan} = \left(\frac{dP}{dz}\right)_{F,d} \sin\theta - \rho_G g \sin\theta \tag{4.52}$$

The liquid hold-up is calculated from the correlation proposed by Suess et al. (Suess and Spiegel, 1992):

$$h_t = C \cdot a_p{}^{0.83} \left(3600 u_{L,s}\right)^x \left(\frac{\mu_L}{\mu_{W,20^oC}}\right)^{0.25} \tag{4.53}$$

In total six characteristic constants are needed in the model. Constants are available for Sulzer Mellapak 250Y/X and BX packing made from metal or plastic (Brunazzi and Pagliante, 1997).

In the Olujic et al. (Olujic et al., 1999) model the vapour flows in a zigzag pattern through the different packing elements along the triangular channels formed by the corrugated sheets. The pressure drop in the preloading region is calculated with the conventional Darcy type pressure drop equation. In calculating the loss coefficient, three contributions to pressure loss are identified. The first is the overall vapour/liquid interaction, into which losses due to vapour/liquid friction is lumped. The second is losses due to vapour interaction between adjacent triangular channels and the third is pressure losses due to directional changes of the vapour and liquid phases:

$$\left(\frac{dP}{dz}\right)_{preload} = \left(\zeta_{GL} + \zeta_{GG} + \zeta_{DC}\right) \frac{\rho_G u_{G,e}{}^2}{2} \tag{4.54}$$

The overall vapour/liquid interaction coefficient is calculated with:

$$\zeta_{GL} = \varphi \xi_{GL} \frac{h_{pb}}{d_{hG} \sin\theta} \tag{4.55}$$

and the vapour/liquid friction factor from:

$$\xi_{GL} = \left\{-2\log\left[\frac{(\delta/d_{hG})}{3.7} - \frac{5.02}{Re_{G,r}}\log\left(\frac{(\delta/d_{hG})}{3.7} + \frac{14.5}{Re_{G,r}}\right)\right]\right\}^{-2} \tag{4.56}$$

The vapour/vapour interaction coefficient is calculated with:

$$\zeta_{GG} = (1-\varphi)\,0.722\,(\cos\theta)^{3.14} \frac{h_{pb}}{d_{hG} \sin\theta} \tag{4.57}$$

Losses due to directional changes are given by:

$$\zeta_{DC} = \frac{h_{pb}}{h_{pe}} \left(\xi_{bulk} + \psi \xi_{wall}\right) \tag{4.58}$$

The fraction of channels ending against a wall is:

$$\psi = \frac{2h_{pe}}{\pi {d_c}^2 \tan\theta}\left({d_c}^2 \frac{{h_{pe}}^2}{\tan^2\theta}\right)^{0.5} + \frac{2}{\pi}\arcsin\left(\frac{h_{pe}}{d_c \tan\theta}\right) \quad (4.59)$$

The loss coefficient at the interface between packing elements is given by:

$$\xi_{bulk} = 1.76(\cos\theta)^{1.63} \quad (4.60)$$

and the loss coefficient of channels ending at a wall by:

$$\xi_{wall} = \frac{4092 {u_{L,s}}^{0.31} + 4715(\cos\theta)^{0.445}}{Re_{G,e}} + 34.19 {u_{L,s}}^{0.44} (\cos\theta)^{0.779} \quad (4.61)$$

The pressure drop in the loading region is calculated using the correlations proposed by Verschoof et al. (Verschoof et al., 1999) for predicting the loading point and loading effect. The same equations are used as discussed in the SRP model. The liquid hold-up is calculated simply from the geometric area of the packing and the liquid film thickness:

$$h_t = \delta a_p \quad (4.62)$$

The liquid film thickness is calculated with the Nusselt formula for falling films, provision being made for the inclination angle of the packing:

$$\delta = \left(\frac{3\mu_L u_{L,s}}{\rho_L g a_p \sin\theta}\right)^{\frac{1}{3}} \quad (4.63)$$

There are no packing specific constants in the model. All the constants needed in the model are calculated using the characteristic lengths B, S and h of corrugated structured packing.

There are a few more recent models that are also classified as channel models. These models are more fundamental in nature and have been developed to predict pressure drop and hold-up in the preloading region. Because of the fundamental nature of these models, the model equations are quite complicated. These models are probably a start to a new generation of hydraulic models. Their complexity and limited range limits their use in hydraulic calculations at present.

Woerlee et al (Woerlee et al., 2001) developed a fundamental model for pressure drop in packed columns. The packed bed is modelled as a series of inclined tubes. The liquid is modelled as a laminar film that totally wets the tube walls. The pressure drop comprises of frictional losses at the vapour-liquid interface and losses due to the geometry or form drag. The friction factor for a smooth liquid interface is calculated

with the Blasius equation. The pressure drop due to form drag and geometry is combined with the interfacial losses using the Ergun equation for packed beds. The friction factors are then determined by fitting the Ergun relation on experimental data (dry packing). The proposed equation for the friction factor is extended to include what is termed as the 'effective' packing inclination angle. This angle is calculated from dry pressure drop data. A modification is also made to take column diameter effects into account. The increase in pressure drop due to the presence of a disturbed liquid film (not smooth any more) is taken into account by defining a vapour-liquid interaction coefficient. The pressure drop for a smooth (non-disturbed) film is then multiplied by this factor to calculate the overall total pressure drop. This interaction coefficient is determined by fitting the model to experimental data. The model did not predict the pressure drop in structured packing accurately. This is thought to be due to liquid entrainment (Woerlee et al., 2001).

Iliuta and Larachi (Iliuta and Larachi, 2001) proposed a hydraulic model for structured packing in the preloading region. The model is based on the hydrodynamic modelling of concurrent two phase flow in a randomly packed trickle bed reactor. In the model the irrigated pressure drop, liquid hold-up and fraction wetted area is simultaneously calculated. Inputs needed are the dry pressure drop for the specific packing and the packing constants. The packing is assumed to be partially wetted. The partially wetted packing is conceptually split up into wet channels and dry channels (or slits). The vapour flow rate is split up between the dry and wet channels. The dimensions of these channels are related to the packing geometry. A few simplifying assumptions regarding the flow are made. A smooth vapour-liquid interface is assumed. The contribution made to the effective surface area by liquid droplets is assumed to be negligible. The effective phase velocities in the channels or slits are identical to the effective velocities in the packing geometry. The friction factors at the wall and at the vapour-liquid interface are equal. There are no discontinuities in the velocity and shear profiles at the vapour-liquid interface and the pressure drop across the conceptual channels (slits) are equal to the pressure drop over the packed bed. Momentum balances are performed for the vapour phase in the dry and wet channels and for the liquid phase in the wet channels. An expression is developed for the liquid velocity at the interface and the average liquid film velocity. After some simplification, the model consists of three non-linear coupled algebraic equations that are solved with an iterative technique. The results compare favourably with experimental results and with the model of Billet (Billet, 1995).

Ranke et al. (Ranke et al., 2000) suggested a model to predict pressure drop and hold-up based on experimental work carried out on two types of structured packing made from aluminium and with a specific surface area of 750m^2/m^3. An organic liquid was used in the experiments and the vapour entering the column was saturated with the liquid. In developing the model it is assumed that the vapour follows the channels provided by the packing. The liquid phase stays on a single corrugated sheet and follows a path down the plane with the steepest inclination angle. The angle at which the liquid flows down the sheet is influenced by the interfacial shear stress at the vapour-liquid interface. In calculating the dry pressure drop, the friction factor is split up into contributions from interfacial friction, losses due to changes in direction between packing elements and losses due to the outflow of vapour from a packed section. A force balance for the liquid film is done and shear at the vapour-liquid interface is taken into account. This yields an equation from which the velocity distribution and film thickness can be obtained (after integration). The dynamic liquid hold-up is determined from the geometric area of the packing and the average liquid film thickness. Complete wetting of the packing is assumed. The irrigated pressure drop is calculated from the dry pressure drop multiplied by the ratio of the 'available cross sectional area' for vapour flow raised to the power 2.5. A radial distribution model was developed for the liquid phase. At each contact point a portion of the liquid flows to the adjacent sheet. Lateral liquid shift is also thought to be generated in the troughs of the channels. The model was fitted on measured distribution data in order to determine the distribution width (and therefore the radial distribution of the liquid phase). The model contains three fitting parameters that have to be determined experimentally for individual types of packing. Unfortunately these constants are only available for the packing investigated in the study. It would be difficult to use the model for other types of packing since the radial distribution of the liquid phase needs to be measured and correlated. This is quite a difficult quantity to measure experimentally.

Particle- or porous bed models

Stichlmair et al. (Stichlmair et al., 1989) developed a model for the prediction of pressure drop and capacity for columns containing random- and structured packing. The model use fundamental studies on capacity and pressure drop in porous beds (fluidised or fixed) to model the hydrodynamics. An expression is developed to calculate the pressure drop for a dry bed (no liquid irrigation) based on the Richardson and Zaki relationship between vapour velocity and porosity for fluidised beds:

$$\frac{dP}{dz} = \frac{3}{4} f_o \left[\frac{(1-\varepsilon)}{\varepsilon^{4.65}} \right] \frac{\rho_G u_{G,s}^{\ 2}}{d_{hG}} \tag{4.64}$$

where

$$f_o = \frac{C_1}{Re_{G,s}} + \frac{C_2}{Re_{G,s}^{\ 0.5}} + C_3 \tag{4.65}$$

C_1, C_2 and C_3 are packing specific and values for quite a few types of random packing and some structured packing are given (Stichlmair et al., 1989). To calculate the pressure drop in an irrigated bed the change in void fraction due to liquid hold-up is considered. The irrigated pressure drop is calculated by using a modified friction factor that takes the hold-up into account:

$$\frac{\Delta P_{irr}}{\Delta P_d} = \left\{ \frac{\left[1-\varepsilon\left(1-h_t/\varepsilon\right) \right]}{1-\varepsilon} \right\}^{2/3} \left(1-\frac{h_t}{\varepsilon} \right)^{-4.65} \tag{4.66}$$

A correlation was fitted on experimental hold-up data for eight types of packing (random and structured) below the loading point:

$$h_{t,0} = 0.555 Fr_{L,s}^{\ 1/3} \tag{4.67}$$

The hold-up above the loading point is calculated with an expression fitted on experimental data:

$$h_t = h_{t,0} \left[1 + 20 \left(\frac{\Delta P_{irr}}{z \rho_L g} \right)^2 \right] \tag{4.68}$$

The irrigated pressure drop is used in this expression. In order to calculate the pressure drop above the loading point an iterative scheme is followed since the irrigated pressure drop is an implicit variable. The flood point is defined as the point where the pressure drop increases infinitely with increasing vapour load. Differentiation of the pressure drop equation yields an equation with which the flooding pressure drop is calculated:

$$\left(\frac{\Delta P_{irr}}{z \rho_L g} \right)_f^{-2} - \frac{40 \frac{2}{3} h_{t,0}}{1-\varepsilon+h_{t,0}\left\{ 1+20\left[\Delta P_{irr}/(z\rho_L g) \right]_f^2 \right\}} - \frac{186 h_{t,0}}{\varepsilon - h_{t,0}\left\{ 1+20\left[\Delta P_{irr}/(z\rho_L g) \right]_f^2 \right\}} = 0 \tag{4.69}$$

The model was validated with experimental data for structured- and random packing.

4.2.4 Discussion

Kister (Kister, 1992) recommends interpolation between packing pressure drop data for determining column pressure drop. In the absence of pressure drop data, empirical pressure drop correlations are recommended. The various empirical correlations for flooding and pressure drop could be used to determine pressure drop and flooding. There is however one aspect that should be kept in mind. The difference between the non-equilibrium model and the equilibrium stage model is the calculation of mass- and heat transfer rates. Models are needed for these transfer rates. Empirical pressure drop correlations will predict the pressure drop but will give no information on the local properties of the liquid and vapour phases, such as effective velocities. The local interaction between liquid and vapour needs to be modelled (or correlated) in order to determine the transfer rates. Good semi-theoretical models are therefore needed in the rate-based approach. There are quite a number of semi-theoretical models, as discussed in section 4.2.1. All of them contain a fair amount of empiricism. This is because counter current two phase flow is complicated and good fundamental models do not yet exist. The models fitted and validated on large experimental databases should therefore give more reliable results than those fitted on small data sets. Models fitted on large data bases are those proposed by Rocha et al. (Rocha et al., 1993), Billet (Billet, 1995), Stichlmair et al. (Stichlmair et al., 1989) and Olujic (Olujic, 1997). A concern in some of these models is the large amount of air/water hold-up and pressure drop data used for fitting and validation of the models. Bennett and Ludwig (Bennett and Ludwig, 1994) highlight the limitations of air/water tests. The model of Billet (Billet, 1995) was fitted on an extensive data set where the liquid properties varied over a wide range. The liquid- and vapour load also varied over a wide range. All the other models rely heavily on air/water experimental data. The model proposed by Rocha et al. (Rocha et al., 1993) was fitted on air-water data from literature (Chen et al., 1983, McNulty and Hsieh, 1982). The model of Olujic (Olujic, 1997) was fitted on experimental air/water data. In the latest versions of the Delft and SRP models, the loading point prediction is improved by a correlation to predict the loading point (Verschoof et al., 1999). This correlation was fitted on a data set containing both air/water and distillation data.

Rather than proposing a new semi-theoretical model fitted on a limited range of experimental data, this study focuses on evaluating the models mentioned above and to identify those more suitable and reliable for use in a rate-based simulation. Pressure drop and hold-up measurements were performed using the systems air/water and air/Kerosol 200. Kerosol 200 is a heavy paraffin cut with a normal

boiling point of around 200°C. It was chosen because of its low surface tension and high viscosity. Because of its high boiling point it has a low vapour pressure at ambient conditions that limits emissions and losses in the open loop system employed. Failures of structured packing in the past in extractive distillation applications are thought to be mainly due to inaccurate predictions of the effect of viscosity on packing capacity. By using this system the effect of viscosity on capacity is investigated. Since air/water data are abundant in the literature, it makes sense to compare the performance of the new generation of high capacity structured packing with that of normal structured packing using this system.

4.3 Experimental

4.3.1 Experimental set-up

The experimental set-up is shown in Figure 4.3. The required airflow rate is obtained by throttling the air intake to the centrifugal blower. The air is fed to the column through a 140mm OD class 4 PVC pipe. The airflow rate is measured with a square edged orifice plate constructed according to ASME standards (Meters, 1959). The orifice plate is situated 20 pipe diameters above the blower outlet to ensure a developed flow profile. Pressure taps are situated at one pipe diameter up stream (1D) and a half pipe diameter down stream (½D). Different sizes orifice plates are used in order to cover the whole operating regime and to avoid large errors caused by small differential pressure measurements. The pressure drop across the orifice plate and the static pressure at the upstream pressure tap are measured with manometers. The air enters the column through a glass 200 mm ID Schott column adaptor with a 90mm ID side inlet. The 140mm ID PVC inlet pipe is reduced to 90mm ID with a reducer. A special flange made from PVC is used to connect the inlet pipe to the glass column adapter. Before entering the column section, the air passes through an inlet section with an ID and height of 200mm made from stainless steel. This section is equipped with a static mixer to ensure good air distribution across the column cross sectional area. On top of this section is a glass 200mm ID Schott column section containing a bed of structured packing. The packed bed contains three structured packing elements. The height of an element is 265mm Flexipac 350Y and 267mm for Flexipac 350Y HC. The packing elements are rotated 90° with respect to one another. The top of the packed bed is situated just below the top flange of the glass column section. This is achieved by using a spacer on top of the static mixer. The spacer is constructed in a manner so as not to obstruct the airflow into the passages of the bottom packing element. On top of the glass column section

is a liquid distributor section followed by the air outlet section. Both these sections are 200mm in height and constructed from stainless steel. The air is vented to the atmosphere through a 140mm ID class 4 PVC pipe that is fastened to the outlet section with a threaded adapter.

The liquid reservoir is situated beneath the column to facilitate gravity drainage from the bottom of the column. The fluid is heated with an electric heater before being pumped to the top of the column. The flow rate is controlled with a glass bellows valve and measured with a rotameter, calibrated for the working fluid. The liquid is distributed over the packed bed with a specially constructed liquid distributor, as shown in Figure 4.4, having a drip point density of 1600 drip points/m^2. The liquid is drained from the column through the 50mm ID bottom exit of the Schott glass column adapter and flows over a constant height overflow to the storage vessel. There is a 2" ball valve situated directly beneath the column in the drain line. This valve is connected with a metal bush to a 1" ball valve in a line that runs from the liquid feed line to the storage vessel (bypass line). A yoke is welded onto the bush and is connected to the push arm of a pneumatic piston assembly. The position of the piston is controlled with compressed air fed to either side of the plunger through the use of solenoid valves. The solenoid valves are controlled from a computer that also controls the pump and blower. The liquid hold-up is determined by measuring the volume of free draining liquid from the column after the air and liquid flows to the column have been switched off. The distributor is constructed so that the liquid feed enters the distributor from the bottom. When the pump and blower are switched off, the liquid left in the distributor is drained through the bypass line to the storage vessel. The bypass line completely fills up with liquid during normal operation. This causes the distributor to be emptied completely and quickly when the ball valve in the bypass line is opened. This coincides with the ball valve in the column drain line being closed and trapping all the liquid draining from the packing. The whole switching operation is computer controlled and is done in less than a second. The temperature of the air and liquid is measured on entering and on exiting the column with grade B PT100's calibrated against a grade A PT100. The column is operated at ambient conditions. The pressure drop over the column is measured with a Shaevitz model 6061 differential pressure cell.

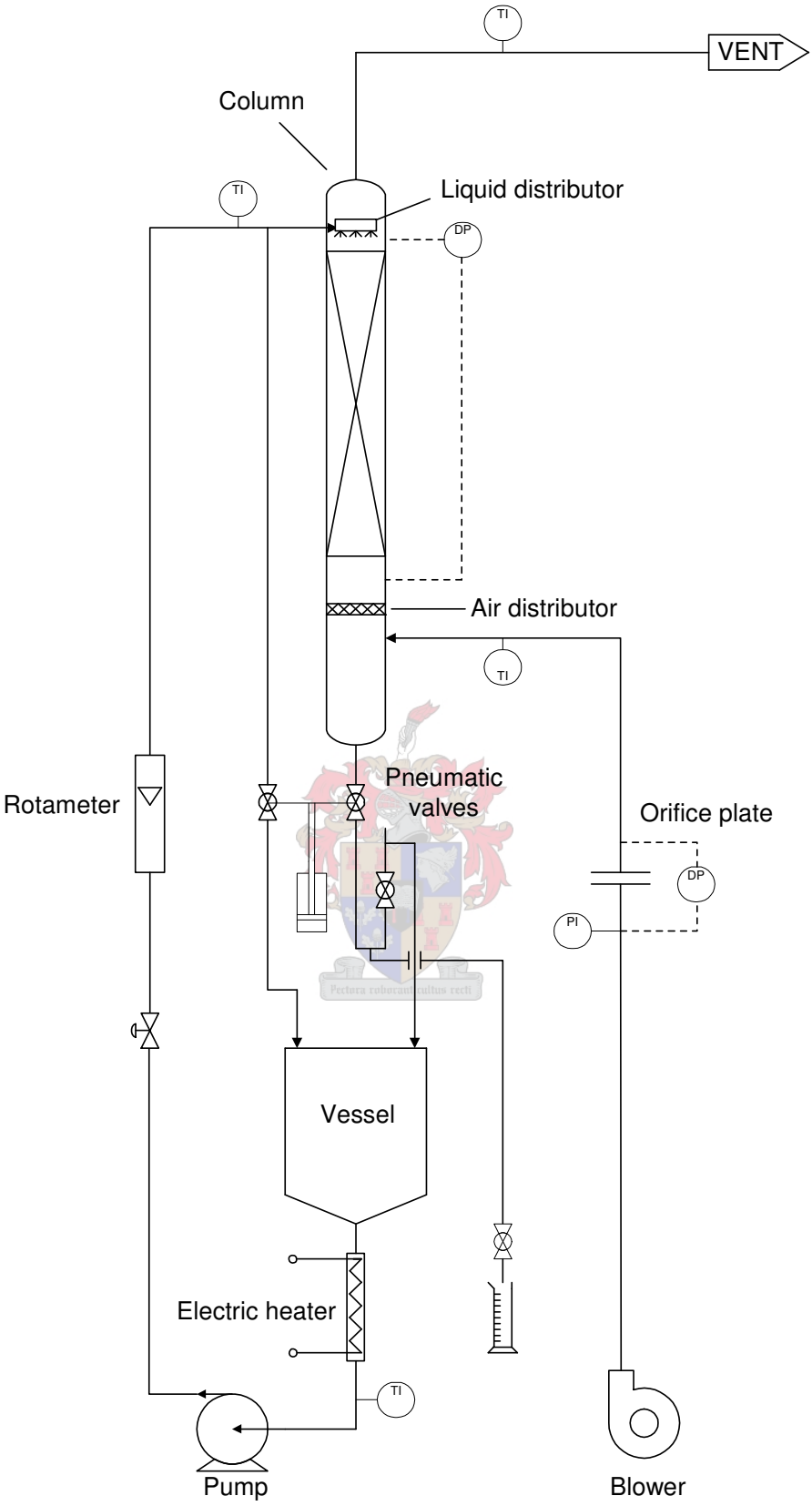

Figure 4.3 Experimental set-up

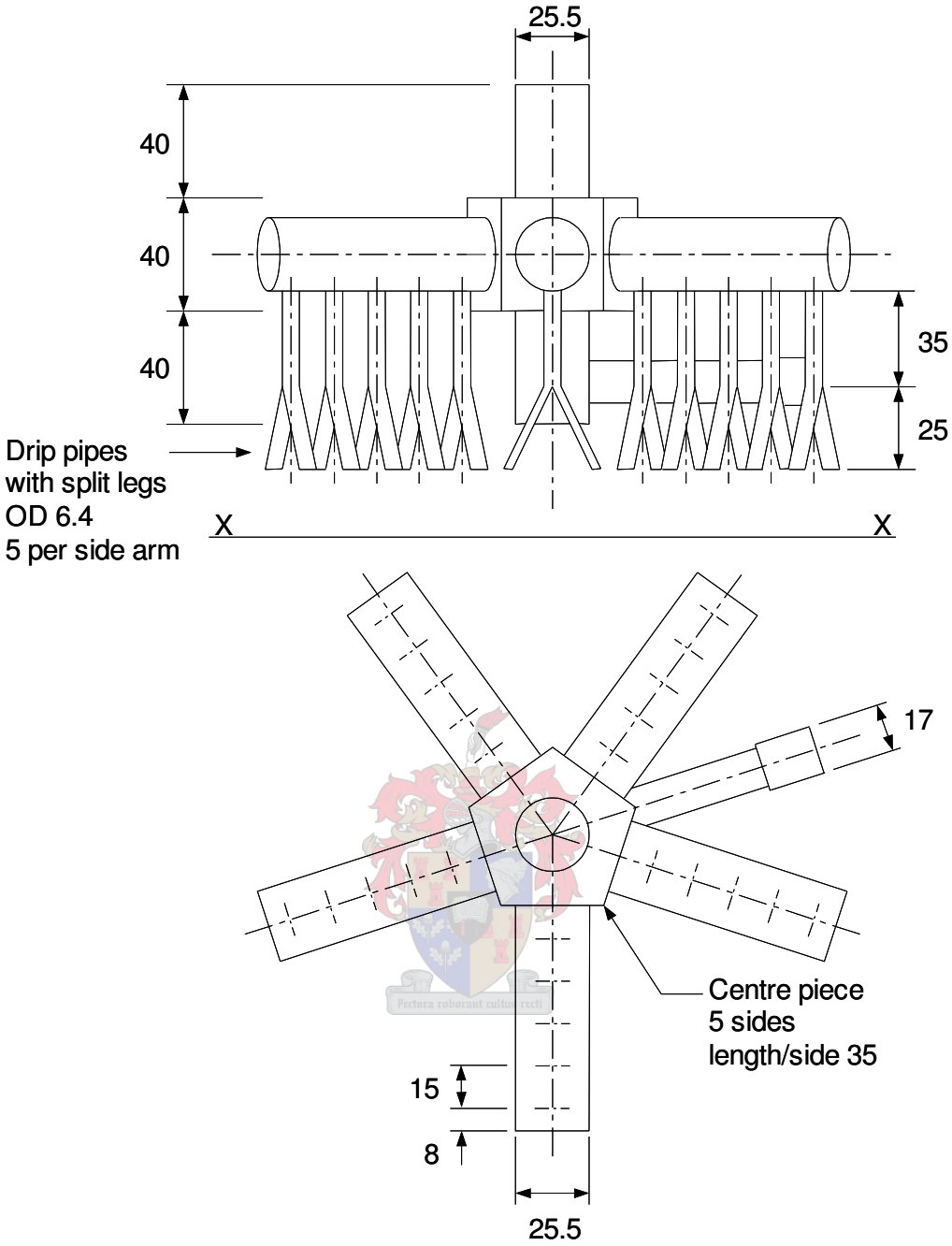

Figure 4.4 Distributor

4.3.2 Experimental procedure

Each structured packing element was washed in an acetone/alcohol mixture before installing it in the column to rid it of oil and grease used in the manufacturing process. Before the start of an experiment, the lines to the DP cell are flushed with air to make sure that the pressure drop readings are not influenced by any condensate build up in these lines. The dry packing pressure drop is measured before the packing is wetted. Before the start of air/liquid experimental operation, the packing is irrigated with the working fluid for about an hour to ensure thorough wetting of the surface of

the packing. The air- and liquid flow rates are then adjusted to their desired values and the column left for between 10-15 minutes to attain steady operation. The air- and liquid feed are then switched off while simultaneously opening the bypass valve and closing the valve in the column drain line. The liquid left in the constant overflow leg of the drain line is allowed to drain and the ball valve in this line is closed. During this time the liquid draining from the packing is collected at the bottom of the column. When all the liquid has drained from the constant overflow leg, the drain valve beneath the column is opened and the volume of liquid draining from the bottom of the column is collected and measured. The liquid is allowed to drain from the packing for a period of 10 to 15 minutes, depending on the liquid being used. Before the start of the next experiment, the packing is irrigated at a high liquid rate to ensure good wetting. The liquid that drains from the column is corrected for the large empty space in the column by performing hold-up experiments with an empty column. The volume of liquid collected with an empty column is multiplied by the total empty height fraction of the packed column and this amount then subtracted from the measured total hold-up in order to determine the packing hold-up. The hold-up measured in this way is the 'dynamic hold-up'. The liquid left on the packing after the allotted time has passed is termed the 'static hold-up'. This hold-up is determined by weighing a dry packing element before submerging it in the working fluid and completely wetting the surface. The packing is then left to drain for the same amount of time allowed in the experiments and then weighed again. The volume of liquid still left on the packing is thus determined and added to the 'dynamic hold-up' determined previously. The total hold-up is determined in this way. This method allows more experiments to be performed in a period of time compared to when leaving the column to drain for a long time in order to determine the total hold-up. Since the static hold-up is not influenced by the liquid load (Billet, 1995, Rocha et al., 1993), only a single measurement is necessary for each liquid used. It is also a small fraction of the total hold-up (Billet, 1995, Rocha et al., 1993) and any errors made in determining it should not have a large impact on the results.

4.3.3 Physical properties and packing dimensions

The physical properties for the test systems are listed in Table 4.1 and the dimensions of the packing in Table 4.2. Figure 4.5 shows the dimensions of a corrugated channel and the modifications made to the inlet and outlet sections of the high capacity packing.

Table 4.1 Physical properties of test system

Component	ρ [kg/m^3]	μ [Pa.s]	σ [N/m]
Air	1.15	1.86×10^{-5}	n/a
Water	1000	8.02×10^{-4}	71.2×10^{-3}
Kerosol 200	763	2.31×10^{-3}	23.9×10^{-3}

Table 4.2 Dimensions of packing

Property	Flexipac 350Y	Flexipac 350Y HC
Corrugation base, B [mm]	15.5	16.5
Corrugation side, S [mm]	11.5	11
Crimp height, h [mm]	8.4	7.5
Void fraction, ε	0.985	0.984
Corrugation angle, θ [^{o}]	45	45
Inlet/exit calming section, z_e [mm]	0	15
Height of element, h_{pe} [mm]	265	267

4.4 Results and discussion

4.4.1 Comparison between normal and high capacity packing

The experimental results are given in table format in Appendix B. In the following graphs the pressure drop and hold-up for the two types of packing are compared at three liquid flow rates. The pressure drops shown in the following graphs are the pressure drops over the packed bed. The pressure drop due to the static vapour head between the pressure taps situated above and below the packed bed was subtracted from the experimentally measured values.

The dry-bed pressure drops for the two packing are compared in Figure 4.6. This graph clearly shows that the dry-bed pressure drop for Flexipac 350Y HC is higher than that for Flexipac 350Y. There are two contributing mechanisms that are thought to cause the higher dry bed pressure drop in the high capacity packing. The first of these are due to the corrugation dimensions that differ slightly (see Table 4.2). The volume of a single 'criss-cross' element is 1.5% smaller in the high capacity packing than in the normal packing.

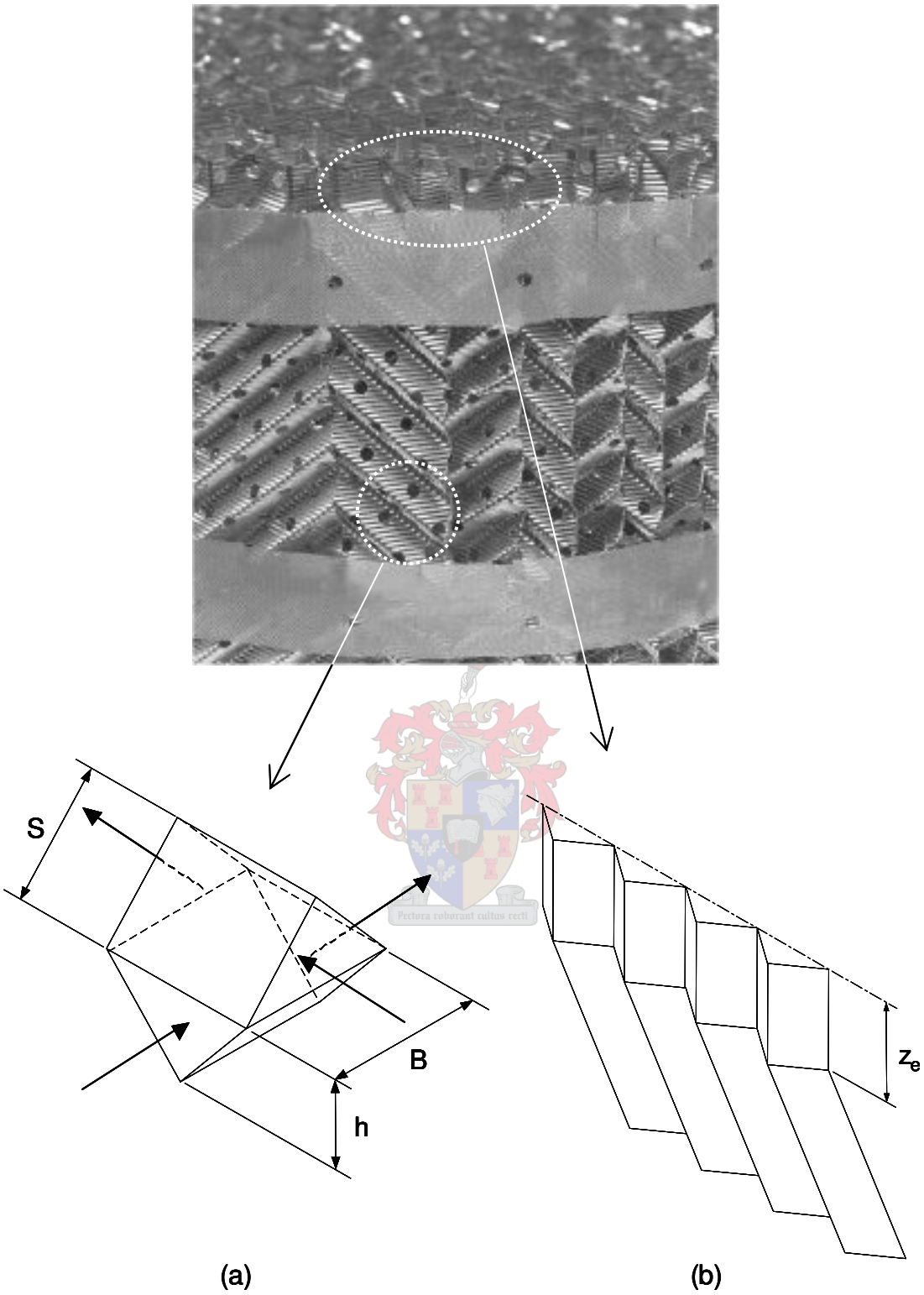

Figure 4.5 Characteristic dimensions of packing (a) Corrugation channel (b) Modification to entrance and exit region (high capacity packing).

This would lead to a higher number of these elements for the high capacity packing in the same column volume compared to the normal packing.

The biggest contribution to the overall dry pressure drop is from the vapour phase interaction at the free shear layer between facing corrugation channels. An increase in the number of these free shear interfaces would therefore lead to an increase in the pressure drop. The second mechanism that is thought to contribute to the higher pressure drop in the high capacity packing is due to the misalignment of adjacent packing sheets.

With the new design the first and last 15 mm of the channels are bent parallel to the vertical column axis. The increase in dry bed pressure drop may also be due to the alignment between sheets being out of phase. Visual inspection of the modified packing elements (see Figure 4.7) showed a number of adjacent sheets being out of phase. Although this would not decrease the available surface area for vapour flow, it would cause a boundary layer to develop in the middle of the corrugated passage. The high capacity packing also has a slightly smaller crimp height (see Table 4.1). This resulted in two more layers of corrugated sheets in a packing segment compared to the normal capacity packing. There will therefore be more corrugated channels in the high capacity packing compared to the normal packing with a larger number of micro elements contributing to the overall dry pressure loss, as discussed before.

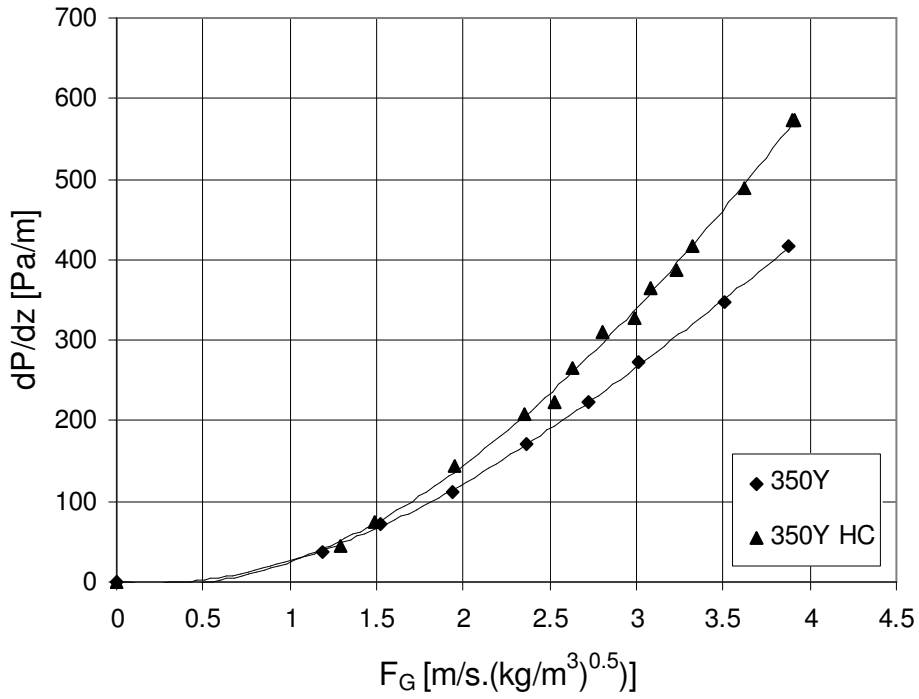

Figure 4.6 Comparison between dry-bed pressure drop for Flexipac 350Y and Flexipac 350Y HC

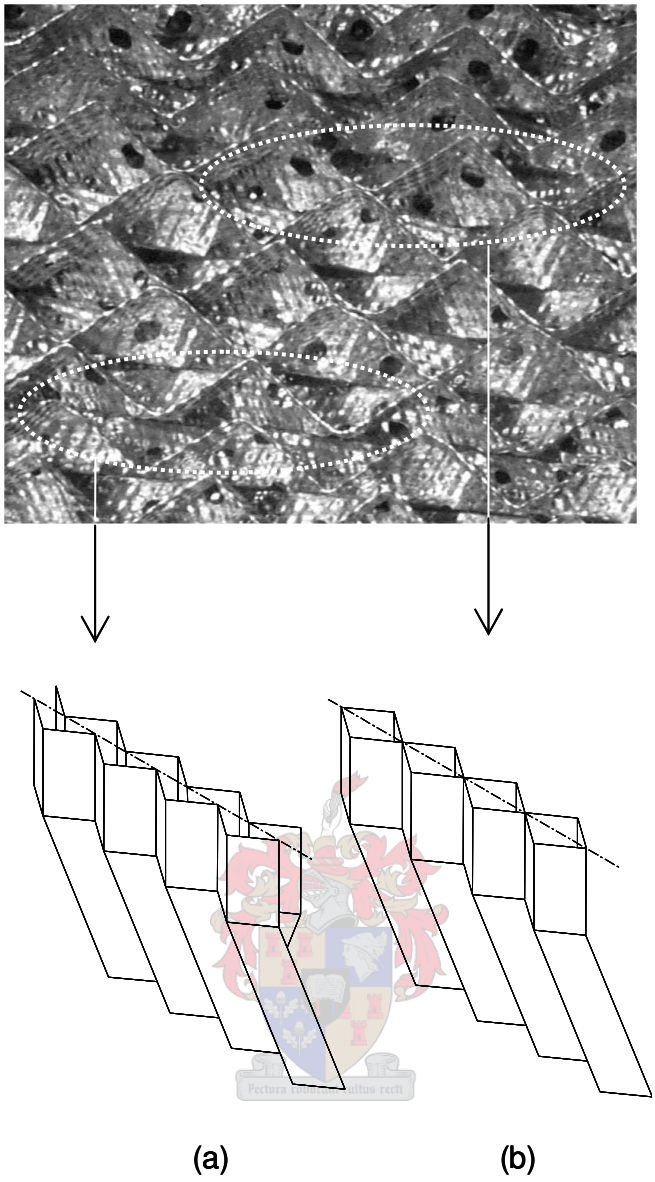

Figure 4.7 Corrugation geometry at top and bottom of packing element. (a) Corrugations out of phase, (b) Corrugations in phase

The pressure drops over the normal and high capacity packing are shown in Figure 4.8 for the air/water system. When comparing the flooding points at different liquid loads for the two types of packing, the figure shows that there is an increase in capacity in the high capacity packing compared to the normal packing for this system. At a liquid load of 35.7 $m^3/(m^2hr)$ the increase in capacity is approximately 20%. This increase in capacity is more evident if the hold-up curves are compared, as is done in Figure 4.9. Although the hold-up is slightly higher for the high capacity packing, the slopes of the hold-up curves for this packing are not nearly as steep as for the normal packing at high pressure drops, i.e. high up in the loading region. The increase in capacity is less evident for the air/Kerosol 200 system. Figures 4.10 and

4.11 compare the pressure drop and hold-up of the two types of packing for this system. The increase in capacity is shown to be marginal. At a liquid load of 35.6 $m^3/(m^2.hr)$ the increase in capacity is 4%. This poorer than expected performance of the high capacity packing may again be due to the corrugations being out of phase at the top and bottom of a packing element. This would cause adjacent sheets to form a narrow channel for the vapour flow (see Figure 4.7) and the development of a boundary layer as discussed before. When the corrugations are out of phase, liquid flowing down the vertical ridge of a corrugation will be exposed to a high shear force caused by the developing boundary layer in the middle of the passage. It would seem that a liquid with a higher viscosity and lower surface tension than water is more likely to be entrained by this mechanism.

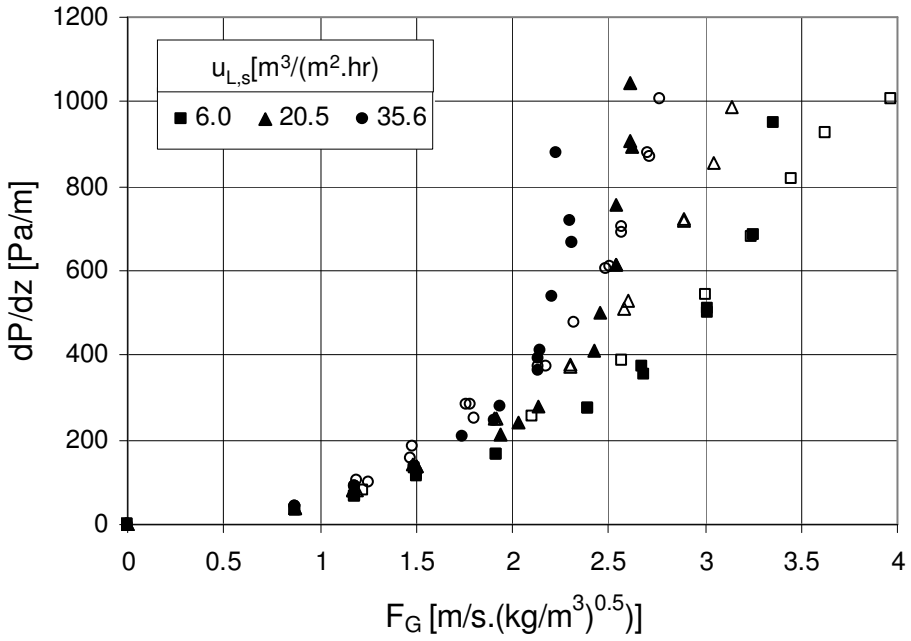

Figure 4.8 Comparison of pressure drop over normal and modified packing for the air/water system. (●): Flexipac 350Y, (○): Flexipac 350Y HC.

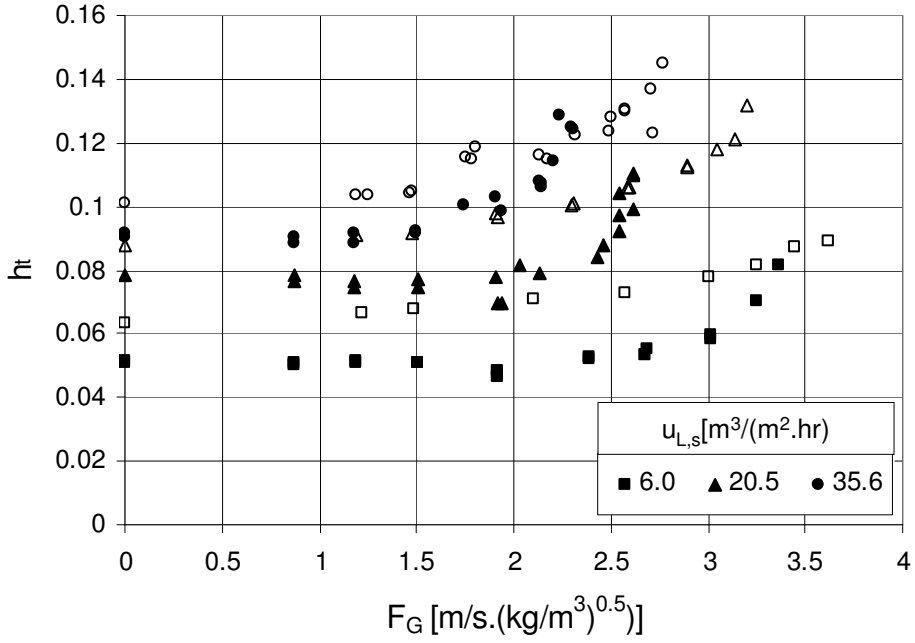

Figure 4.9 Comparison of hold-up on normal and modified packing for the air/water system. (●): Flexipac 350Y, (○): Flexipac 350Y HC.

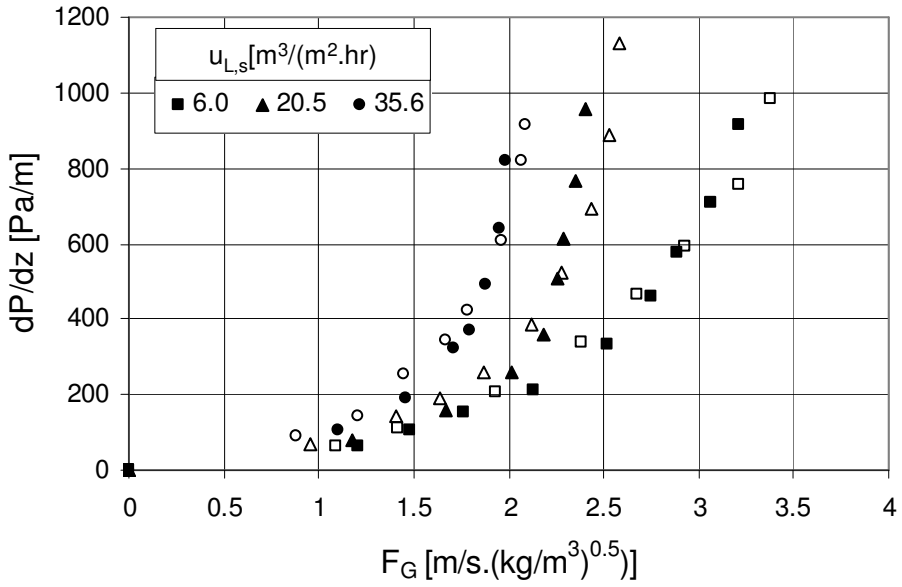

Figure 4.10 Comparison of pressure drops over normal and modified packing for the air/Kerosol 200 system. (●): Flexipac 350Y, (○): Flexipac 350Y HC.

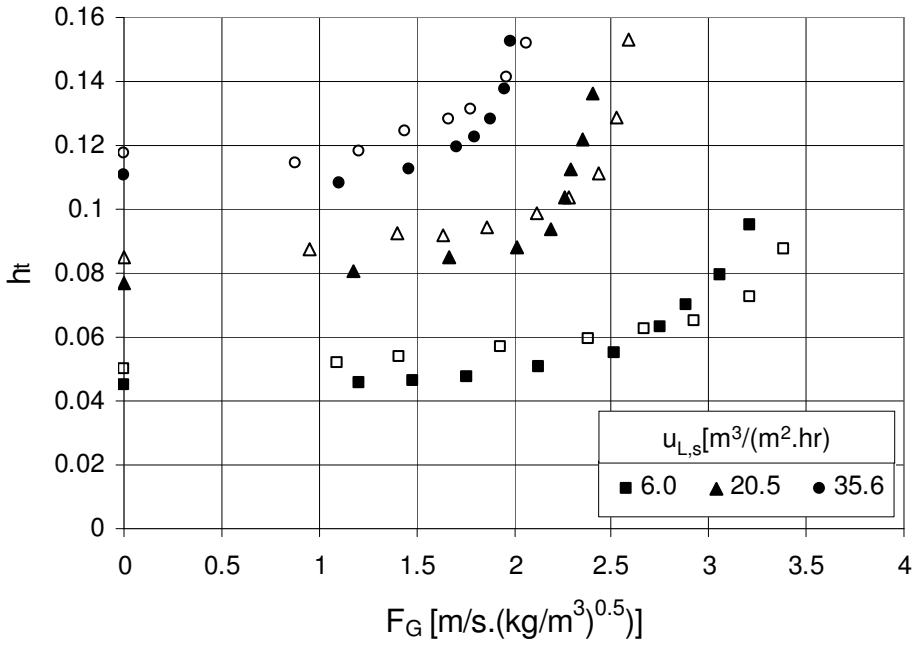

Figure 4.11 Comparison of hold-up on normal and modified packing for the air/Kerosol 200 system. (●): Flexipac 350Y, (○): Flexipac 350Y HC.

4.4.2 Comparison with semi-theoretical models

The pressure drop and hold-up predictions of the semi-theoretical models are compared with the experimental results for the highest and lowest experimental liquid loads used for each test system in this section. Before comparing the results, it is necessary to discuss some of the assumptions made in implementing the models.

For each model, except the Delft model, the proposed dry pressure drop correlation was fitted to the experimental data. For the SRP and Stichlmair models, this is the only additional information needed. A modification had to be made to the Delft model in order to apply it to the packing element heights used in this study. The model was developed for packing element heights (h_{pe}) greater than or equal to the diameter of the column. In this study the column diameter is 200mm and the height of a Flexipac 350Y element is 265mm. The height of a packing element is therefore larger than the diameter of the column. This would cause an error in the model when calculating the fraction of channels ending at the column wall. In this study this fraction was set equal to one and the rest of the model used as proposed. This modification could influence the results obtained with the model.

In order to determine the pressure drop over the packing in the Billet model, two packing specific constants are needed, C_{lp} and C_{fp}. There are no constants published for Flexipac 350Y. There are however constants published for Mellapak 250Y and

Montz B1-300 (Billet, 1995). Both the geometric area and the shape of these packings differ. The Montz B1-300 has a geometric surface area of $300m^2/m^3$ and the passages are circular. The Mellapak 250Y has a geometric area of $250m^2/m^3$ and triangular passages. Given these differences, there is a surprisingly small difference in the loading point constant (C_{lp}=3.157 for Mellapak 250Y and C_{lp}=3.098 for Montz B1-300). Virtually the same pressure drop is calculated by using either one of the constants. The flood point constants for these packing are the same (C_{fp}=2.464). This value is also used for Flexipac 350Y. For the correlation proposed for determining liquid hold-up, an additional packing specific constant is needed. Inspection of the values of these constants for different sizes structured packing shows a decrease in their values with an increase in specific surface area. The packing with the closest specific surface area to Flexipac 350Y for which a constant is supplied, is Montz B1-300. This constant is also used for Flexipac 350Y.

The pressure drop for the air/water system is compared with the values calculated with the different models in Figures 4.12 and 4.13. Figure 4.12 show the results at a liquid load of 6.0 $m^3/(m^2hr)$ and Figure 4.13 the results at a liquid load of 35.7 $m^3/(m^2hr)$. The corresponding liquid hold-up curves are shown in Figures 4.14 and 4.15.

Figures 4.12 and 4.13 show that the model by Stichlmair does not predict the pressure drop trend accurately at all. This is probably due to the fact that this model was fitted mainly on random packing data. In random packing the slope of the pressure drop curve is not as steep in the loading region as is the case with structured packing. It performs reasonably well in predicting hold-up, especially at high liquid loads (see Figure 4.15). The remaining three models predict the pressure drop trend in the loading region. The Delft and SRP models predict the onset of loading at lower vapour phase F-factors compared to the experimental data. The Delft model predicts a higher pressure drop in the preloading region. The SRP model accurately predicts the pressure drop in the preloading region. At high liquid flow rates (Figure 4.13) the predicted slope of the pressure drop curve for the Delft and SRP models in the loading region is not as steep as was measured experimentally. Figures 4.12 and 4.13 show that the model by Billet tends to under predict the pressure drop in the preloading region slightly. It is accurate in predicting the loading point and the slope of the pressure drop curve in the loading region.

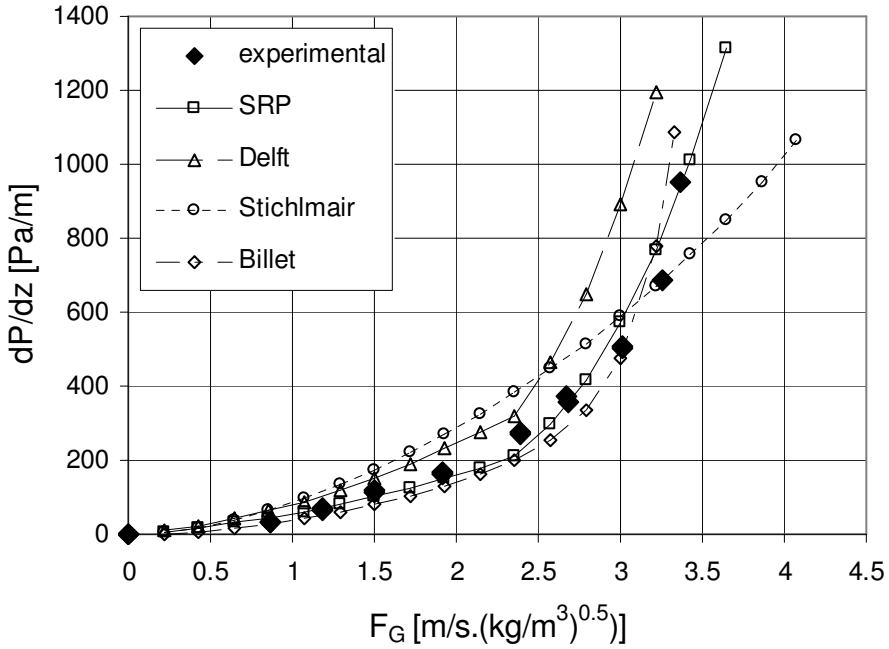

Figure 4.12 Comparison between pressure drop calculated with semi-theoretical models and experimental values. Flexipac 350Y, air/water system, $u_{L,s}$=6.0 $m^3/(m^2hr)$.

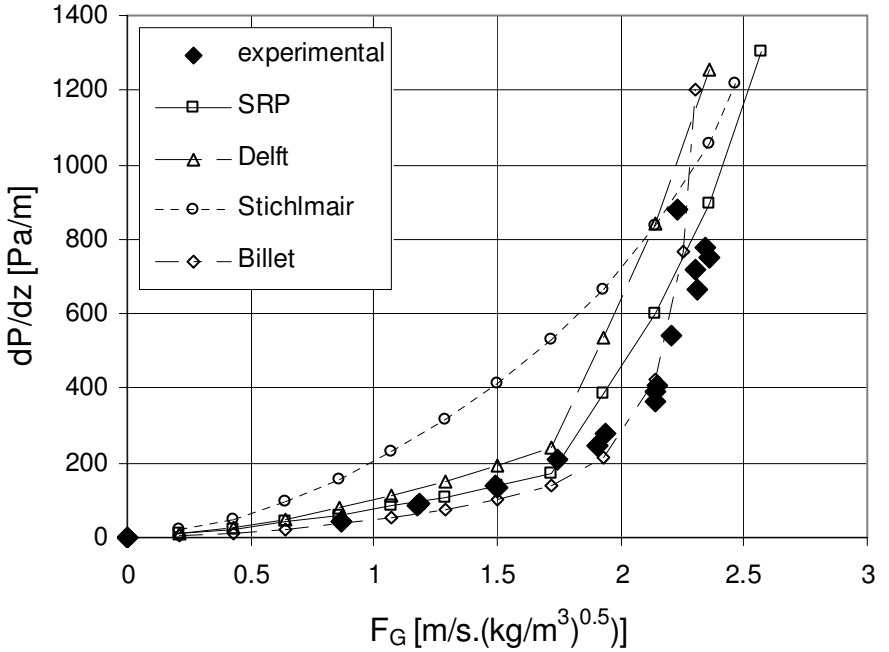

Figure 4.13 Comparison between pressure drop calculated with semi-theoretical models and experimental values. Flexipac 350Y, air/water system, $u_{L,s}$=35.7 $m^3/(m^2hr)$.

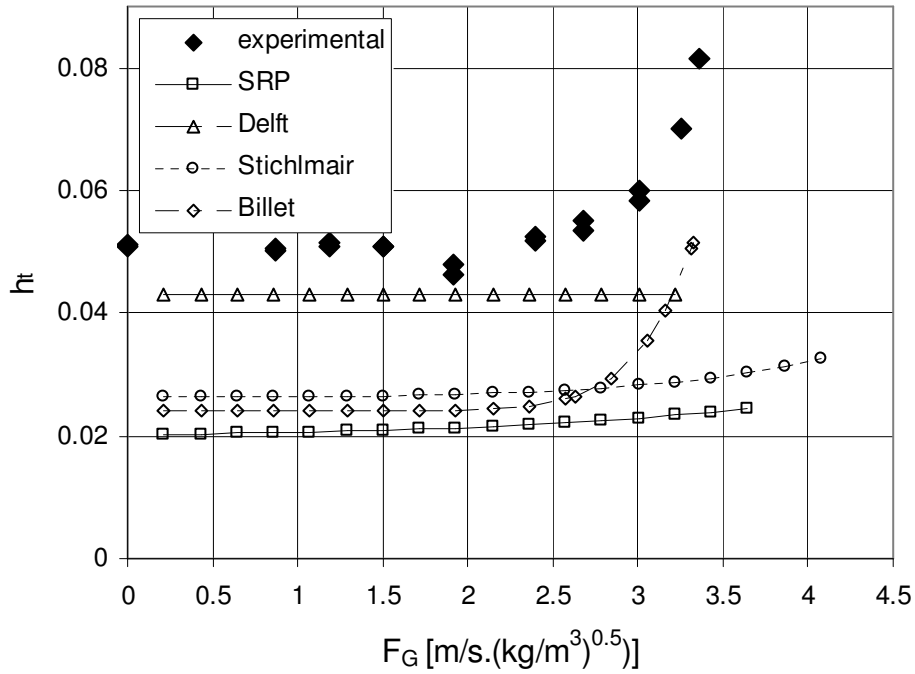

Figure 4.14 Comparison between measured and predicted liquid hold-up. Flexipac 350Y, air/water system, $u_{L,s}$=6.0 $m^3/(m^2hr)$

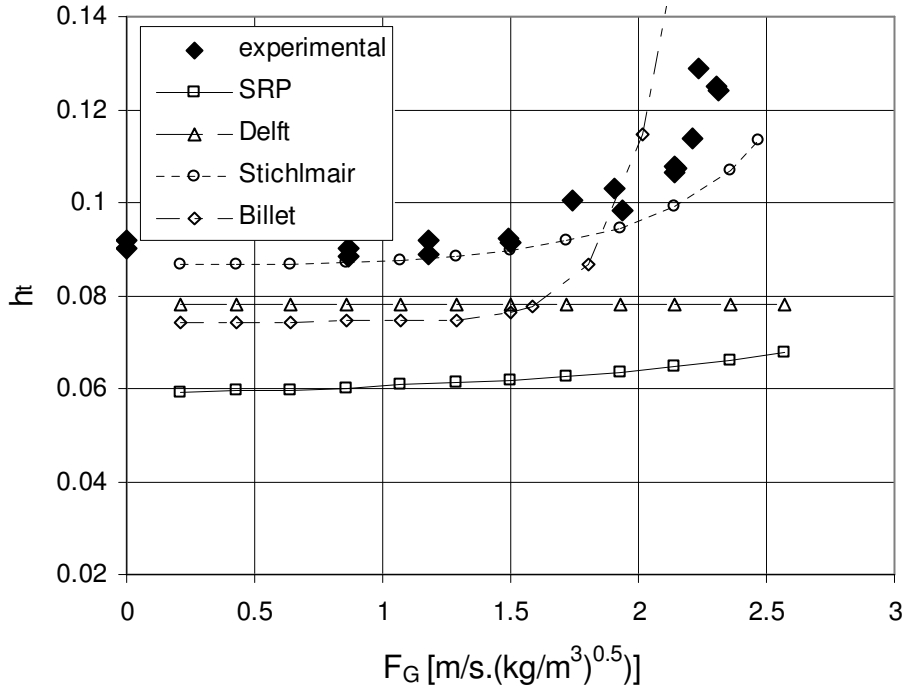

Figure 4.15 Comparison between measured and predicted liquid hold-up. Flexipac 350Y, air/water system, $u_{L,s}$=35.7 $m^3/(m^2hr)$

The Delft model assumes a constant liquid hold-up. Figure 4.14 and 4.15 show that it is rather accurate in the preloading region, but obviously fails to predict hold-up in the loading region. In this model the total surface area of the packing is assumed to be wetted. The SRP model predicts lower than measured liquid hold-up. It also fails to predict the right trend in the loading region. The experimental results of McNulty and Hsieh (McNulty and Hsieh, 1982) formed a large portion of the data used in determining the model constants. In this study the liquid hold-up is determined by measuring the drop in the level of a recirculation tank. The system is calibrated by first operating the column without packing. The hold-up is then determined by subtracting the hold-up in the system without packing from the hold-up measured in the system with packing. The hold-up determined in this way is smaller than the true value. This is because for the empty column there is a volume of liquid free falling in the column between the distribution point and the point where it is collected. The column is therefore not truly 'empty' during calibration experiments. The model by Billet tends to under predict the liquid hold-up. It does however seem to predict the right trend of an increase in the hold-up in the loading region.

The pressure drop for the system air/Kerosol 200 is compared with the semi-theoretical models in Figure 4.16 and 4.17. Figure 4.16 show the results for a liquid load of 6.1 $m^3/(m^2hr)$ and Figure 4.17 the results for a liquid load of 35.6 $m^3/(m^2hr)$. The corresponding hold-up curves are shown in Figures 4.18 and 4.19.

The model by Stichlmair again fails to predict the trend in the pressure drop curve. The SRP and Delft models predict the pressure drop in the preloading region with reasonable accuracy. The onset of loading conditions is predicted prematurely. Caution should however be exercised when using the SRP model for systems where the surface tension and viscosity differ from water. With the surface tension and viscosity shown in Table 4.1, a hold-up correction factor for partial wetting was calculated to be approximately 4. This value is expected to be in the range 0-1 and was subsequently set to unity. The model by Billet is again more accurate in predicting the loading point compared to the other models. The predictions are however not as accurate as in the air/water system. At higher liquid loads (see Figure 4.17) the model predicts a lower than measured pressure drop in the preloading region.

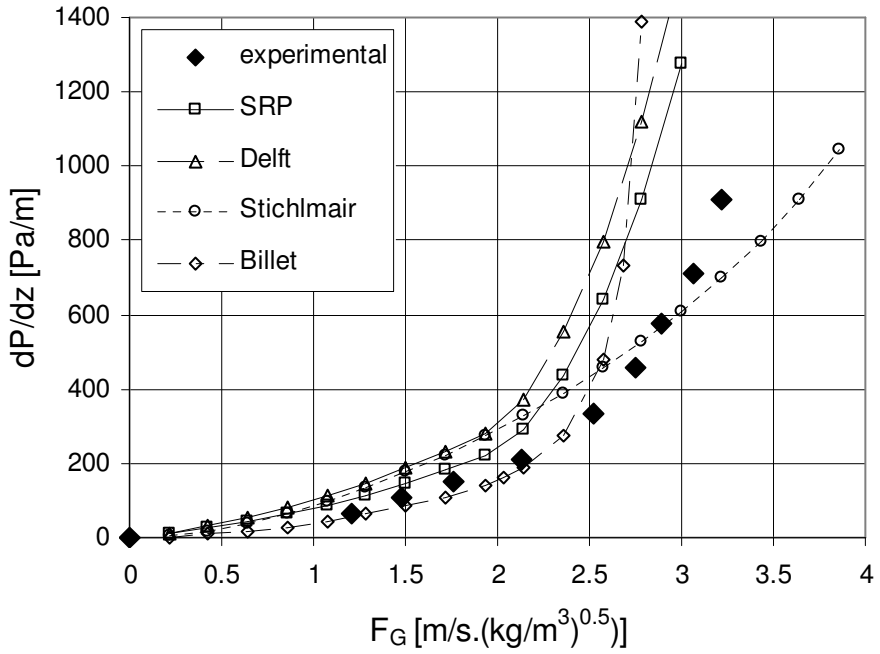

Figure 4.16 Comparison between pressure drop calculated with semi-theoretical models and experimental values. Flexipac 350Y, air/Kerosol 200 system, $u_{L,s}$=6.1 $m^3/(m^2 hr)$.

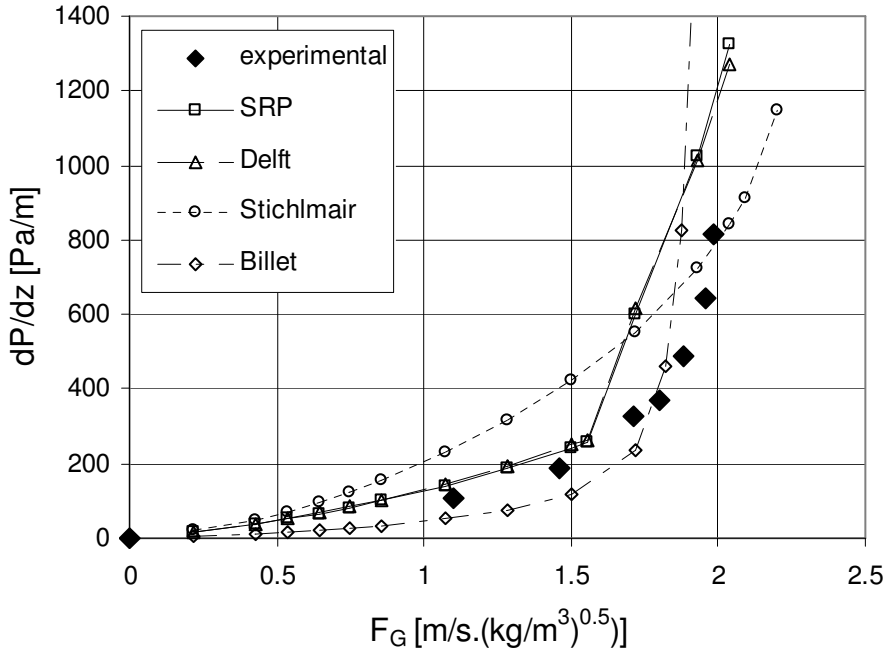

Figure 4.17 Comparison between pressure drop calculated with semi-theoretical models and experimental values. Flexipac 350Y, air/Kerosol 200 system, $u_{L,s}$=35.6 $m^3/(m^2 hr)$

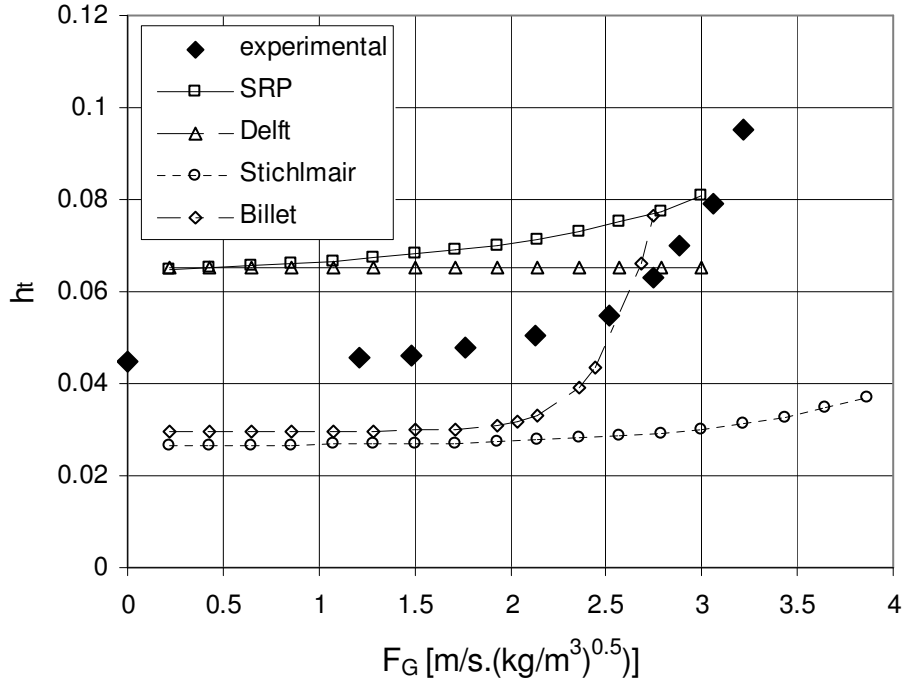

Figure 4.18 Comparison between measured and predicted liquid hold-up. Flexipac 350Y, air/Kerosol 200 system, $u_{L,s}$=6.1 $m^3/(m^2 hr)$

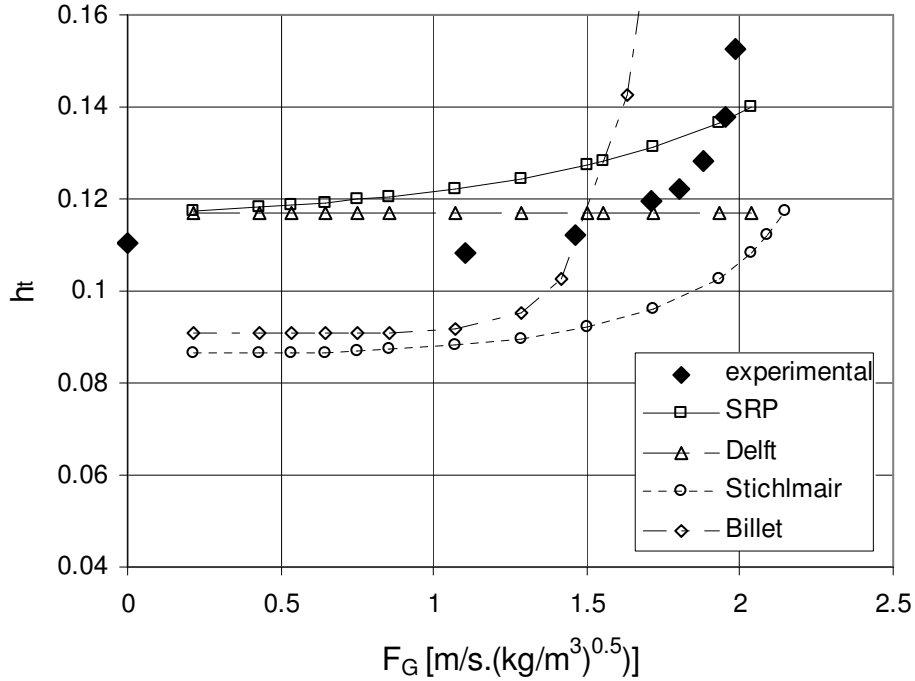

Figure 4.19 Comparison between measured and predicted liquid hold-up. Flexipac 350Y, air/Kerosol 200 system, $u_{L,s}$=35.6 $m^3/(m^2 hr)$

Both the SRP and Delft models tend to over predict the liquid hold-up. At the high liquid load (Figure 4.19) the Delft models predicts the preloading liquid hold-up accurately. The SRP model again fails to predict the steep increase in liquid hold-up in the loading region (Figure 4.18 and 4.19). The model by Billet predicts a too low liquid hold-up, but predicts the correct trend in the loading region.

A comparison between the model predictions for the air/water and air/Kerosol systems show that the semi-theoretical models show a conservative dependence of capacity on liquid viscosity.

4.4.3 Implementation of models in design calculations

A column will typically be designed to operate in the region of the loading point. It is therefore important that any model accurately predicts the onset of loading conditions and the pressure drop at this point. The next important parameter to be calculated is the liquid hold-up at the loading point. The liquid hold-up will influence the effective phase velocities and thus influence the calculated heat- and mass transfer rates

Of all the models evaluated in this study, the model of Stichlmair performed the worst overall. This is, however, to be expected, since the bulk of the data used to fit the model were for random packing. It does not predict the correct trend in the pressure drop curve. It also tends to predict too low a liquid hold-up. The remainder of the models performed reasonably well in predicting the loading point. The SRP model is accurate in predicting the loading point pressure drop. The Delft model prediction is too high, while the Billet model prediction is too low. For predicting the pressure drop in the loading region, the model by Billet outperforms the SRP and Delft models. Although the Delft model does not predict the correct trend of the liquid hold-up in the loading region, it predicts the hold-up in the preloading region more accurately than the SRP or Billet models. The Billet model does however contain a packing specific constant that was estimated in this study. Fitting the model to the experimental data would obviously lead to an improvement in hold-up prediction by this model.

It would seem that a combination of the models should be used. In the preloading region up to the loading point, any of the models may be used. The Delft model should be preferred to calculate liquid hold-up and the SRP model will be more accurate in predicting the loading point pressure drop. In the loading region, the Billet model is superior to the Delft and SRP models. The number of packing constants limits the use of the Billet model. It does however provide an easy means to correlate

experimental data with. It is also demonstrated that the loading and flooding point constants are not 'packing specific' and may be used for packing supplied by different vendors. What is of importance though is the specific surface area of the packing. This will obviously apply to the normal capacity structured packing, and not the high capacity packing.

An advantage of any model would be versatility. High capacity packing is becoming increasingly more popular and models need to be adapted to be able to predict their performance. Al the models rely on empirical correlations. It would therefore seem that no model has a distinct advantage above another.

4.5 Conclusions

The following conclusions may be drawn from the results obtained in this chapter for the hold-up and pressure drop of Flexipac 350Y and Flexipac 350Y HC:

- The high capacity packing used in this study showed a higher dry bed pressure drop compared with the normal capacity packing. This is due to the slight difference in corrugation geometry between the two types of packing.
- There is an increase in capacity of 20% for the new packing compared with the normal packing for the air/water system. The increase in capacity for the air/Kerosol 200 system is only 4%.
- The hydraulic capacity model by Stichlmair fails to predict the correct pressure drop trend.
- The SRP, Delft and Billet models perform reasonably well in predicting the loading point of the normal capacity packing.
- The model by Billet is more accurate in predicting steep slope of the pressure drop curve in the loading region compared to the SRP and Delft models.
- The Delft model is more accurate than the SRP and Billet models in predicting the hold-up in the preloading region.
- The SRP model should be used to predict pressure drop in the preloading region, as it is more accurate than the Billet and Delft models.
- All the models predict a conservative dependency of packing capacity on liquid viscosity.

4.6 Nomenclature

a_e	Effective surface area of packing [m^2/m^3]
A_G	Channel area [m^2]
a_h	Specific hydraulic area [m^2/m^3]
a_p	Geometric area of packing [m^2/m^3]
B	Channel base dimension [m]
Bo	Bond number [-]
C_L	Liquid capacity factor [m/s]
C_G	Vapour capacity factor [m/s]
d_c	Diameter of column [m]
d_h	Hydraulic diameter [m]
d_p	Particle diameter [m]
f	Fraction of flooding [-]
f	friction factor [-]
F_G	Vapour phase load factor [$(m/s)(kg/m^3)^{0.5}$]
F_{load}	Pressure drop enhancement factor for loading region [-]
F_p	Packing factor [ft^2/ft^3]
Fr	Froude number [-]
f_s	Wall factor [m]
F_t	Holdup correction factor for partial wetting [-]
G	Vapour mass flow rate [kg/s]
g	Gravitational acceleration [m/s^2]
g_{eff}	Effective gravitational acceleration [m/s^2]
h	Channel crimp height [m]
h_{pb}	Height of a packed bed [m]
h_{pe}	Height of a packing element [m]
h_t	Total liquid holdup [m^3/m^3]
$h_{t,0}$	Liquid holdup below the loading point [m^3/m^3]
L	Liquid mass flow rate [kg/s]
L_{eq}	Equivalent length of channel [m]
$\ell_{G,pe}$	Length of triangular vapour phase channel [m]
N_C	Number of bends per unit height of packing [-]
P	Pressure [Pa]
Re	Reynolds number [-]
S	Channel side dimension [m]

S_G	Dry channel perimeter [m]
S_i	Wet channel perimeter [m]
u	Velocity [m/s]
We	Weber number [-]
z	Packing height [m]
z_e	Inlet/exit calming section [m]

Greek

θ	Corrugation angle [^{o}]
μ	Dynamic viscosity [Pa.s]
ψ	Flow parameter [-]
φ	Fraction of triangular passage occupied by liquid [-]
ψ	Fraction of vapour channels ending at column wall [-] (Delft model)
δ	Liquid film thickness [m]
δ_0	Liquid film thickness in absence of vapour flow [m]
ξ_{bulk}	Direction change factor for bulk zone [-]
ξ_d	Dry bed resistance factor [-]
ζ_{DC}	Overall coefficient for direction change losses [-]
ξ_{fp}	Flood point resistance factor [-]
ζ_{GG}	Overall coefficient for vapour/vapour friction losses [-]
ξ_{GG}	Vapour/vapour friction factor [-]
ζ_{GL}	Overall coefficient for vapour/liquid friction losses [-]
ξ_{GL}	Vapour/liquid friction factor [-]
ξ_{lp}	Loading point resistance facto [-]
ε	Void fraction [-]
γ	Contact angle between solid and liquid film [^{o}]
ρ	Density [kg/m^3]
σ	Surface tension [N/m]
τ	Shear stress [Pa]

Subscripts

d	Refers to dry bed
e	Effective
fp	Refers to flood point
G	Refers to vapour phase property
i	Refers to vapour/liquid interface

irr	Refers to irrigated (wetted) bed
L	Refers to liquid phase property
lp	Refers to loading point
m	Mean property
s	Superficial
w	Refers to channel wall
W	Refers to property of water

5 MASS TRANSFER

5.1 Introduction

The HETP concept has been used to express the efficiency of column packing for many years (Sherwood et al., 1975). The limitations of this approach have long been known (Chilton and Colburn, 1935). The HETP concept is sufficient to compare the performance of different types of structured packing with one another, as is often done in vendors' brochures. But in order to use both the HTU/NTU method and the non-equilibrium model, accurate mass transfer models and correlations are needed. In this chapter the different mass transfer correlations proposed for structured packing are presented and compared with one another. A simple, classical method is used to measure vapour phase mass transfer coefficients in structured packing. The use of CFD to determine vapour phase mass transfer coefficients is demonstrated. The focus in this chapter is on vapour phase mass transfer, as it is widely accepted that the resistance in the vapour phase determines the overall mass transfer rate in distillation applications (Spiegel and Meier, 1987). Correlations proposed in literature for the liquid phase mass transfer coefficient in structured packing are also discussed.

5.2 Literature survey

5.2.1 Literature Review

The first model proposed to determine the mass transfer coefficients in structured packing is that of Bravo et al. (Bravo et al., 1985). The model was developed for gauze-type structured packing where complete wetting of the packing surface is assumed. The relationship proposed by Johnstone and Pigford (Johnstone and Pigford, 1942) for counter current evaporation in a wetted-wall column is used for the gas phase mass transfer coefficient with minor changes to the constants in the correlation:

$$Sh_G = 0.0338\,Re_{G,e}^{\;0.8}\,Sc_G^{\;0.333} \tag{5.1}$$

The penetration theory of Higbie is used for the liquid side mass transfer coefficient:

$$k_L = 2\sqrt{\frac{D_L u_{L,e}}{\pi S}} \tag{5.2}$$

where the exposure time is taken as the time it takes for a fluid element to flow between corrugation channels. This distance is assumed to be equal to the

corrugation side length (S). The complete model (hydrodynamics and efficiency) is given in Appendix B.

Spiegel and Meier (Spiegel and Meier, 1987) developed correlations for the performance of the Mellapak range of corrugated sheet metal packing in the form of a series of graphs. The resistance to mass transfer in the liquid phase is assumed to be much lower than the resistance to mass transfer in the vapour phase. For the gas phase the same proportionality as that proposed by Bravo et al. (Bravo et al., 1985) was found:

$$Sh_G \propto Re_{G,e}^{0.8}\, Sc_G^{0.333} \tag{5.3}$$

Rocha et al. (Rocha and Bravo, 1996) extended the model proposed by Bravo et al. (Bravo et al., 1985) to include sheet metal structured packing. The constants in the correlation for the gas phase mass transfer coefficient were changed slightly from that first suggested for gauze type packing. A packing specific constant was added in the correlation for the liquid phase mass transfer coefficient. The effective surface area is not assumed to be equal to the geometric surface area. The correlation by Shi and Mersman (Shi and Mersmann, 1985) is used together with a factor that accounts for surface texture to calculate the effective surface area. The complete model is given in Appendix B. The mass transfer correlations are:

$$Sh_G = 0.054\left(\frac{\left(u_{G,e}+u_{L,e}\right)\rho_G S}{\mu_G}\right)^{0.8} Sc_G^{0.33} \tag{5.4}$$

$$k_L = 2\sqrt{\frac{D_L C_E u_{L,e}}{\pi d_{hG}}} \tag{5.5}$$

with $C_E = 0.9$

The model developed by Billet (Billet, 1995) focused primarily on random packing. The model was fitted on a large number of experimental data for distillation and absorption and contains quite a number of packing specific constants. Constants are also available for a limited number of commercially available structured packing. The model is quite extensive and an attempt was made to highlight the most important equations in Appendix B. The correlation for the gas phase mass transfer coefficient is:

$$k_G a_e = C_G \frac{a_p^{1.5}}{\sqrt{d_h}} \frac{1}{\sqrt{\varepsilon - h_t}} D_G\, Re_{G,s}^{\frac{3}{4}}\, Sc_G^{\frac{1}{3}} \frac{a_e}{a_p} \tag{5.6}$$

The correlation for the liquid phase mass transfer coefficient is split into two. Below the loading point:

$$k_L a_e = C_L \, g^{\frac{1}{6}} \left(\frac{\rho_L}{\mu_L} \right)^{\frac{1}{6}} \left(\frac{D_L}{d_h} \right)^{\frac{1}{2}} a_p^{\frac{2}{3}} u_{L,s}^{\frac{1}{3}} \frac{a_e}{a_p} \tag{5.7}$$

Between the loading point and the flood point:

$$k_L a_e = 12^{\frac{1}{2}} C_L a_p u_{L,e}^{\frac{1}{2}} \left(\frac{D_L}{d_h} \right)^{\frac{1}{2}} \frac{a_e}{a_p} \tag{5.8}$$

Laso et al. (Laso et al., 1995) measured the volumetric liquid side mass transfer coefficient ($a_e k_L$) for the desorption of oxygen from water in a column equipped with Mellapak 250Y and 500Y. The proposed correlations are:

$$k_L a_e = 0.574 u_{L,s}^{0.62} \quad \text{(Mellapak 250Y)} \tag{5.9}$$

$$k_L a_e = 0.713 u_{L,s}^{0.71} \quad \text{(Mellapak 500Y)} \tag{5.10}$$

The correlation for the liquid phase mass transfer coefficient of Brunazzi and Paglianti (Brunazzi and Paglianti, 1997) was fitted on experimental desorption and absorption data using Mellapak 250Y and Sulzer BX packing. Data were obtained for the desorption of CO_2 from aqueous solutions and the absorption of chlorinated compounds into liquids of relative high viscosity and relative low surface tension. The correlation was based on a proportionality proposed by Nawrocki and Chuang (Nawrocki and Chuang, 1996) who studied the absorption of carbon dioxide into stable rivulets on an inclined plate. Lower liquid phase mass transfer coefficients were measured than predicted by the correlations of Bravo et al. (Bravo et al., 1985) and Billet (Billet, 1995). The mass transfer coefficients were higher than predicted by the correlation of Laso et al. (Laso et al., 1995). The proposed correlation is:

$$Sh_L = A \frac{Gz^B}{Ka^C} \tag{5.11}$$

The definition of the Graetz (Gz) and Kapitsa (Ka) numbers are given in Appendix B. The constants in the correlation for Mellapak 250Y and Sulzer BX packing are published (Brunazzi and Paglianti, 1997).

In the model by Olujic (Olujic, 1997, Olujic et al., 1999) the vapour phase mass transfer coefficient is calculated as the average of laminar and turbulent contributions.

$$k_G = \sqrt{k_{G,lam}^2 + k_{G,turb}^2} \tag{5.12}$$

The laminar and turbulent mass transfer coefficients are obtained by invoking the heat/mass transfer analogy and using correlations for heat transfer:

$$\frac{k_{G,lam} d_{hG}}{D_G} = 0.664 Sc_G^{1/3} \sqrt{Re_{G,r} \frac{d_{hG}}{\ell_{G,pe}}} \quad (5.13)$$

$$\frac{k_{G,turb} d_{hG}}{D_G} = \frac{Re_{G,r} Sc_G \frac{\xi_{GL} \varphi}{8}}{1 + 12.7 \sqrt{\frac{\xi_{GL} \varphi}{8}} \left(Sc_G^{2/3} - 1 \right)} \left[1 + \left(\frac{d_{hG}}{\ell_{G,pe}} \right)^{2/3} \right] \quad (5.14)$$

Definitions for all the constants and dimensionless numbers may be obtained from Appendix B. The coefficient ξ_{GL} is the so-called gas-liquid interaction coefficient. The expression for the liquid phase mass transfer coefficient is the same as that proposed by Rocha et al. (Rocha and Bravo, 1996).

Weiland et al. (Weiland et al., 1993) studied the mass transfer characteristics of two types of structured packing, Goodloe and Montz A2. The absorption of SO_2 from air into aqueous caustic soda solutions was used to determine the volumetric gas phase mass transfer coefficient ($k_G a_e$). Interfacial area was measured by the absorption of CO_2 into dilute NaOH solutions. The volumetric liquid phase mass transfer coefficient ($k_L a_e$) was measured by the absorption of CO_2 into sodium carbonate/bicarbonate buffer solutions. The results were correlated with a power law series containing the relevant dimensionless numbers. The experimental gas phase mass transfer coefficients were a factor 2 higher than calculated with the correlations proposed by Bravo et al. (Bravo et al., 1985) for Sulzer BX packing. For the gas phase mass transfer the correlations are:

$$Sh_G = 0.0567 Re_{G,s}^{1.10} Sc_G^{1/3} \quad \text{(Goodloe packing)} \quad (5.15)$$

$$Sh_G = 0.0373 Re_{G,s}^{1.02} Sc_G^{1/3} \quad \text{(Montz A2)} \quad (5.16)$$

The values for the liquid phase mass transfer coefficients were substantially lower than that proposed by Bravo et al. (Bravo et al., 1985). The correlations for the two types of packing are:

$$Sh_L = 3.4 Re_{L,s}^{-0.08} Sc_L^{1/2} \quad \text{(Goodloe packing)} \quad (5.17)$$

$$Sh_L = 5.2 Re_{L,s}^{-0.04} Sc_L^{1/2} \quad \text{(Montz A2)} \quad (5.18)$$

In a recent study, the evaporation of pure liquids in a short wetted-wall column was used to develop a gas phase mass transfer correlation for structured packing (Crause and Nieuwoudt, 1999, Crause, 1998). The proposed correlation is:

$$Sh_G = 0.00283 F_p Re_{G,e} Sc_G^{0.5} Re_{L,\delta}^{0.08} \quad (5.19)$$

Liquid phase mass transfer was investigated by evaporating binary liquids. No liquid side resistance was found but rather an enhancement of the gas phase mass transfer rate. By assuming complete wetting of the packing, the packing factor (Fp) for Mellapak 350Y in correlation 5.18 is F_p=1.03.

The effect of the surface treatment of sheet metal structured packing on the gas phase mass transfer rate was investigated in a short wetted-wall column (Erasmus and Nieuwoudt, 2001, Erasmus, 1999). The proposed correlation is:

$$Sh_G = 0.0081 Re_{G,e}^{0.94} Sc_G^{0.5} \quad (5.20)$$

No liquid side resistance was found in the evaporation of binary liquids in the wetted-wall column.

5.2.2 Discussion

The major problem in developing correlations for the liquid and vapour mass transfer coefficients is that, in most experiments, volumetric transfer coefficients are measured ($k_L a_e$ and $k_G a_e$). Since the effective surface area is thought to be mostly dependent on the liquid flow rate and the liquid properties, it would be logical to separate the volumetric gas phase mass transfer coefficient into a gas phase mass transfer coefficient and an effective surface area. The gas phase mass transfer coefficient could then be correlated in terms of the gas phase flow rate and transport properties.

The wetted-wall analogy is often used to develop correlations for gas phase mass transfer in structured packing. It is convenient because the surface area is accurately known and the gas phase mass transfer coefficient is therefore easily calculated from experimental data. A large database of experimental data on the evaporation of pure components and binary mixtures in wetted-wall columns was compiled by Crause and Nieuwoudt (Crause, 1998, Crause and Nieuwoudt, 1999), Erasmus and Nieuwoudt (Erasmus, 1999, Erasmus and Nieuwoudt, 2001) and Kawesha and Nieuwoudt. In all these studies, short wetted-wall columns were used. The reasoning behind using a short column is that entrance effects should be considered in developing a correlation applicable to structured packing (Crause and Nieuwoudt, 1999) (Erasmus and Nieuwoudt, 2001). In structured packing the gas flow changes direction quite often. This happens at the interface between packing elements and also against the column wall. The liquid phase also changes direction where the corrugations of opposing sheets meet. In all three studies, a long gas phase entrance length to the wetted-wall column is allowed. The velocity boundary layer would therefore be completely developed before reaching the wetted-wall section. In the

wetted wall section a concentration boundary layer would then start to develop but would not develop fully because of the short length of the wetted-wall section. A better approach would probably be not to allow a velocity boundary layer to develop before reaching the wetted-wall section. This would be more representative of the flow conditions inside structured packing where a fully developed velocity profile would not be attained due to the number of abrupt changes in the flow path (channels). Another problem with applying a wetted-wall analogy is that the flow is essentially two dimensional in a wetted-wall column while it is essentially three dimensional in structured packing.

In the correlation proposed by Olujic et al. (Olujic et al., 1999) (Equations 5.12-5.14) the analogy between heat- and mass transfer is used. The proposed correlation is analogous to correlations developed for heat transfer in tubes with developing thermal and velocity boundary layers (entrance region). This correlation would therefore also tend to under predict the mass transfer rate in structured packing because it does not take the three-dimensional nature of the flow into account.

In studies on compact heat exchangers (Focke et al., 1985) and rotary air preheaters (Ciofalo et al., 1996, Ciofalo, 1996, Stasiek et al., 1996) the heat/mass transfer rates were found to be enhanced by the swirling motion induced in the flow by the free shear layer at the open interface between two flow channels. These heat exchangers have a geometry quite similar to structured packing. This is especially the case with the rotary air heat exchanger investigated by Stasiek et al. (Stasiek et al., 1996). Correlations developed for heat transfer could be used to predict mass transfer in structured packing by invoking the analogy between heat- and mass transfer. Unfortunately most of the results from this study are proprietary in nature and not published in the open literature.

In the model by Rocha et al. (Rocha and Bravo, 1996, Rocha et al., 1993) the wetted area of the packing are modelled by using a correlation similar to that proposed by Shi and Mersmann (Shi and Mersmann, 1985). The constants in this correlation are obtained by fitting experimental hold-up data. With the wetted surface area known, the liquid phase mass transfer coefficient is modelled with the penetration theory of Higbie. The surface renewal time are determined by fitting the penetration model to experimental data for the desorption of oxygen from water. With the wetted area and the liquid phase mass transfer coefficient known, the gas phase mass transfer coefficient is the only unknown and is determined from experimental distillation data. The problem with this model is that the wetted area is assumed to be equal to the surface area effectively taking part in mass transfer. It has been known for quite some time that the wetted area is not necessarily equal to the effective mass transfer

area in columns with random packing (Danckwerts, 1970). Any errors made in determining the surface area, and assuming $a_w=a_e$, will propagate through the model and lead to an inaccurate determination of the gas phase mass transfer coefficient.

In the remaining models, the gas- or liquid phase volumetric mass transfer coefficients are measured (Brunazzi and Paglianti, 1997, Brunazzi et al., 1995, Laso et al., 1995, Weiland et al., 1993) using either physical or chemical absorption/desorption. In almost all of these studies aqueous systems were used. These systems have high surface tensions and are notorious for their low wetting ability (Rocha and Bravo, 1996). It is therefore not surprising that the results differ considerably from one another. Another factor that will influence the experimental results for the liquid phase mass transfer coefficient considerably is the estimation of the binary diffusion coefficient in the liquid phase. No mention is usually made of physical models used to calculate the diffusion coefficient.

In the present study it is argued that one should first measure the gas phase mass transfer coefficient independently and then use the resulting model or correlation as a starting point for measuring effective surface area and the liquid phase mass transfer coefficient. This could be done by measuring mass transfer coefficients under conditions where the total geometric surface area of the packing contributes to the mass transfer process. Heat transfer rates could also be measured and the mass transfer rates obtained by invoking the heat-/mass transfer analogy. The naphthalene/air system was chosen in this study. It has been used in the past to determine the gas phase mass transfer coefficient and wetted area in random packing (Shulman et al., 1955). There are also accurate data available for vapour pressure (Ambrose et al., 1975) and the diffusion coefficient of naphthalene into air (Cho et al., 1992). In the rest of this chapter the experimental set-up and results for naphthalene sublimation from the surface of structured packing with a geometry similar to Flexipac 350Y is discussed. This is followed by CFD simulation of the results. The measurement and correlation of the liquid phase mass transfer coefficient is not investigated. The focus of the study is on the modelling of distillation in structured packing. The general view is that the mass transfer rate is determined by the resistance in the gas phase.

5.3 Theory

The diffusion of a species away from a liquid-gas or solid-gas interface into the gas phase may be described by diffusion through a stagnant gas, also known as Stefan diffusion (Coulson and Richardson, 1991). In the following derivation species A will

be the component that evaporates/sublimes and species B will be the gas. According to Fick's law, the respective diffusion rates of species A and species B are:

$$N_A = -D_{AB} c_t \frac{dy_A}{dx} \tag{5.21}$$

and

$$N_B = -D_{BA} c_t \frac{dy_B}{dx} \tag{5.22}$$

Because the mole fractions of the two components sum to unity:

$$y_A + y_B = 1 \tag{5.23}$$

the diffusion rate for species B may be written as:

$$N_B = -D_{AB} c_t \frac{d(1-y_A)}{dx} = D_{AB} c_t \frac{d(y_A)}{dx} \tag{5.24}$$

The total mass transfer rate of species B is zero. There must therefore be a bulk flow of the system to the interface to counterbalance the diffusion flux away from the interface. For species B:

$$(N_B)_T = N_B + (N_B)_{BF} = 0 \tag{5.25}$$

Therefore:

$$(N_B)_{BF} = -N_B = -D_{AB} c_t \frac{dy_A}{dx} \tag{5.26}$$

The bulk flow of a will be y_A/y_B that of the bulk flow of B:

$$(N_A)_{BF} = \left(\frac{y_A}{y_B}\right)(N_B)_{BF} = -\left(\frac{y_A}{y_B}\right) D_{AB} c_t \frac{dy_A}{dx} \tag{5.27}$$

The total mass transfer rate for species A is therefore:

$$(N_A)_T = -\left(\frac{y_A}{y_B} + 1\right) D_{AB} c_t \frac{dy_A}{dx} = -\left(\frac{1}{y_B}\right) D_{AB} c_t \frac{dy_A}{dx} \tag{5.28}$$

Integration over the film thickness yields:

$$N_A = -\frac{D_{AB}}{\ell} \frac{c_t}{y_{B,m}} \left(y_{A,b} - y_{A,i}\right) \tag{5.29}$$

where $y_{B,m}$ is the logarithmic mean defined by:

$$y_{B,m} = \frac{y_{B,b} - y_{B,i}}{\ln \dfrac{y_{B,b}}{y_{B,i}}} \tag{5.30}$$

In keeping with the definition of a mass transfer coefficient given in chapter 2, Equation 5.29 is written as:

$$N_A = -k_G \frac{c_t}{y_{B,m}} \left(y_{A,b} - y_{A,i} \right) \tag{5.31}$$

5.3.1 Naphthalene sublimation in structured packing

For naphthalene the sublimation rate is small so that $y_{B,m} \approx 1$. In order to obtain the total mass transfer rate in the column, the following integration has to be performed:

$$n_A = N_A A = \int_0^h \int_0^{2\pi} \int_0^r a_P k_G c_t \left(y_{A,i} - y_{A,b} \right) r dr d\theta dz \tag{5.32}$$

where a_P is the specific surface area of the coated packing. If it is assumed that the variables are independent of r and θ (good radial distribution), the pressure drop is negligible (c_t is constant) and that k_G is uniform over the height of the column, then Equation 5.31 reduces to:

$$n_A = a_P k_G c_t \pi r^2 \int_0^h \left(y_{A,i} - y_{A,b} \right) dz \tag{5.33}$$

A log-mean driving force is used:

$$\Delta y_A = \frac{\left(y_{A,i} - y_{A,b} \right)_h - \left(y_{A,i} - y_{A,b} \right)_0}{\ln \left(\frac{\left(y_{A,i} - y_{A,b} \right)_h}{\left(y_{A,i} - y_{A,b} \right)_0} \right)} \tag{5.34}$$

The total mass transfer rate of A is therefore:

$$\begin{aligned} n_A &= k_G c_t a_P \pi r^2 h \Delta y_A \\ &= k_G c_t a_P V_C \Delta y_A \end{aligned} \tag{5.35}$$

where V_C is the volume of the test section in the column.

The vapour phase mass transfer coefficient is then calculated from:

$$k_G = \frac{n_A}{c_t a_P V_C \Delta y_A} \tag{5.36}$$

To calculate the driving force in Equation 5.36, the interface concentration of species A is needed. If the saturated vapour pressure of species A at the interface is known, the interface mole fraction may simply be calculated from:

$$y_{A,i} = \frac{P_A^{sat}}{P_T} \tag{5.37}$$

5.3.2 Evaporation in a wetted wall column

In a wetted wall column where the concentration of the evaporating species in the gas layer next to the interface is high, the effects of bulk flow may not be ignored. To determine the mass transfer rate, the following integration has to be performed:

$$n_A = N_A A_i = \int_0^h \int_0^{2\pi} k_G \frac{c_t}{y_{B,m}} \left(y_{A,i} - y_{A,b}\right) r d\theta dz \qquad (5.38)$$

If a short column is employed the effects of evaporative cooling may be ignored and $y_{A,i}$ will be constant along the length of the column. If it is assumed that the variables are independent of θ, the mass transfer rate may be determined from:

$$n_A = A_i k_G \frac{c_t}{y_{B,m}} \Delta y_A \qquad (5.39)$$

where the area of the interface is calculated with:

$$A_i = 2\pi r h \qquad (5.40)$$

A logarithmic average of the inlet and outlet driving force is used (Equation 5.34). For a short column, an arithmic mean between the inlet and outlet may be used for $y_{B,m}$ in Equation 5.39. With the mass transfer rate known, the vapour phase mass transfer coefficient is determined from Equation 5.39.

5.4 Experimental

5.4.1 Experimental set-up

The experimental set-up was the same as described in Chapter 4. The naphthalene-coated packing section was sandwiched between two normal Flexipac 350Y packing elements with an element height of 265mm. The packing elements were rotated 90° with respect to one another. The top of the packed bed was situated just below the top flange of the glass column section. This was achieved by using a spacer on top of the static mixer. The spacer was constructed in a manner so as not to obstruct the airflow into the passages of the bottom packing element. The column was operated at ambient conditions. The outlet section of the column was fastened in a manner to facilitate quick removal.

5.4.2 Naphthalene coating

Wire gauze packing was used for the naphthalene coated test section. Preliminary coating tests showed that a smooth and consistent coating could be obtained with wire gauze packing. Coatings applied to sheet metal structured packing tend to crack and flake off. The coatings applied to the wire gauze packing were resistant to a certain amount of deformation of the packing. The packing had the same channel dimensions as Flexipac 350Y. The element height was considerably shorter at 166mm. The packing was not perforated. The packing element was disassembled in order to coat each corrugated wire gauze sheet individually. Before the coating

procedure each sheet was washed in acetone and left to dry. Only half of the sheet was coated. This made it both easier to coat the packing by a dipping procedure and also ensured that the outlet of the packed section was far from being saturated with naphthalene. If the concentration of the air at the outlet of the test section is close to the saturation concentration, then the driving force for mass transfer will vanish. The naphthalene used for the coating had a purity of 99%. Each sheet was weighed before it was coated. This was done to ensure that a coating of similar thickness was applied on each sheet. Each sheet was measured in order to calculate the surface area accurately. The packing was then coated by dipping it repeatedly into molten naphthalene kept at a temperature of 85^{o}C. The container with molten naphthalene was submerged into a thermostat controlled water bath. After each dipping the sheet with naphthalene coating was left to cool and dry (solidify) for a few moments before applying the next layer of coating. In between coating layers the packing was weighed. This was done to determine when a sufficiently thick coating had been applied. After a sheet had been coated it was transferred to a container with an airtight lid. Fine naphthalene crystals at the bottom of the container ensured a saturated naphthalene atmosphere inside the container. After all the sheets had been coated, the packing element was again reconstructed from the different sheets. Wire was used to bind the sheets together. In order for the coated packing element to fit into the column, the two outermost sheets had to be discarded. The loss in surface area due to this action was taken into account. A bit of the coating along the side of the sheets were damaged in the binding process. A brush was used to dislodge any loose pieces of coating. Before the element was weighed, it was inserted into a die that had the same ID as the column. During this operation any of the sharp naphthalene edges protruding from the packing was broken off. The element was then removed from the die and any lose naphthalene pieces was shaken out and brushed off. The element was then weighed and transferred back to the airtight container. After a few experimental runs, the coating had to be re-applied. The only way in which a uniform coating could be obtained was to first remove the old coating. This was done by submerging the sheets into the molten naphthalene container until the naphthalene melted. Increasing the temperature of the naphthalene bath during this stage to 90^{o}C accelerated the process. The coating procedure was then repeated, starting with an acetone wash to remove any remaining naphthalene. The uncoated element weighed approximately 740g. The total mass of naphthalene coated onto the packing varied between 330g and 410g. Table 5.1 show the average dimensions of the coated naphthalene packing section.

Table 5.1 Dimensions of naphthalene coated packing section

Property	Value
Corrugation base, B [mm]	17.4
Corrugation side, S [mm]	11.2
Crimp height, h [mm]	7.05
Void fraction, ε	0.87
Corrugation angle, θ [^{o}]	45
Height of coated section [mm]	83

5.4.3 Experimental procedure

The naphthalene coated packing section was accurately weighed before each experimental run. It was then carefully transferred to the packed bed. It was inserted into the packed bed with the coated section facing either downwards or upwards. The blower was switched on and the temperature of the air before and after the column was logged, together with the pressure drop over the orifice plate and atmospheric pressure. After a suitable amount of time, determined by the airflow rate and the temperature, the blower was switched of and the naphthalene-coated section was removed and weighed. The experimental time varied between 20 and 50 minutes resulting in naphthalene mass losses of between 10g and 40g. After weighing the coated packing element, the element was disassembled and each sheet was visually inspected and weighed. If the coating was found to be too thin on the sheets, the sheets were recoated.

5.5 Results and discussion

5.5.1 Experimental results

The mass loss of naphthalene was converted to a mass transfer coefficient using Equation 5.35. The vapour pressure of naphthalene was calculated using the data of Ambrose et al. (Ambrose et al., 1975). This data was also used in a recent study on the diffusion of naphthalene through air (Cho et al., 1992). The vapour pressure is obviously quite sensitive to temperature. The influence of temperature on the results will be discussed in the next section. In Figure 5.1 an average temperature was used between the inlet and outlet of the column. The average difference between the inlet and outlet temperatures was 0.9^{o}C. The results are presented as a plot of k_G against the Reynolds number. The Reynolds number used in the plots is the effective Reynolds number defined as:

$$Re_{G,e} = \frac{\rho_G u_{G,e} d_h}{\mu_G} \tag{5.41}$$

The effective velocity of the air is calculated from:

$$u_{G,e} = \frac{u_{G,s}}{\varepsilon \sin\theta} \tag{5.42}$$

where $u_{G,s}$ is the superficial air velocity based on the column cross sectional area, ε is the void fraction of the naphthalene coated test section and θ is the packing corrugation angle with respect to the horizontal axis. Since the sublimation rate was low, the density at the outlet was calculated as that of air. The transport properties of air were taken from literature (Incropera and De Witt, 1990). The hydraulic diameter (d_h) was calculated for a unitary 'criss-cross' cell. According to the definition of the hydraulic diameter (Daugherty and Franzini, 1977):

$$d_h = \frac{4V}{A_w} = \frac{Bh}{S} \tag{5.43}$$

B, h and S are the base, side and height of a naphthalene coated triangular passage.

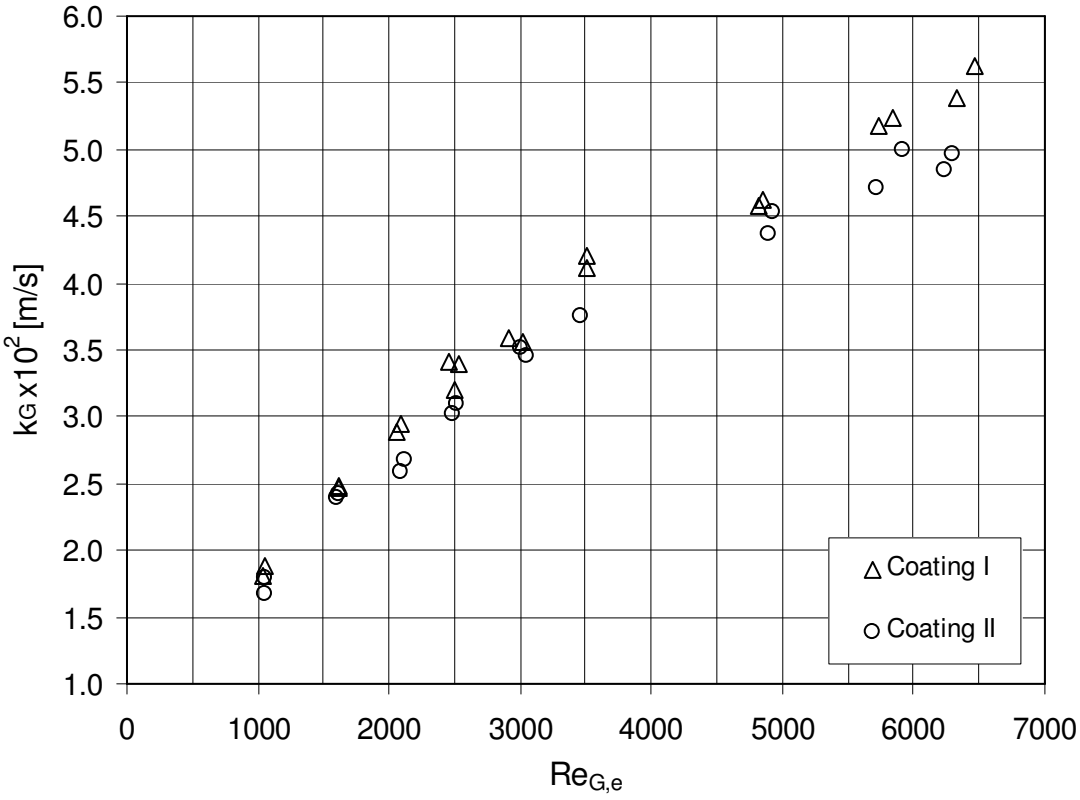

Figure 5.1 Experimental results for naphthalene coated packing. Coating I: coating applied to bottom half of element, Coating II: coating applied to top half of element. Sc_G=2.35.

Figure 5.1 shows that there is not a large difference in the gas phase mass transfer rate between the top and bottom halves of a structured packing element. At a high gas phase Reynolds number ($Re_{G,e}$=6250) the difference is approximately 10% while at a low gas phase Reynolds number ($Re_{G,e}$=1000) there is almost no difference.

5.5.2 Sensitivity analysis

An error that could influence these results is mass losses that could occur from transporting the coated element from the scale to the inside of the column. Before an experiment is carried out, a certain amount of time passes between the weighing of the element and the actual start of an experiment. The element has to be inserted into the column and the outlet section has to be connected. Afterwards the reverse operation has to be performed in order to again weigh the element. To quantify this 'unwanted' mass loss, an experiment was performed without switching the blower on. The coated packing element was weighed, installed in the column, retrieved and weighed again. The mass loss was 0.3g. When compared to the amount of naphthalene that sublimes during an experiment, this amount is between 0.75% and 3.0% of the total mass lost. When subtracting this amount from the total and recalculating the mass transfer coefficients, the average difference between the corrected and uncorrected values is 1.4%. Since some of the experiments were performed on cooler days the unwanted mass loss should be less than the 0.3g found on a warm day and the average difference substantially lower than the calculated 1.4%. The unwanted mass loss would then approach the accuracy of the scale (0.1g). It was subsequently decided to ignore this error.

A second and more serious error could result from the accuracy of the temperature measurements. The inlet and outlet temperature was measured with class B PT100 sensors. For these sensors the maximum deviation at the experimental conditions is ±0.4^{o}C. If this amount is subtracted from the average temperature (average between inlet and outlet) and then used to recalculate the mass transfer coefficients, then their values are on average 4.5% lower. If the average temperature is lowered by 0.4^{o}C and the mass transfer coefficients recalculated, then the value is on average 4.8% higher. The experimental error in the data represented in Figure 5.1 is therefore estimated to be in the order of 5%.

5.5.3 Comparison with existing correlations

Correlations used to calculate the gas phase mass transfer coefficient in structured packing are given in Table 5.1. The correlation in the Delft (Olujic, 1997) model contains liquid/vapour interaction terms and was omitted for obvious reasons. The

correlation proposed by Billet (Billet, 1995) is also not included since no parameters for Flexipac 350Y (or Mellapak) could be found. The correlation by Gilliland and Sherwood (Gilliland and Sherwood, 1934) is also given

Table 5.2 Correlations for the gas phase mass transfer coefficient in Figure 5.2

Correlation	Reference
$Sh_G = 0.0338\,Re_{G,e}^{0.8}\,Sc_G^{0.333}$	(Bravo et al., 1985)
$Sh_G = 0.054\,Re_{G,e}^{0.8}\,Sc_G^{0.33}$	(Rocha and Bravo, 1996)
$Sh_G = 0.00526\,Re_{G,e}^{0.978}\,Sc_G^{0.532}$	(Crause and Nieuwoudt, 1999)
$Sh_G = 0.0081 Re_{G,e}^{0.94}\,Sc_G^{0.5}$	(Erasmus and Nieuwoudt, 2001)

The correlation proposed by Rocha et al. (Rocha and Bravo, 1996) is frequently used and often referenced in the literature (Fair et al., 2000, Brunazzi and Paglianti, 1997, De Brito et al., 1994, Shetty and Cerro, 1997). The remaining correlations are wetted wall based correlations. The correlations from Crause and Nieuwoudt (Crause and Nieuwoudt, 1999) and Erasmus and Nieuwoudt (Erasmus and Nieuwoudt, 2001) given in Table 5.1 are those that do not contain a liquid term. The correlation proposed by Bravo et al. (Bravo et al., 1985) is also included. These correlations are compared with the experimental results in Figure 5.2. This figure show that all the correlations underestimate the gas phase mass transfer coefficient. The correlation proposed by Rocha et al. (Rocha and Bravo, 1996) and used in the SRP model (Fair et al., 2000) estimates mass transfer coefficients that are considerably closer to the experimental points than the other correlations shown in the figure.

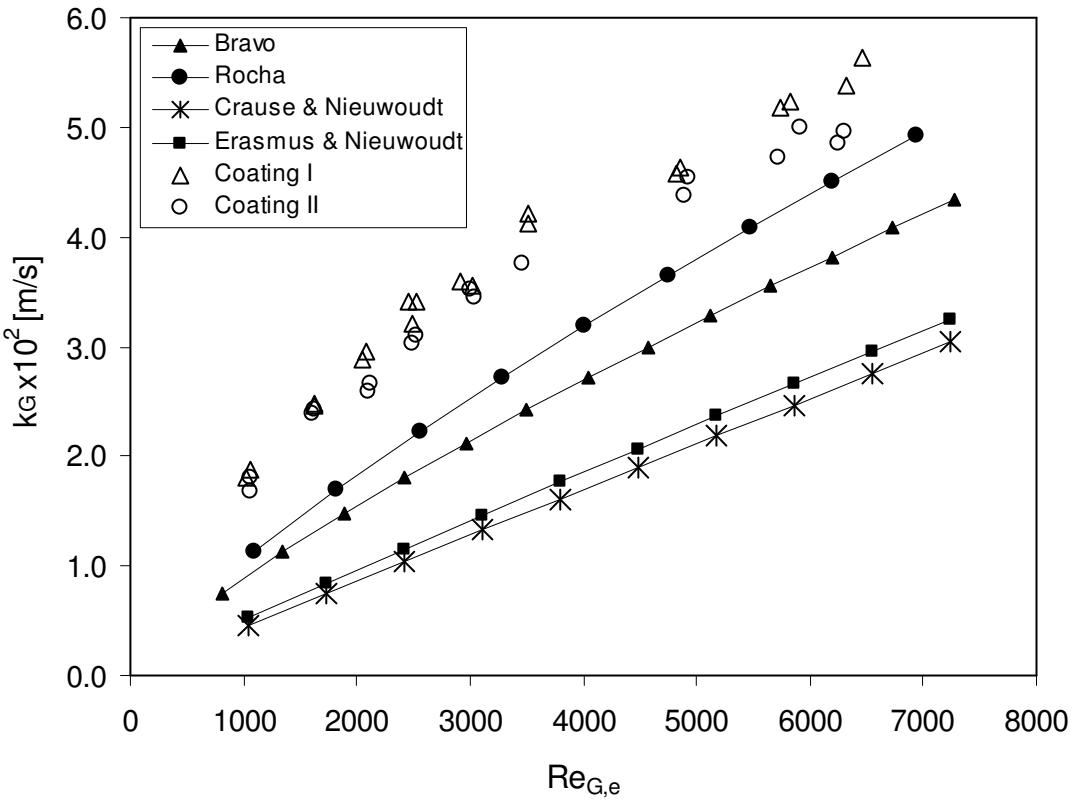

Figure 5.2 Comparison between experimental results and existing k_G correlations.

5.5.4 Correlation of experimental results

The experimental data are correlated with a simple power law series similar to that used in the other correlations:

$$Sh_G = a\,Re_{G,e}^{b}\,Sc_G^{c} \tag{5.44}$$

Since only air was used in the experiments, some assumption regarding the dependency of the mass transfer coefficient on the Schmidt number (and therefore the diffusion coefficient) must be made. This is done in order to extrapolate the correlation to systems other than air/naphthalene. In most mass transfer correlations for the evaporation of liquids in a wetted wall column, the Schmidt number is raised to a power of between 0.33 and 0.5. This suggests the following dependency of the mass transfer coefficient on the diffusion coefficient:

$$k_G \propto D^{2/3} \text{ for } Sh_G \propto Sc_G^{1/3} \tag{5.45}$$

$$k_G \propto \sqrt{D} \text{ for } Sh_G \propto Sc_G^{0.5} \tag{5.46}$$

In a recent publication (Dudukovic et al., 1996) it is suggested that for fluid-fluid transfer, the Schmidt number should be raised to the power 0.5 and for solid-fluid

transfer to the power 0.33. These suggestions are based on a model for the turbulent viscosity near the liquid-gas interface (free surface) proposed by Levich (Levich, 1962). For wetted-wall experimental data the accuracy of the correlation was slightly improved by setting the Schmidt number coefficient equal to 0.5 ($k_G \propto D^{0.5}$). The theory on which their suggestion is based is for the transport of a species from the bulk fluid phase to the free surface. Since all the experimental data that are referred to are for the evaporation of pure components in a wetted wall column, transport in the liquid phase should not be considered at all. There are quite a few analytical models and expressions proposed for the turbulent transport of heat and mass near interfaces (Sideman and Pinczewski, 1975). For turbulent transport at interfaces in fluids with molecular Prandtl/Schimdt numbers close to unity, there is little difference between the different theories. It is only at Prandtl/Schimdt numbers considerably smaller and larger than one that these models differ from one another. In most of the models the Prandtl/Schimdt number is raised to the power 0.33-0.5. For distillation and absorption the gas phase Schmidt number would be in the range $0.5<Sc<5$. It is therefore expected that by choosing either 0.33 or 0.5 would not influence the calculated mass transfer coefficient to a significant extent. The experimental data were fitted to Equation 5.43 using both 0.5 and 0.33 ($k_G \propto D^{0.5}$ and $k_G \propto D^{0.67}$). The data were regressed by using non-linear least square minimization. The regression results for the correlations are given in Table 5.2.

Table 5.3 Regression results for naphthalene sublimation data

Correlation	RMS*	
$Sh_G = 0.2641 Re_{G,e}^{0.62} Sc_G^{0.5}$	2.834	(5.47)
$Sh_G = 0.3053 Re_{G,e}^{0.62} Sc_G^{0.33}$	2.836	(5.48)

$$*RMS = \sqrt{\frac{\sum_n \left(Sh_{exp} - Sh_{calc}\right)^2}{n}}$$

Figure 5.3 shows a parity plot of the values predicted by Correlation 5.47 and 5.48 against the experimental values.

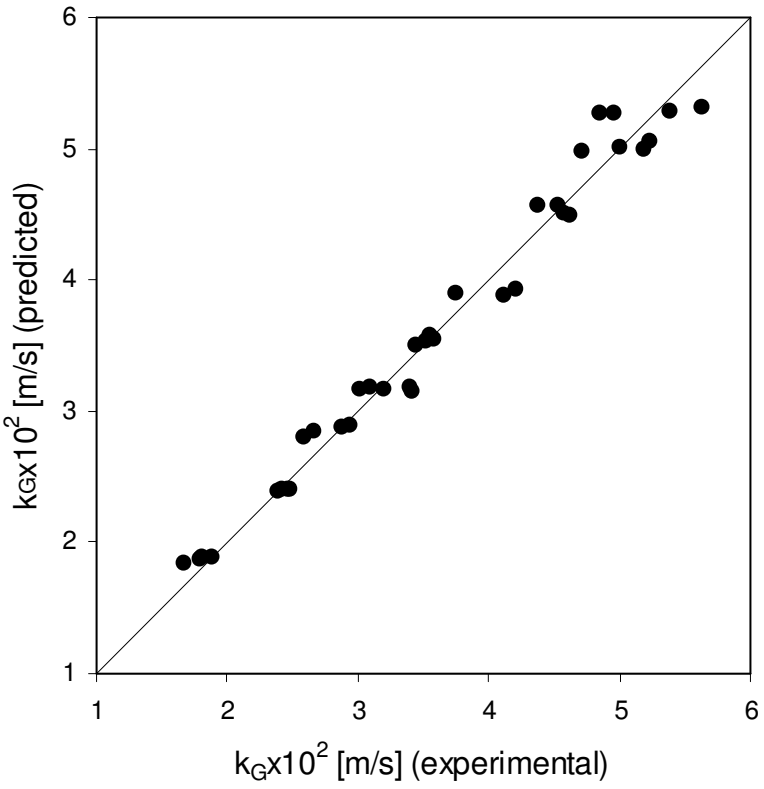

Figure 5.3 Parity plot of mass transfer coefficients predicted with correlation 5.47 and 5.48 against experimental values.

As mentioned before, it was found that by assuming $k_G \propto D^{0.5}$ resulted in a marginally better fit of the correlation on the experimental results for wetted-wall columns (Dudukovic et al., 1996). A wetted-wall type correlation has been used in the past for gas phase mass transfer in structured packing (Bravo et al., 1985) (Rocha and Bravo, 1996). In this correlation $k_G \propto D^{0.67}$ (see Table 5.1). This is also the case for k_G correlations proposed by Billet (Billet, 1995) for random and structured packing. This correlation has been fitted on a large set of experimental data. It would seem that experimental evidence suggests a $k_G \propto D^{0.67}$ dependency in distillation and absorption. This dependency is also used in the remainder of this study. It should however be tested experimentally by varying the Schmidt number in sublimation experiments. One possible way is to use the sublimation of benzoic acid into air. It is a convenient system because benzoic acid is not toxic and inexpensive. Another possibility is to use naphthalene but with a different carrier gas. The experiments would, however, then have to be performed on a much smaller scale since it would be quite expensive to work at high Reynolds numbers with a carrier gas other than air in the present experimental setup.

5.6 CFD modelling

Before attempting to model the results of the naphthalene sublimation, the experimental results for the evaporation of pure components in a wetted wall column (Erasmus, 1999) were first modelled with CFD. This was done to evaluate the ability of the CFD to model vapour phase mass transfer for a simple geometry.

5.6.1 Wetted-wall CFD simulations

Physical domain and boundary conditions

A complete description of the experimental procedure and set-up may be found elsewhere (Erasmus and Nieuwoudt, 2001). A two dimensional axisymmetric geometry is used in the CFD model. The geometry is shown in Figure 5.4.

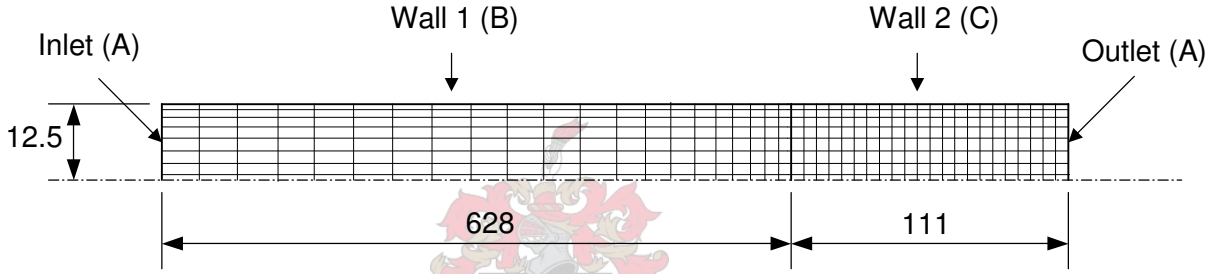

Figure 5.4 Geometry of wetted-wall column in 2D axisymmetric CFD model. Dimensions in (mm).

The column consists of an inlet air calming section and a wetted wall section. The inlet section allows the complete development of the velocity boundary layer before reaching the wetted wall section. The 'wall' in this section is the thin layer of gas next to the liquid film. The detailed modelling of the liquid film flow with the accompanying moving free interface and interface mass transfer is thus ignored. It is assumed that the thin layer of gas next to the interface is in equilibrium with the liquid phase. The concentration of the evaporating species in this gas layer next to the interface is calculated from the saturated vapour pressure at the prevailing temperature. This concentration is then specified as a wall boundary condition. The wall in the wetted wall section is flat in the CFD model. It is well known that waves form on the surface of a free falling liquid film (Sherwood et al., 1975, Gilliland and Sherwood, 1934, Karimi and Kawaji, 1999). In the experimental work on evaporation of liquids in a short wetted wall column, it was found that the formation of waves could be suppressed for the short length of column employed by using a relatively high liquid flow rate (Erasmus, 1999). Only experimental results where no waves were observed

are used in this study for comparison with the CFD model. The assumption of a flat wall to represent the gas layer next to the liquid interface is therefore thought to be reasonable. The boundary conditions for the geometry shown in Figure 5.4 are given in Table 5.3. The mole fraction specified at wall 2 is equal to the equilibrium vapour phase concentration of methanol under the experimental conditions. The properties of the gas phase were assumed to be that of air at the experimental conditions (T=314 K, P =100,67 kPa). The air is assumed to be incompressible.

Table 5.4 Boundary conditions: 2D axisymmetric wetted-wall model.

Boundary	Boundary condition
Inlet	'Dirichlet' type conditions, default turbulence parameters, $x_A = 0.0$
Wall 1	$x_A = 0.0$, no-slip condition
Wall 2	$x_A = 0.314$, no-slip condition (wetted-wall)
Outlet	'Neumann' type conditions (mass flow boundary)

Computational grid

The solution obtained with the CFD model should be independent of the grid used in the computational domain. The computational grid is refined as follows. A decrease in cell size from the centre of the tube to the wall is used in order to decrease the total amount cells while still maintaining a fine grid near the wall (distance A in Figure 5.4). This is also done in the section between the inlet and the start of the wetted-wall section (distance B in Figure 5.4). A fine grid near the wall is important because of the use of a low Reynolds number turbulence model (see Chapter 3). From the centre to the wall the cell size is decreased in a quadratic fashion while a linear decrease is used from the inlet to the start of the wetted-wall section. A uniform spacing of the grid is used between the inlet to the wetted-wall section and the outlet (distance C in Figure 5.4). The grid is refined for the highest Reynolds number until a grid independent solution is obtained. This grid is then used for all lower vapour phase Reynolds numbers. In the wetted-wall simulations three different turbulence models were used. For each turbulence model the grid was refined until a converged solution was obtained. The distance of the first node away from the wall was also varied to determine its influence on the model results. For all models this distance was chosen so that it would fall well within the viscous sublayer. Details of the grid are given in Table 5.5. It shows that almost twice as many elements need to be used for the k-ε model for a grid independent solution to be obtained when compared to the k-ω and BSL models. All the models are quite sensitive to the placement of the

first node away from the wall. The distance was therefore chosen to be well within the viscous sublayer.

Table 5.5 Mesh detail for 2D axisymmetric wetted-wall model.

Model	Total number of elements	Distance of 1st node from wall [mm]	Number of nodes (see Figure 5.4)		
			A	B	C
Laminar	9000	0.15	30	200	111
k-ε	16800	0.005	55	200	111
k-ω	9000	0.005	30	200	111
BSL	9000	0.005	30	200	111

Mathematical models and computational details

Chapter 3 may be consulted for details on the turbulence models and the governing equations of fluid motion. The default turbulence parameters for each of the turbulence models are given in Appendix A. Hybrid differencing was used for all variables with the SIMPLEC algorithm to solve the pressure velocity coupling. Steady state simulations were performed with under relaxation to control the rate of convergence. A simulation was judged to have reached convergence when the global mass source residual was less than 10^{-6}.

Results and discussion

The mass transfer rate is determined from the outlet concentration of the 'evaporating' species. Equation 5.38 is used to calculate a mass transfer coefficient. The results for the different turbulence models are compared with the experimental results in Figure 5.5. Details of the computational grid that resulted in a converged solution are given in Table 5.4 for each turbulence model used. Figure 5.5 show the expected trend for laminar and turbulent flow. At low gas phase Reynolds numbers, the flow is in the laminar regime and the mass transfer rate is predicted with reasonable accuracy by a laminar model (Re_G<2500). At higher Reynolds numbers the laminar model predicts lower than measured mass transfer rates. The BSL model of Menter fails to predict the mass transfer rate up to a gas phase Reynolds of about 4000. Above Re_G=4000 it is more accurate than the other turbulence models. The k-ε and k-ω models give almost identical results over the entire range. The fine grid needed for a converged solution to be obtained for the k-ε model would limit its application in problems with larger computational domains. This was indeed

experienced when attempting to model the naphthalene sublimation results as described in the following section.

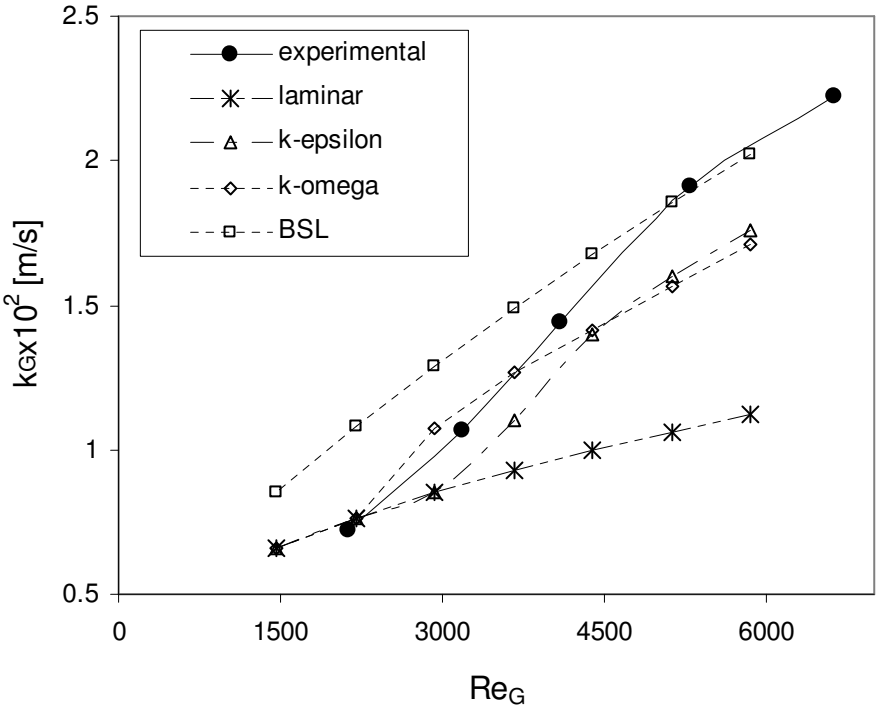

Figure 5.5 CFD results for wetted-wall evaporation. Re_G for experimental results is relative to moving liquid interface, Re_L(exp)=285.

5.6.2 CFD modelling of naphthalene sublimation

The breakdown of a bed of structured packing into re-occurring micro elements is discussed in detail in Chapter 3. From a mass transfer point of view the most important micro element is the junction between two corrugated passages, also referred to as micro element 2 in Chapter 3. When calculating the pressure drop over a bed of packing, the contributions from the other elements are also important since they involve the abrupt change in the flow direction of the vapour phase. It is therefore easy to construct simplified geometries that represent this direction change. Whether these simplified geometries will also be accurate for modelling mass transfer is questionable. In this study the contributions to mass transfer from these micro elements are assumed to be equal to the contribution from the micro element formed at the junction between corrugated channels. These elements may be used to reconstruct the bulk of the packing by arranging a number of them in series.

Physical domain and boundary conditions

There are different geometries used in the literature (Ciofalo et al., 1996, Hodson, 1997, Hodson et al., 1997, Larachi et al., 2003, Petre et al., 2003) to represent the re-occurring micro element in cross-corrugated passages. In earlier studies (Hodson et al., 1997, Ciofalo et al., 1996) the inlet and oulet sections to these micro elements are next to the free shear plane formed at the open interface between corrugated channels. In a recent study on pressure drop in structured packing (Petre et al., 2003), these inlet- and outlet boundaries are moved a distance away from the free shear interface. The reasoning behind this extension is that a developed flow profile is assumed when applying boundary conditions at an inlet- and outlet boundary. By placing an inlet- or an outlet boundary close to the free shear interface, these boundary conditions will be violated. In a study where these boundaries were placed next to the free shear interface, the results obtained agreed with experimental data (Ciofalo et al., 1996). This was also the case for results obtained with boundaries removed from the free shear interface (Petre et al., 2003). In this study, both these approaches are followed and compared with experimental results. Figure 5.6 shows details of the physical domain. The physical domain where the inlet- and outlet boundaries are moved up- and downstream from the free shear interface will be referred to as geometry 1. For this geometry the distance f in Figure 5.6 (a) is greater than zero. The physical domain where the inlet and outlet boundaries are next to the free shear interface will be referred to as geometry 2. For this geometry the distance f in Figure 5.6 (a) is equal to zero. The average dimensions of the naphthalene-coated channels are used in constructing the geometry. The properties used are that of air and naphthalene at the experimental conditions and are listed in Table 5.6. The air is assumed to be incompressible. The boundary conditions are shown in Table 5.7.

Table 5.6 Properties of air/naphthalene system

Property	Units	Value
ρ	[kg/m^3]	1.162
D_{AB}	[m^2/s]	6.72×10^{-6}
μ	[Pa.s]	1.85×10^{-5}
P^{sat}(naphthalene)	[Pa]	14.5

Dirichlet boundary conditions are specified at the inlet boundaries. For the first micro element a uniform inlet velocity profile is specified normal to the boundary interface. The outlet from the first micro element is used as the inlet to the next micro element. The mass flow boundary specified at the outlets imposes Neumann boundary

conditions on all the variables (see Chapter 3). A complete developed flow profile is assumed when imposing this boundary condition. All transported variables, except the components of velocity, are given zero gradients normal to the boundary.

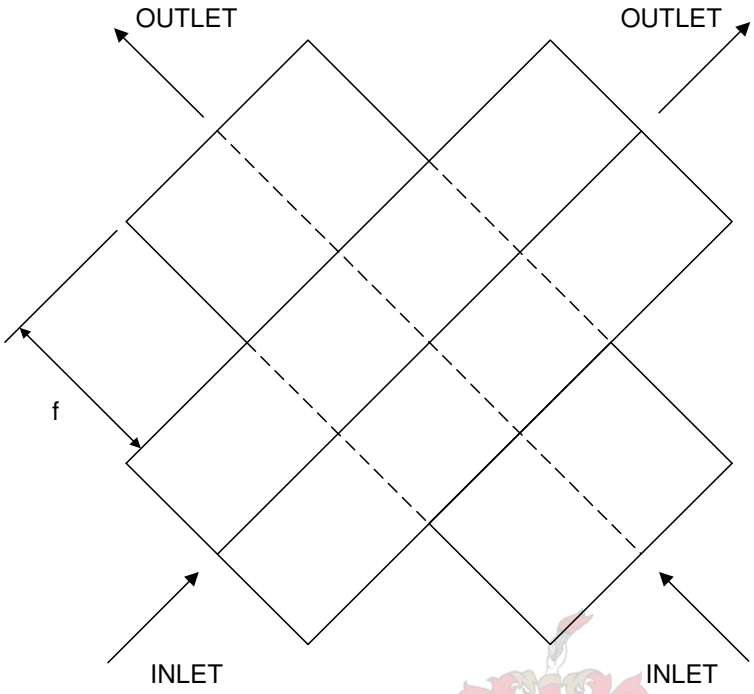

(a)

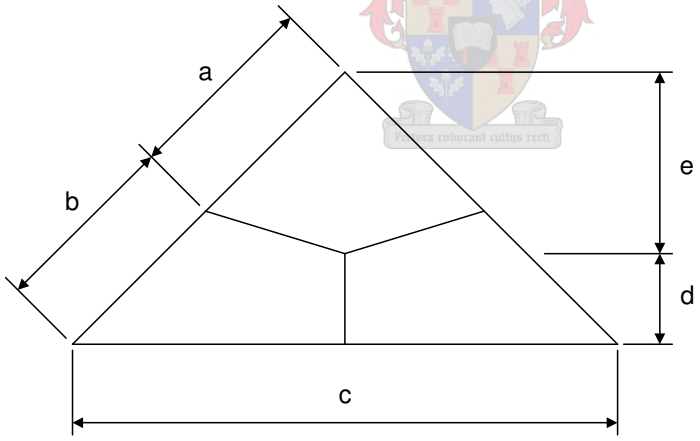

(b)

a	5.6
b	5.6
c	17.4
d	2.35
e	4.7
f	17.4

Figure 5.6 Computational domain. (a) Top view of cross-corrugated channels. (b) View of inlet- and outlet boundary, dimensions in [mm].

The gradients for the velocity components are set equal to a constant value, calculated from global mass convergence considerations. The distance that the outlet boundaries are moved down stream from the free shear interface must therefore be sufficient to allow any recirculation vortex to get completed before reaching the outlet boundary. This distance was found to be equal to the length of the base of a channel

(distance c in Figure 5.6) by Petre et al. (Petre et al., 2003). This distance is also used in this study. Simulations where this distance was set equal to half the length of the corrugation base (distance c in Figure 5.6) failed to converge. An extra condition imposed on the outlet boundaries is that of equal flux splitting. The mass flow is divided equally between the two outlet boundaries. A constant mass fraction is specified against the walls in the section where the two triangular channels meet. This mass fraction is calculated from the naphthalene vapour pressure at the experimental conditions. The vapour pressure of naphthalene is calculated with the equation proposed by Ambrose et al. (Ambrose et al., 1975). For the geometry where the inlet and outlet boundaries are removed from the free shear interface (geometry 1), an extra wall boundary condition is imposed. The bottom 'wall' of the channel leading up the free shear interface is specified to be a free slip boundary (see Figure 5.6). A velocity boundary layer is therefore not allowed to develop next to this wall. On all the remaining walls a 'no-slip' condition is imposed.

Table 5.7 Boundary conditions for micro element

Boundary	Boundary condition
Inlets 1 & 2	'Dirichlet' type boundary condition, default turbulence parameters, $x_A = 0.0$
Wall (1)	$x_A = 6.4\times10^{-4}$, no-slip condition
Wall (2)*	free slip condition
Outlets 1 & 2	'Neumann' type boundary condition

*This boundary is only present if distance f > 0 (see Figure 5.6)

Computational grid

In order to generate a rectangular structured grid (see Chapter 3), the triangular passages are divided into three rectangular blocks (shown in Figure 5.6). The use of a low Reynolds number turbulence model requires a fine grid in the near wall region. In order to use the minimum amount of volume elements while still maintaining a fine grid near the wall, a quadratic decrease in grid spacing is used from the middle of the passage to the wall (distance a in Figure 5.6). A fine grid is also necessary in the region of the free shear interface. The properties of the flow will change over short distances in this region. A quadratic decrease in cell size is used between the middle of the passage and the free shear interface (distance b in Figure 5.6). For the geometries where the inlet and outlet boundaries are placed a distance away from the free shear interface, the grid is also quadratically expanded from the free shear interface to the outlet boundary (distance f in Figure 5.6). The same procedure was

used to obtain a grid independent solution as discussed in the previous section. The grid is refined for the highest Reynolds number until a grid independent solution is obtained. This grid is then used for all lower Reynolds numbers. For both geometries the first grid point was placed at a distance of 0.01 mm away from the wall boundary. At the highest gas phase Reynolds number (ReG ≈ 6200), this distance translated into an average dimensionless distance away from the wall of $y^+ \approx 0.18$ for geometry 1 and $y^+ \approx 0.23$ for geometry 2. This is well within the viscous sublayer of the boundary layer. This distance was also use for all lower Reynolds numbers. Details of the converged grid for the two geometries are given in Table 5.8. The number of node points on distance b was reduced to 20 for geometry 1 in order to reduce the total number of volume elements. Doing so did not influence the solution. When the number of nodes were reduced from 30 to 20 for geometry 2, there was a significant change in the solution.

Table 5.8 Details of converged grid for packing micro element

Geometry	Number of nodes*			Distance 1st node from wall [mm]	Total number of volume elements
	a	b	F		
1	30	20	40	0.01	540 000
2	30	30	n/a	0.01	290 000

* See Figure 5.6 for description

Mathematical model and computational details

The k-ω and BSL turbulence model were used. Chapter 3 may be consulted for details on these turbulence models and the governing equations of fluid motion. Hybrid differencing was used for all variables with the SIMPLEC algorithm to solve the pressure-velocity coupling. Steady state simulations were performed with a combination of false time stepping and under relaxation to control the rate of convergence. A simulation was judged to have reached convergence when the global mass source residual was less than 10^{-6}.

Results and discussion

The sublimation rate of naphthalene is determined by simulating the airflow through a micro element and calculating the difference in concentration of naphthalene between the inlet and outlet boundaries. A mass transfer coefficient is calculated with Equation 5.35 for each micro element and the gas phase Reynolds number is calculated using Equation 5.40. Seven micro elements in series are modelled. This corresponds to the longest channel found in the coated structured packing element.

In preliminary runs both the k-ω and BSL turbulence models were used. From Figure 5.5 it would seem that the k-ω model should be used at low Reynolds numbers (up to about $Re_G \approx 4000$) and the BSL model for Reynolds numbers $Re_G > 4000$. In these preliminary runs a normal no-slip boundary was specified on the bottom wall of the channel leading into and out of the 'criss-cross' element (geometry 1). The total number of elements was also less than shown in Table 5.8. (332 000 volume elements). Figure 5.7 show the results obtained with the two turbulence models. The mass transfer coefficient shown is the average calculated for the seven micro elements. Figure 5.7 show that the same result is obtained with the two turbulence models at low Reynolds numbers ($Re_G < 4000$). At high Reynolds numbers ($Re_G > 4000$) the BSL model predicts a higher mass transfer rate compared to the k-ω model.

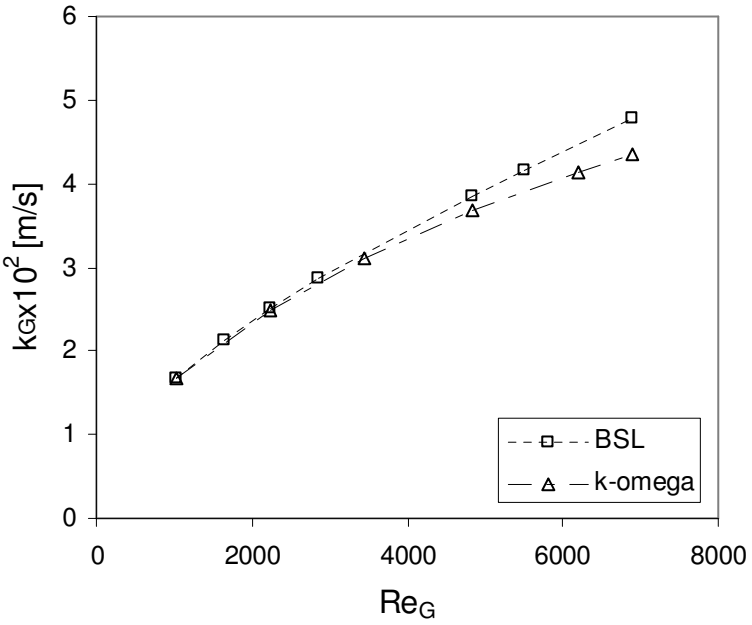

Figure 5.7 Mass transfer coefficients calculated at different Re_G with the k-ω and BSL turbulence models.

In subsequent simulations only the BSL turbulence model was used since it gave the same result at low Reynolds numbers compared to the k-ω model. It is also expected (see Figure 5.5) that the BSL model will be more accurate than the k-ω model at high Reynolds numbers ($Re_G > 4000$).

Figure 5.8 show the results obtained for the micro element where the boundaries are located next to the free shear interface (geometry 2). The results shown in this figure

were obtained with the BSL turbulence model. Details of the converged grid are given in Table 5.8. Figure 5.9 show the results for the geometry where the inlet and outlet boundaries are moved a distance away from the free shear interface (geometry 1). The BSL turbulence model was used with the details of the converged grid given in Table 5.8.

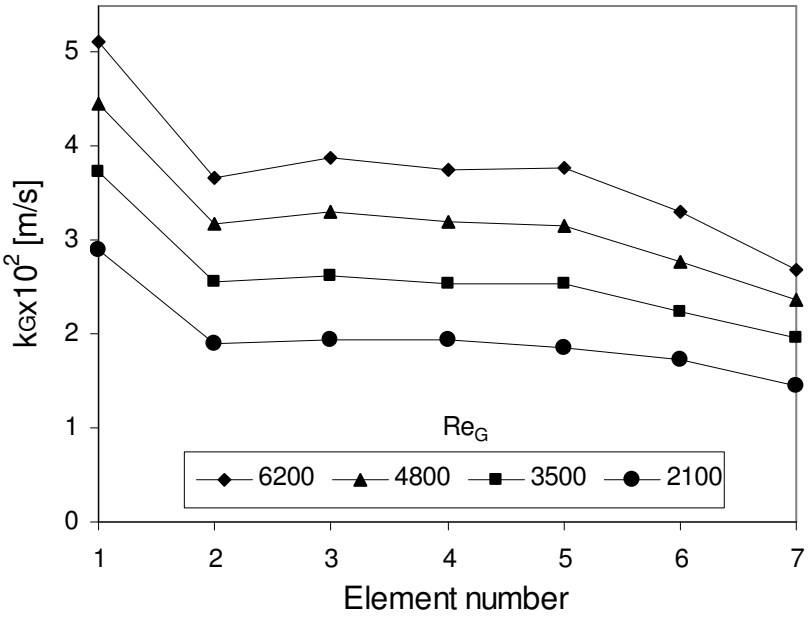

Figure 5.8 Mass transfer coefficients calculated at different Re_G for geometry2 (boundaries next to free shear interface).

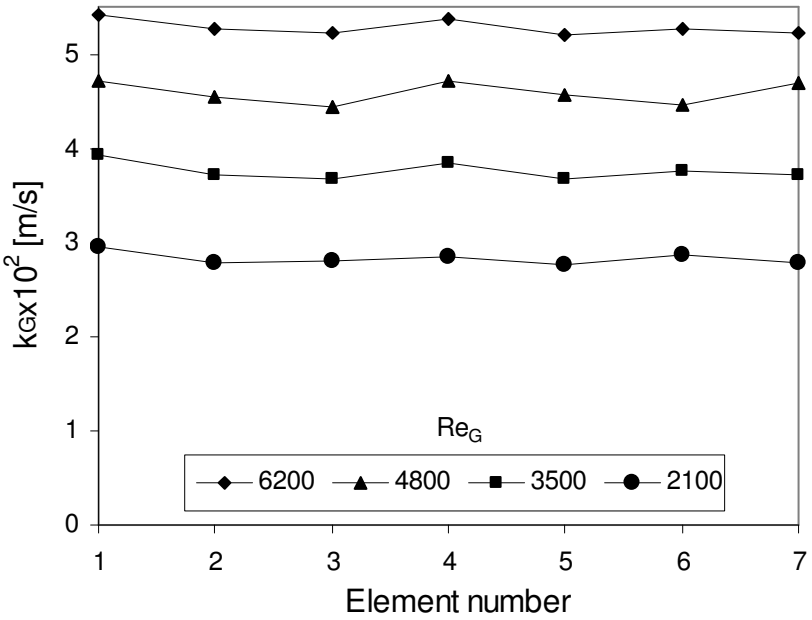

Figure 5.9 Mass transfer coefficients calculated at different Re_G for geometry 1 (boundaries a distance away from free shear interface).

Figure 5.8 show that there is a decrease in the mass transfer rate as the flow progresses from micro element 1 to micro element 7. The highest mass transfer rate is found in the first element and the lowest mass transfer rate in the last element. A decrease in the heat transfer rate from element 1 to element 2 was found in the numerical work of Ciofalo et al. (Ciofalo et al., 1996) on heat transfer in corrugated channels. In their work the heat transfer rate decreases up to the third element. After this element a steady value is reached.

Figure 5.9 show that this trend is not observed for the geometry where the boundaries are located a distance c away from the free shear interface (geometry 1). The mass transfer rate is almost independent of element location. This was also found to be the case for the simulated pressure loss coefficient in the study by Petre et al. (Petre et al., 2003).

Figure 5.10 shows the average mass transfer coefficients as a function of Reynolds number for the two modelling approaches. The figure shows that the mass transfer rate modelled with the geometry 1 is 40% higher than for geometry 2.

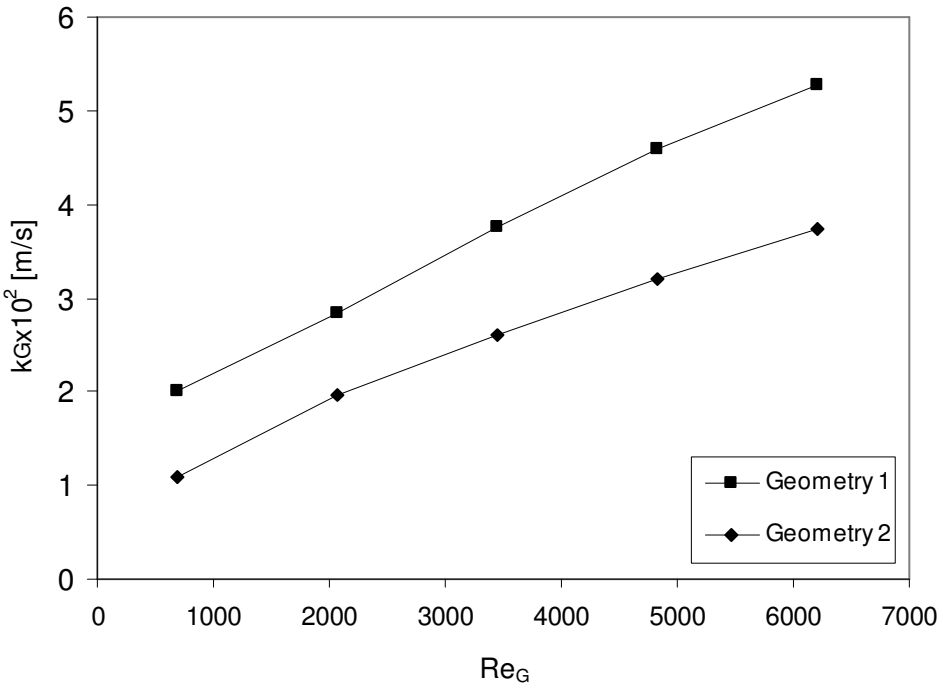

Figure 5.10 Comparison between mass transfer coefficients calculated with the two physical domains used in CFD simulations. Re_G calculated with eq. 5.41.

In Figures 5.12 to 5.14 (see end of chapter) the differences in mass transfer rates between the two geometries are investigated by flow visualization. Figure 5.12 show

the turbulent kinetic energy distribution through the centre plane of each geometry at a Reynolds number of 6200. This quantity represents the kinetic energy of the turbulent velocity fluctuations. A high value would indicate regions with high levels of turbulence. Figure 5.12 (a) to (c) represent the first, fourth and seventh elements of geometry 1. Figure 5.12 (d) to (f) represent the corresponding elements for geometry 2. Figure 5.13 shows the turbulent (eddy) viscosity distribution through the mid plane for the same elements. In regions with a high turbulent viscosity the turbulent diffusivity would also be high. If these regions are close to the solid wall this would lead to high heat- and mass transfer rates from the wall. Airflow path lines are shown in Figure 5.14. The path is traced from one of the inlet boundaries. These path lines give an indication of where vortices are formed and the level of mixing between two corrugation channels. Figures 5.12 and 5.13 show that the distribution of the turbulent kinetic energy and turbulent viscosity is different for the two geometries. For geometry 1 there is a more uniform distribution throughout the flow domain. With geometry 2 a region of high turbulence is clearly seen in the region of the interface between the two channels (Figure 5.12 (e) and (f)). There is a deeper penetration of turbulence into the apex of the channels for geometry 1 when compared to geometry 2 (Figure 5.12 and 5.13). This would lead too higher heat- and mass transfer rates from the wall in the apex region for geometry 1 when compared to geometry 2. Regions of high turbulence are also closer to the wall over the entire flow domain for geometry 1 compared to geometry 2. This is especially true for the wall on the inlet side of the physical domain for elements 4 and 7 (Figure 5.12 (b) and (c) compared to Figure 5.12 (e) and (f)). The airflow path lines (Figure 5.14) show that mixing between the two channels occur for geometry 1 up to the seventh element (Figure 5.14 (b) and (c)). There is almost no mixing between the two channels for geometry 2 at elements 4 and 7 (Figure 5.14 (e) and (f)). From the flow visualization figures the higher mass transfer rate in geometry 1 may be contributed too:

- More uniform turbulent flow field, enhancing mixing.
- Regions of high turbulent kinetic energy close to the wall.
- Mixing between channels occurring at each intersection.

The CFD results are compared with the experimental results in Figure 5.11.

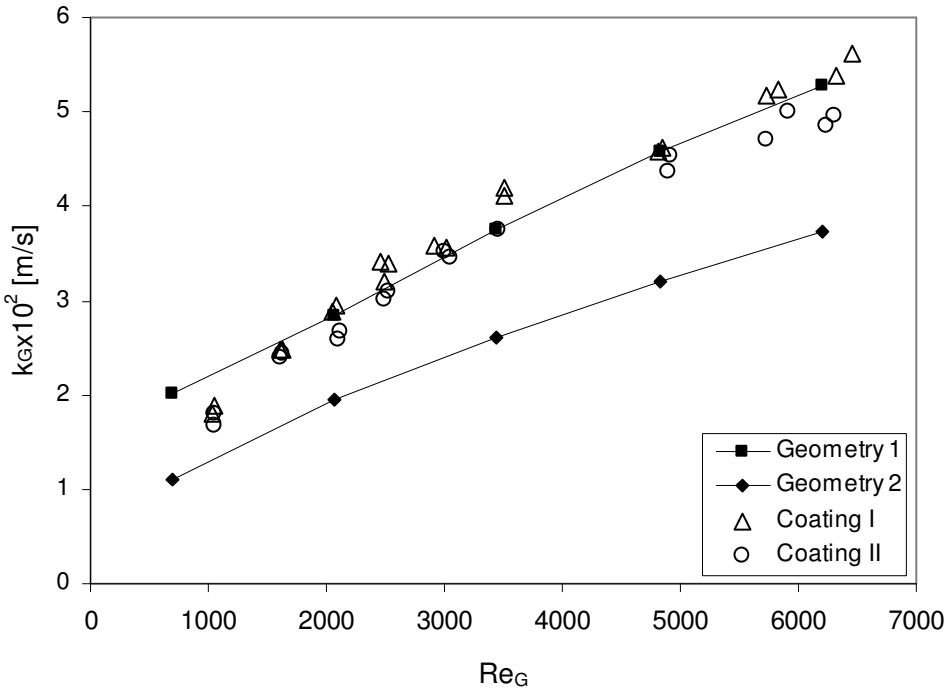

Figure 5.11 Comparison of CFD and experimental results for naphthalene sublimation.

Figure 5.11 show the experimental results to be in close agreement with the CFD results obtained with geometry 1. The CFD results obtained with this geometry suggest that the mass transfer rate is the same throughout the length of a corrugation channel. At high Reynolds numbers (Re_G > 5000) a 10% increase in the mass transfer rate was measured for the bottom half of a packing element compared to the top half. This slightly higher mass transfer rate at high Reynolds numbers is not predicted by the CFD model using geometry 1. A possible explanation for this is that there is a sharp 90° bend at the bottom entrance of a packing element. In the sublimation experiments there will therefore be a sharp direction change of the air flow as it enters the base of the packing element. This will cause a high mass transfer rate from the naphthalene wall that forces this change in direction. Visual inspection of the packing sheets after an experimental run also showed the naphthalene coating to be thinner on the corrugation passage wall at the base of the element. This sharp direction change would be absent in the top half of the packing and there would therefore be a slightly lower mass transfer rate when the top half is coated (coating 2) with naphthalene compared to when the bottom half is coated (coating 1). In the CFD model the inlet velocity profile is specified to be normal to the inlet face. The transition region between two packing elements is quite complex and would be difficult to model with CFD. The relative small difference in the mass

transfer rates between the top and bottom half do not justify a more complex CFD model.

CFD simulations with geometry 2 show a decrease in the mass transfer rate as the flow progresses down a channel (Figure 5.8), leading to a lower overall mass transfer coefficient. The much lower average mass transfer rate obtained with geometry 2 would again suggest that the complex nature of the flow is not fully captured when using this geometry (see Figures 5.12 to 5.14).

An advantage of the CFD simulations using geometry 1 is that only a single element needs to be modelled in order to predict the mass transfer rate for a whole packing element with reasonable accuracy. In future this would reduce the computational effort immensely.

5.7 Conclusions

From the experimental investigation of the gas phase mass transfer in structured packing, the following conclusions may be drawn:

- Current wetted-wall type correlations predict lower than measured gas phase mass transfer coefficients in Flexipac 350Y.
- Naphthalene sublimation experiments performed with Flexipac 350Y led to the following correlations for the gas phase mass transfer rate:

$$Sh_G = 0.2641 Re_{G,e}^{0.62} Sc_G^{0.5}$$

$$Sh_G = 0.3053 Re_{G,e}^{0.62} Sc_G^{0.33}$$

- The gas phase mass transfer rate was found to be the same for the bottom- and top half of a structured packing element.
- Results from the CFD simulations of the gas phase mass transfer rate in structured packing show that:
- The BSL turbulence model of Menter (Menter, 1994) may be used to predict the gas phase mass transfer rate in structured packing.
- The results obtained are sensitive to the placement of inlet- and outlet boundaries. These boundaries should be moved away from the open free shear interface between two corrugated channels. A distance equal to the corrugation base was found to be adequate (See Figure 5.6).
- Only a single representative micro element needs to be modelled to determine the overall mass transfer rate with reasonable accuracy.

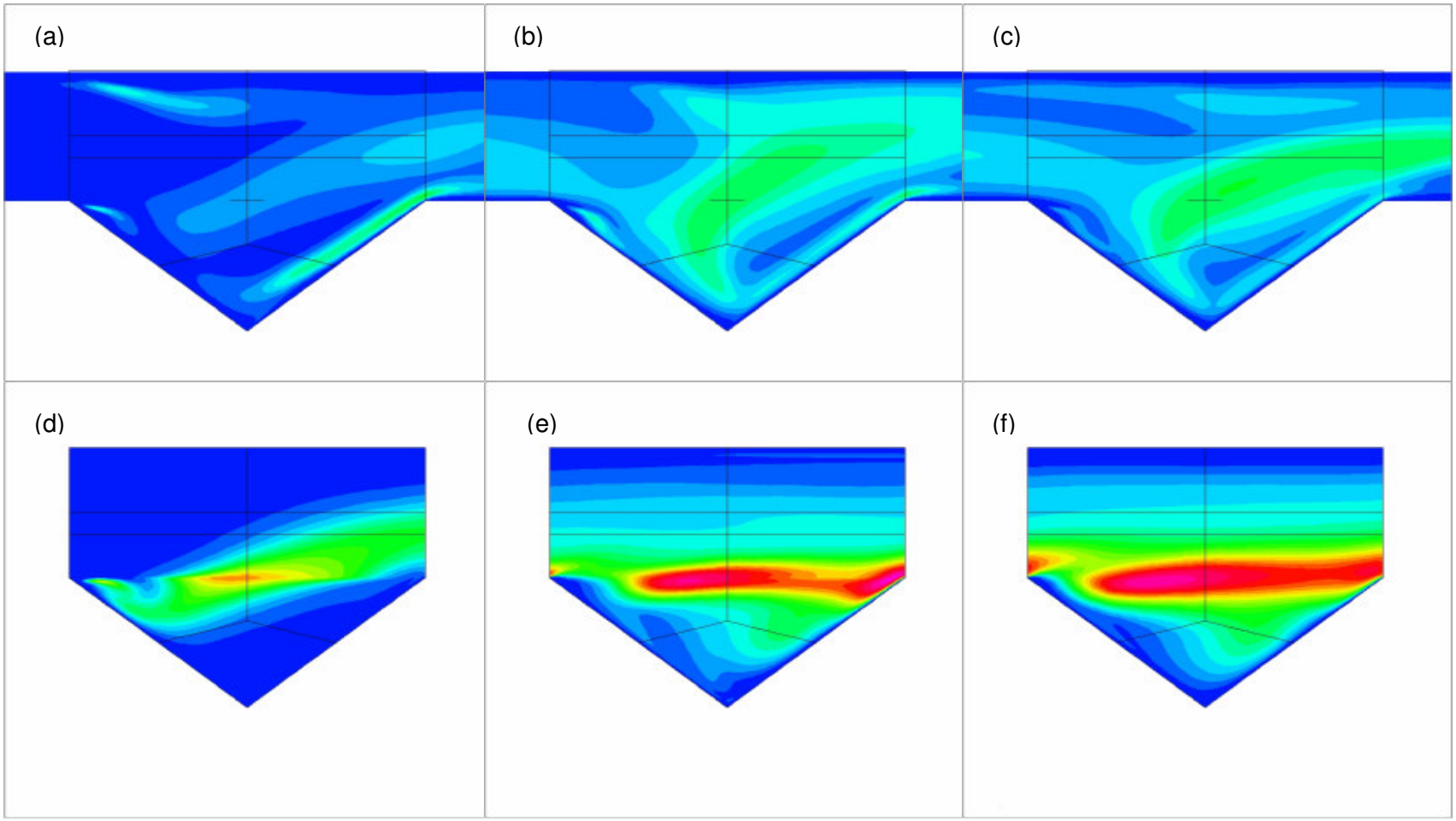

Figure 5.12 Plot of turbulent kinetic energy (k) at Re_{δ} = 6200. Figures (a) to (c) are plots for k in element 1, 4 and 7 of geometry 1. Figures (d) to (f) are for the corresponding elements in geometry 2. Flow enters from the left.

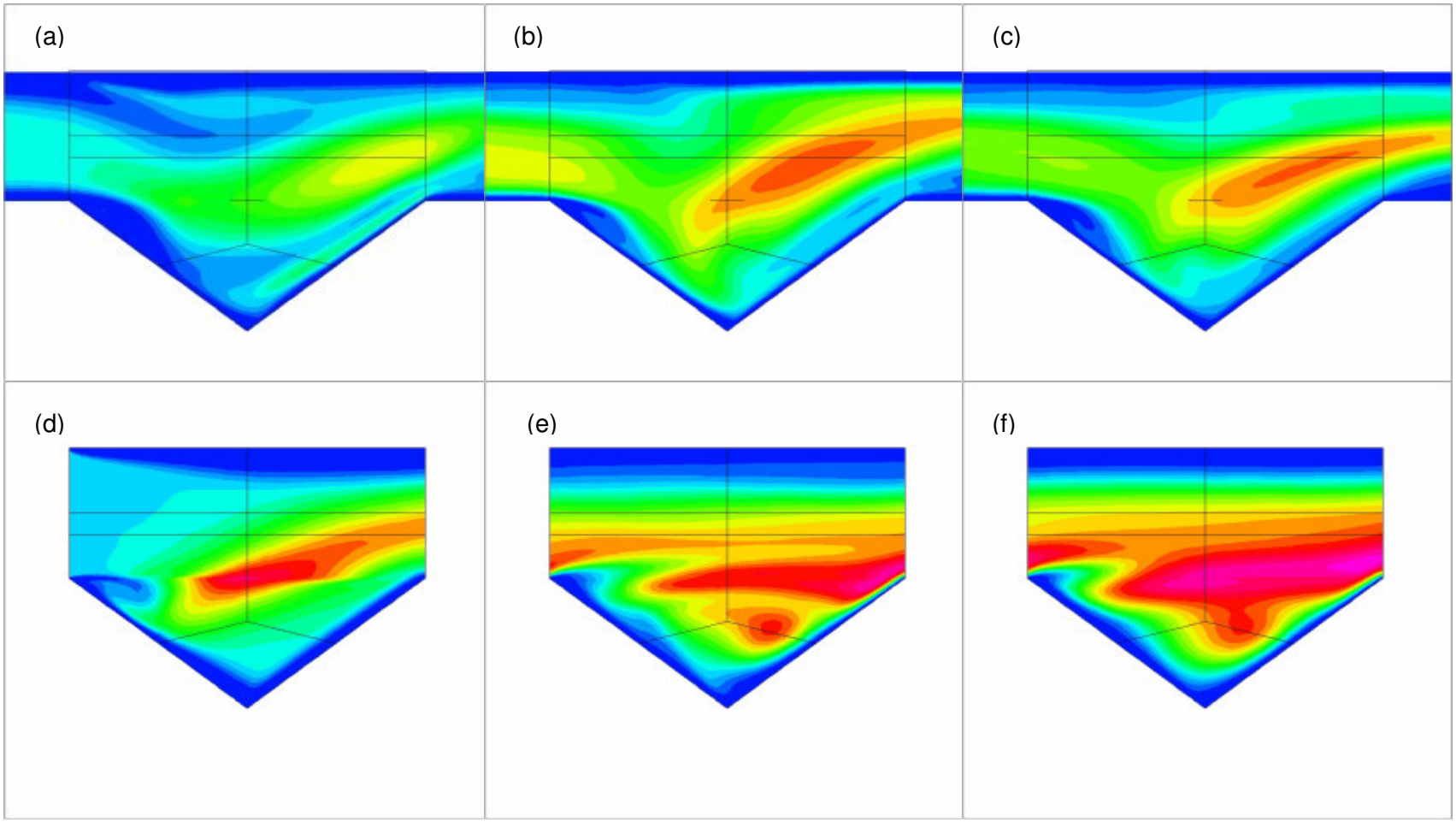

Figure 5.13 Plot of eddy viscosity at Re_{σ} = 6200. Figures (a) to (c) are plots for eddy viscosity in element 1, 4 and 7 of geometry 1. Figures (d) to (f) are for the corresponding elements in geometry 2. Flow enters from the left.

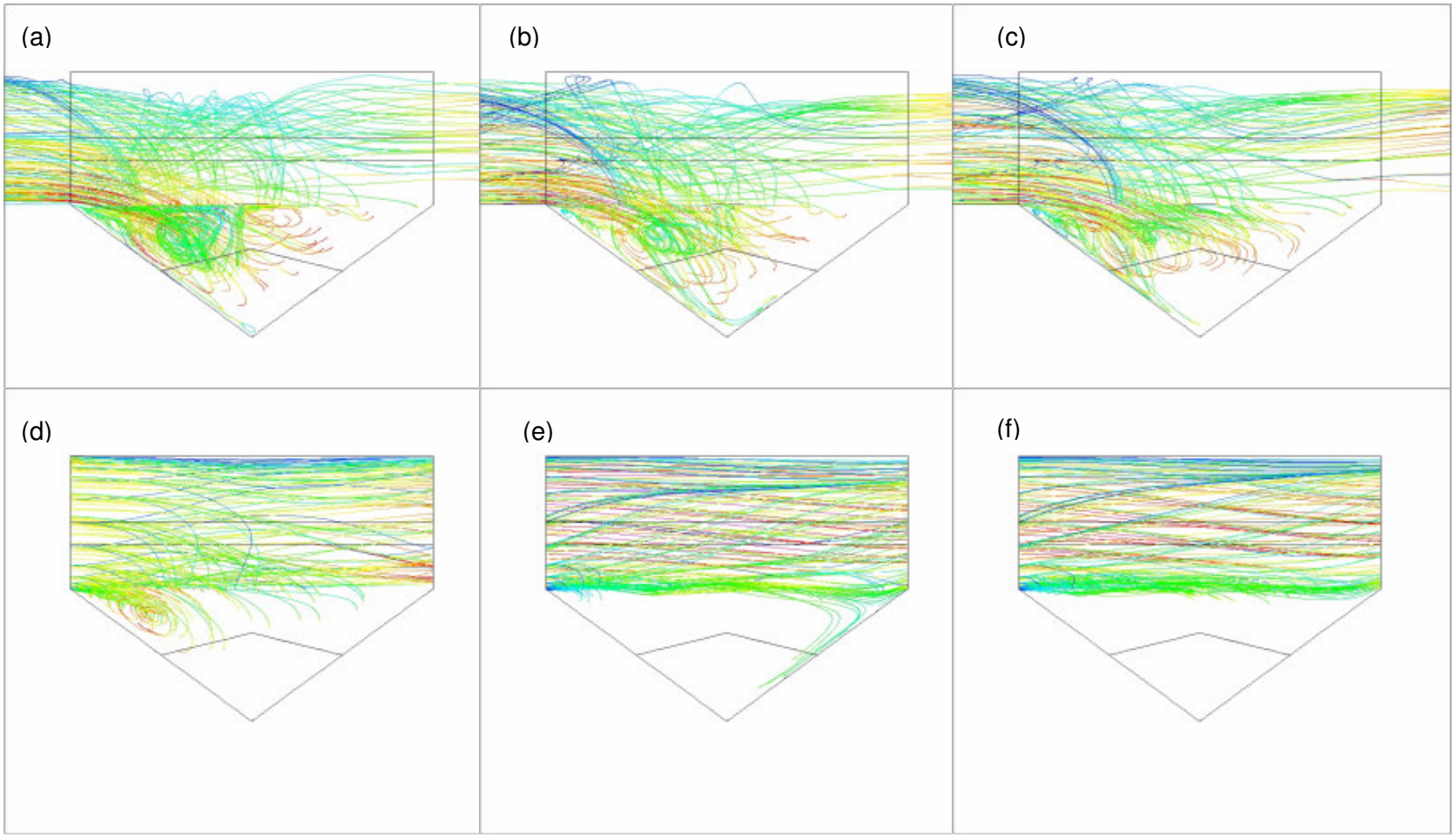

Figure 5.14 Air flow path lines at Re_s = 6200. Figures (a) to (c) are for element 1, 4 and 7 of geometry 1. Figures (d) to (f) are for the corresponding elements in geometry 2. Flow enters from left.

5.8 Nomenclature

A	Area [m^2]
a_e	Effective surface area of packing [m^2/m^3]
a_p	Geometric area of packing [m^2/m^3]
A_w	Wetted perimeter [m2]
B	Channel base dimension [m]
c	Concentration [mol/m^3]
D	Diffusion coefficient [m^2/s]
d_h	Hydraulic diameter [m]
dx	Differential distance in x coordinate direction [m]
Gz	Graetz number
h	Channel crimp height [m]
h	Height of packed bed [m]
h_t	Total liquid holdup [m^3/m^3]
k	Mass transfer coefficient [m/s]
Ka	Kapitsa number
ℓ	Film thickness [m]
$\ell_{G,pe}$	Length of triangular vapour phase channel [m]
n	Molar flux [mol/s]
N	Specific molar flux [$mol/(m^2.s)$]
P^{sat}	Saturated vapour pressure [Pa]
P_T	Total pressure at vapour/liquid interface [Pa]
r,θ,z	Cylindrical coordinates: radius, angle, height
Re	Reynolds number
S	Side dimension of corrugated channel [m]
Sc	Schmidt number
Sh	Sherwood number
u	Velocity [m/s]
V_c	Volume of packed bed [m^3]
x	Mass fraction in vapour phase [-]
y	Mole fraction in vapour phase [-]
$y_{B,m}$	Logarithmic mean mole fraction [-]
y^+	Dimensionless distance

Greek

π	= 3.14159…
θ	Corrugation angle [^{o}]
μ	Dynamic viscosity [Pa.s]
φ	Fraction of triangular passage occupied by liquid [-]
ξ_{GL}	Vapour/liquid friction factor [-]
ε	Void fraction [-]
ρ	Density [kg/m^3]

Subscripts

A	Refers to component A
b	Refers to bulk of phase
B	Refers to component B
BF	Refers to 'bulk flow' molar flux
e	Effective
G	Refers to vapour phase property
i	Refers to vapour/liquid interface
L	Refers to liquid phase property
s	Superficial
T	Refers to total molar flux

6 EFFECTIVE INTERFACIAL AREA

6.1 Introduction

The efficiency of structured packing depends strongly on the effective interfacial area for gas phase mass transfer between the liquid and vapour phases. This quantity is, however, difficult to measure and conflicting results were obtained by different studies on effective interfacial area in the past (Weimer and Schaber, 1997, De Brito et al., 1994). When determining the effective interfacial area in structured packing, aqueous systems have almost exclusively been used. Aqueous systems are notorious for their bad wetting characteristics of stainless steel surfaces. In this chapter the use of an organic system to determine effective interfacial area of Flexipac 350Y is explored.

6.2 Literature survey

6.2.1 Definitions of effective interfacial area

There are quite a few definitions for interfacial area in a packed column. Shi and Mersmann (Shi and Mersmann, 1985) lists these as:

- Actual interfacial area between gas and liquid (a_i)
- Interfacial area between packing and liquid (a_w)
- Active interfacial area for gas phase mass transfer (a_G)
- Active interfacial area for liquid phase mass transfer (a_L)
- Active interfacial area for evaporation (a_V)
- Active interfacial area for mass transfer accompanied by a chemical reaction (a_C).

The term 'effective interfacial area' could therefore refer to a_G, a_L, a_V or a_c, depending on the process under consideration. In this study the focus will be on the active interfacial area for gas phase mass transfer (a_G). In the paragraphs that follow this area will be represented by a_e.

6.2.2 Methods for determining interfacial area

There are various methods used to determine effective interfacial area in gas-liquid contactors. They are broadly classified as physical or chemical techniques (Charpentier, 1981).

A popular method used for structured packing that could be classified as a physical technique, is the use of liquid hold-up data to determine the wetted area. If the liquid film thickness is known, the interfacial area between the liquid and vapour phases could be calculated from the liquid hold-up. Other physical techniques used for gas-liquid contactors include physical absorption, photographic techniques and light scattering. All of these are of limited use when determining effective interfacial area in structured packing. Only physical absorption could be considered for determining the effective interfacial area for gas phase mass transfer (a_G). The large surface area per volume of packing makes it difficult to determine a_G by pure physical absorption due to saturation of the liquid- or gas phases. Physical absorption also suffers from mass transfer rates governing the overall absorption rate. The effective interfacial area could thus be influenced by errors made in calculating the mass transfer coefficients. Photographic techniques and light scattering are used to determine the interfacial area between the vapour and liquid phases and are of limited use in structured packing. The rely on light to be conveyed through the medium. These methods are usually used where liquid is the continuous phase with gas being the dispersed phase, as encountered in plate- and bubble columns.

In the chemical technique the effective surface area is determined by combining physical absorption with a chemical reaction in the liquid phase. Under certain conditions the absorption rate is independent of the mass transfer resistance in the liquid phase and directly dependent on the effective interfacial area. The condition that has to be satisfied is that of a fast psuedo m,n^{th} order reaction in the liquid phase (Charpentier, 1981, Danckwerts, 1970, Sharma and Danckwerts, 1970). This reaction regime is described in detail in the section 6.3. Various chemical systems have been proposed to measure effective interfacial area in gas-liquid contactors (Sridharan and Sharma, 1976, Sharma and Danckwerts, 1970). The most popular system is the absorption CO_2 diluted with air into aqueous NaOH and KOH solutions.

In the following section the use of physical and chemical methods to determine effective interfacial area in structured packing and the correlations proposed by various investigators are discussed.

6.2.3 Interfacial area in structured packing

In the model by Billet (Billet, 1995) the effective interfacial area is assumed to be equal to the interfacial area between the vapour and the liquid. At the loading point it is calculated with:

$$\left(\frac{a_e}{a_p}\right)_{lp} = 3\varepsilon^{0.5}\,Re_{L,s}^{-0.2}\,We_{L,s}^{0.75}Fr_{L,s}^{-0.45} \tag{6.1}$$

The effective interfacial area between the load- and flood point is calculated with an expression similar to that for hold-up (see Chapter 4) in the loading region:

$$\left(\frac{a_e}{a_p}\right)_{u_{G,s}>(u_{G,s})_{lp}} = \left(\frac{a_e}{a_p}\right)_{lp} + \left[\left(\frac{a_e}{a_p}\right)_{fp} - \left(\frac{a_e}{a_p}\right)_{lp}\right]\left(\frac{u_{G,s}}{(u_{G,s})_{fp}}\right)^{13} \tag{6.2}$$

with the effective interfacial area at the flood point calculated from:

$$\left(\frac{a_e}{a_p}\right)_{fp} = 7\left(\frac{\sigma_L}{\sigma_W}\right)^{0.56}\left(\frac{a_e}{a_p}\right)_{lp} \tag{6.3}$$

For negative surface tension gradient systems in distillation applications, the effective surface area is reduced by surface destabilization:

$$\left(\frac{a_e}{a_p}\right)_{neg} = \left(1 - 2.4\cdot 10^{-4}\,|Ma_L|^{0.5}\right)\frac{a_e}{a_p} \tag{6.4}$$

where Ma_L is the Marangoni number defined by:

$$Ma_L = \frac{\Delta x}{D_L \mu_L a_p} \tag{6.5}$$

The methodology used to arrive at these expressions are not clearly stated (Billet, 1995).

It is common practice to assume that the effective interfacial area is equal to the wetted surface area. In the model proposed by Bravo et al. (Bravo et al., 1985) for gauze packing, complete wetting of the packing is assumed. The wetted area is assumed to be equal to the effective interfacial area, and is taken to be equal to the geometric area of the packing:

$$a_e = a_w = a_p \tag{6.6}$$

For gauze packing this may be a reasonable approximation. For sheet metal structured packing the packing surface may not be completely wetted and Fair and Bravo (Fair and Bravo, 1990) suggests incorporating a discount factor in calculating the effective surface area from the packing surface area:

$$a_e = \beta a_p \tag{6.7}$$

where

$$\beta = 0.50 + 0.0058\times(\%\text{flood}) \tag{6.8}$$

Shi and Mersmann (Shi and Mersmann, 1985) developed an expression for the wetted surface area for a liquid flowing down an inclined plate. Rocha et al. (Rocha et al., 1993, Rocha and Bravo, 1996) used this expression to correlate experimental hold-up and efficiency data for structured packing. This resulted in the following equation to calculate the ratio of effective- to geometric surface area:

$$\frac{a_e}{a_p} = F_{SE} \frac{29.12\left(We_{L,s}Fr_{L,s}\right)^{0.15} S^{0.359}}{Re_{L,s}^{0.2}\,\varepsilon^{0.6}\,(1-0.93\cos\gamma)(\sin\theta)^{0.3}} \qquad (6.9)$$

The factor F_{SE} accounts for the surface treatment of the packing (lancing, fluting, embossing etc.). The wettability of the surface is accounted for by the contact angle γ.

Nawrocki et al. (Nawrocki et al., 1991) developed a detailed liquid distribution model to determine the wetted area in structured packing. According to the model, a volume of liquid (or rivulet) flowing in a channel is split up into two equal portions at an intersection point. A portion of the liquid continues down the same channel while the other portion flows down through the intersection point into the next channel. The split ratio is assumed to be uniform through the packing and is determined by fitting the model to experimental hold-up data. The model uses the correlation proposed by Shi and Mersmann (Shi and Mersmann, 1985) to determine the rivulet width. The effective surface area is assumed to be equal to the wetted surface area and may therefore be calculated from the rivulet width in each section of the packing.

Brunazzi et al. (Brunazzi et al., 1995) proposed an expression for the ratio of the effective interfacial area to geometric area. The equation is based on the classical laminar falling film thickness for a liquid flowing down an inclined tube and the liquid hold-up calculated with a suitable correlation:

$$\frac{a_e}{a_p} = \left(\frac{d_{hG}}{4}\right)\left(\frac{h_t}{\varepsilon}\right)^{1.5}\left(\frac{\rho_L g \sin\theta}{3\mu_L}\frac{\varepsilon \sin\theta}{u_{L,s}}\right)^{0.5} \qquad (6.10)$$

In most of the methods discussed up to this point, the effective surface area is assumed to be equal to the interfacial area between the vapour and liquid phases or the wetted area. It is convenient to make this assumption since this area may be determined from liquid hold-up data. As explained previously, the interfacial area between the vapour and liquid phases may not be equal to the effective area for mass transfer. Some stagnant pockets of liquid may exist. In these stagnant areas the driving force for mass transfer is low because of vanishing differences in

concentration between the liquid and vapour phases. The only way to determine the effective area for mass transfer in systems where stagnant pockets of liquid exists, is to use the chemical method. It has been used to determine effective interfacial area for some types of structured packing. The absorption of carbon dioxide diluted with air into aqueous sodium hydroxide solutions is almost exclusively used.

De Brito et al. (De Brito et al., 1994) used this system to determine the effective interfacial area for the Mellapak range of structured packing made from stainless steel. The effective surface area was found to be higher than the geometric area for all the packing studied. This higher than anticipated effective surface area was thought to be due to flow instabilities in the liquid film resulting in waves and liquid detachment. The effective interfacial area was largely independent of the gas phase flow rate and the proposed correlation for the Mellapak range of packing is:

$$\frac{a_e}{a_p} = 0.465 Re_{L,s}^{0.30} \qquad (6.11)$$

Weiland et al. (Weiland et al., 1993) also used the CO_2/NaOH system to measure effective surface area for Goodloe and Montz A2 packing. The interfacial area was found to be independent of the liquid flow rate and correlated directly with the gas side F-factor. The proposed correlations for the different types of packing are:
Goodloe packing:

$$a_e = 356 F_G^{-0.2} \qquad (6.12)$$

Montz A2:

$$a_e = 265 F_G^{-0.4} \qquad (6.13)$$

This is in contrast to results obtained by De Brito et al. (De Brito et al., 1994) for the Mellapak range of packing where the effective interfacial area was independent of the gas flow rate.

Weimer and Schaber (Weimer and Schaber, 1997) measured effective interfacial area in structured and random packing. The absorption of atmospheric carbon dioxide into caustic solutions was used as test system. The system has the advantage of very low heat and mass transfer rates which leads to approximately constant temperatures and concentrations throughout the column. Mellapak 250Y made out of polypropylene and stainless steel was used and the results compared with that of polypropylene Hiflow rings (25 mm). The gas phase mass transfer resistance was neglected in calculating the effective surface area. Both sodium and

potassium hydroxide solutions were used in the absorption experiments. The effective interfacial area calculated by using KOH solutions was approximately 5% lower compared with NaOH solutions. It is argued that the KOH solutions produce more accurate results. For all the packing tested the effective interfacial area was less than the geometric surface area. For the stainless steel structured packing the effective surface area was approximately 90% of the geometric area. The polypropylene packing had a much lower effective surface area at roughly 65% of the geometric area.

The effective surface area correlation used in the mass transfer model by Olujic et al. (Olujic et al., 1999) was fitted on experimental data for the absorption of CO_2 in aqueous NaOH solutions (Stoter, 1993):

$$a_e = a_p \frac{(1-\Omega)}{\left(1+\frac{A}{(u_{L,s})^B}\right)} \tag{6.14}$$

The constants in the correlation are packing specific. For Montzpak B1-250 the constants are:

$$A = 2.143\times10^{-6}, \quad B = 1.5 \tag{6.15}$$

The effective interfacial area curve calculated with this correlation exhibit a flat profile and is close to the geometric surface area of the packing at liquid loads above $10 m^3/(m^2 hr)$.

The results differ widely in the studies on chemical absorption to determine effective interfacial area. In some cases opposing results for the same packing are obtained. For the same type of structured packing (Mellapak 250Y) using the same test system (CO_2/NaOH), although at different concentrations of CO_2, De Brito et al. (De Brito et al., 1994) and Weimer and Schaber (Weimer and Schaber, 1997) obtain different and contrasting results. For a liquid load of $20 m^3/(m^2.hr)$ De Brito et al. (De Brito et al., 1994) measured an effective interfacial area of $300 m^2/m^3$ while at the same liquid load Weimer and Schaber (Weimer and Schaber, 1997) measured an effective interfacial area of $170 m^2/m^3$. The results obtained by Weiland et al. also differ from the rest. No dependency of the effective interfacial area on the liquid flow rate was found. Instead the interfacial area could be correlated directly with the gas flow rate.

The widely differing results obtained with the chemical method to determine effective interfacial area in structured packing warrants further investigation. As stated in chapter 4, aqueous systems are notorious for their bad wetting of stainless steel surfaces. An organic system would be more suitable for structured packing.

6.2.4 Chemical systems for determining effective interfacial area

The need for alternative organic and/or viscous systems to determine effective interfacial area in gas-liquid contactors has long been recognised (Danckwerts, 1970). It was found that most systems used in aqueous solutions are unsuitable in organic solvents (Sridharan and Sharma, 1976). Difficulties encountered included immiscibility of the species in the solvent and precipitation of the product. The reaction of CO_2 with amines in organic media does not suffer these difficulties and was found to be suitable (Sridharan and Sharma, 1976). A wide range of organic solvents may be used. These include hydrocarbon-, polar- and viscous solvents.

Considerable effort has gone into determining reaction rate constants for amines reacting with mainly CO_2 but also with H_2S in aqueous media (Blauwhoff et al., 1982, Sada et al., 1976, Danckwerts, 1979, Littel et al., 1992). This is largely due to the fact that the absorption of acid gases from natural- and synthetic gas streams is an important industrial process (Danckwerts and Sharma, 1966). The reaction is reversible and the loaded solution is regenerated by stripping of the CO_2 and H_2S. Aqueous amine solutions have traditionally been used in industrial processes (Danckwerts and Sharma, 1966) (Wall, 1975). Other solvents are also used. The Amisol process is an example of an industrial process that uses methanol as solvent (Bratzler and Doerges, 1974). Alcoholic solution offers advantages that include high solubility and capacity of acid gases and low energy consumption during regeneration (Sada et al., 1985). Viscous organic solvents have also been proposed for the absorption of CO_2 (Davis and Sandall, 1993).

The reaction kinetics have been determined for a number of amines reacting with CO_2 in alcoholic solvents. The reaction kinetics for primary, secondary and tertiary ethanol amines have been determined using methanol, ethanol and isopropanol as solvents (Sada et al., 1985, Sada et al., 1986, Sada et al., 1989). The reactions between primary- and secondary ethanol amines with CO_2 in ethanol and ethylene glycol have been investigated for determining interfacial areas and mass transfer coefficients in gas-liquid contactors (Alvarez-Fuster et al., 1981). These reactions were found to exhibit rapid pseudo m,n^{th} order kinetics that makes them suitable for

determining effective interfacial area (see Section 6.3). The reaction between CO_2 and amines in other organic solvents has also been investigated. An example is the reaction between CO_2 and cyclohexylamine in a toluene solution (Alvarez-Fuster et al., 1980).

From the above it would seem possible to use the reaction between CO_2 and ethanol amine in an organic solution to determine effective interfacial area in structured packing. For the reagents and solvents mentioned above, the reaction falls into the rapid pseudo m,nth order reaction regime. Some practical implications should be considered when choosing a system. Ideally the reagents should be inexpensive, not toxic and losses due to evaporation should be kept to a minimum. In order to minimize temperature changes in the contactor, the incoming gas is saturated with the solvent in a humidifier before entering the contactor. When using a solvent with a high vapour pressure at the experimental conditions, this would lead to high evaporation rates in the humidifier and high consumption rates of solvent. It is possible to strip the solvent vapour out of the exit gas, but this would make the experimental setup quite complex. It is therefore important that the chosen solvent have a low vapour pressure at the experimental conditions. Solvents with very low vapour pressures at ambient experimental conditions usually have a high viscosity. If solvents of low viscosity are preferred for measuring interfacial area, solvent losses due to evaporation would therefore have to be tolerable. Unfortunately most of the organic systems mentioned do not meet this criteria. Low boiling alcohols were used in most of the studies and their use would lead to substantial losses. The use of the cyclohexylamine in toluene system is also not considered a viable option since toluene is toxic and should preferably not be released into the atmosphere in large quantities. The use of higher boiling alcohols, such as n-propanol and n-butanol, would be favourable from an experimental point of view. The choice of amine is also important. The absorption rate decreases in the order primary amines > secondary amines > tertiary amines. Small amounts of primary amine in secondary amines may therefore enhance the absorption rate drastically (Blauwhoff et al., 1982). The same is true for small amounts of primary and secondary amines in tertiary amines. It would therefore be wise to use a primary amine were small amounts of secondary amine could be tolerated without influencing the absorption rate by much.

With all the above considerations taken into account, a system that would seem to be suitable for the determination of interfacial are in structured packing would be the

absorption of CO_2 into monoethanolamine solutions with either n-propanol or n-butanol as solvent. These systems are investigated in this study.

6.3 Theory

6.3.1 Gas-liquid absorption with chemical reaction

There are several good reviews of the theory of the absorption of a gas in the liquid phase followed by a reaction governed by fast pseudo m,nth reaction kinetics (Astarita, 1967, Danckwerts, 1970, Charpentier, 1981).

In the absence of a chemical reaction, the diffusion of a dissolved gas in the liquid phase is governed by the diffusion equation (Danckwerts, 1970):

$$D_A \frac{\partial^2 C_A}{\partial x^2} = \frac{\partial C_A}{\partial t} \qquad (6.16)$$

The rate of transfer of the dissolved gas across a plane parallel to the surface is calculated from:

$$(N_A)_x = -D_A \frac{\partial C_A}{\partial x} \qquad (6.17)$$

The analytical solution of Equation 6.16 is given by Danckwerts (Danckwerts, 1970) and forms the basis of the surface renewal model for mass transfer in the liquid phase.

When the absorption of a gas is accompanied by a chemical reaction in the liquid phase, the governing equation is:

$$D_A \frac{\partial^2 C_A}{\partial x^2} = \frac{\partial C_A}{\partial t} + r(x,t) \qquad (6.18)$$

The extra term r(x,t) is the rate at which the dissolved gas reacts in the liquid phase at time t and at a distance x from the interface. Analytical solutions have been developed for Equation 6.18 for first order reactions and a few examples are given by Danckwerts (Danckwerts, 1970).

For a second order chemical reaction under steady state conditions where a dissolved gas (specie A) reacts with a reagent (specie B), material balances for the two components are given by:

$$D_A \frac{\partial^2 C_A}{\partial x^2} = k_2 C_A C_B \qquad (6.19)$$

$$D_B \frac{\partial^2 C_B}{\partial x^2} = z k_2 C_A C_B \qquad (6.20)$$

D_A and D_B are the diffusivities of species A and B in the liquid phase and x is the distance from the interface. z is the number of moles of specie B reacting with one mole of specie A. At the gas liquid interface (x=0) the following boundary conditions apply:

$$C_A = C_{A,i} \qquad \text{and} \qquad \frac{dC_B}{dx} = 0 \qquad (6.21)$$

At the edge of the liquid film (x=d) the boundary conditions for component B is:

$$C_B = C_{B,b} \qquad (6.22)$$

The boundary condition for component A is more complicated since an amount of A reacts in the film while the rest is transferred through the film and reacts in the bulk of the liquid phase. According to Charpentier (Charpentier, 1981), the boundary condition for component A at the film edge is given by:

$$-D_A \left(\frac{dC_A}{dx} \right)_{x=\delta} = k_2 C_{A,b} C_{B,b} \left(\frac{h_t}{a} - \delta \right) \qquad (6.23)$$

where h_t is the liquid hold-up and a the specific interfacial area.

An analytical solution to Equations 6.19 to 6.23 is not possible and numerical techniques have to be resorted to. It is convenient to express the results in terms of an enhancement factor that is the ratio of the amount of gas absorbed in the presence of a chemical reaction to the amount absorbed in the absence of chemical reaction. The absorption rate in the presence of a chemical reaction may then be expressed as:

$$N_A = E k_L \left(C_{A,i} - C_{A,b} \right) \qquad (6.24)$$

where $C_{A,i}$ and $C_{A,b}$ are the concentrations of the reacting species at the interface and in the bulk of the liquid respectively. The numerical solution to Equation 6.19 to 6.23 may be expressed mathematically as (Charpentier, 1981, Danckwerts, 1970):

$$E = \frac{Ha\left[(E_i - E)/(E_i - 1) \right]^{0.5}}{\tanh\left\{ Ha\left[(E_i - E)/(E_i - 1) \right]^{0.5} \right\}} \qquad (6.25)$$

where Ha is the Hatta number defined by:

$$Ha = \frac{\sqrt{D_A k_2 C_{B,b}}}{k_L} \qquad (6.26)$$

and E_i is the limiting value of E for instantaneous reactions:

$$E_i = 1 + \left(\frac{D_B}{zD_A}\right)\left(\frac{C_{B,b}}{C_{A,i}}\right) \tag{6.27}$$

Different reaction regimes may be identified from the numerical solution. The different reaction regimes as given by Charpentier (Charpentier, 1981) are:

- Very slow reaction in the bulk of the liquid.
- Slow reaction in the bulk of the liquid
- Moderately fast reaction
- Fast reaction in the diffusion film

The reaction regimes may be explained with reference to Figure 6.1, where the enhancement factors are calculated with Equation 6.25 (Charpentier, 1981, Danckwerts, 1970).

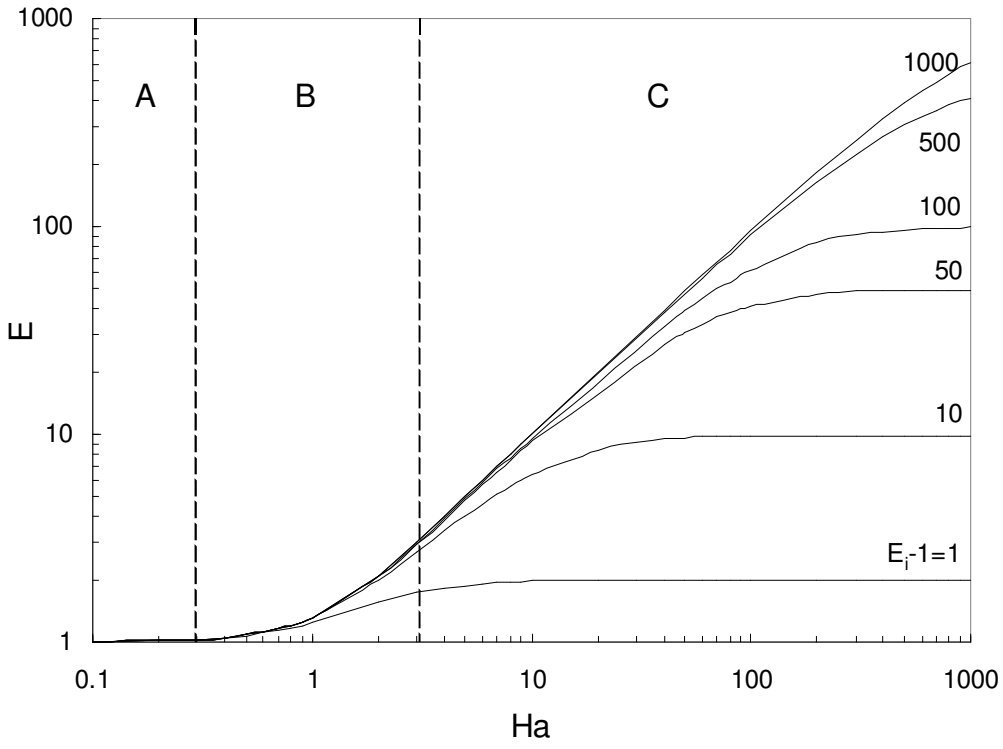

Figure 6.1 Enhancement factors for second order reactions as a function of Hatta number (Charpentier, 1981, Danckwerts, 1970)

For Ha < 0.02 (not shown in Figure 6.1), no reaction takes place in the liquid film next to the interface. The rate of adsorption of species A is entirely controlled by the chemical reaction rate. This corresponds to the 'Very slow reaction in the bulk liquid' regime (Charpentier, 1981). There is almost no change in the concentration of both species A and B in the liquid film next to the interface.

For 0.02 < Ha < 0.3, region A in Figure 6.1, a small amount of species A reacts in the diffusion film. The reaction takes place in the bulk of the liquid phase. There is a slight change in the concentration of species A across the liquid film next to the interface. This regime is termed the 'Slow reaction in the liquid phase'.

For 0.3 < Ha < 3.0, region B in Figure 6.1, a substantial amount of component A reacts in the liquid film. The concentration of component A is almost zero in the bulk of the liquid phase. This is the 'Moderately fast' reaction regime.

For Ha > 3.0 the entire reaction takes place in the liquid film next to the interface. This corresponds to region C in Figure 6.1 and is termed the 'fast reaction' regime. Two situations may now arise:

For 3 < Ha < $E_i/2$, the concentration of component B is much higher in the bulk of the liquid phase than the concentration of species A at the liquid interface. The enhancement factor (E) lies close to the limiting diagonal line in Figure 6.1 (E ≈ Ha). The kinetics of the reaction becomes pseudo first order with the reaction rate constant changing to:

$$k_1 = k_2 C_{B,b} \tag{6.28}$$

The diffusion rate of component B is sufficiently fast to prevent the reaction from causing significant depletion of component B at the interface. The concentration of species B at the interface is almost the same as in the bulk of the liquid phase. The absorption rate then follow fast psuedo-first-order kinetics. The liquid side mass transfer coefficient becomes irrelevant and the average absorption rate may be calculated from:

$$n_A = N_A a = a C_{A,i} \sqrt{D_A k_2 C_{B,b}} \tag{6.29}$$

This reaction regime forms the basis for measuring the interfacial area directly from the rate of absorption. The specific absorption rate should however be known.

For Ha > $10E_i$, the limiting value of E = Ei is reached (horizontal lines in region C in Figure 6.1). This situation arises when the concentration of reactant B is less than the solubility of the gas or the mass transfer rate of reactant B from the bulk of the liquid to the interface is low and the dissolved gas reacts instantaneously with component B. A reaction plane exists beneath the interface where the concentration of both species is zero. The rate of the reaction is completely determined by the rate at

which the components diffuse towards the reaction plane. This reaction regime forms the basis for measuring either $k_G a$ or $k_L a$.

The above results for a second order reaction may be generalized for an m,nth order irreversible reaction ($r_A=k_{m,n}C_A{}^m C_B{}^n$). The enhancement factor may be approximated by (Hikita and Asai, 1964, Charpentier, 1981, Danckwerts, 1970):

$$E = \frac{Ha\left[(E_i - E)/(E_i - 1)\right]^{n/2}}{\tanh\left\{Ha\left[(E_i - E)/(E_i - 1)\right]^{n/2}\right\}} \tag{6.30}$$

with the Hatta number defined as:

$$Ha = \left(\frac{1}{k_L}\right)\left[\left(\frac{2}{m+1}\right)k_{m,n}D_A C_{A,i}{}^{m-1} C_{B,b}{}^n\right]^{0.5} \tag{6.31}$$

and the enhancement factor for instantaneous reaction is the same as for second order reaction kinetics (Equation 6.27). If the reaction is fast and the concentration of reagent B does not change significantly through the film, the reaction is pseudo mth order with the rate constant given by:

$$k_m = k_{m,n} C_{B,b}{}^n \tag{6.32}$$

The condition that has to be satisfied for a pseudo mth order reaction is 1 << Ha << E_i. The average rate of absorption is then independent of k_L and given by:

$$n_A = N_A a = a\left\{\left(\frac{2}{m+1}\right)k_{m,n}D_A C_{A,i}{}^{m+1} C_{B,b}{}^n\right\}^{0.5} \tag{6.33}$$

When determining the reaction kinetics in the fast pseudo mth order regime, it is often necessary to dilute the soluble gas with an insoluble gas in order to satisfy the constraint on the Hatta number for the psuedo mth order regime (1 << Ha << E_i) (Charpentier, 1981, Danckwerts, 1970). Failure to do so will force the reaction into the instantaneous reaction regime with depletion of the reactant B in the film next to the interface. When diluting the soluble gas, gas side resistance to mass transfer may arise. For a pseudo mth order reaction in the liquid phase, the absorption rate is then given by (Charpentier, 1981):

$$n_A = N_A a = \frac{p}{\dfrac{1}{k_G a} + \dfrac{H}{a\left\{\left(\dfrac{2}{m+1}\right)k_{m,n}D_A C_{A,i}{}^{m+1} C_{B,b}{}^n\right\}^{0.5}}} \tag{6.34}$$

where k_G is the gas phase mass transfer coefficient, p the partial pressure of the soluble gas in the bulk gas phase and H the Henry's law constant.

In order to determine the interfacial area with the chemical technique, it is important that the chosen gas-liquid reaction system fall into the rapid pseudo m^{th} order reaction regime. In order to determine the reaction kinetics for a given gas-liquid reaction system, knowledge of some physicochemical parameters need to be obtained. These include the kinetics of the reaction, the diffusivities of the soluble gas and the reactant in the liquid phase and the solubility of the gas in the liquid. These parameters are usually not determined separately but combined into the terms (Charpentier, 1981, Danckwerts, 1970):

$$C_{A,i}\sqrt{D_A} \qquad \text{and} \qquad \left\{\left(\frac{2}{m+1}\right)k_{m,n}D_A C_{A,i}^{\,m+1} C_{B,b}^{\,n}\right\}^{0.5} \qquad (6.35)$$

For rapid pseudo first order reactions, it is possible to determine the reaction rate constant and the product of the solubility and the root of the diffusivity (the first term in Equation 6.35) from experimental absorption data. A so-called 'Danckwerts plot' is used (Danckwerts, 1970). For a reaction in the pseudo m^{th} order regime, it is not possible to determine these parameters separately from experimental absorption data. A neutral gas that have the same properties as the solute gas but that do not react with the reagent have to be used to determine the property $C_{A,i}(D_A)^{0.5}$. When determining interfacial area in a gas-liquid contactor, it is not necessary to determine the reaction kinetics and the physicochemical properties separately (Danckwerts, 1970, Charpentier, 1981). The specific absorption rate may be determined in a laboratory apparatus with a known interfacial area. The rapid pseudo m^{th} order reaction regime may be tested for by varying the contact time. If the absorption rate is independent of contact time, the reaction is suitable. If the solute gas is diluted with a non-absorbing carrier gas, gas phase resistance may arise. Steps may be taken to eliminate this resistance or it may be taken into account in the calculations. It is preferable to eliminate gas phase resistance all together and determine the interfacial area separately from k_G.

6.3.2 Laboratory apparatus for determining absorption rates

Various laboratory apparatus are used to determine absorption rates in gas-liquid reactions. The essential features of such an apparatus are the interfacial area for gas liquid contact and the contact time. There are a number of apparatus commonly used. These include (Danckwerts, 1970) the rotating drum absorber, the moving band absorber, the wetted-wall column, the laminar jet, the string of disks and the stirred vessel. The gas-liquid contact time may be varied over a wide range by using

a combination of these absorbers for a given gas-liquid reaction. In this study a wetted wall column absorber is used. The contact times obtained with a wetted wall column fall into the range of 0.1-2.0 seconds. This is close to the middle of the range obtained with the various devices. The choice of the wetted-wall column is also in part due to previous experience and existing laboratory equipment (Erasmus and Nieuwoudt, 2001). A detailed description of the column is given in the experimental section. The contact (or exposure) time of a liquid surface element to the gas phase is calculated from classical laminar falling film theory (Danckwerts, 1970):

$$t = \frac{h}{u_i} = \frac{2h}{3}\left(\frac{3\mu_L}{g\rho}\right)^{1/3}\left(\frac{\pi d}{V_L}\right)^{2/3} \qquad (6.36)$$

where h is the height of the column, d the diameter of the column and V_L the volumetric liquid flow rate.

Reaction mechanism between monoethanolamine (MEA) and CO_2

The stoichiometric reaction between carbon dioxide and monoethanolamine in aqueous solution may be expressed as (Danckwerts, 1979, Sada et al., 1985):

$$CO_2 + 2RNH_2 \rightarrow RNHCO_2^- + RNH_3^+ \qquad (6.37)$$

where R represents HO-CH_2-CH_2-. The reaction is first order with respect to both carbon dioxide and monoethanolamine and overall second order (Danckwerts, 1979, Sada et al., 1985, Alvarez-Fuster et al., 1980). The proposed reaction mechanism involves two steps (Danckwerts, 1979). In the first step a 'zwitterion' is formed:

$$CO_2 + RNH_2 \rightarrow RNH_2^+COO^- \qquad (6.38)$$

This is followed by the removal of a proton by a base B:

$$RNH_2^+COO^- + B \rightarrow RNH^+COO^- + BH^+ \qquad (6.39)$$

In aqueous medium the base may be H_2O, OH^- or the amine itself. The second step is rate determining (Danckwerts, 1979). When the reaction takes place in an alcoholic medium, the deprotonation of the 'zwitterion' is depressed. The rate of the deprotonation step (Equation 6.39) decreases relative to the rate of the reverse reaction (equation 6.38) (Versteeg and Van Swaaij, 1988). The alcohol solvent is not able to produce the 'zwitterion' in complete ionic form and it is less stable. The overall reaction order then increases from 2 up to 3 (Versteeg and Van Swaaij, 1988). With a steady state approximation of the 'zwitterion', the rate of the reaction may be expressed as (Sada et al., 1985):

$$r = \frac{C_A C_B}{\frac{1}{k_1} + \frac{k_2}{k_1 k_3 C_B}} \qquad (6.40)$$

where B represents the amine and A carbon dioxide.

In this work the absorption rates were measured and used as is to determine the interfacial area in structured packing by the method discussed in the preceding section as recommended by Danckwerts (Danckwerts, 1970) and Charpentier (Charpentier, 1981). The rate constants were therefore not determined.

6.4 Experimental

6.4.1 Experimental setup

Wetted-wall column

The wetted-wall column was constructed using the guidelines as suggested by Roberts and Danckwerts (Roberts and Danckwerts, 1962). The final design reflected ideas obtained from the designs of Roberts and Danckwerts (Roberts and Danckwerts, 1962) and Davies et al. (Davies et al., 1967). The wetted-wall column is shown in Figure 6.2. The column is made from stainless steel pipe with an outside diameter of 25.1mm. The length of the column could be varied between 60mm and 120mm by extending or collapsing it into the outlet section. The liquid is distributed around the circumference of the tube by a special cap. The cap fits tightly over the top 10mm of the wetted-wall column. This is followed by a 5 mm section that is machined to a diameter of 28mm. The liquid enters this section through 12 evenly spaced holes around the circumference of the wetted wall column. This is followed by a section in the cap that has an inside diameter of 25.8mm, thus forming an annular gap of 0.35mm for the liquid to pass through. After passing through this annular passage (length approximately 15mm), the liquid finally free falls down the outside of the tube where contact with the gas phase is made. At the bottom of the column the liquid exits through a special receiver (also called an exit collar (Roberts and Danckwerts, 1962)) that channels the liquid into 3 grooves (width 3mm) and finally into the exit annular passage formed between the bottom part of the wetted-wall column and the base section. The base section screws into a stainless steel flange. The column is enclosed by a special glass QVF 3" pipe section bolted onto the flange. The flange is equipped with the gas inlet and gas outlet pipes and a drainpipe in case of spillage. It is also equipped with three holes for threaded rod that is used to

level the column with the horizontal axis. The exit collar is included in the design because it prevents a stagnant film from developing at the bottom of the column (Roberts and Danckwerts, 1962). This stagnant film reduces the absorption rate in this part of the column. Roberts and Danckwerts (Roberts and Danckwerts, 1962) found that using an exit collar could reduce this error. The stagnant film is then confined to the exit grooves of the collar. The liquid surface area in the grooves is small compared to the rest of the wetted-wall column and may safely be ignored.

Figure 6.3 shows a flow diagram of the experimental setup. The whole wetted-wall column assembly is submerged into a thermostat controlled water bath to ensure isothermal operation. The air is routed through a coil submerged in the water bath and the flow rate is controlled by a regulating valve. The flow rate is measured with a soap bubble meter that is also submerged into the water bath. It is then saturated with the solvent and mixed with carbon dioxide. The carbon dioxide flow rate is controlled through a regulating valve. The air/carbon dioxide mixture may either be passed through the wetted wall column and then to the carbon dioxide analyser, or it may bypass the column and flow directly to the carbon dioxide analyser. The desired carbon dioxide concentration is obtained by bypassing the column and regulating the inlet pressure of the carbon dioxide until the desired concentration is obtained. Care is taken to ensure the same pressure drop through the system when the gas mixture is routed through the column assembly or when bypassing it and flowing directly to the carbon dioxide analyser. This is done to ensure a constant air and carbon dioxide flow rate. The air/carbon dioxide/solvent mixture passes through a cold trap to condense as much of the solvent as possible before entering the analyser. The liquid is fed from a container elevated above the experimental setup to obtain gravity flow through the system. The flow rate is measured with a rotameter and controlled with a needle valve. It passes through a coil submerged in the water bath before entering the base of the wetted wall column. After exiting from the base section it flows over a constant height overflow that is used to control the liquid level in the base section just underneath the 'exit collar'. The constant height overflow may be bypassed by opening a drain valve to drain the liquid in the base section. The height of the column may be varied by disconnecting the liquid feed line at the base and sliding the column up or down through a tube fitting at the bottom of the base section. All the materials in contact with the liquid are either stainless steel or PTFE for corrosion resistance. PTFE ferrules are used at the base of the column to facilitate repeated lengthening and shortening of the column.

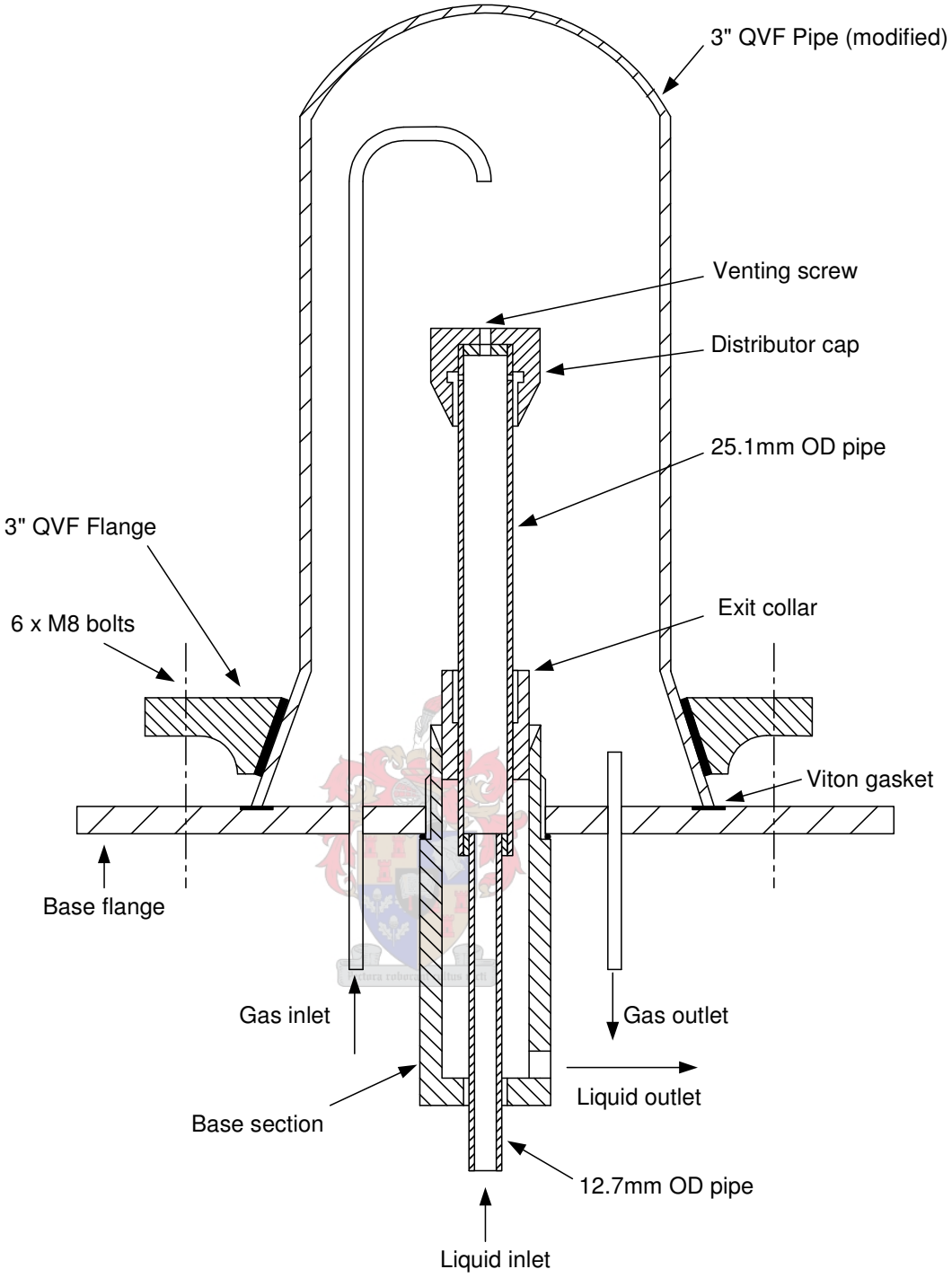

Figure 6.2 Wetted-wall column

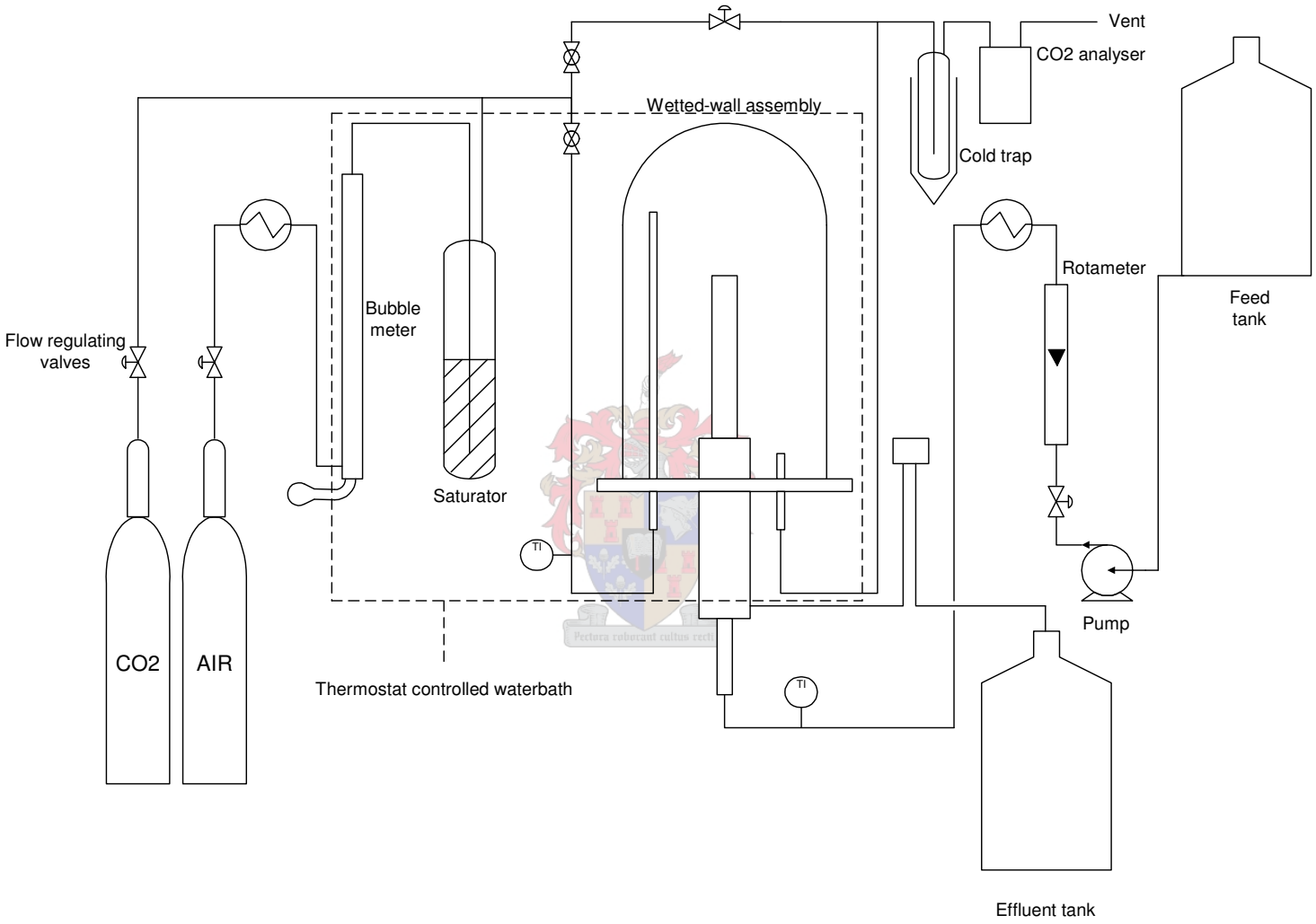

Figure 6.3 Wetted-wall flow diagram

Pilot plant

The pilot plant used in determining the effective surface area is to a large extent the same as described in Chapter 4 and is shown in Figure 6.4. The column contains two packed beds with a chimney tray between them. The desired airflow rate is obtained by throttling the intake to a centrifugal blower. The flow rate is measured with a square-edged orifice plate. Carbon dioxide is mixed with the incoming air before entering the bottom packed bed. Liquid carbon dioxide is drawn from a cylinder with a dip tube. It is heated up to approximately 70°C before evaporating in the regulator that also controls the flow rate. In the lower packed bed the air is saturated with the solvent. The solvent is circulated in a closed loop and replenished from time to time. The temperature of the air after the saturation bed is controlled with the temperature of the recirculating solvent. The solvent is heated with an electric heater. The air/carbon dioxide mixture enters the second packed bed through a chimney tray. The absorption of CO_2 into the monethanolamine/alcohol solution takes place in this bed. The liquid solution is pumped from a storage vessel through a rotameter and a heat exchanger to the top of the column. It is distributed evenly over the packed bed with the distributor described and shown in Chapter 4. Liquid is drawn from the chimney tray through a constant height overflow. The constant height overflow may also be changed to operate as a liquid siphon draw. This is done at high liquid flow rates in order to prevent the chimney tray from overflowing. The loaded liquid then flows under gravity to a storage vessel. The temperature of the air/carbon dioxide mixture and the MEA/alcohol mixture is measured on entering and on exiting the absorption section. Gas sampling points are provided before and after the absorption section. The gas sample stream flows through a cold trap to condense as much of the solvent possible before entering the CO_2 analyser. The air/carbon dioxide/solvent mixture from the top of the column is vented to the outside of the building.

The liquid from the absorption column is regenerated and recycled. This operation is performed in a glass distillation column with a diameter of 200mm that is operated as a reboiled stripper. The column contains four beds of structured packing (Flexipac 250Y HC) with the feed entering at the top. All the overhead vapour is condensed and returned back to the top of the column. Regenerated liquid is drawn from the reboiler and flows through a cooler under a nitrogen blanket to a storage vessel. Because of the low cooling capacity of the bottom product cooler, the whole absorption/regeneration cycle has to be performed in batch cycles.

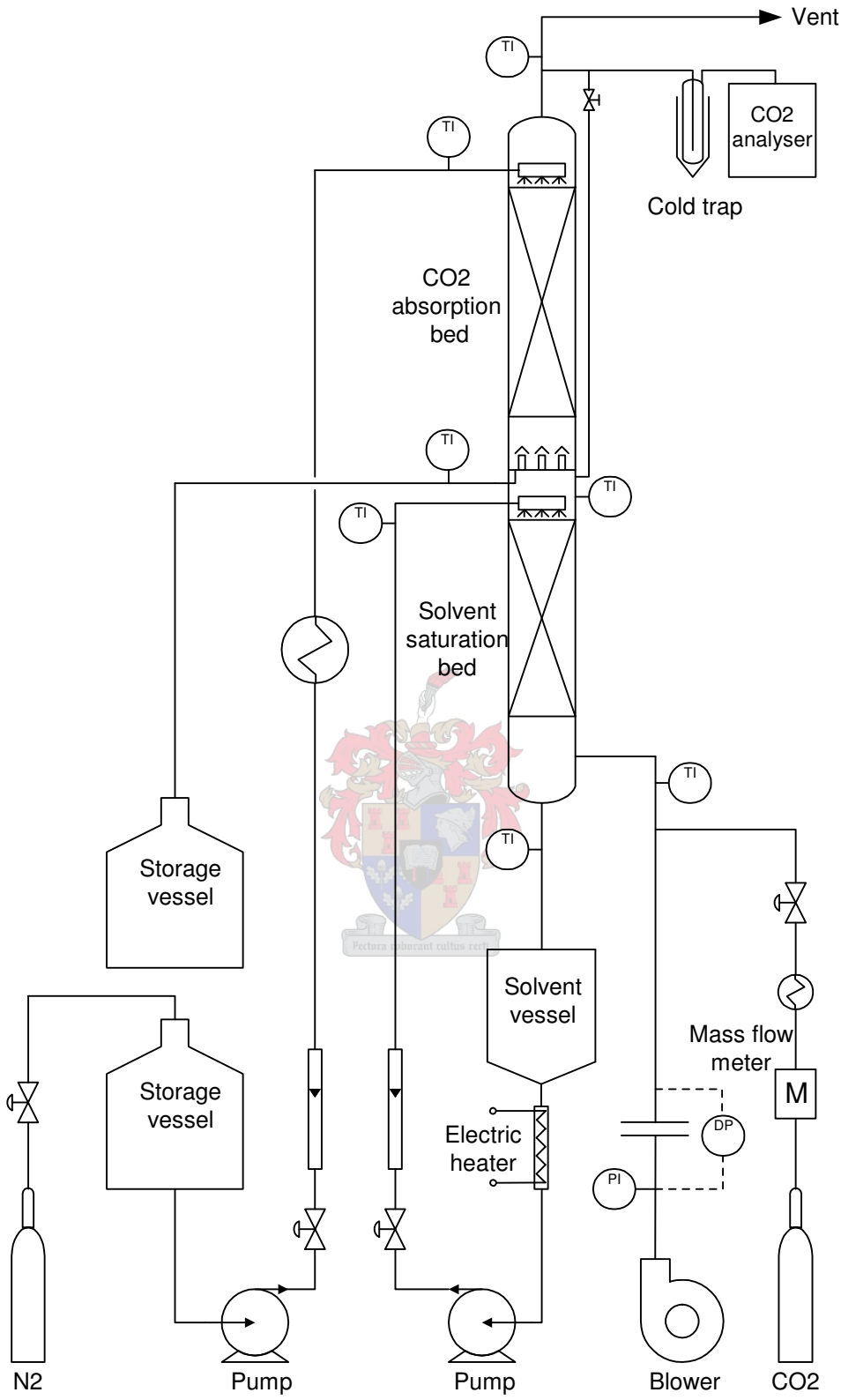

Figure 6.4 PFD of pilot plant absorption column

6.4.2 Experimental procedure

Wetted-wall column

Before doing absorption experiments in the wetted wall column reactor, a residence time distribution experiment was performed. The RTD curve obtained corresponded to that of a CSTR and the gas phase could thus be assumed to be well mixed. The concentration of carbon dioxide in the exit gas stream is therefore equal to the bulk concentration of carbon dioxide in the reactor.

Before the start of an experiment, the wetted wall column reactor was flushed with air at the desired flow rate. The bulb of the soap bubble meter was then removed and a manometer was used to measure the pressure at the base of the soap bubble meter. The wetted-wall reactor was then bypassed and the balancing valve on the outlet line adjusted until the same pressure was measured at the base of the soap bubble meter. The manometer was removed and replaced with the bulb with soap solution. Carbon dioxide was now added and the flow rate adjusted until the desired concentration in the exit stream was obtained. The airflow rate was now measured. The air/carbon dioxide mixture was then routed through the reactor. The airflow rate was again measured to make sure that it was the same as when bypassing the reactor. Sufficient time was allowed for the exit stream carbon dioxide concentration to reach the inlet stream concentration. The liquid feed was introduced and adjusted to the desired flow rate. The outlet concentration of carbon dioxide was monitored until a steady value was reached. The temperatures of the liquid feed and air/carbon dioxide/solvent gas feed as well as the pressure inside the reactor were recorded together with the flow rates and carbon dioxide concentrations. The liquid feed mixture was made up before the start of a series of experiments. The 'loaded liquid' was regenerated before being used again. This was achieved by distillation under a slightly reduced pressure at total reflux for approximately half an hour. The mixture was then left to cool under a nitrogen blanket. After sufficiently cooling down, the liquid was transferred to airtight bottles.

A problem encountered when using a wetted-wall column is the formation of ripples in the bottom part of the column (Danckwerts, 1970, Roberts and Danckwerts, 1962). These ripples were found to enhance absorption rates of soluble gases into a falling film (Emmert and Pigford, 1954, Stirba and Hurt, 1955). A common method to eliminate these ripples is to add an amount of surface active agent to the feed (Danckwerts, 1970, Roberts and Danckwerts, 1962, Sada et al., 1985). Two

surfactants were tested in this study. The agent used by Sada et al. (Sada et al., 1985), Tween 80 (polyoxyethylene solbitan monoleate), was successful in eliminating the ripples. There were however some concerns when using this surfactant. The quantity suggested by the authors had to be doubled in order to obtain a ripple free surface. This may give rise to a surface resistance that will influence the absorption rate (Roberts and Danckwerts, 1962). When regenerating the CO_2 loaded solution, the surfactant was found to be thermally labile. The common surfactant Triton 100 was also used but did not suppress the formation of ripples. Another method to eliminate the ripples is to work with short column lengths. Because of the problems encountered with the addition of a surfactant, only short column lengths were used in this study (maximum length of 90mm).

Pilot plant

Before doing absorption experiments on the structured packing, the packing was thoroughly washed with an acetone/alcohol mixture to rid it of any dirt and oil used in the manufacturing process. The liquid feed was made up beforehand and left under a nitrogen blanket to prevent atmospheric carbon dioxide from being absorbed.

With the start of an experiment the blower was switched on and throttled until the desired flow rate was obtained. Carbon dioxide was mixed with the air and the flow rate adjusted until the desired concentration was obtained. The use of the carbon dioxide analyser and the mass flow meter also enabled the accuracy of the orifice plate to be measured. The error in the flow rate measured with the orifice plate was calculated to be less than 5%. The solvent was then introduced into the saturation bed and the temperature adjusted until the desired exit temperature of the air/carbon dioxide/solvent mixture was obtained. This temperature could be controlled to be within 3^{o}C of the liquid feed. The liquid feed was then introduced into the absorption bed. The flow rates and temperatures of all the inlet and exit streams were noted, as well as the pressure inside the column. The concentration carbon dioxide in the inlet and outlet gas streams was then measured. The absorption rate was measured at different liquid loads for the same gas load by altering the liquid feed rate. The amount of liquid feed was sufficient for the absorption rate to be measured at four different liquid loads before regeneration. This corresponded to the total amount of measurement at a specific gas flow rate. After regeneration the feed liquid was left to cool down overnight under a nitrogen blanket.

Analysis

There are a few methods commonly used determine the loading of CO_2 in amines in aqueous media (Shahi et al., 1994). In the volumetric method sulphuric acid is added to a known amount of loaded sample and the amount of evolved CO_2 is measured. With the wet chemistry method the CO_2 in the sample is precipitated by adding a $BaCl_2$ solution to the sample. The precipitate may then either be weighed or dissolved in water and titrated against a standard acid solution. These methods were however found to be tedious and not accurate when the CO_2 loading is low (Shahi et al., 1994). The extension of these methods to organic media is difficult. One of the main difficulties is the formation of two liquid phases when titrating against a standard acid or base. A GC technique was recently developed (Shahi et al., 1994) where the CO_2 loading and concentration of amine could be determined simultaneously. The methods uses a Tenax GC column with a TCD detector. The CO_2/amine complex (also called a carbamic acid) is thermally unstable and decomposes in the injector port (Alvarez-Fuster et al., 1981) (Shahi et al., 1994). The main difficulty is calibration for CO_2. The method was tested in this study, but no reproducible calibration results could be obtained to determine CO_2 content. Because of the difficulty and inaccuracy of determining the CO_2 content of the liquid phase, only the gas phase was analysed for CO_2 concentration. The GC technique was used to determine the CO_2 content in the feed samples qualitatively after regeneration. The regeneration column was operated in such a manner (low feed rate, high boil-up rate) that there was no CO_2 detectable in the GC chromatogram. The feed was kept in a closed container under a nitrogen blanket to eliminate the possibility of absorbing atmospheric CO_2. The concentration of the amine in the liquid phase was determined with the GC technique. For the wetted-wall experiments the concentration was determined by weighing the reagents.

The CO_2 concentration in the gas phase was measured with an infrared carbon dioxide analyser (Dräger Multiwarn Multi-Gas Monitor equipped with an infrared CO_2 sensor).

6.5 Results and discussion

Both n-propanol and n-butanol were identified as possible solvents. Problems were, however, encountered with the analysis of n-butanol liquid samples in the preliminary stages of the investigation. This was mainly due to immiscible phases forming when using titration with a standard acid to determine MEA content. No separation

between MEA and n-butanol could be obtained in the Tenax GC column. Separation between MEA and n-propanol could be obtained with this column and the use of n-butanol as solvent was subsequently abandoned in favour of n-propanol. The physical properties for the system MEA/n-propanol are given in Appendix E. The density and viscosity dependence was found to be the same as determined by Alvarez-Fuster et al. (Alvarez-Fuster et al., 1981) for the system MEA/ethanol.

6.5.1 Experimental determined absorption rates

The rate of absorption of CO_2 into MEA with n-propanol as solvent was determined with the wetted-wall column reactor described in the previous section. When diluting the solute gas (CO_2) with a carrier gas (air) as was done in this study, gas phase resistance to mass transfer may arise. This resistance may be eliminated by working at high gas flow rates with a subsequent small change in the inlet and outlet concentrations of CO_2 (Danckwerts, 1970). There should however still be a large enough difference between the inlet and outlet concentration to accurately determine the amount absorbed in the liquid phase, since in this study the liquid phase was not analysed for CO_2 content. High absorption rates with a significant resistance in the gas phase were encountered at high concentrations of MEA (0.5-1.0 mol/dm^3) and large CO_2 partial pressures (2.0-5.0 kPa). The experimental setup could not be converted to facilitate large enough airflow rates to eliminate gas phase resistance. The absorption rates were therefore determined at the highest MEA and CO_2 concentrations possible with the experimental setup without substantial gas phase resistance. This corresponded to a maximum MEA concentration of 0.3 mol/dm^3 and a maximum CO_2 partial pressure of 1.2 kPa. The absorption rates were determined at two temperatures, 288K and 303K. This was done because the pilot plant experiments were performed at ambient conditions and the ambient temperature varied in this range. The contact time was varied by working with wetted-wall column heights of 60 mm and 90 mm and using liquid flow rates of 1.0 cm^3/s and 1.6 cm^3/s. For the reaction to be in the pseudo m-nth order regime, the absorption rate must be independent of the contact time. Figure 6.5 show the specific absorption rate at different contact times for a MEA concentration of 0.3 mol/dm^3 at a temperature of 288 K. The figure shows that the absorption rates are practically the same at different contact times. The marginally higher specific absorption rates at lower contact times are within the experimental error. These errors are mainly due to the resolution of the infrared CO_2 analyser (0.01 vol% CO_2) and the adjustment of the column length (±1mm). Figure 6.6 show the specific absorption rates as a function of the CO_2 partial

pressure at different MEA concentrations (T=288 K). The absorption rate increases as the amine concentration increases.

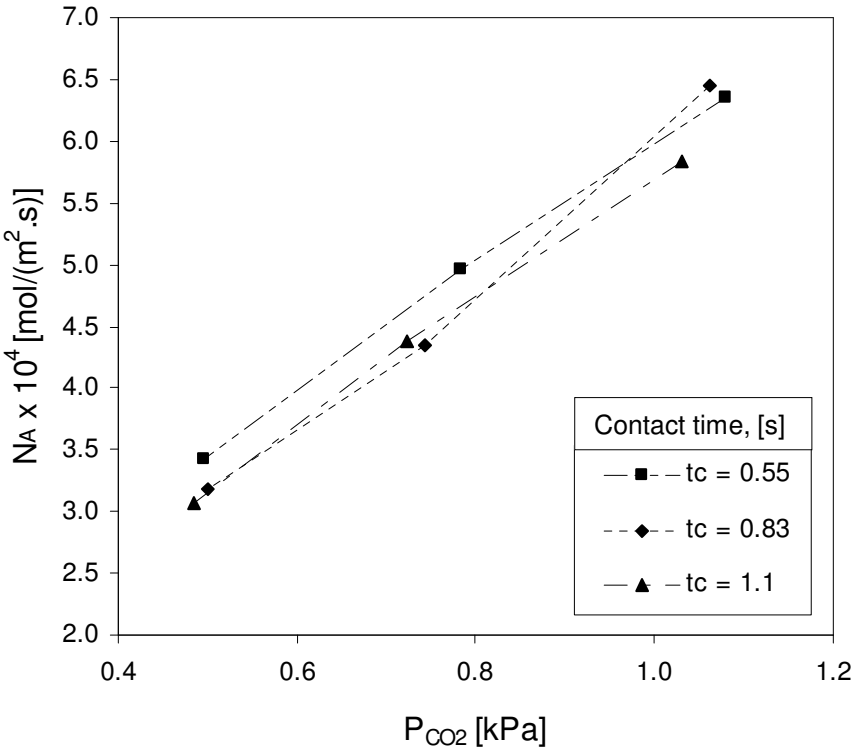

Figure 6.5 Verification of pseudo m,nth order reaction. C_{MEA}=0.3 mol/dm3, T=288K.

Figure 6.7 show the specific absorption rates at 288 K and 303 K for a MEA concentration of 0.2 mol/dm^3. The absorption rate is higher at the lower temperature. At low CO_2 partial pressures (<0.5 kPa) the absorption rate is almost the same at 288 K and 303 K.

The experimental determined absorption rates were correlated with a power law series with amine concentration (C_B) and CO_2 partial pressure (P_A) as variables:

$$N_A = kP_A{}^m C_B{}^n \qquad (6.41)$$

Equations similar to that proposed by Sada et al. (Sada et al., 1985) (Equation 6.40) and Alvarez-Fuster et al. (Alvarez-Fuster et al., 1980) for the reaction rate did not result in a better fit. Equation 6.41 was preferred because it contains only a single constant (k) instead of the two constants in the rate equations of Sada et al. (Equation 6.40) and Alvarez-Fuster et al.

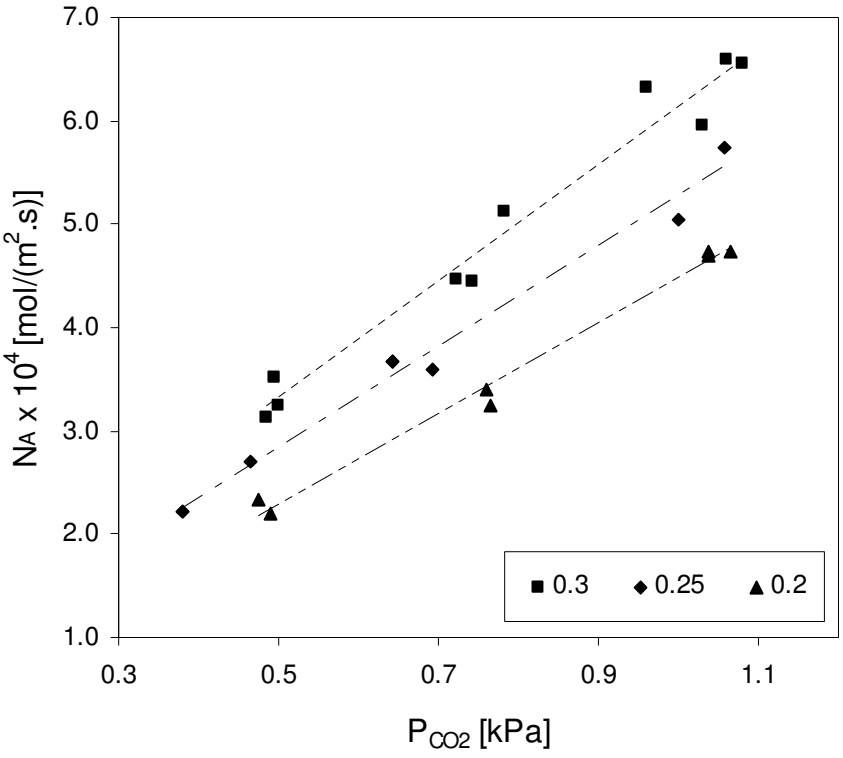

Figure 6.6 Specific absorption rates for MEA concentrations of 0.3, 0.25 and 0.2 mol/dm^3 (T=288K).

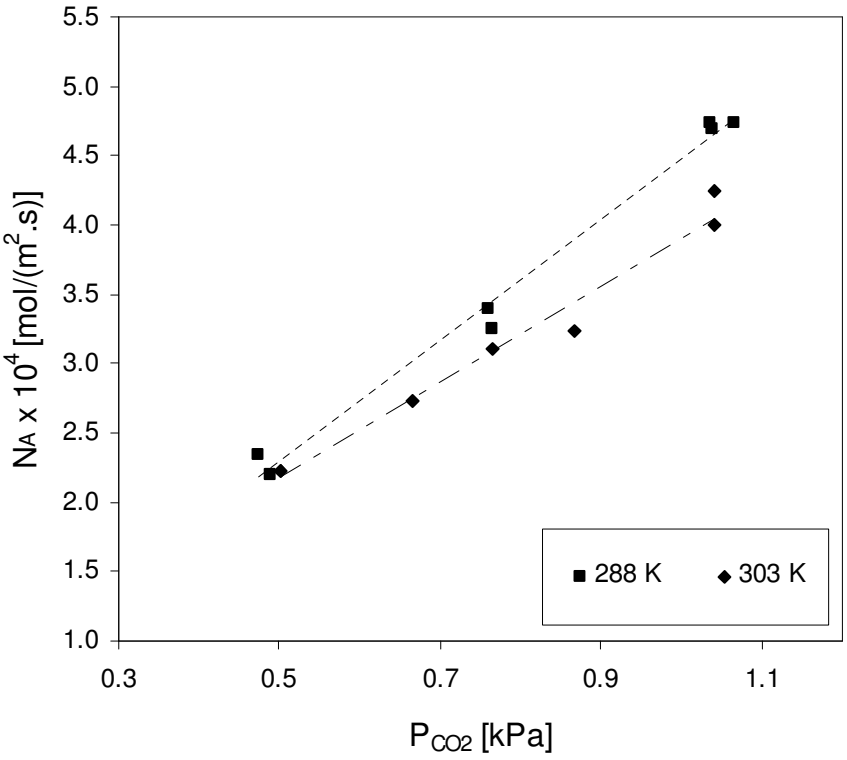

Figure 6.7 Temperature dependence of specific absorption rate. MEA concentration 0.2 mol/dm^3.

Because of the small difference in the absorption rates at 288 K and 303 K (see Figure 6.7), and the measurement of absorption rates at only two temperatures, a linear dependence on temperature is assumed in this study, and not the Arrhenius equation commonly used (Danckwerts, 1970). The best fit through the experimental data was obtained with:

$$N_A = kP_A^{0.9}C_B^{0.93} \tag{6.42}$$

with k being temperature dependent:

$$k = -3.818\times10^{-6}T + 2.985\times10^{-3} \tag{6.43}$$

Figure 6.8 and 6.9 show the absorption rates predicted by Equation 6.42 and 6.43 at 288 K and 303 K respectively.

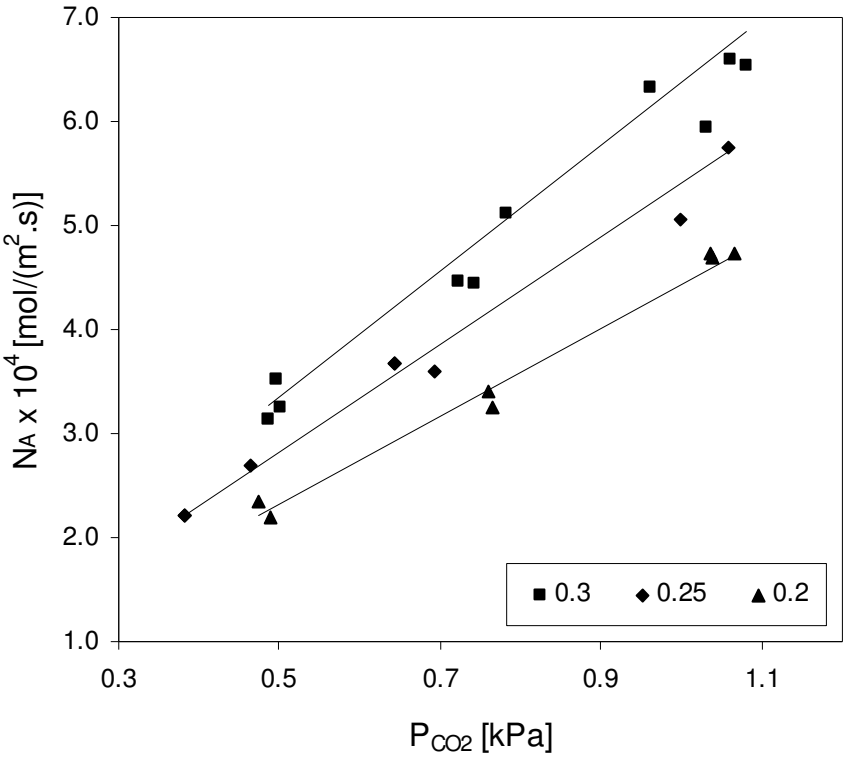

Figure 6.8 Experimental absorption rates compared to that predicted by Equation 6.42, T = 288K. r^2=0.98. MEA concentrations of 0.3, 0.25 and 0.2 mol/dm^3

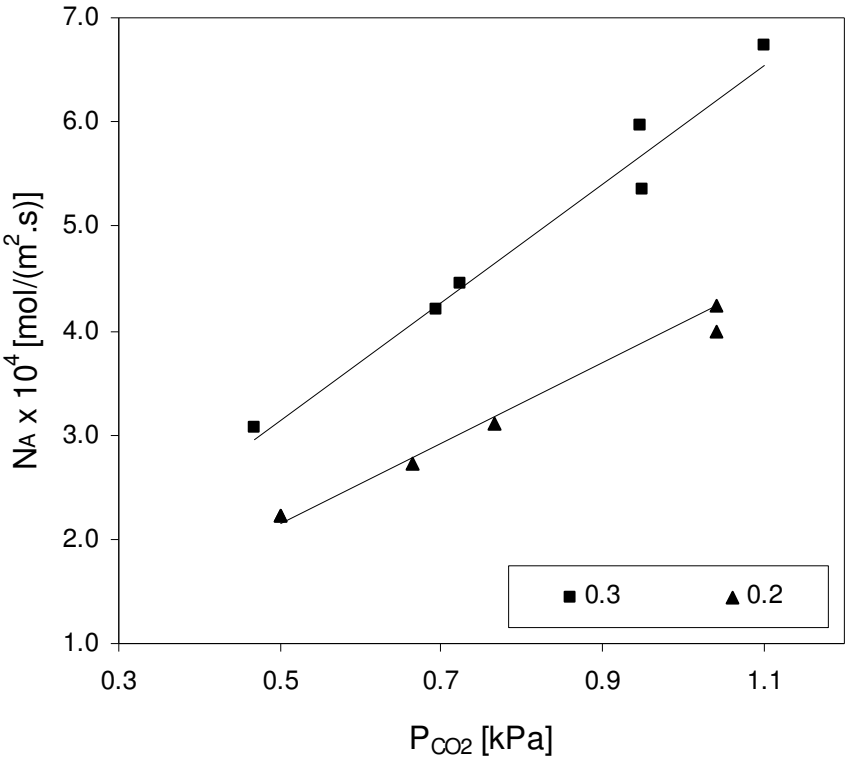

Figure 6.9 Experimental absorption rates compared to that predicted by equation 6.42, T = 303K. r^2=0.96. MEA concentrations of 0.3 and 0.2 mol/dm^3

6.5.2 Effective surface area of Fexipac 350Y

The same batch of solvent and reagent used in the wetted-wall reactor was also used in the pilot plant to determine the effective surface area of Flexipac 350Y. This eliminated the possibility of impurities in either the solvent or the reagent influencing the absorption rate. A mole balance for the solute gas around a differential packing section of height dz, yields the following equation for the amount of solute gas absorbed:

$$Vdy = a_e N_A A_s dz \qquad (6.44)$$

where V is the molar gas flow rate, y the mole fraction of CO_2 in the gas phase, a_e is the effective surface area, h the height of the absorption bed and A_S the cross sectional area of the column. The absorption rate changes between the top and the bottom of the absorption bed because the CO_2 partial pressure and amine concentration vary between the inlet and the outlet. The total amount of CO_2 absorbed may be calculated from:

$$n_A = \int_{z=0}^{z=h} a_e N_A A_s dz \qquad (6.45)$$

If it is assumed that gas phase resistance is negligible, N_A may be calculated with Equation 6.42. If it is assumed that the effective surface area is uniform throughout the bed, then it may be calculated from:

$$a_e = \frac{n_A}{A_s \int_{z=0}^{z=h} N_A dz} \qquad (6.46)$$

In the pilot plant experiments the amount of CO_2 absorbed was calculated by doing a mole balance on the gas phase. This determined the absorption rate (n_A). The integral in Equation 6.46 was calculated numerically. A linear profile was assumed for the amine concentration and the CO_2 partial pressure over the height of the absorption bed. An average temperature was calculated from the inlet and outlet temperatures of the liquid and vapour phases and used to determine the constant k (Equation 6.43). This is a reasonable assumption since the average difference between the largest and smallest temperature was only 2.5°C for all the experimental data points. The effective surface area calculated from Equation 6.46 and the measured absorption rates is shown in Figure 6.10 as a function of liquid load at different gas phase load factors (F_G). The experimental results are given in tables in Appendix E.

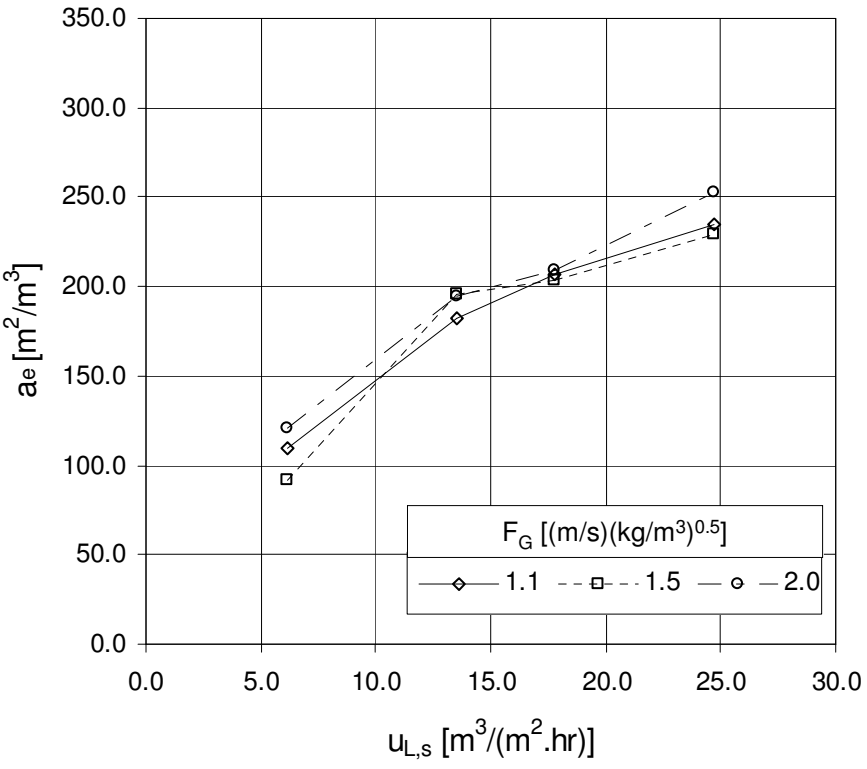

Figure 6.10 Effective surface area as a function of liquid load for Flexipac 350Y.

If there is a significant resistance in the gas phase, this would result in large differences between the effective surface area calculated at different vapour flow rates (load factors). Figure 6.10 clearly show that there is only a small difference in the effective surface area determined at the different vapour load factors. The assumption of negligible gas phase resistance is therefore valid.

Sensitivity analysis

Because of the relative small difference in the CO_2 concentration between the inlet and exit of the absorption bed, the main source of experimental error is the accuracy of the infrared CO_2 analyser. Another error that may influence the results obtained is the measurement of the airflow rate. The accuracy of the orifice plate was determined as follows. The CO_2 flow rate was adjusted to a relative large value and the concentration in the exit stream measured with the CO_2 analyser. From this value the air flow rate was back calculated and compared with the value calculated from the pressure drop over the orifice plate. The difference between the two values was 5%. This would translate into a difference of ±5% in the amount of CO_2 absorbed and subsequently to a ±5% difference in effective surface area shown in Figure 6.10.

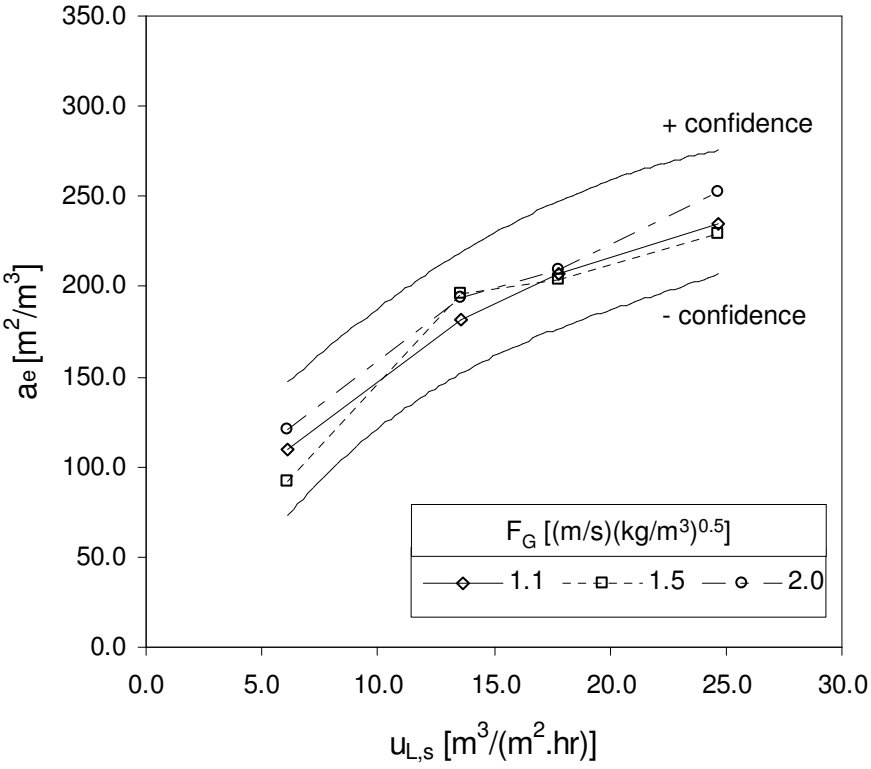

Figure 6.11 Experimental data plotted with upper and lower confidence limits

The sensitivity of the effective surface shown in Figure 6.10 to the accuracy of the infrared CO_2 analyser was determined as follows. The resolution of the digital display

(0.01vol%) was added to or subtracted from the difference between the inlet and outlet concentrations. This resulted in a difference in the calculated effective surface area of ±6% at the highest absorption rate and ±15% at the lowest absorption rate. The experimental error at the lowest absorption rate ($u_{L,s}$ ≈ 6.0 $m^3/(m^2.hr)$) is therefore in the order of 20% while at the highest liquid load it is in the order of 10%. These confidence limits are plotted with the data in Figure 6.11.

6.5.3 Comparison with existing correlations

The experimentally determined effective interfacial area is compared with that calculated from the correlations and methods discussed in Section 6.2 in Figure 6.12.

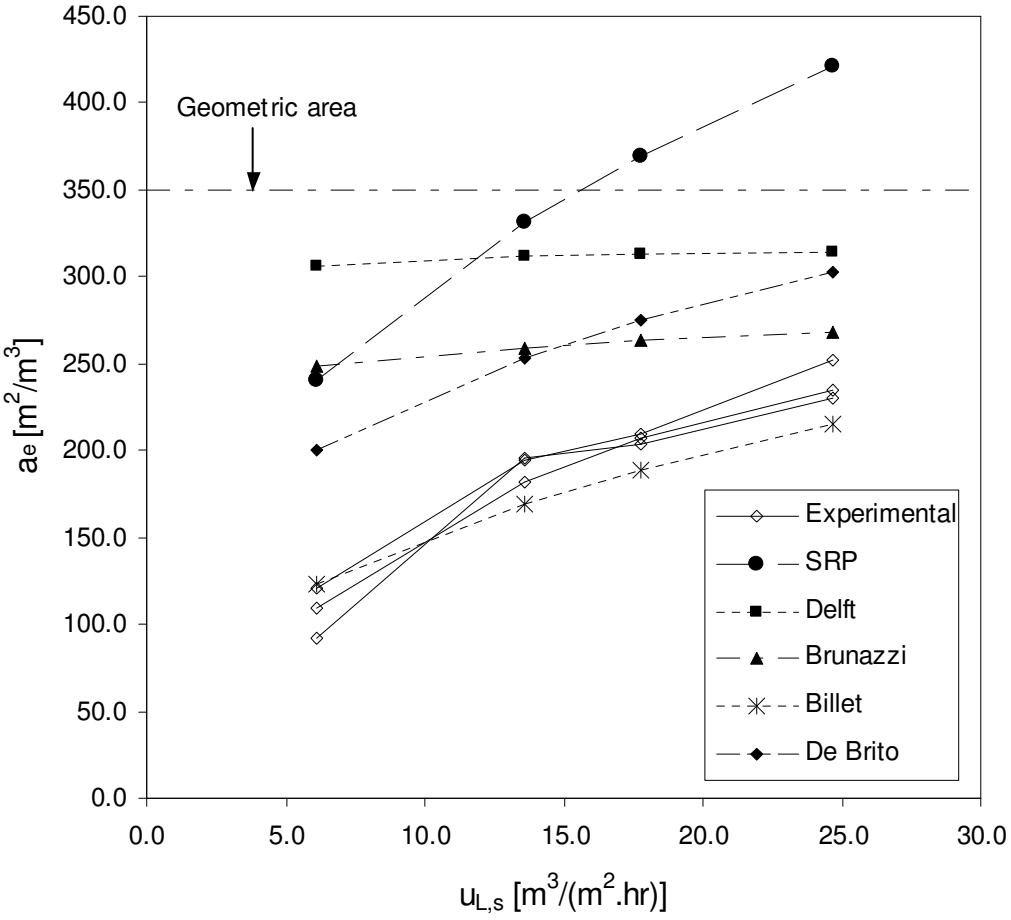

Figure 6.12 Comparison between experimental determined effective interfacial area and correlations proposed in literature.

Figure 6.12 show that most correlations proposed in literature are rather optimistic in their prediction of the effective interfacial area. The SRP model (Fair et al., 2000, Rocha and Bravo, 1996) predicts an effective interfacial area larger than the geometric area at liquid loads above $u_{L,s}$=16 $m^3/(m^2.hr)$. It does however predict the right trend and slope and it would seem that there is an almost constant ratio

between the effective surface area obtained with their correlation and the experimental values obtained in this study.

The correlation of De Brito et al. (De Brito et al., 1994) should predict an effective surface area larger than the geometric area. In their experimental results on the absorption of CO_2 into aqueous NaOH solutions, the effective surface area was found to be larger than the geometric area by a factor of between one and two. The liquid Reynolds number (Re_L) was used in their correlation (Equation 6.11) Extrapolation of this correlation to the higher viscosity liquid used in this study, resulted in the predicted effective surface area being lower than the geometric area. Although the predicted values are closer to the experimental values, it emphasizes the dangers of extrapolating correlations outside the physical properties of the system that it was fitted on. It may be argued that liquid viscosity does have an influence on the effective interfacial area. The much lower effective interfacial area measured by Weimer and Schaber (Weimer and Schaber, 1997) for the same packing used by De Brito et al. with the same test system (same liquid viscosity) nullifies this argument. It raises serious concerns as to the accuracy of the results obtained by De Brito et al. (see Section 6.2).

In calculating the effective surface area according to the correlation proposed by Olujic (Olujic et al., 1999) (Equation 6.14) in the 'Delft' model (Fair et al., 2000), the same constants were used for Flexipac 350Y as proposed for Montzpak B1-250 (Equation 6.15). In the absence of any values published for Flexipac 350Y, this is thought to be appropriate since the ratio of effective interfacial area to geometric area is calculated with the correlation (Equation 6.14). The correlation predicts a flat profile for a_e for the liquid load range ($u_{L,s}$=6-25 $m^3/(m^2.hr)$) investigated in this study. The predicted effective interfacial area is about 90% of the geometric area (see Figure 6.12). This is in contrast with the experimental results that show an increase in a_e with an increase in $u_{L,s}$.

The correlation proposed by Brunazzi et al. (Brunazzi et al., 1995) (Equation 6.10) also predicts a flat profile for the effective interfacial area. The liquid hold-up in this correlation is calculated with the correlation by Suess et al. (Suess and Spiegel, 1992) as proposed by the authors. Although the calculated values of a_e are closer to the experimental values, the trend of an increase in a_e with an increase in $u_{L,s}$ is not predicted.

The correlation proposed by Billet (Billet, 1995) for the effective interfacial area below the loading point (Equation 6.1) is remarkably close to the experimental determined values (see Figure 6.12). It falls within the confidence limits of the experimental results. The curve shown in Figure 6.12 is for a vapour load factor of F_G=1.1 [(m/s).(kg/m^3)$^{0.5}$]. Practically the same curve is obtained at a vapour load factor of F_G=1.5. At the highest vapour load factor (F_G=2.0), the hydraulic model of Billet (see Chapter 4) predicts the packing to be operating in the loading region. The effective interfacial area has to be calculated with Equations 6.1 to 6.3. This results in a drastic increase in the effective surface area. This drastic increase is however not reflected in the experimental results.

6.5.4 Correlation of experimental results

In this study the transport properties of the liquid phase were not varied. The results could therefore only be correlated in terms of the liquid load ($u_{L,s}$). Using the liquid Reynolds number to correlate the data with would severely limit the use of the correlation, as demonstrated by the results obtained with the correlation of De Brito et al. From the comparison of existing correlations with the experimental data, it would seem that the correct trends are predicted by the SRP correlation and the correlation by Billet. The correlation by Billet is remarkably accurate in predicting the experimental results. More experimental data on the effective surface area using the chemical method are however necessary in order to verify the dependency of the effective surface area on the liquid transport properties as suggested by the correlation of Billet and the correlation in the SRP model.

Figure 6.10 shows the increase in effective surface area follows a logarithmic trend with an increase in the liquid load. This is to be expected since at an almost zero liquid load very little of the packing will be wetted. At high liquid loadings almost all of the geometric area of the packing will be wetted. All the geometric area will not be effective for gas phase mass transfer. The effective surface area will therefore approach the geometric area asymptotically with an increase in the liquid load. The ratio of the effective surface area to the geometric surface area was therefore correlated with the following logarithmic relationship:

$$\frac{a_e}{a_p} = 0.331 \cdot \mathrm{Ln}\left(u_{L,s} + 1\times10^{-3}\right) + 2.29 \qquad (6.47)$$

where $u_{L,s}$ is the superficial liquid velocity with units [$m^3/(m^2.s)$]. This equation is valid for a superficial liquid load in the range $6.0 \leq u_{L,s}$ [$m^3/(m^2.hr)$] ≤ 25.0. The properties of the liquid phase are:

μ : 2.0×10^{-3} [Pa.s]

ρ : 800 [kg/m^3]

σ : 23.5 [mN/m]

The values obtained with this equation are compared with the experimental results in Figure 6.13.

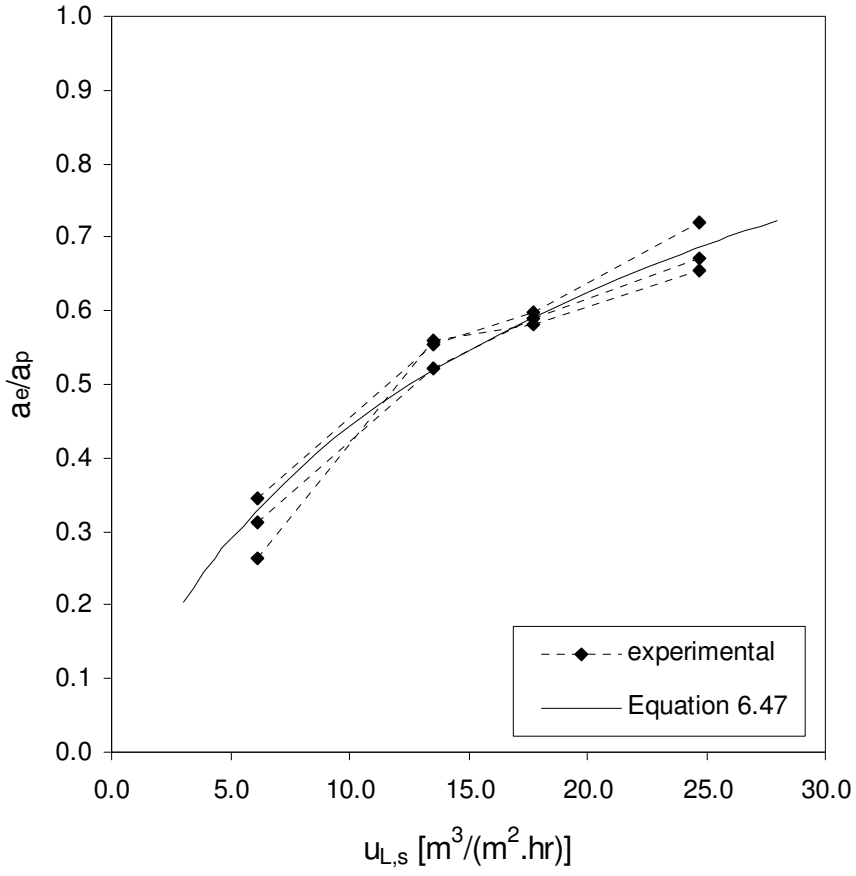

Figure 6.13 Comparison of experimental results with that predicted by Equation 6.47

At liquid loads in excess of $u_{L,s}$ = 30 [$m^3/(m^2.hr)$], Equation 6.47 predicts a gradual increase in a_e up to about $u_{L,s}$ = 80 [$m^3/(m^2.hr)$] where the effective surface is equal to the geometric area (a_e/a_p=1). Equation 6.47 would be conservative in estimating the effective surface area at liquid loads higher than $u_{L,s}$ = 30 [$m^3/(m^2.hr)$] coupled with vapour load factors higher than $F_{G=}$ 2.0 [$(m/s).(kg/m3)^{0.5}$].

6.6 Conclusions

The following conclusions may be drawn from the investigation of the effective surface area of structured packing and more specifically Flexipac 350Y:

- A literature review revealed conflicting results obtained in the measurement of effective interfacial area in structured packing.
- The absorption of CO_2 into monoethanolamine with n-propanol as solvent was identified as an alternative organic system for determining effective interfacial area in structured packing.
- The measurement of specific absorption rates in a wetted-wall reactor showed that the kinetics of the reaction between CO_2 and MEA with n-propanol as solvent falls into the rapid pseudo m,nth order reaction regime.
- The specific absorption rate of CO_2 ($0.45 \leq P_A$ [kPa] ≤ 1.1) into MEA with n-propanol as solvent ($0.2 \leq C_B$ [mol/dm^3] ≤ 0.3) is predicted by:

  $$N_A = kP_A^{0.9}C_B^{0.93}$$

  with k being temperature dependent ($288 \leq T$ [K] ≤ 303):

  $$k = -3.818\times10^{-6}T + 2.985\times10^{-3}$$

- Current correlations available in literature tend to over predict the effective interfacial area of Flexipac 350Y. The correlation proposed by Billet (Billet, 1995) is an exception and predicts the effective surface area of Flexipac accurately below the loading point.
- The experimental determined effective surface area of Flexipac 350Y shows a logarithmic trend with increasing liquid load. The experimental results were correlated with:

  $$\frac{a_e}{a_p} = 0.331\cdot\mathrm{Ln}\left(u_{L,s} + 1\times10^{-3}\right) + 2.29$$

  $u_{L,s}$ is the superficial liquid velocity with units [m^3/(m^2.s)].
- This equation is valid for a superficial liquid load in the range $6.0 \leq u_{L,s}$ [m^3/(m^2.hr)] ≤ 25.0. The liquid phase had the following properties:

  μ : 2.0×10^{-3} [Pa.s]

  ρ : 800 [kg/m^3]

  σ : 23.5 [mN/m]
- The effective surface area was found to be independent of the vapour load factor in the range $1.1 \leq F_G$ [(m/s).(kg/m3)$^{0.5}$] ≤ 2.0 for the experimental liquid loads investigated.

6.7 Nomenclature

a	Area [m^2]
a_e	Effective surface area [m^2/m^3]
a_p	Geometric area of packing [m^2/m^3]
A_s	cross sectional area of column [m^2]
C	Concentration [mol/m^3]
D	Diffusion coefficient [m^2/s]
d_h	Hydraulic diameter [m]
dx	Differential distance in x-coordinate direction [m]
E	Enhancement factor due to chemical reaction [-]
E_i	Enhancement factor due to instantaneous chemical reaction [-]
F_G	Vapour phase capacity factor [$(m/s)(kg/m^3)^{0.5}$]
Fr	Froude number [-]
F_{SE}	Factor accounting for surface treatment of packing [-]
g	Acceleration due to gravity [m/s^2]
h	height of wetted-wall column [m]
H	Henry's law constant [$Pa.m^3/mol$]
Ha	Hatta number [-]
h_t	Total liquid holdup [m^3/m^3]
k_G,k_L	Mass transfer coefficients [m/s]
k	Reaction rate constant [dependant on order of reaction]
Ma	Marangoni number [-]
n	Molar flux [mol/s]
N	Specific molar flux [$mol/(m^2.s)$]
P	Pressure [Pa]
Re	Reynolds number [-]
S	Channel side dimension [m]
T	Temperature [K]
t	time [s]
u	Velocity [m/s]
V	Volumetric flow rate [m^3/s] or molar flow rate [mol/s]
We	Weber number [-]
x	Mole fraction [-]
z	Stoichiometric relationship [-]

Greek

π	= 3.14159…
θ	Corrugation angle [^{o}]
β	Discount factor for incomplete wetting [-]
μ	Dynamic viscosity [Pa.s]
Ω	Fraction of packing area occupied by holes [-]
σ	Surface tension [N/m]
δ	Film thickness [m]
ε	Void fraction [-]
γ	Contact angle between solid and liquid [^{o}]
ρ	Density [kg/m^3]

Subscripts

lp	Refers to loading point
fp	Refers to flood point
e	Effective
G	Refers to vapour phase property
L	Refers to liquid phase property
s	Superficial
W	Refers to property of water
neg	Refers to surface negative systems
A	Refers to component A
B	Refers to component B
i	Refers to interface between vapour/liquid phases
b	Refers to bulk phase

7 BINARY DISTILLATION IN STRUCTURED PACKING

7.1 Introduction

There is a large amount of data on the efficiency of structured packing published in the brochures of different packing vendors. These data are however only available in the form of efficiency and pressure drop curves and are therefore of limited use when developing mass transfer correlations and pressure drop models. In this study, a large databank of binary distillation data was developed. This was done in order to test the correlations for the vapour phase mass transfer coefficient and effective surface area developed in Chapters 5 and 6 and to compare them with existing models in the literature for efficiency and pressure drop. The increase in capacity offered by the new range of high capacity packing was also investigated. This chapter is therefore divided into two parts. The first deals with the characterization of the different types of packing and the comparison between the normal capacity packing and the new generation of high capacity packing. In the second part the efficiency and pressure drop are compared to those predicted by the different models in literature and the correlations developed in this study.

7.2 Characterization of structured packing

It is common practice to state the efficiency of structured packing in terms of the HETP or height equivalent to a theoretical plate. In order to determine the HETP of a packing, a standard binary test mixture is used for which the VLE is accurately known. The HETP is then determined from the total packing height and the number of equilibrium stages necessary to achieve the experimental determined separation. An equilibrium model simulator was developed in this study to determine the number of equilibrium stages. The test mixture chlorobenzene/ethylbenzene was used. It is a standard test mixture recommended by the IChemE (Onken and Arlt, 1990) for columns operating under atmospheric and vacuum conditions and with a number of theoretical stages of between 10 and 30. One of the goals of this study, as set out in Chapter 1, was to quantify the increase in capacity offered by the high capacity structured packing over the older third generation structured packing. Flexipac 350Y HC is compared with Flexipac 350Y.

7.3 Predicting separation efficiency and pressure drop for Flexipac 350Y

The large amount of data generated enabled thorough testing of existing efficiency and pressure drop models and the new correlations for vapour phase mass transfer and effective surface area developed in this study. The SRP, Delft and Billet models were identified to be suitable for determining the capacity and efficiency of Flexipac 350Y. The pressure drop and holdup equations used in the different models are discussed in detail in Chapter 4. The mass transfer correlations and effective surface area equations are given in Chapters 5 and 6. A short summary of the mass transfer correlations and effective surface area equations are given in the following paragraphs for each of these models. A more detailed summary of each model is given in Appendix B and the various chapters dealing with the specific subject. For definitions of the various dimensionless numbers, Appendix B should be consulted.

The SRP model use a wetted-wall type correlation for the vapour phase mass transfer coefficient:

$$Sh_G = 0.054\left(\frac{\left(u_{G,e}+u_{L,e}\right)\rho_G S}{\mu_G}\right)^{0.8} Sc_G{}^{0.33} \qquad (7.1)$$

The liquid phase mass transfer coefficient is calculated according to the penetration theory of Higbie with the surface exposure time calculated as the time it takes for a liquid element to flow a distance equal to the side dimension of the packing. A discount factor (C_E) is incorporated to account for parts of the bed that do not encourage rapid surface renewal:

$$k_L = 2\sqrt{\frac{D_L u_{L,e}}{\pi C_E d_{hG}}} \qquad (7.2)$$

The effective surface area is calculated with a correlation adapted from Shi and Mersmann (Shi and Mersmann, 1985) for rivulet width on an inclined plate (as discussed in Chapter 6):

$$\frac{a_e}{a_p} = F_{SE}\frac{29.12\left(We_{L,s}Fr_{L,s}\right)^{0.15} S^{0.359}}{Re_{L,s}{}^{0.2}\,\varepsilon^{0.6}\left(1-0.93\cos\gamma\right)\left(\sin\theta\right)^{0.3}} \qquad (7.3)$$

The vapour phase mass transfer coefficient in the Delft model is calculated from laminar and turbulent contributions according to

$$k_G = \sqrt{k_{G,lam}{}^2 + k_{G,turb}{}^2} \qquad (7.4)$$

with the laminar contribution calculated with:

$$\frac{k_{G,lam} d_{hG}}{D_G} = 0.664 Sc_G^{1/3} \sqrt{Re_{G,r} \frac{d_{hG}}{\ell_{G,pe}}} \tag{7.5}$$

The turbulent contribution is calculated from:

$$\frac{k_{G,turb} d_{hG}}{D_G} = \frac{Re_{G,r} Sc_G \frac{\xi_{GL}\varphi}{8}}{1+12.7\sqrt{\frac{\xi_{GL}\varphi}{8}}\left(Sc_G^{2/3}-1\right)} \left[1+\left(\frac{d_{hG}}{\ell_{G,pe}}\right)^{2/3}\right] \tag{7.6}$$

The gas-liquid interaction coefficient (ξ_{GL}) follows from their hydraulic model (see Chapter 4). The liquid phase mass transfer coefficient is calculated with the same equation proposed by the SRP model but with a characteristic length equal to the hydraulic diameter of the vapour phase:

$$k_L = 2\sqrt{\frac{D_L u_{L,e}}{\pi 0.9 d_{hG}}} \tag{7.7}$$

The effective surface area is calculated from:

$$a_e = a_p \frac{(1-\Omega)}{\left(1+\frac{A}{(u_{L,s})^B}\right)} \tag{7.8}$$

The vapour phase mass transfer coefficient in the Billet model is calculated from:

$$k_G a_e = C_G \frac{a_p^{1.5}}{\sqrt{d_h}} \frac{1}{\sqrt{\varepsilon - h_t}} D_G Re_{G,s}^{\frac{3}{4}} Sc_G^{\frac{1}{3}} \frac{a_e}{a_p} \tag{7.9}$$

Different correlations are used for the liquid phase mass transfer coefficient below and above the loading point. Below the loading point k_L is calculated from:

$$k_L a_e = 12^{\frac{1}{2}} C_L a_p u_{L,e}^{\frac{1}{2}} \left(\frac{D_L}{d_h}\right)^{\frac{1}{2}} \frac{a_e}{a_p} \tag{7.10}$$

and above the loading point with:

$$k_L a_e = 12^{\frac{1}{2}} C_L a_p u_{L,e}^{\frac{1}{2}} \left(\frac{D_L}{d_h}\right)^{\frac{1}{2}} \frac{a_e}{a_p} \tag{7.11}$$

The ratio of effective surface area to geometric surface at and below the loading point is given by:

$$\left(\frac{a_e}{a_p}\right)_{lp} = 3\varepsilon^{0.5}\,Re_{L,s}^{-0.2}\,We_{L,s}^{0.75}Fr_{L,s}^{-0.45} \qquad (7.12)$$

The equations for the effective surface area above the loading point and for the increase in effective surface area due to Marangoni convection are given in Chapter 6.

Some packing specific constant are needed in all of the models. The values of these constants used in this study for calculating the efficiency and pressure drop of Flexipac 350Y are listed in the Tables 7.1 to 7.3. For the SRP model a total of 4 packing specific constants are needed. Two of these are for the calculation of the dry friction factor (A and B in Table 7.1). These constants were fitted on dry pressure drop data for the packing measured in this study (see Chapter 4). The same surface enhancement factor (F_{SE}) was used as suggested by the authors for sheet metal packing (Fair et al., 2000). A flooding pressure drop of 1100 Pa/m was used for Flexipac 350Y. The hydraulic equations could not be solved at high vapour load factors when using the suggested flooding pressure drop of 1025 Pa/m.

Table 7.1 Constants for Flexipac 350Y used in the SRP model

Constant	Description	Value
A	dry $\Delta P/\Delta z$ friction constant	0.122
B	dry $\Delta P/\Delta z$ friction constant	104.0
F_{SE}	Surface enhancement factor	0.35
$(\Delta P/\Delta z)_{flood}$ [Pa/m]	Flooding pressure drop	1100

Only two packing specific constants are needed for the Delft model. These are used to calculate the ratio of the effective to geometric surface area. The only constants available are for Montzpak B1-250. Since a ratio is calculated, the same constants were used for Flexipac 350Y. The Delft model was developed for columns where the diameter of the column is larger than the height of a packing element. In this study the height of a packing element (h_{pe}=265 mm) is larger than the column diameter (200 mm). This would lead to a numerical error when calculating the directional change loss coefficient. In order to overcome this problem, the fraction of channels ending at the column wall was set equal to unity. The values for the constants in the effective surface area correlation are given in Table 7.2

Table 7.2 Constants for Flexipac 350Y used in the Delft model

Constant	Description	Value
A	a_e/a_p correlation	2.143×10^{-6}
B	a_e/a_p correlation	1.5

A total of six packing specific constants are needed in the Billet model. No packing specific constants could be obtained for Flexipac 350Y. The packing specific constant needed for calculating the dry bed resistance factor (C_P) was fitted on the experimentally measured dry bed pressure drop. The loading (C_{lp}) and flooding (C_{fp}) constants needed to calculate the resistance factors at the load point and flood point are the same as that published for Mellapak 250Y (metal) and were found to be accurate in predicting the pressure drop for the air/water and air/kerosol 200 systems in Chapter 4. The constants published for Montzpak B1-300 were used in the vapour- and liquid phase mass transfer correlations (C_G and C_L) and effective surface area (C_h). There are only a small number of constants published for the mass transfer correlations and effective surface area. In this small database, Montzpak B1-300 has a geometric area closest to that of Flexipac 350Y and these constants were subsequently chosen.

Table 7.3 Constants for Flexipac 350Y used in the Billet model

Constant	Description	Value
C_P	dry bed resistance factor	0.172
C_{lp}	loading point resistance factor	3.157
C_{fp}	flood point resistance factor	2.464
C_h	ratio of wetted to geometric area	0.482
C_G	vapour phase mass transfer constant	0.422
C_L	Liquid phase mass transfer constant	1.165

The efficiencies predicted by the various models are calculated by modelling the experimental results with an equilibrium simulator. An equilibrium simulator was developed in this study for this purpose. It was extensively tested with a commercially available simulator (ProII) and yielded the same results. The number of theoretical stages, vapour and liquid flow rates on each stage as well as the composition of the vapour and liquid leaving each stage are obtained from the simulation results. These values are then used in the HTU/NTU method (see Chapter 2) to determine the height of packing needed to achieve the separation for each theoretical stage. The

mass transfer coefficients and effective surface area needed in this method are calculated with the different models discussed in Section 7.3. A more detailed description of each model is given in Appendix B. This appendix may also be consulted for the definition of the various dimensionless numbers. The height of packing for each theoretical stage is also calculated with the correlations developed in this study. This is done by assuming no resistance to mass transfer in the liquid phase and using Equation 5.48 for the vapour phase mass transfer coefficient and Equation 6.47 for the effective surface area. The effective vapour phase velocity ($u_{G,e}$) needed to determine the effective vapour phase Reynolds number ($Re_{G,e}$) in Equation 5.48 is calculated from:

$$u_{G,e} = \frac{u_{G,s}}{\varepsilon(1-h_t)\sin\theta} \tag{7.13}$$

The liquid holdup (h_t) is calculated with the equation proposed in the Delft model (Equation 4.62 and 4.63). The effective vapour phase Reynolds number in Equation 5.48 is calculated with:

$$Re_{G,e} = \frac{\rho_G u_{G,e} d_{hG}}{\mu_G} \tag{7.14}$$

The hydraulic diameter for the vapour phase is the same as defined in Chapter 5:

$$d_{hG} = \frac{Bh}{S} \tag{7.15}$$

The total height of packing is calculated by summing the heights of packing (or HETP) calculated for each stage. An average HETP is calculated by dividing the total height by the number of stages. Linear interpolation is used to calculate fractions of a theoretical stage in order to achieve the experimentally determined separation.

7.4 Experimental

7.4.1 Setup

The column used in this study was specifically set up to operate under conditions of total reflux and is shown in Figure 7.1. The column is constructed from four 200 mm ID glass segments. The height of each segment is 1m and accommodates 3 structured packing elements. The column therefore contained 4 packed beds with the height of packing in each bed equal to the height of 3 packing elements. When installing the elements in the column segments, each element was rotated 90° with respect to the previous one. At the bottom of the column the first packing element was installed with the channels aligned with the reboiler return line. This was done to

eliminate any possible vapour phase maldistribution. A modification had to be made to the standard column segments commercially available. They are supplied with support rings about 100mm from the bottom. These support rings are used to hold a support grid in place when packing the column with random packing. At these support rings the diameter of the column is reduced from 200mm to 160mm. It was found that these support rings drastically reduced the capacity of the column and they were subsequently removed. The condenser is located at the top of the column and all the distillate simply falls back into the top redistribution pan. A thermosyphon type reboiler without a baffle in the sump is used. The packed sections as well as the reboiler and condenser were insulated with ceramic wool and polyethylene foam.

Between each segment (or bed) the liquid is redistributed with chimney type pan liquid distributors, as shown in Figure 7.2. The distributors had a drip point density of 765 drip points/m^2. A distributor was also installed below the bottom packed bed. The function of this distributor is to collect liquid in order to draw a representative sample.

7.4.2 Procedure

The low inventory in the reboiler of the column (about 14 litres) made it possible to reach steady state in a short period of time. After start up the column was left for 3 hours to reach equilibrium before the first samples were drawn. A small change in the heating duty was made and the column was then left for 2-2½ hours before the next samples were drawn. The following temperatures were measured:

- Reboiler return temperature
- Temperature below the packing
- Temperature at the top of each packed segment
- Cooling water inlet and outlet of the condenser

The pressure drop over the column as well as the cooling water- and condensate flow rates were also measured.

In the experiments to determine the efficiency and capacity of Flexipac 350Y and 350Y HC, a sample of the distillate was drawn beneath the top liquid redistributor and the bottoms sample was collected out of the sump. The holdup in the sample lines was approximately 25ml and this amount was drawn off before collecting a sample. The samples at the top and at the bottom were drawn simultaneously. For experiments conducted at ambient pressure, the samples were drawn under gravity flow. At reduced pressures the samples were collected in special glass vacuum flasks where the pressure was adjusted to the top column pressure when sampling.

The sampling bottles and vacuum flasks were kept in ice to reduce the vapour pressure of the hot liquid in order to obtain a representative sample. A Varian CP3380 GC with FID detector and auto sampler was used to analyse the samples. An SGE-BP1 capillary column of 100 m length was used. The retention time difference between the two components was approximately 2 minutes.

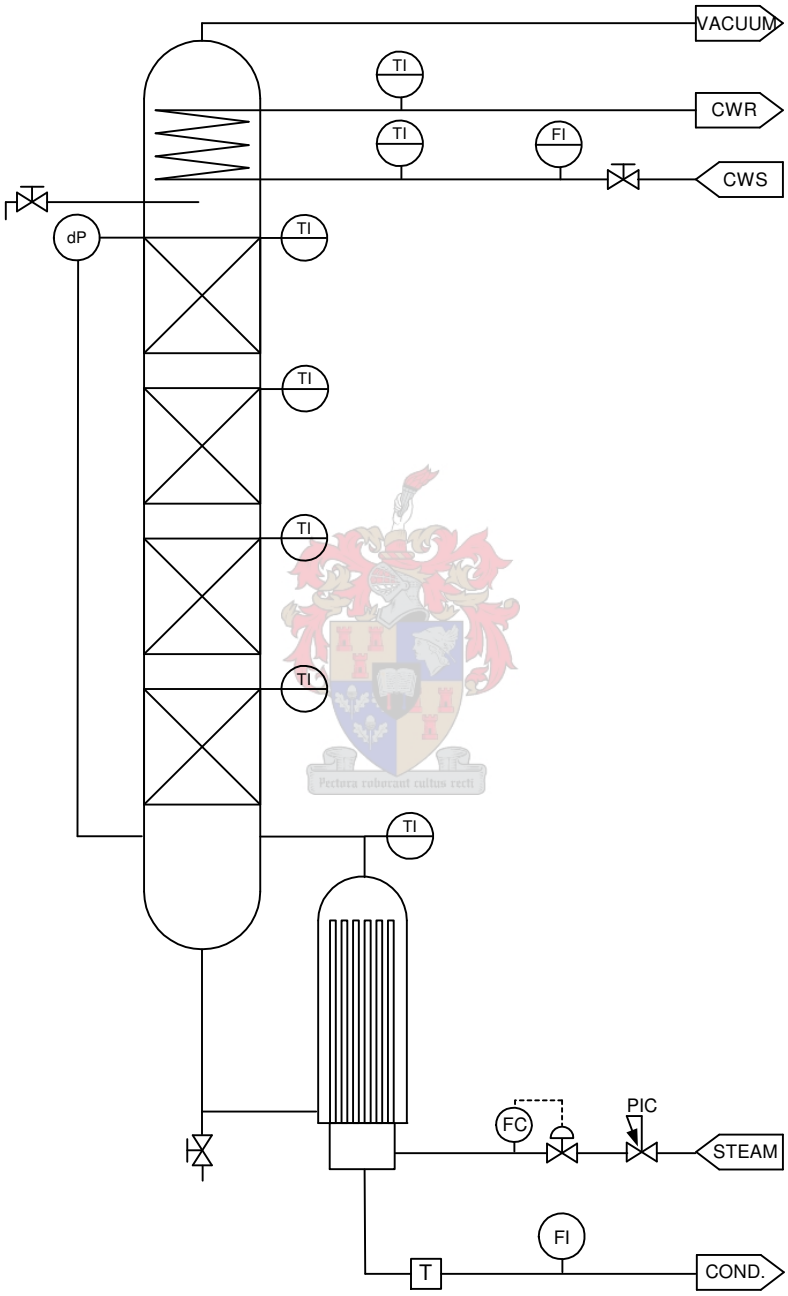

Figure 7.1 PFD of total reflux distillation column

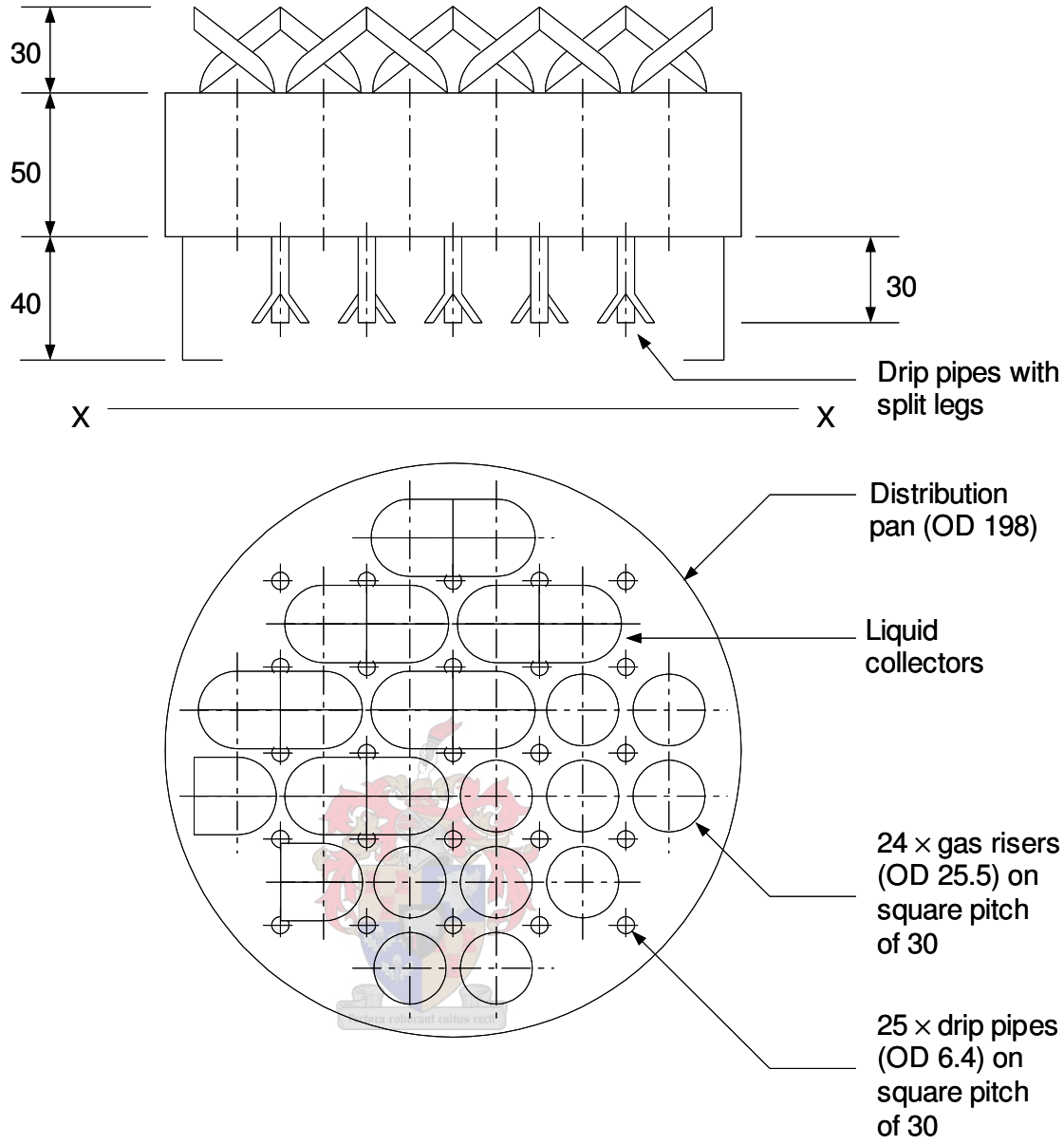

Figure 7.2 Liquid distributor

7.5 Thermodynamic data and transport properties

VLE data for the system chlorobenzene/ethylbenzene are available in the Dechema data series (Stephan and Hildwein, 1987) and in the IChemE publication on test mixtures for distillation columns (Onken and Arlt, 1990). A VLE data point measurement (Nieuwoudt, 2001) showed the IChemE data to be more accurate. The liquid activity coefficients were calculated with the NRTL model (Abbott and Prausnitz, 1994) regressed on this data. The constants are given in Appendix F. Pure component transport properties were obtained from the SIMSCI databank. Table 7.4 lists the different models used for mixture transport properties. The models are those tested and recommended by Reid and Prausnitz (Reid et al., 1986)

Table 7.4 Mixture transport properties

Property	Liquid phase	Vapour phase
Viscosity	Grunberg and Nissan	Reichenberg
Diffusion coefficient	Tyn and Callus	Fuller et al.
Surface tension	Winterberg	N/A

7.6 Results and discussion

7.6.1 Experimental results for Flexipac 350Y and 350Y HC

The experimental results for Flexipac 350Y and 350Y HC are given in Figures 7.3 to 7.8. The pressure drop shown in these figures is the pressure drop over the packing. The static pressure drop and pressure drop over the distributors were subtracted from the experimentally determined pressure drop in these figures.

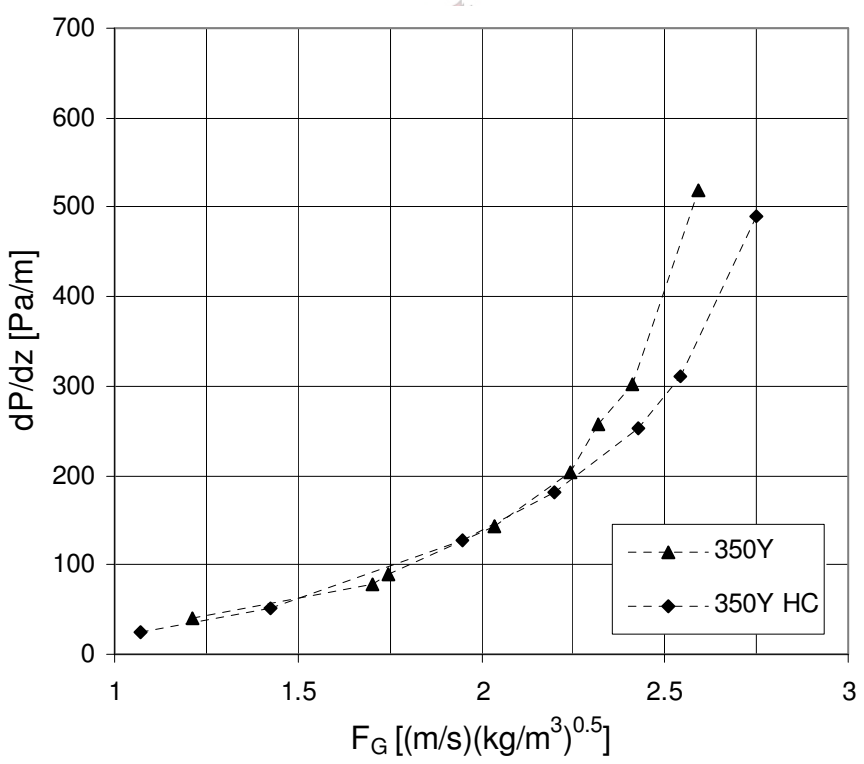

Figure 7.3 Capacity comparison between Flexipac 350Y and 350Y HC at 1.0 bar.

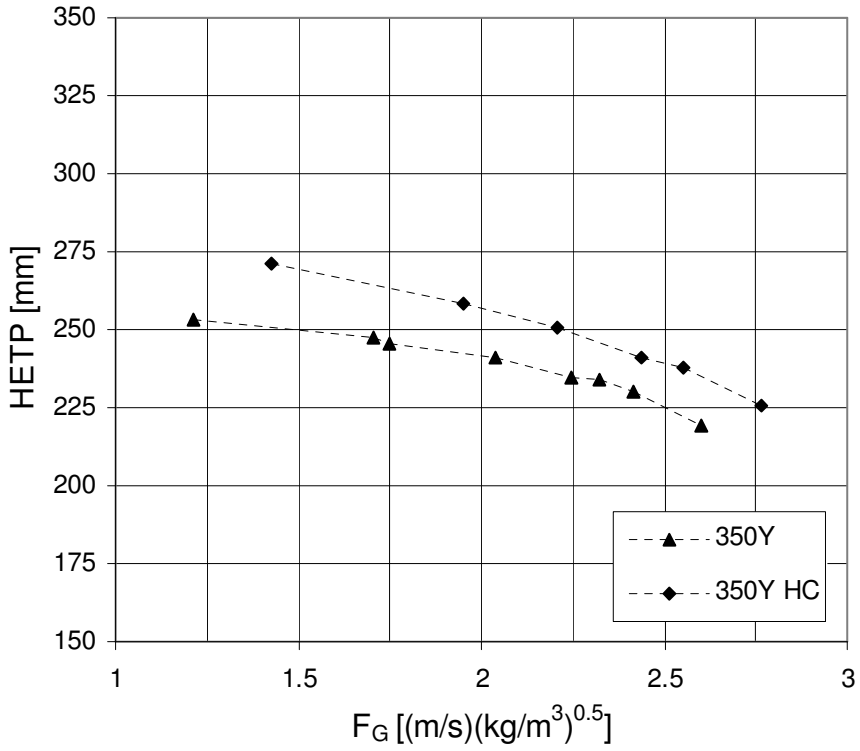

Figure 7.4 Efficiency comparison between Flexipac 350Y and 350Y HC at 1.0 bar.

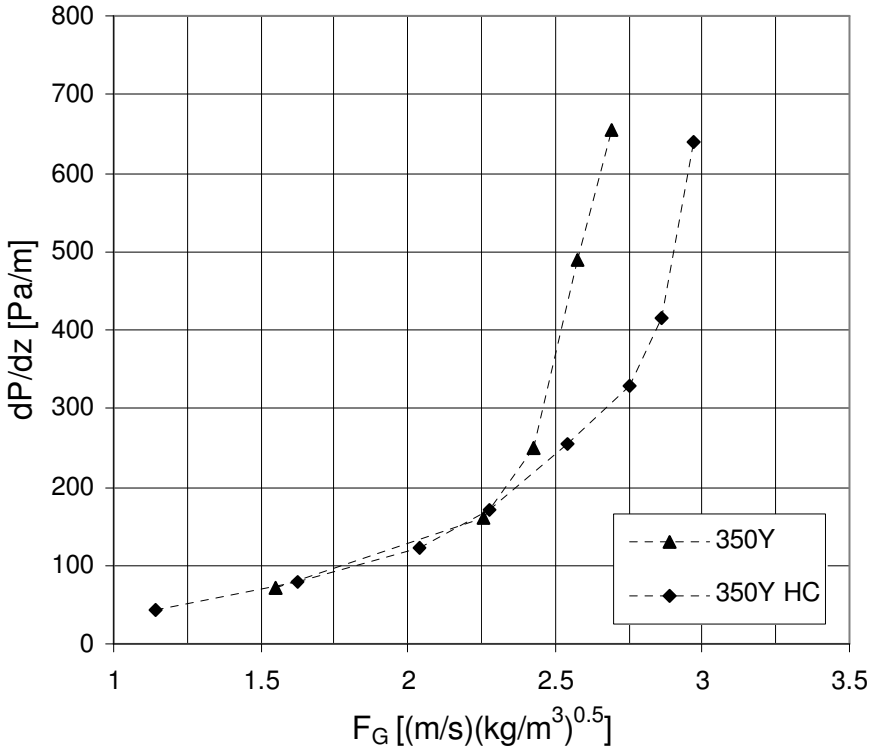

Figure 7.5 Capacity comparison between Flexipac 350Y and 350Y HC at 0.6 bar.

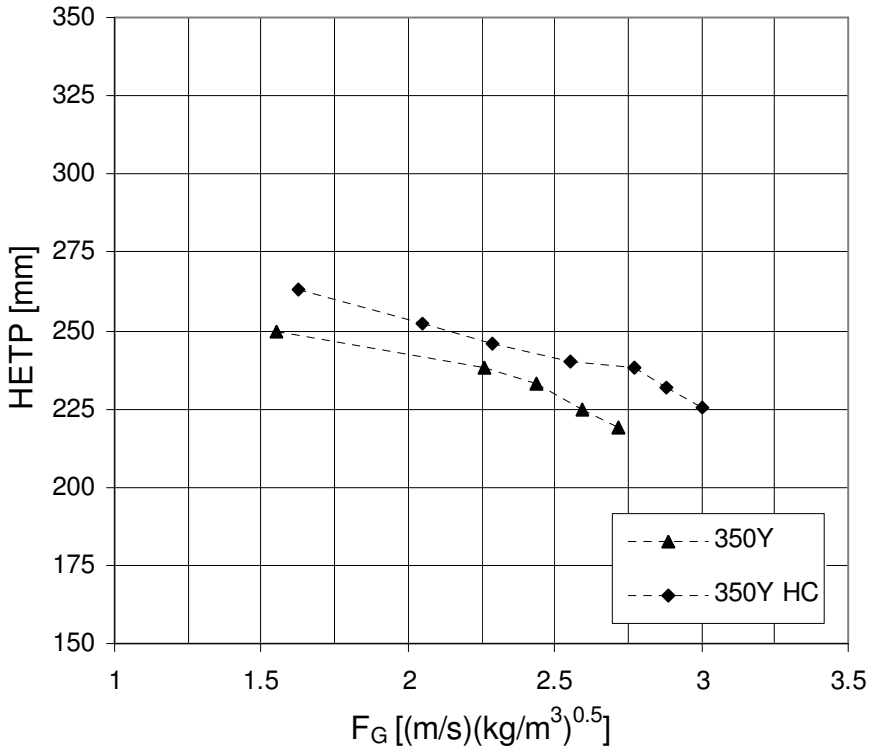

Figure 7.6 Efficiency comparison between Flexipac 350Y and 350Y HC at 0.6 bar.

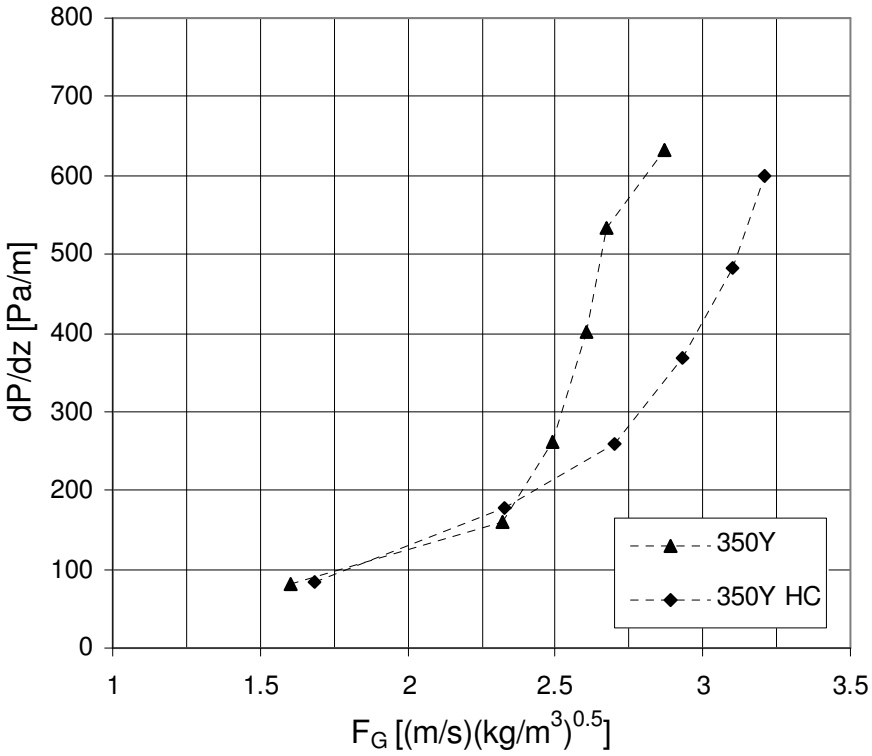

Figure 7.7 Capacity comparison between Flexipac 350Y and 350Y HC at 0.3 bar.

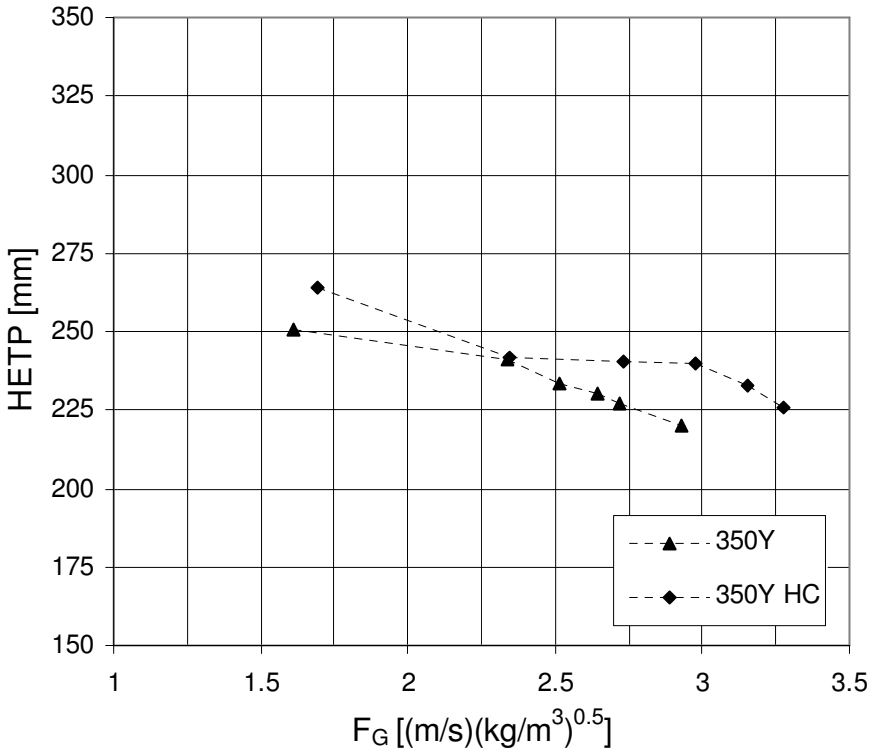

Figure 7.8 Efficiency comparison between Flexipac 350Y and 350Y HC at 0.3 bar.

The efficiency of the normal capacity is incrementally better than the high capacity packing throughout the operating range of the normal capacity packing (see Figures 7.4, 7.6 and 7.8). This is probably due to entry and exit regions of the high capacity packing not contributing as effectively to mass transfer as the normal capacity packing. The capacity advantage offered by the high capacity packing is however clearly shown at high loadings. Figures 7.3, 7.5 and 7.7 show the pressure drop as a function of the vapour phase capacity factor. Each packing was operated at the highest possible stable operating point. For both types of packing some flooding was observed at the base of the bed or between packing elements at this operating point. The high capacity packing could be stably operated at vapour phase capacity factors between 8% and 15% higher than was possible with the normal capacity packing. At an operating pressure of 1.0 bar, the increase in capacity is about 8% (see Figure 7.3), while at an operating pressure of 0.3 bar the increase in capacity is in the order of 15% (see Figure 7.7). This would suggest that the modifications to the entry and exit regions of the packing elements have a larger impact on capacity at higher vapour velocities. There is also an increase in efficiency as the vapour loading is increased. At the maximum loading where stable operation is still possible, the efficiency of the packing is retained and is similar to that obtained with the normal

packing at its maximum loading point where efficiency is still retained. What is also noteworthy is that the slope of the pressure drop curve in the loading region is smaller for the high capacity packing compared to the normal packing. Visual inspection of the base of the structured packing elements showed the liquid drainage to be better for the high capacity packing than for the normal packing. At the maximum stable operating point of the normal packing there was a substantial height of liquid suspended at the base of a packing element. For the high capacity packing this height of liquid was considerably less. It is therefore expected that the efficiency of the normal range of packing would deteriorate more rapidly because of back mixing than the high capacity packing as the flood point is approached. Because of the smaller slope of the pressure drop curve in the loading region for the high capacity packing, it would be possible to operate the column more stably at high loadings with this packing.

7.6.2 Flexipac 350Y: Model predictions

Pressure drop and holdup

In Figures 7.9 to 7.11 the experimentally determined pressure drops over Flexipac 350Y are compared with the results obtained with the models evaluated in Chapter 4. Figure 7.9 compares the pressure drop calculated with the SRP model with the experimental results at the different operating pressures. Figure 7.10 show the results obtained with the Delft model and Figure 7.11 the results for the Billet model.

The experimental pressure drop shown in Figures 7.9 to 7.11 is the pressure drop over the packing. This pressure drop was calculated by subtracting the pressure drop over the liquid distributors and the static pressure drop from the experimental measured pressure drop. A comparison between Figures 7.9 to 7.11 show that the model by Billet is accurate in predicting the pressure drop in the preloading region ($F_G < 2.25$). Both the SRP and Delft models predict the onset of loading conditions, characterized by a sharp increase in the slope of the pressure drop curve, at low gas load factors ($F_G \approx 1.6$). This is not surprising since both models use the same correlation to determine the load point (Verschoof et al., 1999). It would seem that both models predict the correct slope of the pressure drop curve in the loading region. An improvement in the prediction of the loading point would therefore probably lead to an accurate fit on the experimental data. Although the model by Billet is accurate in predicting the preloading pressure drop, it does predict the loading point to be at slightly higher vapour load factors than was determined experimentally (see Figure 7.11).

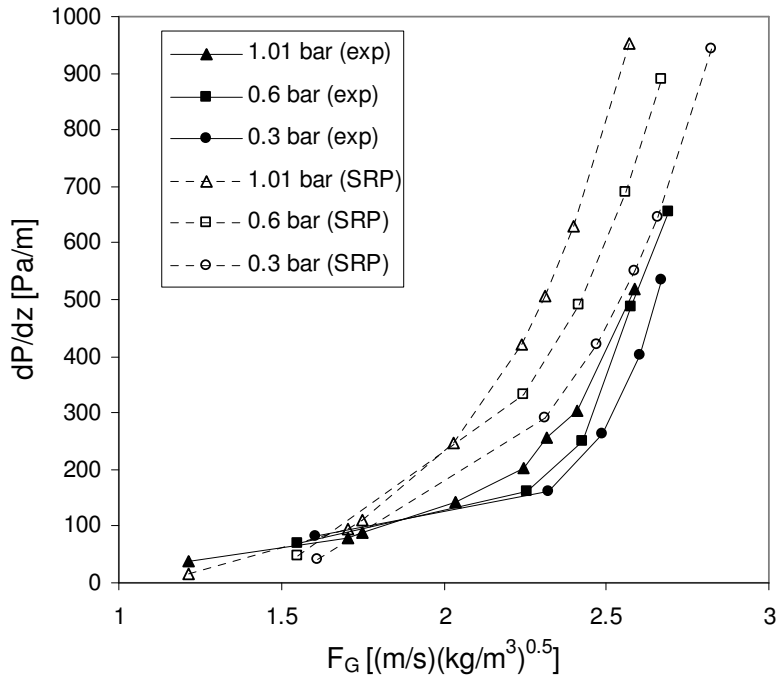

Figure 7.9 Comparison between measured and predicted pressure drop for Flexipac 350Ywith the SRP model. Chlorobenzene/ethylbenzene test system at 1.01 bar, 0.6 bar and 0.3 bar.

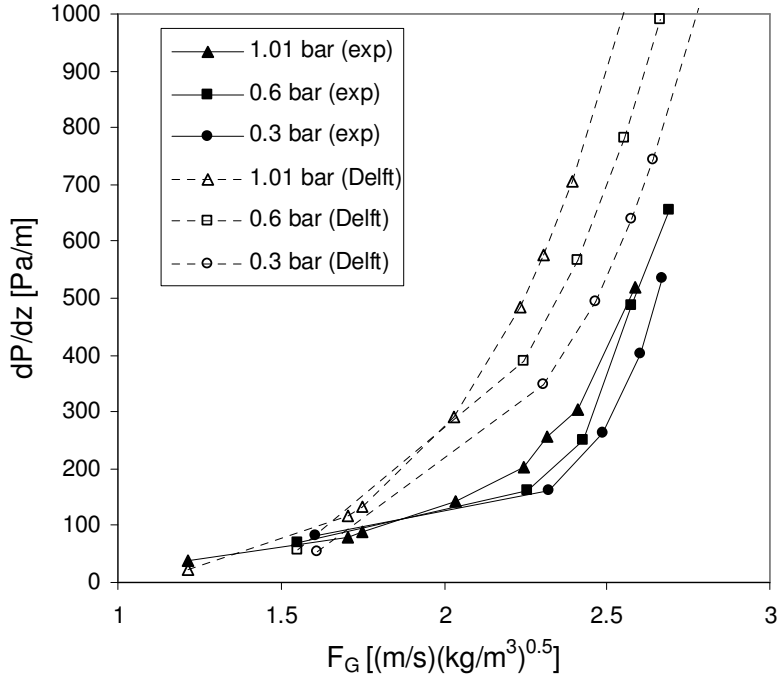

Figure 7.10 Comparison between measured and predicted pressure drop for Flexipac 350Ywith the Delft model. Chlorobenzene/ethylbenzene test system at 1.01 bar, 0.6 bar and 0.3 bar.

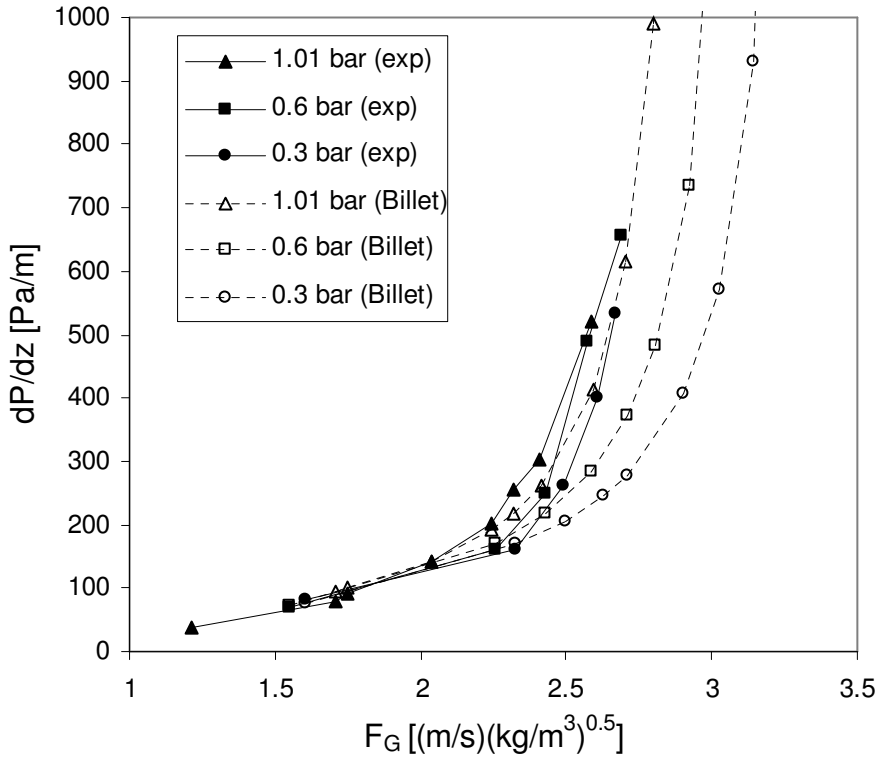

Figure 7.11 Comparison between measured and predicted pressure drop for Flexipac 350Ywith the Billet model. Chlorobenzene/ethylbenzene test system at 1.01 bar, 0.6 bar and 0.3 bar.

Figure 7.12 compares the holdup predicted by the different models. It is difficult or nearly impossible to determine the holdup experimentally when performing distillation experiments. The different models are therefore only compared to one another in this figure. Some qualitative observations of the level in the reboiler are however possible during experimental distillation runs. The total amount of liquid charged to the reboiler before the start of experimental runs is approximately 14 litres. The amount of liquid in the distributors is approximately 1.5 litres when operating at 40% of design capacity. The minimum amount of liquid necessary in the reboiler for normal operation would be in the order of about 7-8 litres. This then translates into the maximum amount of liquid held up on the packing to be in the order of 4.5-5.5 litres, giving a holdup of around $0.045 < ht < 0.055$ (100 litres of packed volume in column). These observations would suggest that there is not quite as sharp an increase in the holdup as predicted by the Billet model. This was also observed when the Billet model was compared to experimental holdup data in Chapter 4. The amount of liquid holdup predicted by the Billet model at high vapour load factors would lead to an insufficient amount of liquid in the thermosyphon reboiler for normal operation. This

rough estimate of the holdup also suggests that the holdup predicted by the SRP model at high vapour load factors (see Figure 7.12) is too high. The Delft model was found to be the most accurate of the three models in predicting the holdup in the preloading region for the air/water and air/kerosol 200 systems (see Chapter 4) It is therefore expected that the experimental holdup in the preloading region would be close to that predicted by the Delft model in Figure 7.12. There would be a definite increase in the holdup in the loading region as the flood point is approached. The Delft model does however not predict this trend.

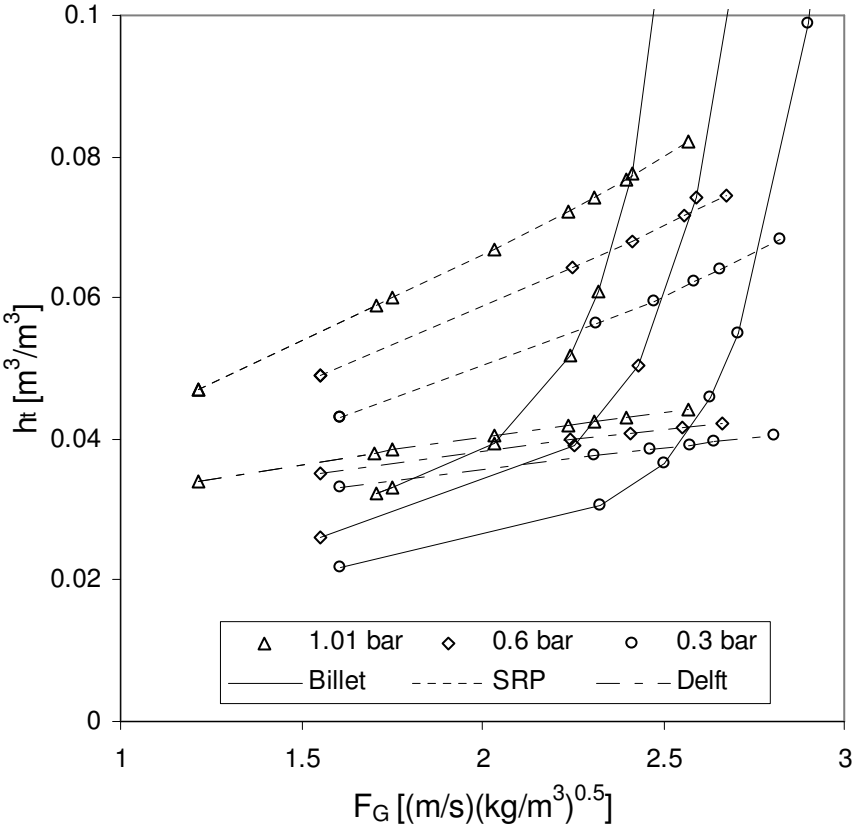

Figure 7.12 Holdup predicted by different models for Flexipac 350Y. Chlorobenzene/ethylbenzene test system at 1.01 bar, 0.6 bar and 0.3 bar.

7.6.3 Efficiency

The HETP predicted by the different models are compared with the experimentally determined HETP in Figures 7.13 to 7.15.

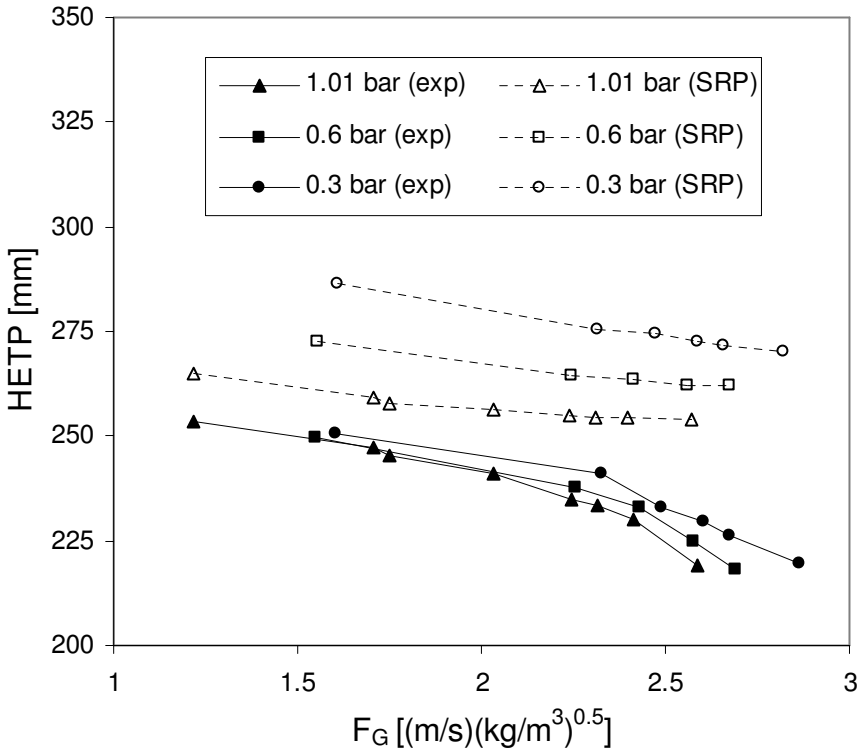

Figure 7.13 Efficiency of Flexipac 350Y predicted by the SRP model. Chlorobenzene/ethylbenzene test system at 1.01 bar, 0.6 bar and 0.3 bar.

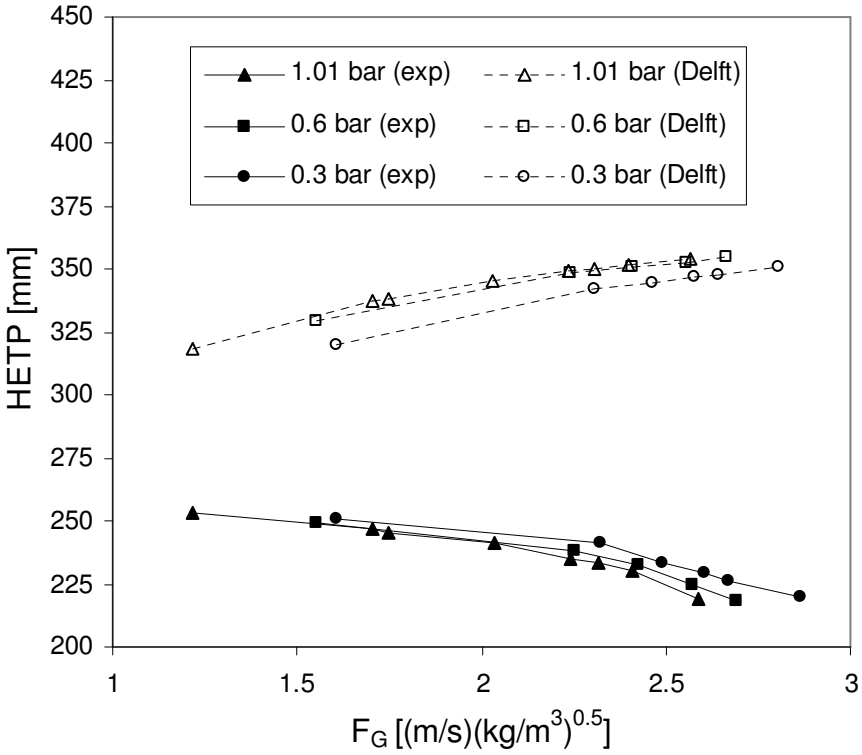

Figure 7.14 Efficiency of Flexipac 350Y predicted by the Delft model. Chlorobenzene/ethylbenzene test system at 1.01 bar, 0.6 bar and 0.3 bar.

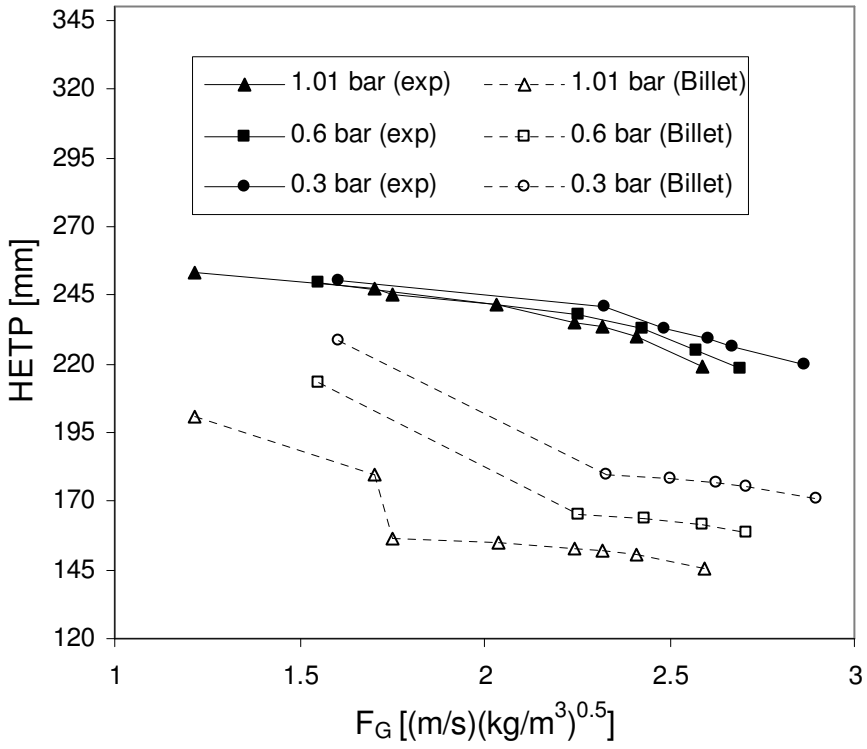

Figure 7.15 Efficiency of Flexipac 350Y predicted by the Billet model. Chlorobenzene/ethylbenzene test system at 1.01 bar, 0.6 bar and 0.3 bar.

The experimental determined efficiency show a decrease in HETP (increase in efficiency) with an increase in the vapour load factor. A comparison between the efficiency calculated with the different models clearly shows that the SRP and Billet models predict this trend. The Delft model predicts a decrease in efficiency with an increase in the vapour load factor (see Figure 7.14). It is expected that high up in the loading region the efficiency will start to decrease as the flood point is approached, but not over the entire operating range as predicted by the Delft model. Figures 7.13 to 7.15 show that the SRP model is the most accurate of the three models in predicting the efficiency of Flexipac 350Y. The model by Billet over predicts the efficiency and the Delft model under predicts the efficiency. The model by Billet also predicts a sharp rise in the efficiency in the loading region (see Figure 7.15). Although the efficiency does increase in the loading region, the increase is not as dramatic as suggested by the Billet model. It is difficult to compare the models based on the overall efficiency shown in Figures 7.13 to 7.15. Since the overall efficiency is calculated from the vapour- and liquid side mass transfer coefficients and the effective surface area (see Chapter 2), it would be more appropriate to compare the model predictions of these quantities. Figure 7.16 shows the gas phase mass transfer coefficient (k_G) predicted by the different models.

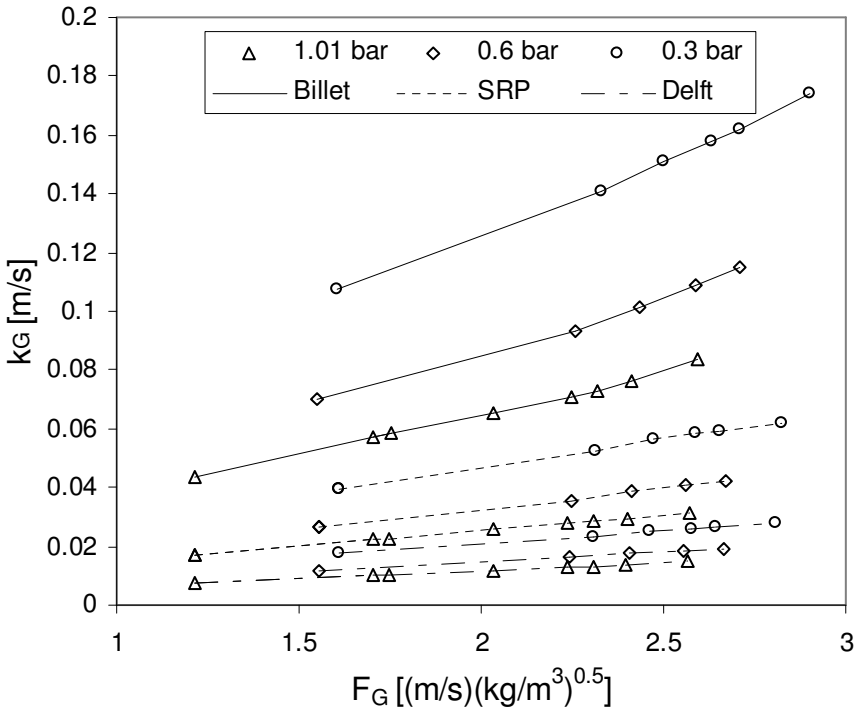

Figure 7.16 Vapour phase mass transfer coefficient predictions by SRP, Delft and Billet models for Flexipac 350Y. Chlorobenzene/ethylbenzene test system at 1.01 bar, 0.6 bar and 0.3 bar.

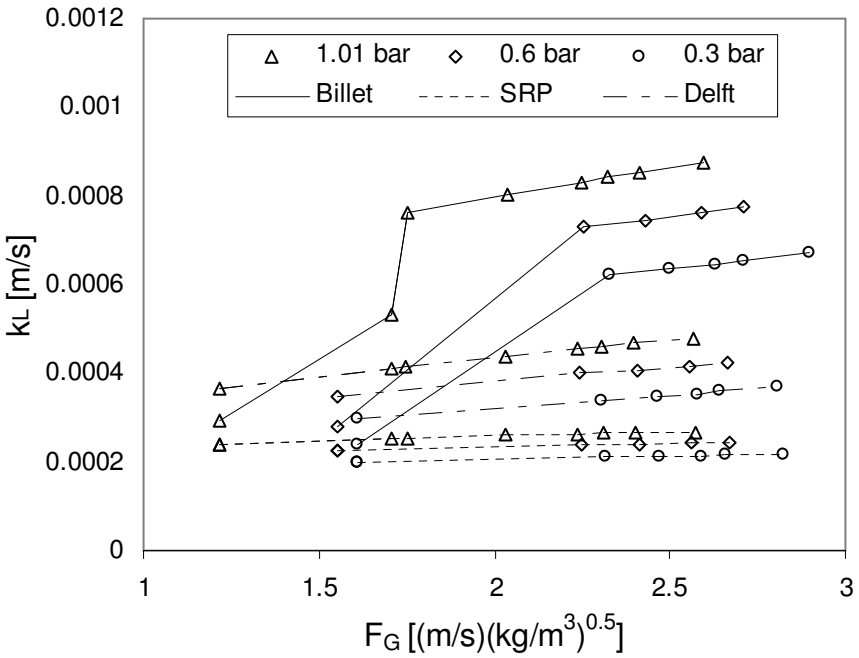

Figure 7.17 Liquid phase mass transfer coefficient predictions by SRP, Delft and Billet models for Flexipac 350Y. Chlorobenzene/ethylbenzene test system at 1.01 bar, 0.6 bar and 0.3 bar.

Figure 7.17 compares the liquid phase mass transfer coefficients (k_L) and Figure 7.18 the effective surface area (a_e). Figures 7.16 to 7.18 show that the models differ widely in their predictions of mass transfer coefficients and effective surface area. The Billet model predicts extremely high vapour phase mass transfer coefficients compared to the SRP and Delft models. For an operating pressure of 1.01 bar, the vapour phase mass transfer coefficient predicted by the Billet model is almost three times higher than the vapour phase mass transfer coefficient predicted by the SRP model and almost six times higher than that predicted by the Delft model (Figure 7.16).

There are also large differences in the prediction of the liquid phase mass transfer coefficient. At an operating pressure of 1.01 bar the Billet prediction is on average a factor three higher than the SRP prediction. The liquid phase mass transfer coefficient predicted the Delft model predicts about half of that by the Billet model. The sharp increase in the liquid phase mass transfer coefficient calculated with the Billet model is due to a sharp increase in the liquid holdup (see Figure 7.12). The Billet model compensates for the very high mass transfer coefficients by predicting a low effective interfacial area, as shown in Figure 7.18. In calculating the effective interfacial area in the Billet model, the increase in effective surface area in the loading region as suggested by Billet (Billet, 1995) was not included since this led to rather large and unrealistic values for the effective surface area. The Delft model compensates for the rather low vapour phase mass transfer coefficient by predicting a large effective surface area. This area is about 90% of the geometric specific surface area of the packing. The SRP effective surface area is about midway between that predicted with the Billet and Delft models.

The reasons for these large differences are unclear. One possible reason may be that volumetric mass transfer coefficients ($k_G.a_e$, $k_L.a_e$) were measured experimentally. These were then split up arbitrarily, or according to some kind of model, into mass transfer coefficients (k_G, k_L) and effective surface area (a_e) and modelled separately.

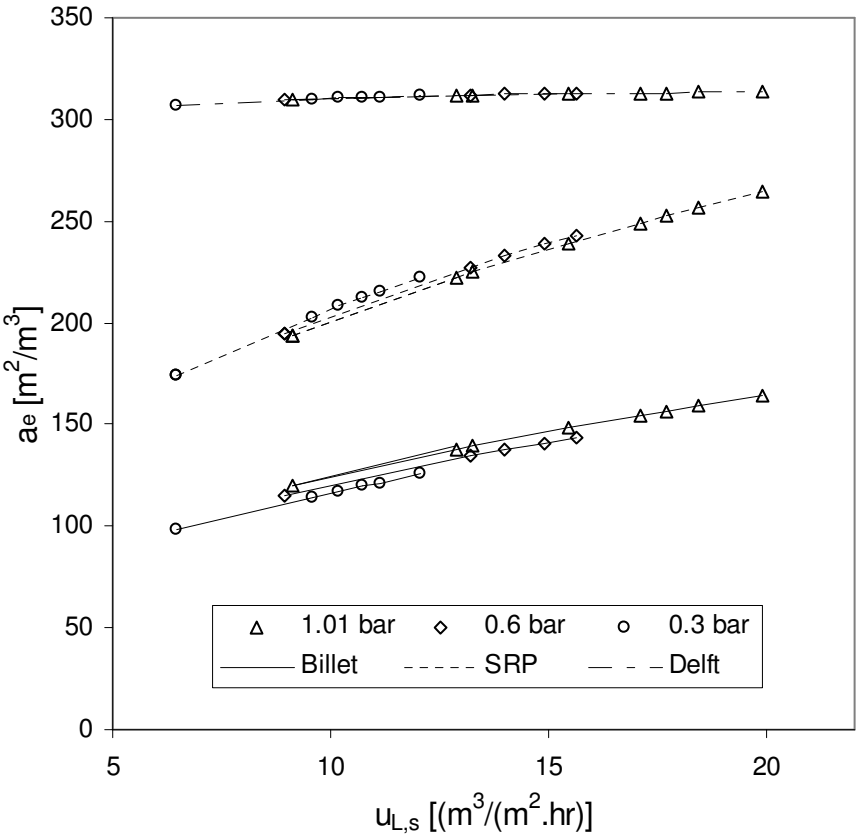

Figure 7.18 Effective surface area predictions by SRP, Delft and Billet models for Flexipac 350Y. Chlorobenzene/ethylbenzene test system at 1.01 bar, 0.6 bar and 0.3 bar.

The vapour phase mass transfer coefficient calculated with the correlation proposed in Chapter 5 (Equation 5.48), is compared with the different models in Figure 7.19. The effective vapour phase Reynolds number used in Equation 5.48 was calculated with the Delft model. The holdup in the preloading region is thought to be more accurately predicted by this model than by the SRP or Billet models (see section on pressure drop and holdup for explanation). The hydraulic diameter (d_{hG}) in $Re_{G,e}$ was calculated with Equation 5.43. Figure 7.19 shows the vapour phase mass transfer coefficient predicted by Equation 5.48 to be in close agreement with that predicted by the SRP model.

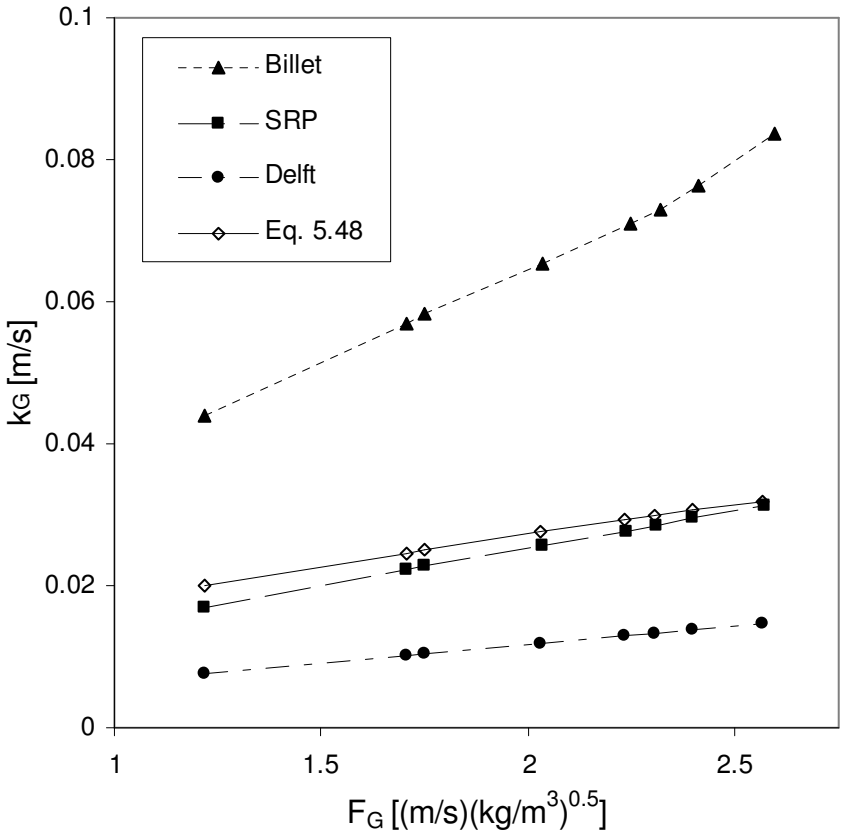

Figure 7.19 Vapour phase mass transfer coefficient predicted with equation 5.48 compared to predictions by SRP, Billet and Delft models. Chlorobenzene/ethylbenzene test system, 1.01 bar.

The effective surface area calculated with Equation 6.47 is compared to that predicted by the different models in Figure 7.20. The effective surface area calculated with Equation 6.47 lies approximately midway between that of the Billet and SRP models. The effective surface area is shown in this graph as a function of the liquid load (superficial liquid velocity).

The efficiency calculated by assuming no resistance to mass transfer in the liquid phase and using Equation 5.48 for the vapour phase mass transfer coefficient and Equation 6.47 for the effective surface area, is shown in Figure 7.21. The predictions are quite close to the experimental points. At an operating pressure of 1.01 bar, the model prediction of HETP is on average 9% lower than the measured HETP. At an operating pressure of 0.6 bar the model predicts a 3% lower HETP and at an operating pressure of 0.3 bar the model predictions are 5% higher.

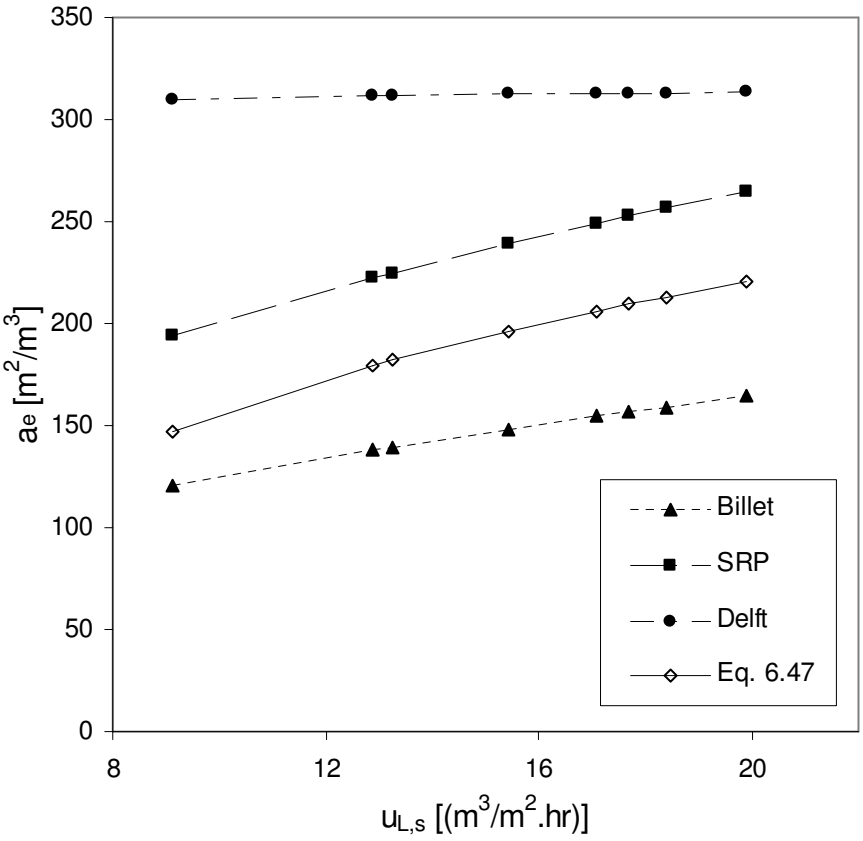

Figure 7.20 Effective surface area predicted with equation 6.47 compared to predictions by SRP, Billet and Delft models. Chlorobenzene/ethylbenzene test system, total reflux, 1.01 bar.

The fact that the predictions are both higher and lower than the experimental determined efficiency would suggest that the liquid phase resistance to mass transfer in the chlorobenzene/ethylbenzene system is indeed negligible. It is expected that if this was not the case, then the model would consistently predict an efficiency higher (lower HETP) than the experimental determined efficiencies for all operating pressures.

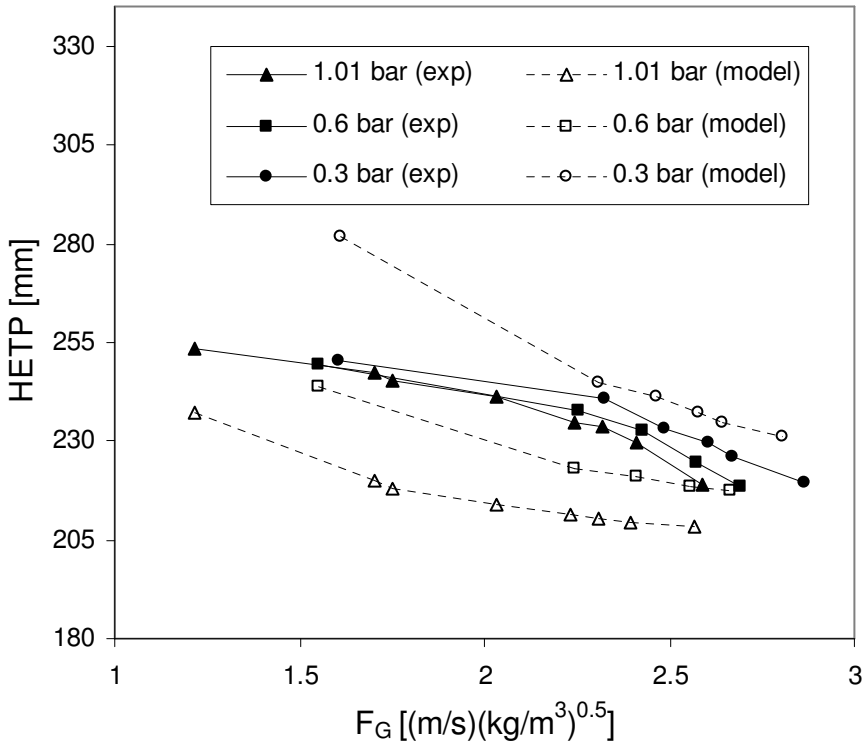

Figure 7.21 Efficiency of Flexipac 350Y predicted with k_G and a_e correlations developed in this study. Chlorobenzene/ethylbenzene test system at 1.01 bar, 0.6 bar and 0.3 bar.

7.7 Conclusions

From the results obtained in this chapter, the following conclusions may be drawn:

- The new high capacity structured packing Flexipac 350Y HC offers an increase in capacity of between 8% and 15% when compared with the normal capacity packing Flexipac 350Y.
- Both Flexipac 350Y and 350Y HC could be operated stably at pressure drops of around 600 Pa/m without losing efficiency. It is expected that the high capacity packing could be operated stably at even higher pressure drops.
- The SRP and Delft models predict the loading point of Flexipac 350Y at lower than measured vapour load factors. The Billet model is accurate in predicting the preloading pressure drop. It predicts the loading point to be slightly higher than was determined experimentally.
- The liquid holdup predicted by the SRP and Billet models in the loading region is too high when compared with rough experimental estimates.
- Overall the Delft model predicts an efficiency 46% lower than was determined experimentally for Flexipac 350Y. The efficiency predicted by the SRP model for

this packing is on average 13% lower. The Billet model predicts an efficiency that is on average 27% higher.

- The models differ widely in their predictions of liquid- and vapour phase mass transfer coefficients. This is a serious cause for concern.
- When ignoring liquid phase resistance and calculating the efficiency for Flexipac 350Y with the correlations developed in this study for the vapour phase mass transfer coefficient and effective surface area, the predicted efficiency is 9% higher than that determined experimentally at 1.01 bar. At an operating pressure of 0.6 bar, the predicted efficiency is on average 3% higher and at an operating pressure of 0.3 bar the predicted efficiency is on average 5% lower than the experimentally determined efficiency.

7.8 Nomenclature

a_e	Effective surface area of packing [m^2/m^3]
a_p	Geometric area of packing [m^2/m^3]
B	Channel base dimension [m]
D	Diffusion coefficient [m^2/s]
d_h	Hydraulic diameter [m]
F_G	Vapour capacity factor [$(m/s)(kg/m^3)^{0.5}$]
Fr	Froude number [-]
F_{SE}	Discount factor for liquid phase mass transfer coefficient [-]
h	Channel crimp height [m]
h_t	Total liquid holdup [m^3/m^3]
k	Mass transfer coefficient [m/s]
$\ell_{G,pe}$	Length of triangular vapour phase channel [m]
Re	Reynolds number [-]
S	Side dimension of corrugated channel [m]
Sc	Schmidt number [-]
Sh	Sherwood number [-]
u	Velocity [m/s]
We	Weber number [-]

Greek

π	= 3.14159…
θ	Corrugation angle [^{o}]
μ	Dynamic viscosity [Pa.s]
Ω	Fraction of packing area occupied by holes [-]
φ	Fraction of triangular passage occupied by liquid [-]
ξ_{GL}	Vapour/liquid friction factor [-]
ε	Void fraction [-]
γ	Contact angle between solid and liquid [^{o}]
ρ	Density [kg/m^3]

Subscripts

e	Effective
fp	Refers to flood point
G	Refers to vapour phase property

L	Refers to liquid phase property
lam	Laminar contribution
lp	Refers to loading point
s	Superficial
turb	Turbulent contribution

8 CONCLUSIONS

The ultimate goal of this study was to arrive at a model for the capacity and the efficiency of the sheet metal structured packing Flexipac 350Y, with the emphasis on the development of accurate correlations for modelling efficiency. In the following paragraphs, the conclusions reached in the different chapters are discussed using these two goals (the modelling of capacity and efficiency) as main themes. The increase in capacity that the new high capacity packing offers is also discussed.

Since there are quite a few capacity models available in literature, no new model was developed. The existing models were tested against experimentally measured hydrodynamic data and those more suitable were identified. From the results obtained with the different hydraulic models, the following conclusions may be drawn:

- The hydraulic capacity model by Stichlmair fails to predict the correct pressure drop trend for Flexipac 350Y. This is thought to be due to the fact that the model was fitted mainly on data for random packing
- The models by the SRP and Delft predict the onset of loading conditions at lower vapour loadings than were measured experimentally. The model by Billet predicts the load point at slightly higher vapour loads, but is more accurate than the SRP and Delft models.
- The Delft model is more accurate than the SRP and Billet models in predicting the holdup in the preloading region. In the loading region both the models of the SRP and Billet predicts too high a liquid holdup.
- The model by Billet is the most accurate in predicting the pressure drop in the preloading region.
- All the models predict a conservative dependency of packing capacity on liquid viscosity.

The efficiency of Flexipac 350Y was determined by performing total reflux distillation using chlorobenzene/ethylbenzene as test system and modelled with different efficiency models available in literature. The efficiency models differ widely in their prediction of the mass transfer coefficients for the liquid- and vapour phases and the effective surface area. In this study the vapour phase mass transfer coefficient and effective surface area were measured and correlated independently from each other. From the experimental and modelling results for the efficiency of Flexipac 350Y, the following conclusions may be drawn:

- For binary total reflux distillation using chlorobenzene/ethylbenzene as test system, the Delft model predicted an efficiency 46% lower than was measured experimentally, the SRP model was on average 13% lower and the Billet model on average 27% higher.
- The sublimation of naphthalene from structured packing was used to determine the vapour phase mass transfer coefficient. Although this is quite an old method to determine vapour phase mass transfer coefficients, it is the first time that this technique has been used to determine the vapour phase mass transfer coefficients in structured packing. The experimentally determined vapour phase mass transfer coefficient was correlated with:

$$Sh_G = 0.3053\,Re_{G,e}^{0.62}\,Sc_G^{0.33}$$

- The vapour phase mass transfer rate was found to be the same for the bottom- and top half of a structured packing element at low vapour phase Reynolds numbers. At vapour phase Reynolds numbers higher than approximately $Re_{G,e}$ = 6000, the vapour phase mass transfer rate is slightly higher for the bottom half of the segment compared to the top half.
- CFD has been used in the past to determine the dry pressure drop through packing and to compare different designs based on the comparison of modelling of hypothetical heat transfer rates. To the author's knowledge, this is the first time that CFD has been used to model real vapour phase mass transfer rates in structured packing.
- In the CFD modelling of structured packing it was necessary to model only a single representative micro element. The BSL turbulence model of Menter was successfully used in modelling the vapour phase mass transfer rate. The results obtained are sensitive to the placement of inlet- and outlet boundaries for such a micro element.
- The absorption of CO_2 into monoethanolamine with n-propanol as solvent was identified as an organic system for determining effective interfacial area in structured packing. To the author's knowledge this is the first time that an organic system with both a low surface tension and low viscosity has been used to determine effective surface area in structured packing.
- For systems with a low surface tension and a low viscosity, it is commonly believed that the effective surface area would be high. The effective surface area was, however, found to be substantially lower than expected. The experimental determined effective surface area of Flexipac 350Y shows a

logarithmic trend with increasing liquid load. The experimental results were correlated with:

$$\frac{a_e}{a_p} = 0.331 \cdot \mathrm{Ln}\left(u_{L,s} + 1\times10^{-3}\right) + 2.29$$

where $u_{L,s}$ is the superficial liquid velocity with units [$m^3/(m^2.s)$].

- When ignoring liquid phase resistance and calculating the efficiency for Flexipac 350Y for the chlorobenzene/ethylbenzene test system with the correlations developed in this study, the predicted efficiency was 9% higher than that determined experimentally at 1.01 bar. At an operating pressure of 0.6 bar, the predicted efficiency was on average 3% higher and at an operating pressure of 0.3 bar the predicted efficiency was on average 5% lower than the experimentally determined efficiency. This is a substantial improvement on existing models.
- These correlations may be used as a starting point in the development of an accurate correlation for the liquid phase mass transfer coefficient.

The capacity and efficiency of the high capacity packing Flexipac 350Y HC were measured experimentally and compared with the normal capacity packing Flexipac 350Y. The following conclusions were reached:

- The high capacity packing used in this study showed a higher dry bed pressure drop compared to the normal capacity packing. This is thought to be due to the slight difference in corrugation geometry between the two types of packing.
- There is an increase in capacity of 20% for the new packing compared with the normal packing for the air/water system. The increase in capacity for viscous liquid systems is only 4%.
- The new high capacity structured packing Flexipac 350Y HC offers an increase in capacity of between 8% and 15% when compared with the normal capacity packing Flexipac 350Y.
- When compared with the high capacity packing, the efficiency of the normal capacity packing is incrementally better (around 3%) over the entire operating range of the normal capacity packing.

From the above conclusions it is clear that the new high capacity packing Flexipac 350Y HC will perform as well or better than the normal capacity packing Flexipac 350Y. For systems where the liquid viscosity is low, as encountered in the binary total reflux distillation work performed in this study, the increase in capacity that the high capacity packing offers more than offsets the higher

efficiency of the normal capacity packing. For viscous systems it is expected that the performance of the two types of packing would be similar.

In summary this project has contributed to the current body of knowledge on the efficiency of structured packing by laying the foundations for an experimental method to characterize packing efficiency. These experimental methods may be used to evaluate the efficiency of new packing designs, compare it with current packing designs and identify areas where improvements may be possible. It has also highlighted the role that CFD may play in the development of vapour phase mass transfer correlations. The inability of current mass transfer models to predict the efficiency of structured packing has lead design engineers to use large safety factors when designing new colums. The correlations developed in this study will hopefully contribute towards more accurate designs for columns containing structured packing. This will have a positive impact on the overall process economics.

REFERENCES

Abbott, M. M. and Prausnitz, J. M. (1994). In *Models for Thermodynamic and Phase Equilibria Calculations*(Ed, Sandler, S. I.) Marcel Dekker, New York.

AEA Technology (2002). CFX-4.4. Harwell, UK.

Alvarez-Fuster, C., Midoux, N., Laurent, A. and Charpentier, J. C. (1980). "Chemical Kinetics of the Reaction of Carbon Dioxide with Amines in Pseudo m,nth Order Conditions in Aqueous and Organic Solutions", *Chem. Eng. Sci.,* **35,** 1717.

Alvarez-Fuster, C., Midoux, N., Laurent, A. and Charpentier, J. C. (1981). "Chemical Kinetics of the Reaction of CO2 with Amines in Pseudo m-nth Order Conditions in Polar and Viscous Organic Solutions", *Chem. Eng. Sci.,* **36,** 1513.

Ambrose, D., Lawrenson, I. J. and Sprake, C. H. S. (1975). "The vapour pressure of naphthalene", *J. Chem. Thermodynamics,* **7,** 1173.

ASME (1959). *Fluid Meters: Their Theory and Application,* The American Society of Mechanical Engineers, New York.

Astarita, G. (1967). *Mass Transfer with Chemical Reaction,* Elsevier, Amsterdam.

Ataki, A. and Bart, H. J. (2002). "Experimental Study of Rivulet Liquid Flow on an Inclined Plate." *International Conference on Distillation & Absorption,* 634th event of the European Federation of Chemical Engineering, Baden-Baden, Germany.

Bennett, D. L. and Ludwig, K. A. (1994). "Understand the Limitations of Air/Water Testing of Distillation Equipment", *Chem. Eng. Prog.,* **90,** 72.

Billet, R. (1995). *Packed Towers in Processing and Environmental Technology,* VCH, Weinheim.

Billingham, J. F. and Lockett, M. J. (1999). "Development of a New Generation of Structured Packings for Distillation", *Trans. IChemE,* **77,** 583.

Bird, R. B., Stewart, W. E. and Lightfoot, E. N. (1960). *Transport Phenomena,* John Wiley & Sons, New York.

Blauwhoff, P. M. M., Versteeg, G. F. and Van Swaaij, W. P. M. (1982). "A Study on the Reaction between CO2 and Alkanolamines in Aqueous Solutions", *Chem. Eng. Sci.,* **39,** 207.

Boston, J. F. and Sullivan, S. L. (1972). "An Improved Algorithm for Solving Mass Balance Equations in Multistage Separation Processes", *Can. J. Chem. Eng.,* **50,** 663.

Bratzler, K. and Doerges, A. (1974). "Amisol process purfies gases", *Hydrocarbon Proc,* **1974,** 78.

Bravo, J. L., Rocha, J. A. and Fair, J. R. (1985). "Mass transfer in gauze packings", *Hydrocarbon Process.,* **64,** 91.

Brunazzi, E. and Pagliante, A. (1997). "Mechanistic Pressure Drop Model for Columns Containing Structured Packings", *AIChE J.,* **43,** 317.

Brunazzi, E. and Paglianti, A. (1997). "Liquid-Film Mass-Transfer Coefficient in a Column Equipped with Structured Packings", *Ind. Eng. Chem. Res.,* **36,** 3792.

Brunazzi, E., Nardini, G., Paglianti, A. and Petarca, L. (1995). "Interfacial Area of Mellapak Packing: Absorption of 1,1,1-Trichloroethane by Genosorb 300", *Chem. Eng. Technol.,* **18,** 248.

Charpentier, J. C. (1981). Mass Transfer Rates in Gas-Liquid Absorbers. In *Advances in Chemical Engineering*, Vol. 11 Academic Press, New York.

Chen, G. K., Kitterman, L. and Shieh, J. H. (1983). "High-Efficiency Packing for Product Separation", *Chem. Eng. Prog.,* **79,** 46.

Chilton, T. H. and Colburn, A. P. (1935). "Distillation and Absorption in Packed Columns", *Ind. Eng. Chem.,* **27,** 255.

Cho, K., Irvine, T. F. j. and Karni, J. (1992). "Measurement of the diffusion coefficient of naphthalene into air", *Int. J. Heat Mass Transfer,* **35,** 957.

Ciofalo, M. (1996). "Large-eddy simulations of turbulent flow with heat transfer in simple and complex geometries using Harwell-FLOW3D", *Appl. Math. Modelling,* **20,** 262.

Ciofalo, M., Stasiek, J. and Collins, M. W. (1996). "Investigation of flow and heat transfer in corrugated passages - 2. Numerical simulations", *Int. J. Heat Mass Transfer,* **39,** 165.

Colburn, A. P. (1941). "Simplified Calculation of Diffusional Processes", *Ind. Eng. Chem.,* **33,** 459.

Coulson, J. M. and Richardson, J. F. (1991). *Coulson & Richardson's Chemical Engineering Vol 1,* Butterworth Heinemann, Oxford.

Crause, J. C. (1998). A fundamental mass transfer model for an extractive distillation application. Stellenbosch, University of Stellenbosch.

Crause, J. C. and Nieuwoudt, I. (1999). "Mass Transfer in a Short Wetted-Wall Column. 1. Pure Components", *Ind. Eng. Chem. Res.,* **38,** 4928.

Cussler, E. L. (1984). *Diffusion: Mass Transfer in Fluid Systems,* Cambridge University Press, Cambridge.

Danckwerts, P. V. (1951). "Significance of Liquid Film Coefficients in Gas Absorption", *Ind. Eng. Chem.,* **43,** 1460.

Danckwerts, P. V. (1970). *Gas-Liquid Reactions,* McGraw-Hill, New York.

Danckwerts, P. V. (1979). "The Reaction of CO2 with Ethanolamines", *Chem. Eng. Sci.,* **34,** 443.

Danckwerts, P. V. and Sharma, M. M. (1966). "The Absorption of Carbon Dioxide into Solutions of Alkalis and Amines", *The Chemical Engineer,* **44,** CE244.

Darton, R. C. (1992). "Distillation and Absorption Technology: Current Market and New Developments", *IChemE Symp. Ser.,* **128,** A385.

Daugherty, R. L. and Franzini, J. B. (1977). *Fluid Mechanics with Engineering Application,* McGraw-Hill, Tokyo.

Davies, G. A., Ponter, A. B. and Craine, K. (1967). "The Diffusion of Carbon Dioxide in Organic Liquids", *Can. J. Chem. Eng.,* **45,** 372.

Davis, R. A. and Sandall, O. C. (1993). "Kinetics of the Reaction of Carbon Dioxide with Secondary Amines in Polyethylene Glycol", *Chem. Eng. Sci.,* **48,** 3187.

De Brito, M. H., Von Stockar, U., Bangerter, A. M., Bomio, P. and Laso, M. (1994). "Effective Mass-Transfer Area in a Pilot Plant Column Equipped with Structured Packings and with Ceramic Rings", *Ind. Eng. Chem. Res.,* **33,** 647.

Deibele, L. (1991). "Die Entwicklung der Destillationstechnik von ihren Anfangen bis zum Jahre 1800", *Chem. Ing. Tech.,* **63,** 458.

Deibele, L. (1994). "Die Entwicklung der Destillationstechnik im 19. Jahrhundert", *Chem. Ing. Tech.,* **66,** 809.

Dudukovic, A., Milosevic, V. and Pjanovic, R. (1996). "Gas-Solid and Gas-Liquid Mass-Transfer Coefficients", *AIChE J.,* **42,** 269.

Emmert, R. E. and Pigford, R. L. (1954). "Interfacial resistance", *Chem. Eng. Progr.,* **50,** 87.

Erasmus, A. B. (1999). Mass Transfer in Structured Packing. University of Stellenbosch, Stellenbosch.

Erasmus, A. B. and Nieuwoudt, I. (2001). "Mass transfer in structured packing: A wetted-wall study", *Ind. Eng. Chem. Res.,* **40,** 2310.

Fair, J. R. and Bravo, J. L. (1990). "Distillation columns containing structured packing", *Chem. Eng. Prog.,* **January,** 19.

Fair, J. R., Seibert, A. F., Behrens, M., Saraber, P. P. and Olujic, Z. (2000). "Structured Packing Performance - Experimental Evaluation of Two Predictive Models", *Ind. Eng. Chem. Res,* **39,** 1788.

Ferzigier, J. H. and Peric, M. (1996). *Computational Methods for Fluid Mechanics,* Springer, Berlin.

Focke, W. W., Zachariades, J. and Olivier, I. (1985). "The effect of the corrugation inclination angle on the thermohydraulic performance of plate heat exchangers", *Int. J Heat Mass Transfer,* **28,** 1469.

Foust, A. S., Wentzel, L. A., Clump, C. W., Maus, L. and Anderson, L. B. (1980). *Principles of Unit Operations,* John Wiley & Sons, New York.

Gilliland, E. R. and Sherwood, T. K. (1934). "Diffusion of vapors into an air stream", *Ind. Eng. Chem.,* **26,** 516.

Henley, E. J. and Seader, J. D. (1981). *Equilibrium-Stage Operations in Chemical Engineering,* Wiley, New York.

Higler, A., Krishna, R. and Taylor, R. (1999a). "Nonequilibrium Cell Model for Multicomponent (Reactive) Separation Processes", *AIChE J.,* **45,** 2357.

Higler, A., Krishna, R. and Taylor, R. (1999b). "Nonequilibrium Cell Model for Packed Distillation Columns - The Influence of Maldistribution", *Ind. Eng. Chem. Res.,* **38,** 3988.

Higler, A., Taylor, R. and Krishna, R. (1998). "Modeling of a Reactive Separation Process Using a Nonequilibrium Stage Model", *Computers Che. Engng.,* **22,** S111.

Hikita, H. and Asai, S. (1964). *Int. Chem. Eng.,* **4,** 332.

Hirsch, C. (1988). *Numerical Computation of Internal and External Flows,* John Wiley & Sons, New York.

Hodson, J. (1997). Computational Fluid Dynamical Studies of Structured Distillation Packings. University of Aston, Birmingham, UK.

Hodson, J. S., Fletcher, J. P. and Porter, K. E. (1997). "Fluid Mechanical Studies of Structured Distillation Packings", *IChemE Symp. Series,* **142,** 999.

Holland, C. D. (1975). *Fundamentals and Modelling of Separation Processes,* Prentice-Hall, New York.

Iliuta, I. and Larachi, F. (2001). "Mechanistic Model for Structured-Packing-Containing Columns: Irrigated Pressure Drop, Liquid Holdup, and Packing Fractional Wetted Area", *Ind. Eng. Chem. Res.,* **40,** 5140.

Incropera, F. P. and De Witt, D. P. (1990). *Fundamentals of Heat and Mass Transfer,* Wiley, New York.
Johnstone, H. F. and Pigford, R. L. (1942). *Trans. Am. Inst. Chem. Engrs.,* **38,** 25.

Jones, W. P. and Launder, B. E. (1972). "The Prediction of Laminarization with a Two-Equation Model of Turbulence", *Int. J. Heat Mass Transfer,* **15,** 301.

Karimi, G. and Kawaji, M. (1999). "Flow charateristics and circulatory motion in wavy falling films with and without counter-current gas flow", *Int. J. Multiphase Flow,* **25,** 1305.

King, C. J. (1980). *Separation Processes,* McGraw-Hill, New York.

Kister, H. Z. (1992). *Distillation Design,* McGraw-Hill, New York.

Kister, H. Z. and Gill, D. R. (1992). In *Distillation and Absorption 1992*, Vol. 1 Hemisphere, Birmingham, pp. A109.

Krishna, R. (1977). "A Generalized Film Model for Mass Transfer in Non-Ideal Fluid Mixtures", *Chem. Eng. Sci.,* **32,** 659.

Krishna, R. and Standart, G. L. (1976). "A Multicomponent Film Model Incorporating an Exact Matrix Method of Solution to the Maxwell-Stefan Equations", *AIChE J,* **22,** 383.

Krishna, R. and Standart, G. L. (1979). "Mass and Energy Transfer in Multicomponent Systems", *Chem. Eng. Commun.,* **3,** 201.

Krishna, R., Martinez, H. F., Sreedhar, R. and Standart, G. L. (1977). "Murphree Point Efficiencies in Multicomponent Systems", *Trans. Inst. Chem. Engrs.,* **55,** 178.

Krishna, R., Van Baten, J. M., Ellenberger, J., Higler, A. P. and Taylor, R. (1999). "CFD Simulations of Sieve Tray Hydrodynamics", *Trans. IChemE,* **77,** 639.

Krishnamurthy, R. and Taylor, R. (1985a). "A Nonequilibrium Stage Model of Multicomponent Separation Processes. Part 1: Model Description and Method of Solution", *AIChE J.,* **31,** 449.

Krishnamurthy, R. and Taylor, R. (1985b). "A Nonequilibrium Stage Model of Multicomponent Separation Processes. Part 2: Comparison with Experiment", *AIChE J.,* **31,** 456.

Krishnamurthy, R. and Taylor, R. (1985c). "A Nonequilibrium Stage Model of Multicomponent Separation Processes. Part 3: The Influence of Unequal Component-Efficiencies in Process Design Problems", *AIChE J.,* **31,** 1973.

Larachi, F., Petre, C. F., Iliuta, I. and Grandjean, B. (2003). "Tailoring the pressure drop of structured packing through CFD simulations", *Chem. Eng. Proc.,* **42,** 535.

Laso, M., De Brito, M. H., Bomio, P. and Von Stockar, U. (1995). "Liquid-side mass transfer characteristics of a structured packing", *Chem. Eng. J.,* **58,** 251.

Levich, V. G. (1962). *Physicochemical Hydrodynamics,* Prentice-Hall, New York.

Littel, R. J., Versteeg, G. F. and Van Swaaij, W. P. M. (1992). "Kinetics of CO2 with Primary and Secondary Amines in Aqueous Solutions - I. Zwitterion Deprotonation Kinetics for DEA and DIPA in Aqueous Blends of Alkanolamines", *Chem. Eng. Sci.,* **47,** 2027.

McNulty, K. J. and Hsieh, C. L. (1982). "Hydraulic Performance and Efficiency of Koch Flexipac Structured Packings." *AIChE Annual Meeting,* Los Angeles, California.

Menter, F. R. (1992). "Influence of Freestream Values on k-ω Turbulence Model Predictions", *AIAA J.,* **30,** 1657.

Menter, F. R. (1994). "Two-Equation Eddy-Viscosity Turbulence Models for Engineering Applications", *AIAA J.,* **32,** 1598.

Menter, F. R. and Grotjans, H. (2000). In *Calculation of Complex Turbulent Flows* (Ed, Tzabiras, G.) WIT Press, Southampton.

Mohamed Ali, A., Jansens, P. and Olujic, Z. (2002). "Experimental Characterisation and CFD Simulation of Gas Distribution Performance of Liquid (Re)Distributors and Collectors in Packed Columns." *International Conference on Distillation & Absorption,* Baden-Baden, Germany.

Naphtali, L. M. and Sandholm, D. P. (1971). "Multicomponent Separation Calculations by Linearization", *AIChE J.,* **17,** 148.

Nawrocki, P. A. and Chuang, K. T. (1996). "Carbon Dioxide Absorption into a Stable Liquid Rivulet", *Can. J. Chem. Eng.,* **74,** 247.

Nawrocki, Z. A., XU, Z. P. and Chuang, K. T. (1991). "Mass Transfer in Structured Corrugated Packing", *Can. J. Chem. Eng.,* **69,** 1336.

Nesic, S. and Postlethwaite, J. (1992). "Calculation of wall-mass transfer rates in separated flow using a low Reynolds number k-ε model", *Int. J. Heat Mass Transfer,* **35,** 1977.

Nesic, S., Adamopoulos, G., Postlethwaite, J. and Bergstrom, D. J. (1993). "Modelling of Turbulent Flow and Mass Transfer with Wall Function and Low-Reynolds Number Closures", *Can. J. Chem. Eng.,* **71,** 28.

Nieuwoudt, I. (2001). "Structured packing evaluation 350Y HC & 350Y", Confidential research report, Institute for Thermal Separations, Stellenbosch.

Nieuwoudt, I. (December 2003). Private communication.

Olujic, Z. (1997). "Development of a Complete Simulation Model for Predicting the Hydraulic and Separation Performance of Distillation Columns Equipped with Structured Packings.", *Chem. Biochem. Eng. Q.,* **11,** 31.

Olujic, Z., Kamerbeek, A. B. and De Graauw, J. (1999). "A corrugation geometry based model for the efficiency of structured distillation packing", *Chem. Eng. Process.,* **38,** 683.

Onken, U. and Arlt, W. (1990). *Recommended Test Mixtures for Distillation Columns,* The Institution of Chemical Engineers, Rugby, Warwickshire, England.

Patankar, S. V. (1980). *Numerical Heat Transfer and Fluid Flow,* McGraw-Hill, New York.

Patel, V. C., Rodi, W. and Scheurer, G. (1985). "Turbulence Models for Near-Wall and Low Reynolds Number Flows: A Review", *AIAA J.,* **23,** 1308.

Petre, C. F., Larachi, F., Iliuta, I. and Grandjean, B. P. A. (2003). "Pressure drop through structured packings: Breakdown into the contributing mechanisms by CFD modeling", *Chem. Eng. Sci.,* **58,** 163.

Porta (1553). *Natural Magic,* Naples.

Powers, M. F., Vickery, D. J., Arehole, A. and Taylor, R. (1988). "A Nonequilibrium Stage Model of Multicomponent Separation Processes - V. Computational Methods for Solving the Model Equations", *Comput. Chem. Engng.,* **12,** 1229.

Ranke, H., Lerzer, R. and Becker, O. (2000). "Hydraulic Calculations for Cross-channeled Packings in Distillation Units Based on a Physical Model", *Chem. Eng. Technol.,* **23,** 691.

Reid, R. C., Prausnitz, J. M. and Polling, B. E. (1986). *The Properties of Gases and Liquids,* McGraw-Hill, New York.

Rhie, C. M. and Chow, W. L. (1983). "Numerical Study of the Turbulent Flow Past an Airfoil with Trailing Edge Separation", *AIAA J.,* **21,** 1525.

Rieger, R., Weiss, C., Wigley, G., Bart, H. J. and Marr, R. (1996). "Investigating the Process of Liquid-Liquid Extraction by Means of Computational Fluid Dynamics", *Computers Chem. Engng.,* **20,** 1467.

Robbins, L. A. (1991). "Improve Pressure-Drop Prediction With a New Correlation", *Chem. Eng. Prog.,* **87**.

Roberts, D. and Danckwerts, P. V. (1962). "Kinetics of CO2 absorption in alkaline solutions - I Transient absorption rates and catalysis by arsenite", *Chem. Eng. Sci.,* **17,** 961.

Rocha, J. A. and Bravo, J. L. (1996). "Distillation Columns Containing Strutured Packings: A comprehensive Model for their performance. 2. Mass-Transfer Model", *Ind. Eng. Chem. Res.,* **35,** 1660.

Rocha, J. A., Bravo, J. L. and Fair, J. R. (1993). "Distillation Columns Containing Structured Packings: A Comprehensive Model for Their Performance. 1. Hydraulic Models", *Ind. Eng. Chem. Res.,* **32,** 641.

Rocha, J. A., Bravo, J. L. and Fair, J. R. (1993). "Distillation Columns Containing Structured Packings: A Comprehensive Model for Their Performance. 1. Hydraulic Models", *Ind. Eng. Chem. Res.,* **32,** 641-651.

Sada, E., Kumazawa, H. and Butt, M. A. (1976). "Gas Absorption with Consecutive Chemical Reaction: Absorption of Carbon Dioxide into Aqueous Amine Solutions", *Can. J. Chem. Eng.,* **54,** 421.

Sada, E., Kumazawa, H., Han, Z. Q. and Matsuyama, H. (1985). "Chemical Kinetics of the Reaction of Carbon Dioxide with Ethanolamines in Nonaqueous Solvents", *AIChE J.,* **31,** 1297.

Sada, E., Kumazawa, H., Ikehara, Y. and Han, Z. Q. (1989). "Chemical Kinetics of the Reaction of Carbon Dioxide with Triethanolamine in Non-aqueous Solvents", *Chem. Eng. J.,* **40,** 7.

Sada, E., Kumazawa, H., Osawa, Y., Matsuura, M. and Han, Z. Q. (1986). "Reaction Kinetics of Carbon Dioxide with Amines in Non-aqueous Solvents", *Chem. Eng. J.,* **33,** 87.

Schlichting, H. (1979). *Boundary Layer Theory,* McGraw-Hill, New York.

Seader, J. D. and Henley, E. J. (1998). *Separation Process Principles,* John Wiley & Sons, New York.

Shahi, P., Hu, Y. and Chakma, A. (1994). "Gas chromatographic analysis of acid gases and single/mixed alkanolamines", *J. Chromatogr. A,* **687,** 121.

Shanley, A. (2000). "CFD for the Real World", *Chemical Engineering,* October**,** 139.

Sharma, M. M. and Danckwerts, P. V. (1970). "Chemical methods of measuring interfacial area and mass transfer coefficients in two-fluid systems.", *British Chem. Eng.,* **15,** 522.

Sherwood, T. K., Pigford, R. L. and Wilke, C. R. (1975). *Mass Transfer,* McGraw-Hill, New York.

Shetty, S. and Cerro, R. L. (1997). "Fundamental Liquid Flow Correlations for the Computation of Design Parameters for Ordered Packings", *Ind. Eng. Chem. Res.,* **36,** 771.

Shi, M. G. and Mersmann, A. (1985). "Effective Interfacial Area in Packed Columns", *Ger. Chem. Eng.,* **8,** 87.

Shulman, H. L., Ullrich, C. F., Proulx, A. Z. and Zimmerman, J. O. (1955). "Wetted and Effective-interfacial Areas, Gas- and Liquid-phase Mass Transfer Rates", *AIChE J.,* **1,** 253.

Sideman, S. and Pinczewski, W. V. (1975). Turbulent Heat and Mass Transfer at Interfaces: Transport Models and Mechanisms. In *Transport Phenomena* (Ed, Gutfinger, C.) Hemisphere, Washington.

Spiegel, L. and Meier, W. (1987). "Correlations of the performance characteristics of the various Mellapak types", *Inst. Chem. Eng. Symp. Ser.,* **104,** A203.

Sridharan, K. and Sharma, M. M. (1976). "New Systems and Methods for the Measurement of Effective Interfacial Area and Mass Transfer Coefficients in Gas-Liquid Contactors", *Chem. Eng. Sci.,* **31,** 767.

Stasiek, J., Collins, M. W., Ciofalo, M. and Chew, P. E. (1996). "Investigation of flow and heat transfer in corrugated passages - 1. Experimental results", *Int. J. Heat Mass Transfer,* **39,** 149.

Stephan, K. and Hildwein, H. (1987). *Recommended Data of Selected Compounds and Binary Mixtures,* Dechema, Frankfurt.

Stichlmair, J., Bravo, J. L. and Fair, J. R. (1989). "General model for prediction of pressure drop and capacity of countercurrent gas/liquid packed columns", *Gas Sep. Purif.,* **3,** 19.

Stirba, C. and Hurt, D. M. (1955). "Turbulence in falling liquid films", *AIChE J.,* **1,** 178-184.

Stoter, C. F. (1993). Modelling of Maldistribution in Structured Packings: From detail to column design. Delft University of Technology, Delft.

Suess, P. and Spiegel, L. (1992). "Hold-up of Mellapak structured packings", *Chem. Eng. Process.,* **31,** 119.

Taylor, R. and Krishna, R. (1993). *Multicomponent Mass Transfer,* John Wiley & Sons, New York.

Taylor, R., Kooijman, H. A. and Hung, J.-S. (1994). "A Second Generation Nonequilibrium Model for Computer Simulation of Multicomponent Separation Processes", *Computers Chem. Engng.,* **18,** 205.

Tomich, J. F. (1970). "A New Simulation Method for Equilibrium Stage Process", *AIChE J.,* **16,** 229.

Toor, H. L. and Marchello, J. M. (1958). "Film-penetration Model for Mass and Heat Transfer", *AIChE J,* **4,** 97.

Van Baten, J. M., Ellenberger, J. and Krishna, R. (2001). "Radial and axial dispersion of the liquid phase within a KATAPAK-S structure: experiments vs. CFD simulations", *Chem. Eng. Sci.,* **56,** 813.

Van Doormal, J. P. and Raithby, G. D. (1984). "Enhancements to the SIMPLE Method for Predicting Incompressible Fluid Flows", *Numer. Heat Transfer,* **7,** 147.

Verschoof, H.-J., Olujic, Z. and Fair, J. R. (1999). "A General Correlation for Predicting the Loading Point of Corrugated Sheet Structured Packings", *Ind. Eng. Chem. Res.,* **38,** 3663-3669.

Versteeg, G. F. and Van Swaaij, P. M. (1988). "On the Kinetics between CO2 and Alkanolamines both in aqueous and Non-aqueous Solutions - I. Primary and Secondary Amines", *Chem. Eng. Sci.,* **43,** 573.

Vogelpohl, A. (1979). "Murphree Efficiencies in Multicomponent Systems", *Int. Chem. Eng. Symp. Ser.,* **56,** 25.

Wall, J. (1975). "Gas Processing Handbook", *Hydrocarbon Process,* **54,** 79.

Wang, J. and Shirazi, S. A. (2001). "A CFD based correlation for mass transfer coefficient in elbows", *Int. J. Heat Mass Transfer,* **44,** 1817.

Wang, J. C. and Henke, G. E. (1966). "Tridiagonal Matrix for Distillation", *Hydrocarbon Process*., August**,** 155.

Wehrli, M., Hirschberg, S. and Schweizer, R. (2002). " Influence of Vapor Feed Design on the Flow Distribution." In *International Conference on Distillation & Absorption,* 634th event of the European Federation of Chemical Engineering, Baden-Baden, Germany.

Weiland, R. H., Ahlgren, K. R. and Evans, M. (1993). "Mass-Transfer Characteristics of Some Structured Packings", *Ind. Eng. Chem. Res.,* **32,** 1411.

Weimer, T. and Schaber, K. (1997). " Absorption of CO_2 from the atmosphere as a method for the estimation of effective interfacial areas in packed columns." In *Distillation and Absorption '97*(Ed, Darton, R.) IChemE.

Wesselingh, J. A. (1997). "Non-Equilibrium Modelling of Distillation", *Trans. IChemE,* **75,** 529.

Whitman, W. G. (1923). "The Two-film Theory of Absorption", *Chem. Met. Eng.,* **29,** 146.

Wilcox, D. C. (1988). "Reassessment of the Scale Determining Equation for Advanced Turbulence Models", *AIAA J.,* **26,** 1299.

Wilcox, D. C. (1993a). "Comparison of Two-Equation Turbulence Models for Boundary Layers with Pressure Gradient", *AIAA J.,* **31,** 1414.

Wilcox, D. C. (1993b). *Turbulence Modelling for CFD,* .DCW Industries, La Canada, California.

Woerlee, G. F., Berends, J., Olujic, Z. and De Graauw, J. (2001). "A comprehensive model for the pressure drop in vertical pipes and packed columns", *Chem. Eng. J.,* **84,** 367.

Yin, F. H., Sun, C. G., Afacan, A., Nandakumar, K. and Chuang, K. T. (2000). "CFD Modeling of Mass-Transfer Processes in Randomly Packed Distillation Columns", *Ind. Eng. Chem. Res.,* **39,** 1369.

APPENDIX A

Constants and production terms for turbulence equations

A1 The k-ε model

Production term:

$$P_k = 2\mu_t\left[\left(\frac{\partial \bar{U}_x}{\partial x}\right)^2+\left(\frac{\partial \bar{U}_y}{\partial y}\right)^2+\left(\frac{\partial \bar{U}_z}{\partial z}\right)^2\right]+ \mu_t\left[\left(\frac{\partial \bar{U}_x}{\partial y}+\frac{\partial \bar{U}_y}{\partial x}\right)^2+\left(\frac{\partial \bar{U}_y}{\partial z}+\frac{\partial \bar{U}_z}{\partial y}\right)^2+\left(\frac{\partial \bar{U}_z}{\partial x}+\frac{\partial \bar{U}_x}{\partial z}\right)^2\right] \quad \text{(A1.1)}$$

Model constants:

$$C_\mu = 0.09 \qquad \sigma_t^k = 1.0 \qquad \sigma_t^\varepsilon = 1.3 \qquad C_{\varepsilon 1} = 1.44 \qquad C_{\varepsilon 2} = 1.92 \quad \text{(A1.2)}$$

A2 The k-ω model

Production term:

$$P_k = \mu_t \nabla \mathbf{U}\cdot\left(\nabla \mathbf{U}+(\nabla \mathbf{U})^T\right)-\frac{2}{3}\nabla\bullet\mathbf{U}(\mu_T\nabla\bullet\mathbf{U}+\rho k) \quad \text{(A1.3)}$$

Model Constants:

$$\alpha^* = \frac{\alpha_0^* + Re_T/R_k}{1+Re_T/R_k} \quad \text{(A1.4)}$$

$$\alpha = \frac{5}{9}\frac{\alpha_0+Re_T/R_\omega}{1+Re_T/R_\omega}\frac{1}{\alpha^*} \quad \text{(A1.5))}$$

$$\beta^* = \frac{9}{100}\frac{5/18+\left(Re_T/R_\beta\right)^4}{1+\left(Re_T/R_\beta\right)^4} \quad \text{(A1.6)}$$

$$\beta = 3/40 \qquad \sigma_t^k = 0.5 \qquad \sigma_t^\omega = 0.5 \qquad \alpha_0^* = \beta/3 \qquad \alpha_0 = 0.1$$

$$R_\beta = 8.0 \qquad R_k = 6.0 \qquad R_\omega = 2.7 \quad \text{(A1.7)}$$

The turbulence Reynolds number is defined as:

$$Re_t = \frac{\rho k}{\omega\mu} \quad \text{(A1.8)}$$

A3 The BSL model

Production term:

$$P_k = \mu_t \nabla \mathbf{U} \cdot \left(\nabla \mathbf{U} + (\nabla \mathbf{U})^T\right) - \frac{2}{3}\nabla \bullet \mathbf{U}(\mu_T \nabla \bullet \mathbf{U} + \rho k) \quad \text{(A1.9)}$$

The constants for set 1 (C_1) are:

$$\sigma_{t1}^k = 0.5 \qquad \sigma_{t1}^\omega = 0.5 \qquad \beta_1 = 0.075$$

$$\beta^* = 0.09 \qquad \kappa = 0.41 \qquad \gamma_1 = \beta_1 / \beta^* - \sigma_{\omega 1}^t \kappa^2 / \sqrt{\beta^*} \quad \text{(A1.10)}$$

The constants for set 2 (C_2) are:

$$\sigma_{t2}^k = 1.0 \qquad \sigma_{t2}^\omega = 0.856 \qquad \beta_2 = 0.0828$$

$$\beta^* = 0.09 \qquad \kappa = 0.41 \qquad \gamma_2 = \beta_2 / \beta^* - \sigma_{\omega 2}^t \kappa^2 / \sqrt{\beta^*} \quad \text{(A1.11)}$$

The following definitions also apply:

$$\nu_t = \frac{k}{\omega} \quad \text{(A1.12)}$$

$$F_1 = \tanh\left(\arg_1^4\right) \quad \text{(A1.13)}$$

where

$$\arg_1 = \min\left[\max\left(\frac{\sqrt{k}}{0.09\omega y}; \frac{500\nu}{y^2\omega}\right); \frac{4\rho\sigma_{\omega 2}^t k}{CD_{k\omega} y^2}\right] \quad \text{(A1.14)}$$

and

$$CD_{k\omega} = \max\left(2\rho\sigma_{\omega 2}^t \frac{1}{\omega} \nabla k \nabla \omega; 10^{-20}\right) \quad \text{(A1.15)}$$

y is the distance to the nearest wall.

APPENDIX B

Table B.1 SRP model equations

(A) Hydraulic diameter

Vapour phase:

$$d_{hG} = \frac{\frac{(Bh - 2\delta S)^2}{Bh}}{\left[\left(\frac{Bh - 2\delta S}{2h}\right)^2 + \left(\frac{Bh - 2\delta S}{b}\right)^2\right]^{0.5} + \frac{Bh - 2\delta S}{2h}} \quad \text{(B1.1)}$$

(B) Effective phase velocities

$$u_{G,e} = \frac{u_{G,s}}{\varepsilon(1 - h_t)\sin\theta} \quad \text{(B1.2)}$$

$$u_{L,e} = \frac{u_{L,s}}{\varepsilon h_t \sin\theta} \quad \text{(B1.3)}$$

(C) Liquid hold-up

$$h_t = \left(4\frac{F_t}{S}\right)^{\frac{2}{3}} \left(\frac{3\mu_L u_{L,s}}{\rho_L (\sin\theta)\varepsilon g_{eff}}\right)^{\frac{1}{3}} \quad \text{(B1.4)}$$

where

$$g_{eff} = g\left[\left(\frac{\rho_L - \rho_G}{\rho_L}\right)\left(1 - \frac{\Delta P/\Delta z}{(\Delta P/\Delta z)_{flood}}\right)\right] \quad \text{(B1.5)}$$

and

$$F_t = \frac{29.12\left(We_{L,s}Fr_{L,s}\right)^{0.15} S^{0.359}}{Re_{L,s}^{0.2}\,\varepsilon^{0.6}\,(1 - 0.93\cos\gamma)(\sin\theta)^{0.3}} \quad \text{(B1.6)}$$

$$\cos\gamma = 0.9 \quad \text{for} \quad \sigma < 0.055 \quad [N/m] \quad \text{(B1.7)}$$

$$\cos\gamma = 5.211\times10^{-16.835\sigma} \quad \text{for} \quad \sigma > 0.055 \quad [N/m] \quad \text{(B1.8)}$$

(D) Pressure drop

Dry pressure drop:

$$\frac{\Delta P_d}{\Delta z} = \frac{f\rho_G u_{G,e}^{\,2}}{S} \quad \text{(B1.10)}$$

with the friction factor calculated from:

$$f = A + \frac{B}{Re_{G,s}} \quad \text{(B1.11)}$$

Pressure drop in preloading region:

$$\frac{\Delta P}{\Delta z} = \frac{\Delta P_d}{\Delta z}\left[\frac{1}{1 - K_2 h_t}\right]^5 \quad \text{(B1.12}$$

with $K_2 = 0.614 + 71.35S$ (B1.13)

Table B.1 SRP model equations (continued)

(D) Pressure drop (continued)

Loading region pressure drop:

$$\frac{\Delta P}{\Delta z} = \left(\frac{\Delta P}{\Delta z}\right)_{preload} F_{load} \tag{B1.14}$$

Pressure drop enhancement factor for loading region:

$$F_{load} = 3.8\left(\frac{F_G}{F_{G,lp}}\right)^{2/\sin\alpha}\left(\frac{u_{L,s}{}^2}{\varepsilon^2 g d_{hG}}\right)^{0.13} \tag{B1.15}$$

loading point F-factor

$$F_{G,lp} = \left(0.053\varepsilon^2 g d_{hG}\left(\rho_L - \rho_G\right)\left(\frac{u_{L,s}}{u_{G,s}}\sqrt{\frac{\rho_L}{\rho_G}}\right)^{-0.25}\left(\sin\theta\right)^{1.15}\right)^{0.5} \tag{B1.16}$$

(E) Mass transfer coefficients and effective surface area

Vapour phase:

$$Sh_G = 0.054\left(\frac{\left(u_{G,e} + u_{L,e}\right)\rho_G S}{\mu_G}\right)^{0.8} Sc_G{}^{0.33} \tag{B1.17}$$

Liquid phase:

$$k_L = 2\sqrt{\frac{D_L u_{L,e}}{\pi 0.9 S}} \tag{B1.18}$$

Effective surface:

$$\frac{a_e}{a_p} = F_{SE} \times F_t \tag{B1.19}$$

with F_{SE} = 0.35 for stainless steel sheet metal packing.

(F) Dimensionless groups

$$Fr_{L,s} = \frac{u_{L,s}{}^2}{Sg} \tag{B1.20}$$

$$Re_{G,s} = \frac{u_{G,s} S \rho_G}{\mu_G} \tag{B1.21}$$

$$Re_{L,s} = \frac{u_{L,s} S \rho_L}{\mu_L} \tag{B1.22}$$

$$Sc_G = \frac{\mu_G}{D_G \rho_G} \tag{B1.23}$$

$$Sh_G = \frac{k_G S}{D_G} \tag{B1.24}$$

$$We_{L,s} = \frac{u_{L,s}{}^2 S \rho_L}{\sigma} \tag{B1.25}$$

Table B.2 Delft model equations

(A) Hydraulic diameter for vapour phase and related parameters

Hydraulic diameter for vapour phase:

$$d_{hG} = \frac{\frac{(Bh - 2\delta S)^2}{Bh}}{\left[\left(\frac{Bh - 2\delta S}{2h}\right)^2 + \left(\frac{Bh - 2\delta S}{B}\right)^2\right]^{0.5} + \frac{Bh - 2\delta S}{2h}} \quad \text{(B2.1)}$$

Length of triangular gas flow channel in a packing element:

$$\ell_{G,pe} = \frac{h_{pe}}{\sin\alpha} \quad \text{(B2.2)}$$

V-shaped fraction of cross section of triangular channel occupied by liquid:

$$\varphi = \frac{2S}{b + 2S} \quad \text{(B2.3)}$$

(B) Effective phase velocities

$$u_{G,e} = \frac{u_{G,s}}{\varepsilon(1 - h_t)\sin\theta} \quad \text{(B2.4)}$$

$$u_{L,e} = \frac{u_{L,s}}{\varepsilon h_t \sin\theta} \quad \text{(B2.5)}$$

(C) Liquid hold-up

$$h_t = \delta a_p \quad \text{(B2.6)}$$

where

$$\delta = \left(\frac{3\mu_L u_{L,s}}{\rho_L g a_p \sin\theta}\right)^{\frac{1}{3}} \quad \text{(B2.7)}$$

(D) Pressure drop

Preloading region pressure drop:

$$\Delta P_{preload} = (\zeta_{GL} + \zeta_{GG} + \zeta_{DC})\frac{\rho_G u_{G,e}^{\ 2}}{2} \quad \text{(B2.8)}$$

overall vapour/liquid interaction coefficient

$$\zeta_{GL} = \varphi\xi_{GL}\frac{h_{pb}}{d_{hG}\sin\alpha} \quad \text{(B2.9)}$$

vapour/liquid friction factor

$$\xi_{GL} = \left\{-2\log\left[\frac{(\delta/d_{hG})}{3.7} - \frac{5.02}{Re_{G,r}}\log\left(\frac{(\delta/d_{hG})}{3.7} + \frac{14.5}{Re_{G,r}}\right)\right]\right\}^{-2} \quad \text{(B2.10)}$$

vapour/vapour interaction coefficient

$$\zeta_{GG} = (1 - \varphi)0.722(\cos\theta)^{3.14}\frac{h_{pb}}{d_{hG}\sin\theta} \quad \text{(B2.11)}$$

Table B.2 Delft model equations (continued)

(D) Pressure drop (continue)

directional change loss coefficient

$$\zeta_{DC} = \frac{h_{pb}}{h_{pe}}\left(\xi_{bulk} + \psi\xi_{wall}\right) \tag{B2.12}$$

with

$$\psi = \frac{2h_{pe}}{\pi {d_c}^2 \tan\theta}\left({d_c}^2 \frac{{h_{pe}}^2}{\tan^2\theta}\right)^{0.5} + \frac{2}{\pi}\arcsin\left(\frac{h_{pe}}{d_c \tan\theta}\right) \tag{B2.13}$$

$$\xi_{bulk} = 1.76(\cos\theta)^{1.63} \tag{B2.14}$$

$$\xi_{wall} = \frac{4092 {u_{L,s}}^{0.31} + 4715(\cos\theta)^{0.445}}{Re_{G,e}} + 34.19 {u_{L,s}}^{0.44}(\cos\theta)^{0.779} \tag{B2.15}$$

Loading region pressure drop:

$$\frac{\Delta P}{\Delta z} = \left(\frac{\Delta P}{\Delta z}\right)_{preload} F_{load} \tag{B2.16}$$

pressure drop enhancement factor for loading region:

$$F_{load} = 3.8\left(\frac{F_G}{F_{G,lp}}\right)^{2/\sin\alpha}\left(\frac{{u_{L,s}}^2}{\varepsilon^2 g d_{hG}}\right)^{0.13} \tag{B2.17}$$

loading point F-factor

$$F_{G,lp} = \left(0.053\varepsilon^2 g d_{hG}(\rho_L - \rho_G)\left(\frac{u_{L,s}}{u_{G,s}}\sqrt{\frac{\rho_L}{\rho_G}}\right)^{-0.25}(\sin\theta)^{1.15}\right)^{0.5} \tag{B2.18}$$

(E) Mass transfer coefficients and effective surface area

Vapour phase:

$$k_G = \sqrt{{k_{G,lam}}^2 + {k_{G,turb}}^2} \tag{B2.19}$$

with

$$\frac{k_{G,lam} d_{hG}}{D_G} = 0.664 {Sc_G}^{1/3}\sqrt{Re_{G,r}\frac{d_{hG}}{l_{G,pe}}} \tag{B2.20}$$

$$\frac{k_{G,turb} d_{hG}}{D_G} = \frac{Re_{G,r}\, Sc_G \frac{\xi_{GL}\varphi}{8}}{1 + 12.7\sqrt{\frac{\xi_{GL}\varphi}{8}}\left({Sc_G}^{2/3} - 1\right)}\left[1 + \left(\frac{d_{hG}}{\ell_{G,pe}}\right)^{2/3}\right] \tag{B2.21}$$

Liquid phase:

$$k_L = 2\sqrt{\frac{D_L u_{L,e}}{\pi 0.9 d_{hG}}} \tag{B2.22}$$

Table B.2 Delft model equations (continued)

(E) Mass transfer coefficients and effective surface area (cont.)

Effective surface area:

$$a_e = a_p \frac{(1-\Omega)}{\left(1+\frac{A}{(u_{Ls})^B}\right)} \quad \text{(B2.23)}$$

with $A = 2.143\times10^{-6}$, $B = 1.5$ for Montzpak B1-250 (B2.24)

(F) Dimensionless groups

$$Re_{G,r} = \frac{(u_{G,e}+u_{L,e})d_{hG}\rho_G}{\mu_G} \quad \text{(B2.25)}$$

$$Sc_G = \frac{\mu_G}{D_g\rho_G} \quad \text{(B2.26)}$$

Table B.3 Billet model equations

(A) Hydraulic diameter and related parameters

Particle diameter (used as hydraulic diameter for vapour phase in pressure drop calculations):

$$d_p = 6\frac{1-\varepsilon}{a_p} \quad \text{(B3.1)}$$

Hydraulic diameter in mass transfer correlations:

$$d_p = 6\frac{1-\varepsilon}{a_p} \quad \text{(B3.2)}$$

Film thickness for uniformly wetted packing:

$$\delta = \frac{h_t}{a_p} \quad \text{(B3.3)}$$

(B) Effective phase velocities

$$u_{G,e} = \frac{u_{G,s}}{\varepsilon - h_t} \quad \text{(B3.4)}$$

$$u_{L,e} = \frac{u_{L,s}}{\delta a_p} \quad \text{(B3.5)}$$

(C) Loading point

Vapour velocity at loading point:

$$(u_{G,s})_{lp} = \sqrt{\frac{g}{\xi_{lp}}}(\varepsilon - h_{t,lp})\sqrt{\frac{h_{t,lp}}{a}}\sqrt{\frac{\rho_L}{\rho_G}} \quad \text{(B3.6)}$$

Hold-up at loading point

$$h_{t,lp} = 12^{\frac{1}{3}}\left(\frac{u_{L,s}\rho_L}{a\mu_L}\right)^{-\frac{1}{3}}\left(\frac{{u_{L,s}}^2 a}{g}\right)^{\frac{1}{3}} \quad \text{(B3.7)}$$

Table B.3 Billet model equations (continued)

(C) Loading point (continued)

Resistance factor for loading point calculation:

$$\xi_{lp} = \frac{g}{C_{lp}^{\,2}\left[\psi\left(\frac{\mu_L}{\mu_G}\right)^{0.4}\right]^{2n_{lp}}} \tag{B3.8}$$

C_{lp} is packing specific and:

$$\begin{aligned}\psi \le 0.4 &\rightarrow n_{lp} = -0.326\\ \psi > 0.4 &\rightarrow n_{lp} = -0.723\end{aligned} \tag{B3.9}$$

and with the flow parameter defined as:

$$\psi = \frac{L}{G}\sqrt{\frac{\rho_G}{\rho_L}} \tag{B3.10}$$

(D) Flood point

Vapour velocity at flood point:

$$\left(u_{G,s}\right)_{fp} = \sqrt{\frac{2g}{\xi_{fp}}}\frac{\left(\varepsilon - h_{t,fp}\right)^{\frac{3}{2}}}{\varepsilon^{\frac{1}{2}}}\sqrt{\frac{h_{t,fp}}{a_p}}\sqrt{\frac{\rho_L}{\rho_G}} \tag{B3.11}$$

Liquid velocity at flood point:

$$\left(u_{L,s}\right)_{fp} = \frac{g}{3}\frac{1}{a_p^{\,2}}\frac{\rho_L}{\mu_L}h_{t,fp}^{\,3}\left(1 - \frac{3}{2}\frac{\left(\varepsilon - h_{t,fp}\right)}{\varepsilon}\right) \tag{B3.12}$$

Hold-up at flood point:

$$h_{t,fp} = 0.3741\varepsilon\left(\frac{\mu_L}{\rho_L}\frac{\rho_W}{\mu_W}\right)^{0.05} \quad \mu_L > 1\times10^{-4}\,[\mathrm{kg/(ms)}] \tag{B3.13}$$

Resistance factor for flood point calculation:

$$\xi_{fp} = \frac{g}{C_{fp}^{\,2}\left[\psi\left(\frac{\mu_L}{\mu_G}\right)^{0.2}\right]^{2n_{fp}}} \tag{B3.14}$$

C_{fp} is packing specific and:

$$\begin{aligned}\psi \le 0.4 &\rightarrow n_{fp} = -0.194\\ \psi > 0.4 &\rightarrow n_{fp} = -0.708\end{aligned} \tag{B3.15}$$

(E) Pressure drop

Pressure drop for dry bed:

$$\frac{\Delta P_d}{\Delta z} = \xi_d\frac{a}{\varepsilon^3}\frac{u_{G,s}^{\,2}}{2}\rho_G f_s \tag{B3.16}$$

Table B.3 Billet model equations (continued)

(E) Pressure drop (continued)

Resistance factor for dry bed

$$\xi_d = C_p\left(\frac{64}{Re_G} + \frac{1.8}{Re_G^{0.08}}\right) \quad \text{(B3.17)}$$

with the 'wall factor' calculated from:

$$\frac{1}{f_s} = 1 + \frac{4}{ad_c} \quad \text{(B3.18)}$$

Pressure drop for wet bed:

$$\frac{\Delta P}{\Delta P_d} = \frac{\xi_w}{\xi_d}\left(\frac{\varepsilon}{\varepsilon - h_t}\right)^3 \quad \text{(B3.19)}$$

Resistance factor for wet bed:

$$\xi_w = C_p W\left(\frac{64}{Re_{G,s}} + \frac{1.8}{Re_{G,s}^{0.08}}\right)\left(\frac{\varepsilon - h_t}{\varepsilon}\right)^{(3-x)} \quad \text{(B3.20)}$$

with

$$Re_{G,s} = \frac{u_{G,s} d_p \rho_G}{(1-\varepsilon)\mu_G} f_s \quad \text{(B3.21)}$$

and

$$W = \left[\exp\left(\frac{Re_{L,s}}{200}\right)\right]\left(\frac{h_t}{h_{t,lp}}\right)^{0.3} \quad \text{(B3.22)}$$

Numerical value for exponent x determined as x = 1.5

For determining pressure drop, the hold-up at (and below) the loading point is calculated with equation B3.6. The hold-up between load & flood points is calculated with:

$$(h_t)_{u_{G,s} > (u_{G,s})_{lp}} = h_{t,lp} + (h_{t,fp} - h_{t,lp})\left(\frac{u_{G,s}}{(u_{G,s})_{fp}}\right)^{13} \quad \text{(B3.23)}$$

(F) Liquid hold-up

Hold-up below the loading point:

$$(h_t)_{u_{G,s} \le (u_{G,s})_{lp}} = h_{t,lp} = \left(12\frac{\mu_L a_p^2 u_{L,s}}{\rho_L g}\right)^{\frac{1}{3}}\left(\frac{a_h}{a_p}\right)^{\frac{2}{3}} \quad \text{(B3.24)}$$

with the hydraulic area calculated from:

$$\left(\frac{a_h}{a_p}\right)_{Re_L < 5} = C_h Re_{L,s}^{0.15} Fr_{L,s}^{0.1} \quad \text{(B3.25)}$$

Table B.3 Billet model equations (continued)

(F) Liquid hold-up (continued)

$$\left(\frac{a_h}{a_p}\right)_{Re_L \geq 5} = 0.85 C_h \, Re_{L,s}^{0.25} \, Fr_{L,s}^{0.1} \qquad \text{(B3.26)}$$

Hold-up at the flood point:

$$h_{t,fp} \cong 2.2 h_{t,lp} \qquad \text{(B3.27)}$$

For hold-up between loading- and flood point, use equation B3.23

(G) Mass transfer coefficients and effective surface area

Liquid phase mass transfer coefficient below loading point:

$$k_L a_e = C_L \, g^{\frac{1}{6}} \left(\frac{\rho_L}{\mu_L}\right)^{\frac{1}{6}} \left(\frac{D_L}{d_h}\right)^{\frac{1}{2}} a^{\frac{2}{3}} u_{L,s}^{\frac{1}{3}} \frac{a_e}{a_p} \qquad \text{(B3.28)}$$

liquid phase mass transfer coefficient between loading- and flood point:

$$k_L a_e = 12^{\frac{1}{2}} C_L a_p u_{L,e}^{\frac{1}{2}} \left(\frac{D_L}{d_h}\right)^{\frac{1}{2}} \frac{a_e}{a_p} \qquad \text{(B3.29)}$$

Vapour phase mass transfer coefficient:

$$k_G a_e = C_G \frac{a^{1.5}}{\sqrt{d_h}} \frac{1}{\sqrt{\varepsilon - h_t}} D_G \, Re_{G,s}^{3/4} \, Sc_G^{1/3} \frac{a_e}{a_p} \qquad \text{(B3.30)}$$

C_L and C_G are packing specific.

Effective surface area at loading point:

$$\left(\frac{a_e}{a_p}\right)_{lp} = 3\varepsilon^{0.5} \, Re_{L,s}^{-0.2} \, We_{L,s}^{0.75} Fr_{L,s}^{-0.45} \qquad \text{(B3.31)}$$

Effective surface area between loading- and flood point:

$$\left(\frac{a_e}{a_p}\right)_{u_{G,s} > (u_{G,s})_{lp}} = \left(\frac{a_e}{a_p}\right)_{lp} + \left[\left(\frac{a_e}{a_p}\right)_{fp} - \left(\frac{a_e}{a_p}\right)_{lp}\right] \left(\frac{u_{G,s}}{(u_{G,s})_{fp}}\right)^{13} \qquad \text{(B3.32)}$$

Effective interfacial area at flood point:

$$\left(\frac{a_e}{a_p}\right)_{fp} = 7 \left(\frac{\sigma_L}{\sigma_W}\right)^{0.56} \left(\frac{a_e}{a_p}\right)_{lp} \qquad \text{(B3.33)}$$

effective interfacial area for negative surface tension gradient systems:

$$\left(\frac{a_e}{a_p}\right)_{neg} = \left(1 - 2.4 \cdot 10^{-4} \left|Ma_L\right|^{0.5}\right) \frac{a_e}{a_p} \qquad \text{(B3.34)}$$

where

$$Ma_L = \frac{\Delta x}{D_L \mu_L a_p} \qquad \text{(B3.35)}$$

Δx is concentration difference between bulk liquid and surface liquid

Table B.3 Billet model equations (continued)

(H) Dimensionless numbers

$$Re_{G,s} = \frac{u_{G,s}\rho_G}{a_p\mu_G} \quad \text{(B3.36)}$$

$$Re_{L,s} = \frac{u_{L,s}\rho_L}{a_p\mu_L} \quad \text{(B3.37)}$$

$$We_{L,s} = \frac{u_{L,s}^2\rho_L}{\sigma_L a_p} \quad \text{(B3.38)}$$

$$Fr_{L,s} = \frac{u_{L,s}^2 a_p}{g} \quad \text{(B3.39)}$$

$$Sc_G = \frac{\mu_G}{D_G\rho_G} \quad \text{(B3.40)}$$

APPENDIX C

Experimental data for Flexipac 350Y

The experimental pressure drop and hold-up data for Flexipac 350Y for the air/water system are given in Figures C.1 and C.2. The experimental data for the air/Kerosol 200 system are given in Figures C.3 and C.4. The experimental data are given in table format for the two test systems in Table C.1 and C.2. The dry pressure drop data are included in Table C.1.

Experimental data for Flexipac 350Y HC

The experimental pressure drop and hold-up data for Flexipac 350Y HC for the air/water system are given in Figures C.5 and C.6. The experimental data for the air/Kerosol 200 system are given in Figures C.7 and C.8. The experimental data are given in table format for the two test systems in Table C.3 and C.4. The dry pressure drop experimental data are included in Table C.3.

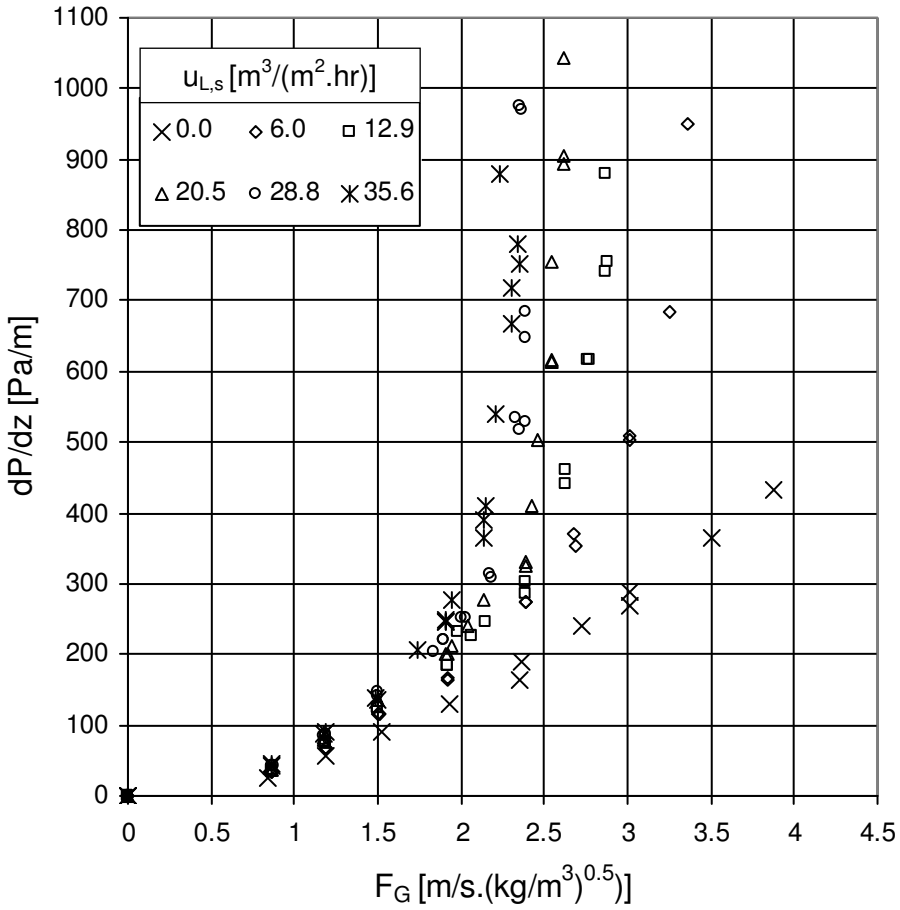

Figure C.1 Pressure drop as function of F-factor for Flexipac 350Y, air/water system

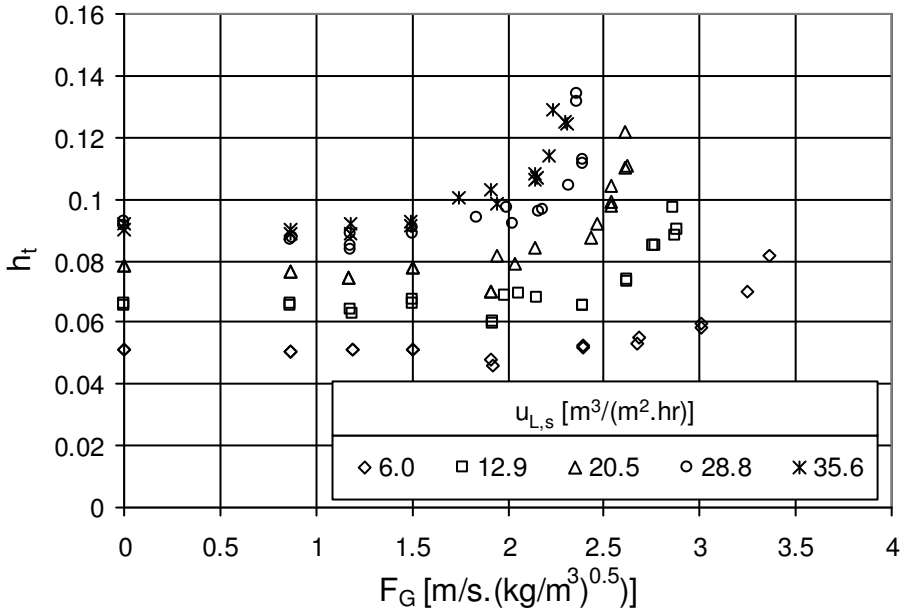

Figure C.2 Holdup as function of F-factor for Flexipac 350Y, air/water system

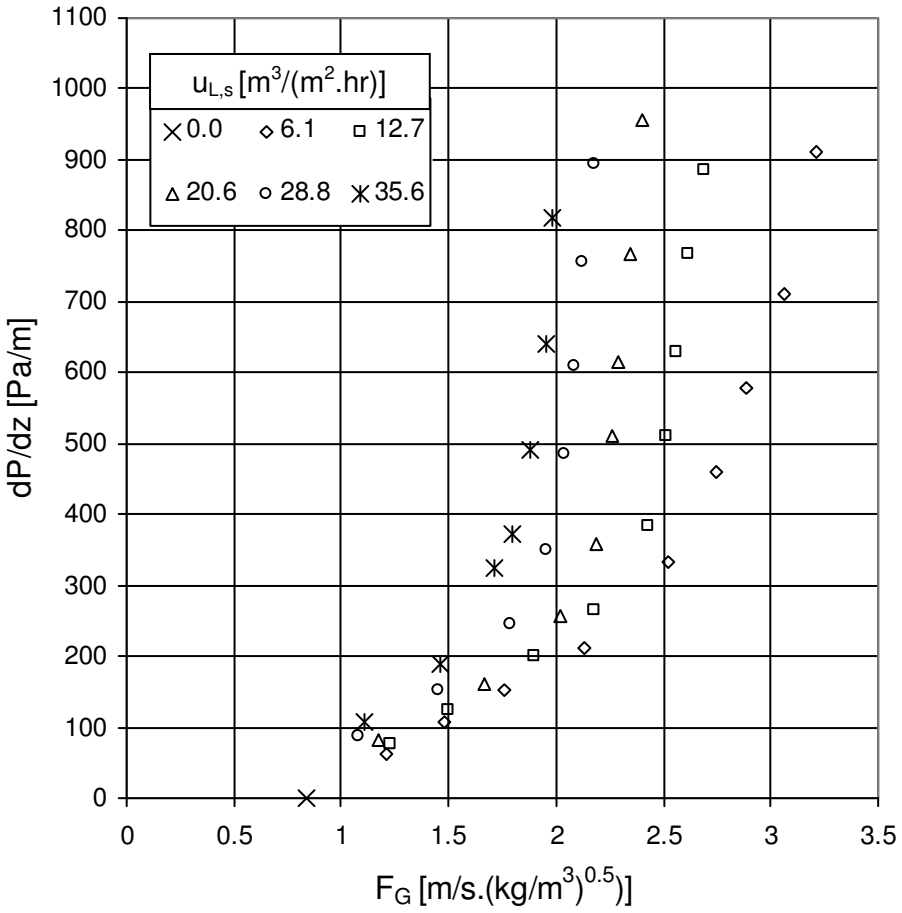

Figure C.3 Pressure drop as function of F-factor for Flexipac 350Y, air/Kerosol 200 system

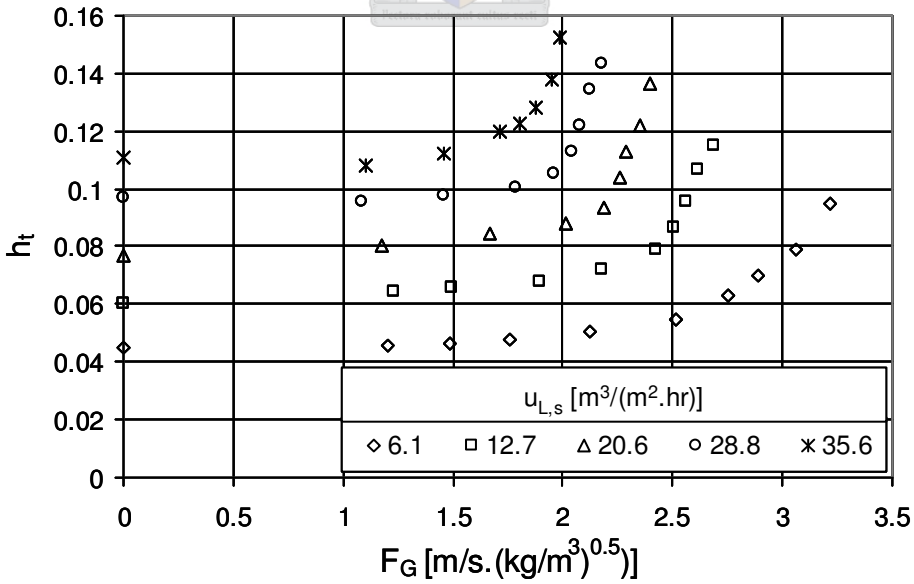

Figure C.4 Holdup as function of F-factor for Flexipac 350Y, air/Kerosol 200 system

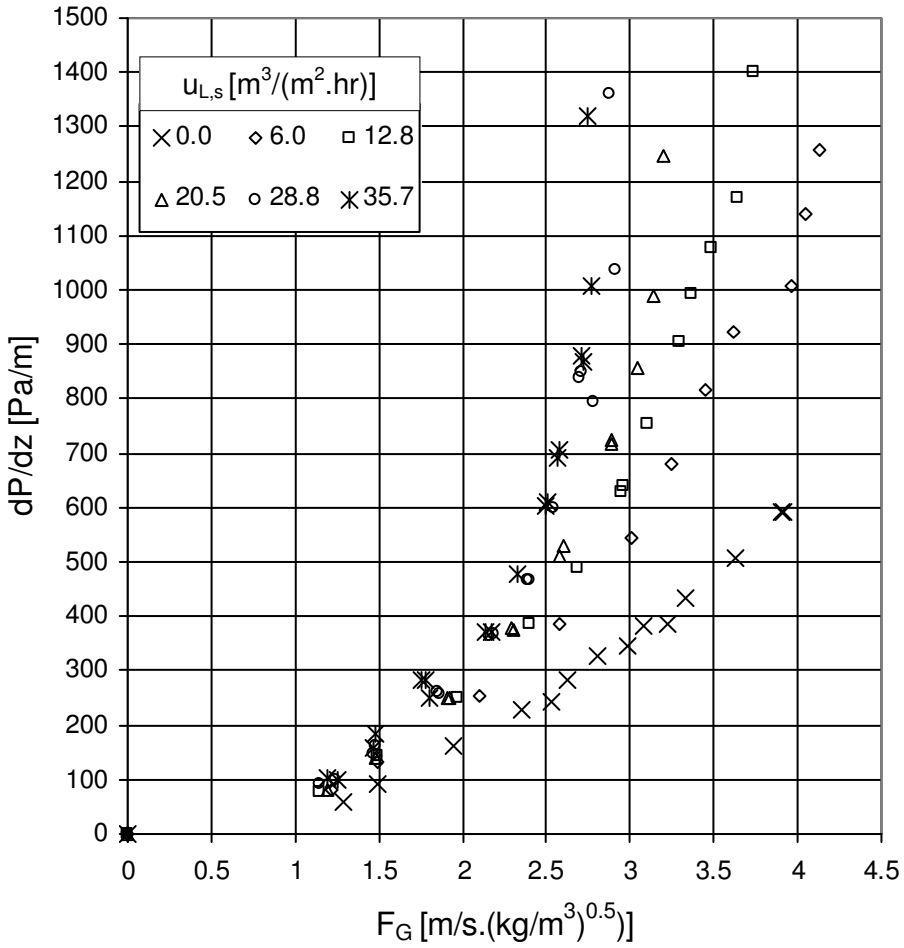

Figure C.5 Pressure drop as function of F-factor for Flexipac 350Y HC, air/water system

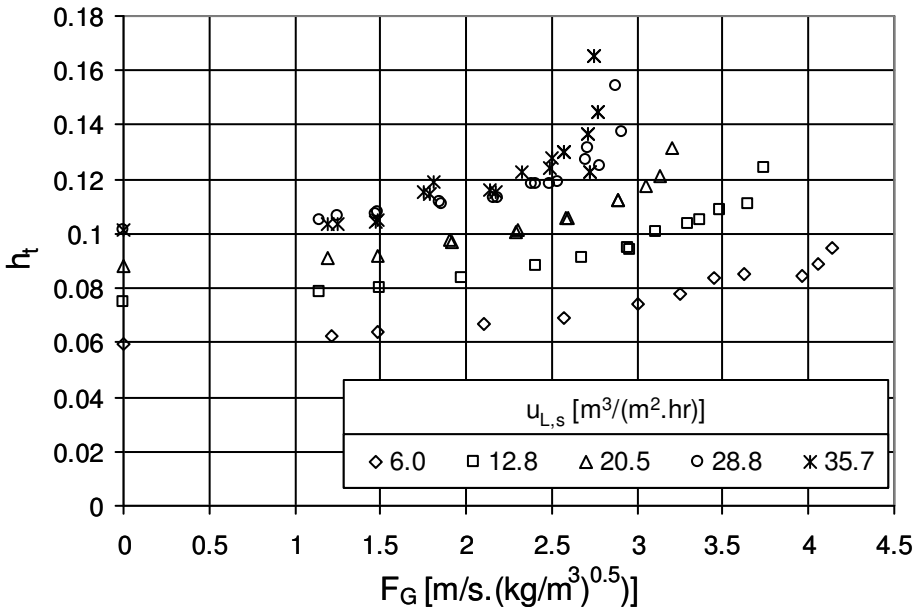

Figure C.6 Holdup as function of F-factor for Flexipac 350Y HC, air/water system

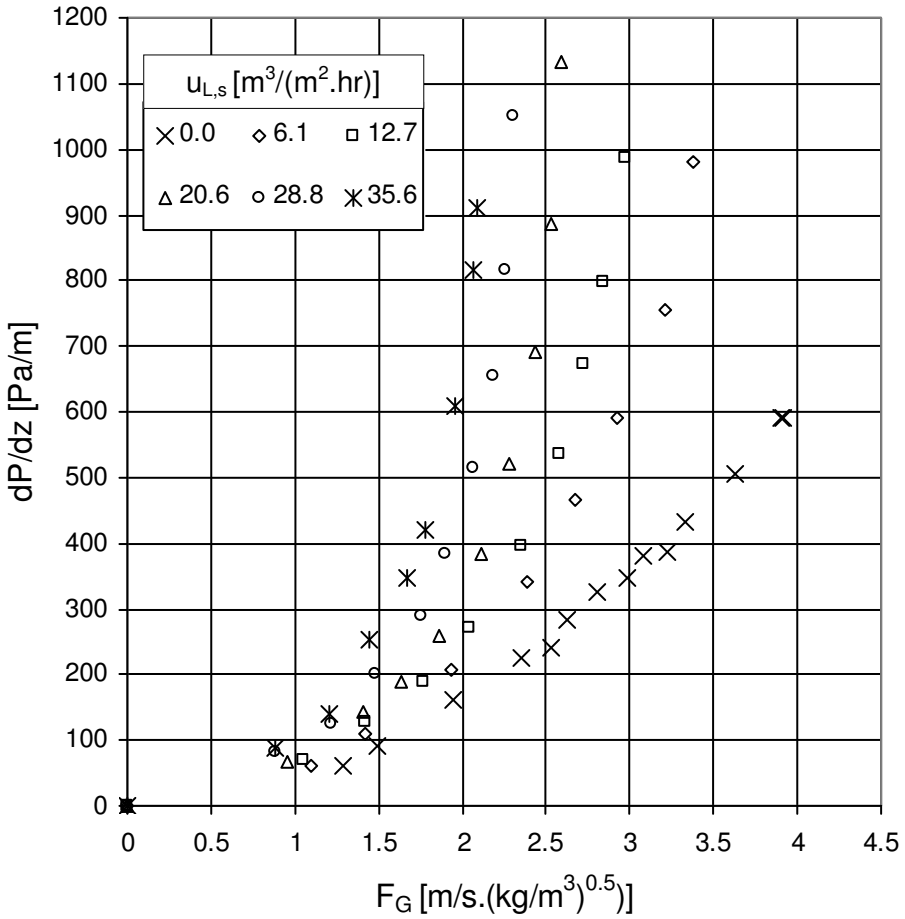

Figure C.7 Pressure drop as function of F-factor for Flexipac 350Y HC, air/Kerosol 200 system

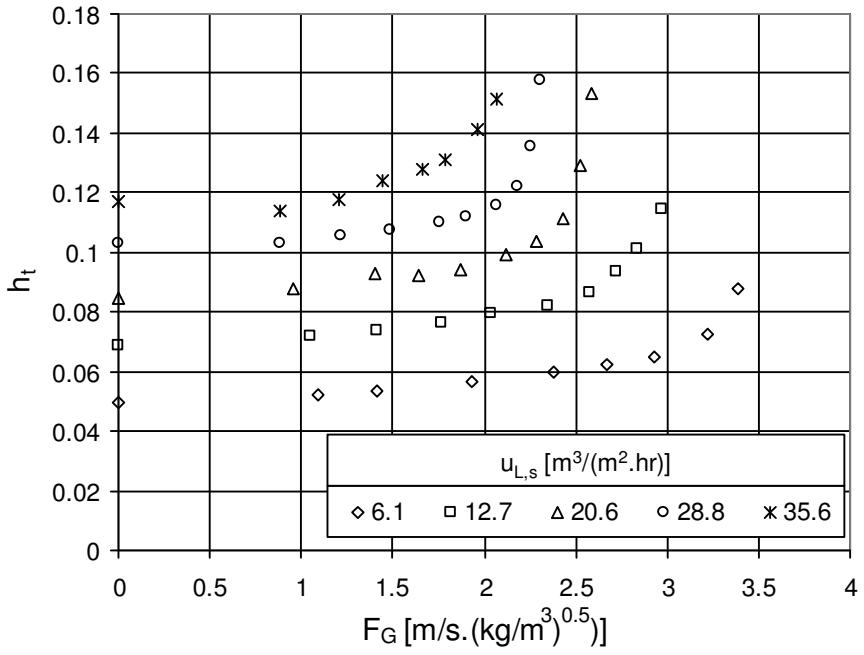

Figure C.8 Holdup as function of F-factor for Flexipac 350Y HC, air/Kerosol 200 system

Table C.1 Experimental data for Flexipac 350Y, air/water system

T1 [°C]	T2 [°C]	T3 [°C]	T4 [°C]	Pt [mmHg]	$u_{G,s}$ [m/s]	F [(Pa)$^{0.5}$]	dP/dz [Pa/m]	h_t [m^3/m^3]
$u_{L,s}$ = 35.6 [m^3/(m^2.hr)]								
n/a	n/a	25.3	25.4	n/a	0	0	0	0.090
n/a	n/a	25.7	25.8	n/a	0	0	0	0.092
29.4	25.2	25.4	25.2	752	0.80	0.87	43	0.090
30	25.2	25.5	24.8	752	0.81	0.87	44	0.089
30.4	25	25.2	24.7	748	1.09	1.18	88	0.092
30	25	25.2	24.7	748	1.10	1.18	91	0.089
29.1	25	25.2	24.6	749	1.38	1.49	138	0.092
29.1	24.9	25.2	24.3	749	1.38	1.50	136	0.091
28.5	25	25.5	24.6	753.5	1.61	1.75	208	0.100
24.7	23.3	23.6	22.4	754	1.75	1.90	248	0.088
26	23.7	24	22.6	754	1.75	1.91	247	0.086
29.5	23.5	23.5	23.2	753.5	1.76	1.91	245	0.103
27.8	24.7	25.1	24.2	754	1.79	1.94	277	0.098
30.6	25.1	25.3	24.7	752	1.98	2.14	365	0.108
30.9	24.7	24.7	24.2	752	1.98	2.14	390	0.106
30.1	24.2	24.8	23.6	753	1.98	2.15	409	0.107
29.5	25.5	25.7	24.4	753.5	2.04	2.21	541	0.114
30	25	25.4	24.2	752	2.06	2.23	881	0.129
31	25.1	25.1	24.4	752	2.13	2.30	717	0.125
30.7	25.1	25.3	24.4	752	2.13	2.31	667	0.124
26.4	24.2	24.5	22.7	754	2.16	2.35	780	0.113
26.9	23.9	24	22.4	754	2.17	2.36	752	0.109
$u_{L,s}$ = 28.8 [m^3/(m^2.hr)]								
n/a	n/a	25.6	25.5	n/a	0	0	0	0.093
n/a	n/a	26	25.9	n/a	0	0	0	0.091
26	25.5	25.8	25.5	752.5	0.80	0.87	42	0.087
30.2	25.4	25.5	24.8	752	0.81	0.87	42	0.087
28.5	25	25.2	24.7	748	1.09	1.18	86	0.089
25.8	24.6	25.3	24	752.5	1.09	1.18	87	0.084
27.6	24.9	25.3	24.4	752.5	1.09	1.18	86	0.085
29.6	25.1	25.1	24.4	749	1.39	1.50	146	0.089
29.8	25	25.2	24.2	749	1.39	1.50	142	0.091
29.3	24.5	25	23.9	753	1.70	1.84	204	0.094
27.7	24.2	24.4	23	753.5	1.75	1.90	221	0.078
27.8	24.2	24.4	23.3	753.5	1.75	1.90	220	0.079
29.5	25	25.1	24.1	753.5	1.85	2.00	252	0.097
27.8	24.8	25.2	23.7	754	1.87	2.02	252	0.092
30.6	24.8	25.3	24.3	752	2.00	2.17	314	0.096
30.8	24.8	25.2	24.2	752	2.02	2.19	309	0.096
28.5	24.7	25.2	23.8	754	2.14	2.32	535	0.104
26.3	24.2	24.7	22.5	754	2.16	2.36	518	0.093

Table C.1 Continued

T1 [°C]	T2 [°C]	T3 [°C]	T4 [°C]	Pt [mmHg]	$u_{G,s}$ [m/s]	F [(Pa)$^{0.5}$]	dP/dz [Pa/m]	h_t [m^3/m^3]
$u_{L,s}$ = 28.8 [m^3/(m^2.hr)]								
29.5	25.1	25.1	24	752	2.17	2.36	975	0.134
28.5	24.8	25	23.8	752	2.18	2.36	969	0.131
27.2	23.9	24.7	22.6	754	2.19	2.38	528	0.091
30.3	24.8	25	24.2	751	2.21	2.39	686	0.111
30.9	25.1	25.2	24.3	751	2.21	2.39	648	0.113
$u_{L,s}$ = 20.5 [m^3/(m^2.hr)]								
n/a	n/a	26.1	26.1	n/a	0	0	0	0.079
n/a	n/a	26.4	26.4	n/a	0	0	0	0.079
27.8	25.5	25.5	25.1	752.5	0.80	0.87	38	0.077
29	25.4	25.4	25	752.5	0.80	0.87	38	0.076
28.5	25.1	25.2	24.2	752	1.08	1.17	82	0.075
28.5	25	25.2	24.2	752.5	1.08	1.17	81	0.074
30	25.1	25.3	23.9	748.5	1.39	1.50	136	0.078
29.9	24.8	25.2	23.7	749	1.39	1.50	136	0.077
27.8	24.2	24.4	22.9	753.5	1.76	1.91	201	0.070
25.8	24.2	24.5	22.9	753.5	1.76	1.92	201	0.070
29.3	25	25.2	23.5	753	1.79	1.94	211	0.081
28.1	24.6	25.2	23.3	754	1.88	2.04	242	0.079
29.8	24.9	25.5	23.8	753	1.97	2.14	277	0.084
27.2	24.5	24.8	22.4	751	2.20	2.38	331	0.076
29.1	24.6	25.2	22.6	751	2.21	2.39	326	0.076
28.7	24.5	25.1	22.9	754	2.24	2.43	409	0.088
29.9	25	25.5	23.4	753	2.27	2.46	503	0.092
29.7	25.1	25	23.5	752	2.34	2.54	616	0.098
30	24.9	25.3	23.1	752.5	2.34	2.54	755	0.104
30.1	25	25.3	23.5	752	2.35	2.54	614	0.099
27.1	24.2	24.6	21.9	750	2.41	2.61	906	0.110
30.3	25.2	25.5	23.4	752	2.42	2.62	1044	0.122
27.2	24.6	25	22	750	2.41	2.62	893	0.111
$u_{L,s}$ = 12.9 [m^3/(m^2.hr)]								
n/a	n/a	27	26.8	n/a	0	0	0	0.065
n/a	n/a	26.2	26.2	n/a	0	0	0	0.066
29.8	25.3	25.3	24.6	752.5	0.80	0.87	35	0.066
30.4	25.1	25.3	24.7	752	0.81	0.87	36	0.066
28.9	25.1	25.4	23.9	752	1.09	1.18	75	0.064
29.1	25.2	25.4	23.8	752	1.10	1.19	73	0.063
30.2	25.5	25.5	23.3	748.5	1.39	1.50	126	0.067
30	25.5	25.5	23.2	748.5	1.39	1.50	126	0.066
27.2	24.3	24.5	22.1	753.5	1.77	1.92	184	0.059
27.6	24.3	24.5	22.1	753.5	1.77	1.92	185	0.061
29.5	24.7	25.5	22.5	753	1.83	1.99	233	0.069

Table C.1 Continued

T1 [°C]	T2 [°C]	T3 [°C]	T4 [°C]	Pt [mmHg]	$u_{G,s}$ [m/s]	F [(Pa)$^{0.5}$]	dP/dz [Pa/m]	h_t [m^3/m^3]
$u_{L,s}$ = 12.9 [m^3/(m^2.hr)]								
30	25.1	25.5	23	752.5	1.91	2.06	226	0.069
28.3	24.6	25.5	22.2	754	1.98	2.15	245	0.068
29.7	24.7	25.5	21.4	751	2.21	2.39	286	0.066
29.5	24.2	25.5	21.5	751	2.21	2.39	302	0.065
28	24.5	25.2	20.8	750	2.42	2.62	440	0.073
27.8	24.3	25.3	20.7	750	2.42	2.62	462	0.074
31.3	25	25.6	22.6	752	2.55	2.76	616	0.085
31.2	25	25.5	22.8	752	2.56	2.77	616	0.085
30	24.6	25.7	22.3	752	2.64	2.86	881	0.097
28.5	24	25.2	20.8	749.5	2.65	2.87	742	0.088
28.4	24.4	25.5	20.6	749.5	2.65	2.88	755	0.090
$u_{L,s}$ = 6.0 [m^3/(m^2.hr)]								
n/a	n/a	27	26.6	n/a	0	0	0	0.051
n/a	n/a	27.3	26.6	n/a	0	0	0	0.051
29.4	26.5	26.8	24.6	752	0.80	0.87	34	0.050
30.1	26.8	27	24.3	752	0.81	0.87	33	0.051
29.5	25.8	26.5	22.9	752	1.10	1.19	67	0.051
29.5	25.6	26.1	22.8	752	1.10	1.19	68	0.051
30.2	25.1	26	21.2	748.5	1.39	1.50	116	0.051
30	25.1	25.8	21.2	748.5	1.39	1.51	117	0.051
26	23.9	25.7	20.3	753.5	1.76	1.92	164	0.048
27.5	23.4	25.8	20	753.5	1.77	1.92	166	0.046
29.8	23.4	25.5	19.7	751	2.21	2.39	273	0.053
29.9	23.4	25.5	19.6	751	2.21	2.39	274	0.052
28.3	22.8	25.8	19.2	750	2.47	2.68	371	0.053
28.1	22.9	26.2	19	750	2.47	2.68	355	0.055
29.1	22.8	26	19.5	749.5	2.77	3.01	503	0.060
29.1	22.5	25.7	19.2	749.5	2.77	3.01	509	0.058
29.9	23	25.8	20.7	752	3.00	3.25	686	0.070
29.5	22.9	25.5	20.4	752	3.10	3.36	950	0.081
$u_{L,s}$ = 0.0 [m^3/(m^2.hr)]								
23.5	21.7	n/a	n/a	753.5	0.77	0.84	8	0
27.1	25	n/a	n/a	753.5	1.09	1.19	38	0
27.2	25.6	n/a	n/a	753.5	1.40	1.53	72	0
27.5	26	n/a	n/a	753.5	1.79	1.94	112	0
26.8	25.4	n/a	n/a	754	2.17	2.35	146	0
27.6	26.6	n/a	n/a	753.5	2.18	2.36	171	0
27.6	26.8	n/a	n/a	753.5	2.51	2.73	223	0
27.2	26.8	n/a	n/a	753.5	2.77	3.01	272	0
26.2	24.6	n/a	n/a	754	2.78	3.02	252	0
25.6	23.9	n/a	n/a	754	3.22	3.50	347	0
25.6	23.7	n/a	n/a	754	3.55	3.88	416	0

Table C.2 Experimental data for Flexipac 350Y, air/Kerosol 200 system

T1 [°C]	T2 [°C]	T3 [°C]	T4 [°C]	Pt [mmHg]	$u_{G,s}$ [m/s]	F [(Pa)$^{0.5}$]	dP/dz [Pa/m]	h_t [m^3/m^3]
$u_{L,s}$ = 35.6 [m^3/(m^2.hr)]								
n/a	n/a	31.6	31.4	n/a	0	0	0	0.111
29.5	30	30.9	30.5	751.5	1.02	1.10	107	0.108
29.1	31.4	32	31.4	751.5	1.35	1.46	189	0.112
27.5	29.9	30.3	29.7	754.5	1.58	1.71	325	0.120
32.1	31.1	31.2	31.1	753	1.68	1.80	371	0.122
32.0	31.4	31.6	31.4	753	1.75	1.88	491	0.128
31.6	31.4	31.7	31.4	753	1.82	1.95	642	0.138
30.6	31	31	30.9	753	1.84	1.98	818	0.153
$u_{L,s}$ = 28.8 [m^3/(m^2.hr)]								
n/a	n/a	31.2	31	n/a	0	0	0	0.097
30.0	30.7	31.3	31.3	751.5	1.00	1.08	88	0.095
29.8	30.6	31.2	30.8	751.5	1.35	1.45	151	0.098
30.0	30.8	31.7	31	757	1.66	1.79	245	0.101
32.0	31.1	31.6	31.5	753	1.82	1.96	350	0.105
32.1	30.8	31.6	31.5	753	1.90	2.04	484	0.113
32.1	31.1	31.4	31.5	753	1.93	2.08	610	0.122
32.0	31.1	31.4	31.4	753	1.97	2.12	755	0.134
31.7	30.8	31.3	31.3	753	2.02	2.18	893	0.144
$u_{L,s}$ = 20.6 [m^3/(m^2.hr)]								
n/a	n/a	31.4	31.3	n/a	0	0	0	0.077
30.6	30.6	31.4	31.1	751.5	1.09	1.17	82	0.081
29.4	30.3	30.9	30.4	756	1.54	1.67	161	0.085
29.3	30.2	30.8	30.2	756	1.87	2.02	258	0.088
29.8	30.6	31	30.5	756.5	2.02	2.19	358	0.094
29.7	30.2	31.2	30.2	756.5	2.09	2.26	509	0.104
29.5	30.2	30.9	30.2	756.5	2.11	2.29	614	0.113
29.1	30.2	31	30	756.5	2.17	2.35	767	0.122
29.1	30	30.8	29.9	757	2.21	2.40	956	0.136
$u_{L,s}$ = 12.7 [m^3/(m^2.hr)]								
n/a	n/a	31.7	31.1	n/a	0	0	0	0.060
30.5	30.7	31.3	30.6	751.5	1.14	1.23	75	0.065
30.3	31.4	32.1	31.1	751.5	1.39	1.50	123	0.066
27.8	29.9	30.8	29.3	754.5	1.76	1.90	201	0.068
29.1	30.4	31.3	29.7	752.5	2.02	2.18	264	0.072
28.8	30.6	31.6	30	752.5	2.25	2.43	384	0.079
29.9	30.6	31.2	30	756	2.32	2.51	509	0.087
29.8	30.6	31.3	30	756	2.37	2.56	629	0.096
29.5	30.6	31.2	29.8	756	2.41	2.61	767	0.106
29.0	30	30.9	29.3	756	2.48	2.69	887	0.115

Table C.2 Continued

T1 [°C]	T2 [°C]	T3 [°C]	T4 [°C]	Pt [mmHg]	$u_{G,s}$ [m/s]	F [(Pa)$^{0.5}$]	dP/dz [Pa/m]	h_t [m^3/m^3]
$u_{L,s}$ = 6.1 [m^3/(m^2.hr)]								
n/a	n/a	31.7	30.5	n/a	0	0	0	0.045
30.4	30.3	32	30.1	751	1.12	1.21	63	0.046
30.4	31.2	31.9	30.4	751.5	1.37	1.48	107	0.046
28.1	30.4	31.3	28.4	754.5	1.63	1.76	151	0.048
30.2	31.9	33	30.4	751.5	1.98	2.13	211	0.051
29.8	31.2	32.5	29.7	752	2.34	2.52	333	0.055
29.4	31	32.7	29.2	752	2.55	2.75	459	0.063
29.0	30.9	32.9	29.2	752	2.67	2.89	579	0.070
30.2	31.2	33	30	751.5	2.84	3.06	711	0.079
30.2	30.3	31.3	30	751.5	2.98	3.21	912	0.095

Table C.3 Experimental data for Flexipac 350Y HC, air/water system

T1 [°C]	T2 [°C]	T3 [°C]	T4 [°C]	Pt [mmHg]	$u_{G,s}$ [m/s]	F [(Pa)$^{0.5}$]	dP/dz [Pa/m]	h_t [m^3/m^3]
$u_{L,s}$ = 35.7 [m^3/(m^2.hr)]								
n/a	n/a	25.9	25.5	754	0	0	0	0.101
30	25.1	25.3	24.8	748	1.11	1.19	104	0.103
35.1	26.2	26.4	26	746	1.17	1.25	101	0.103
35.4	26.4	26.5	26	746	1.37	1.47	157	0.104
30.3	24.8	25	24.6	748	1.37	1.48	182	0.105
30	25	25.5	24.7	752	1.63	1.76	283	0.116
30.2	24.9	25	24.5	752	1.65	1.78	283	0.115
30.6	25.2	25	24.4	747	1.68	1.81	252	0.119
29.5	25	25	24.4	751.5	1.98	2.14	371	0.116
27.2	24.7	25	24.3	751.5	2.00	2.17	371	0.115
28.1	24.5	24.8	23	755	2.14	2.32	478	0.122
30.2	24.9	25	24.4	751.5	2.30	2.49	604	0.124
30.1	25.1	25.1	24.4	751.5	2.31	2.51	610	0.128
30.2	25	25	24.5	751.5	2.37	2.57	692	0.130
27.4	24.7	25	24	751.5	2.37	2.57	704	0.130
27	24.1	24.4	22.8	754	2.49	2.71	881	0.137
29.9	24.7	25	24.3	751.5	2.51	2.72	868	0.123
32.4	25	25	24.4	748.5	2.54	2.74	1321	0.165
30.3	25	25	24.3	748.5	2.57	2.77	1006	0.145
$u_{L,s}$ = 28.8 [m^3/(m^2.hr)]								
n/a	n/a	25.5	25.5	754	0	0	0	0.101
30.6	25.1	25.2	24.7	748	1.06	1.15	91	0.105
34.7	26.3	26.4	25.9	746	1.16	1.25	98	0.107
34.4	26.2	26.1	25.7	746	1.37	1.47	148	0.107
30	24.6	25	24.2	748	1.37	1.48	164	0.108

Table C.3 Continued

T1 [°C]	T2 [°C]	T3 [°C]	T4 [°C]	Pt [mmHg]	$u_{G,s}$ [m/s]	F [(Pa)$^{0.5}$]	dP/dz [Pa/m]	h_t [m^3/m^3]
$u_{L,s}$ = 28.8 [m^3/(m^2.hr)]								
27.2	24.5	25	23.2	755.5	1.70	1.85	260	0.111
27	24.6	25	23.3	755.5	1.71	1.86	258	0.111
26.8	24.2	24.3	22.5	755.5	1.99	2.16	365	0.113
27	24	24.4	22.6	755	2.01	2.18	369	0.113
26.9	23.9	24	22.4	755.5	2.19	2.38	468	0.119
27.5	23.8	24	22.3	755.5	2.21	2.40	465	0.118
23.3	24	24	21.9	755	2.28	2.49	981	0.119
26	23.8	24	21.8	755	2.33	2.54	597	0.119
29.8	25	25	23.8	752	2.49	2.70	836	0.127
29.1	24.6	25	23.4	752	2.50	2.71	849	0.132
26.9	24.2	24.4	22.1	754	2.56	2.78	792	0.125
33	25	25	24.1	747.5	2.67	2.88	1358	0.154
33.2	25	25.1	24.1	748	2.70	2.91	1038	0.138
$u_{L,s}$ = 20.5 [m^3/(m^2.hr)]								
n/a	n/a	25.6	25.4	754	0	0	0	0.088
34.5	25.9	25.8	25.5	746	1.11	1.19	81	0.091
34.3	25.9	25.7	25	746	1.38	1.48	141	0.092
28.2	24.7	25.1	22.5	756	1.76	1.91	249	0.098
28	25	25	22.4	756	1.77	1.92	249	0.097
27.8	24.4	24.6	21.9	756	2.11	2.30	377	0.100
28.1	24.6	25	21.7	756	2.12	2.31	375	0.101
26.7	24.2	24.4	21.4	756	2.37	2.58	509	0.106
27.2	24.3	24.6	21.3	756	2.39	2.60	528	0.106
26.6	23.8	24	20.8	756	2.65	2.89	723	0.113
24.9	24.2	24.4	20.8	756	2.65	2.89	717	0.112
25.1	24.5	25	21.4	754	2.80	3.05	855	0.118
27.3	23.7	24	21	754	2.88	3.14	987	0.121
33	25	25	23.5	747.5	2.97	3.20	1245	0.131
$u_{L,s}$ = 12.8 [m^3/(m^2.hr)]								
n/a	n/a	25.4	25	754	0	0	0	0.075
30.7	25.4	25.5	24.2	748	1.06	1.14	78	0.078
30.8	25.2	25.2	23.8	748	1.38	1.49	145	0.080
28.5	25	25.1	21.4	755	1.82	1.97	249	0.084
28.5	24.3	24.7	20.5	755.5	2.21	2.40	387	0.089
28	24.2	24.7	19.8	755.5	2.46	2.68	491	0.091
27.6	23.8	24.8	19.3	755.5	2.70	2.95	629	0.095
27.2	23.4	25.2	19.4	755.5	2.71	2.96	642	0.094
26.6	23.9	25	19.9	752.5	2.86	3.11	755	0.101
27.6	23.7	24.7	19.8	752.5	3.03	3.29	906	0.103

Table C.3 Continued

T1 [°C]	T2 [°C]	T3 [°C]	T4 [°C]	Pt [mmHg]	$u_{G,s}$ [m/s]	F $[(Pa)^{0.5}]$	dP/dz [Pa/m]	h_t $[m^3/m^3]$
$u_{L,s}$ = 12.8 $[m^3/(m^2.hr)]$								
27.8	23.7	24.9	19.8	752.5	3.10	3.37	994	0.105
33.1	25.1	25.3	23.2	746	3.24	3.49	1075	0.109
30.8	24.6	25.6	21.7	747	3.38	3.65	1170	0.111
30.6	24.8	25.5	22.1	748	3.46	3.74	1403	0.124
$u_{L,s}$ = 6.0 $[m^3/(m^2.hr)]$								
n/a	n/a	26	26	754	0	0	0	0.060
30.8	25.4	25.8	22.8	748	1.13	1.22	82	0.063
30.6	24.5	25	22.5	748	1.38	1.49	132	0.064
28.5	23.6	26	18.3	755	1.93	2.10	254	0.067
28.4	22.5	26.4	17.9	755	2.37	2.57	387	0.069
27.7	22	25.3	17.6	755	2.75	3.00	543	0.074
28.1	22.3	26.5	18.5	752.5	2.99	3.25	679	0.078
28.1	21.8	26.1	18.2	752.5	3.17	3.45	818	0.084
27.8	21.7	26.5	18.1	752.5	3.32	3.62	925	0.085
30.2	23	25.8	21	747	3.67	3.97	1006	0.084
30.7	23.2	25.7	21.7	747.5	3.75	4.05	1138	0.089
30.5	22.9	26	21.4	748	3.82	4.13	1258	0.095
$u_{L,s}$ = 0.0 $[m^3/(m^2.hr)]$								
35.4	30.2	n/a	n/a	746	1.20	1.29	43	0
35.2	28.8	n/a	n/a	746	1.39	1.49	74	0
30.7	29.8	n/a	n/a	751.5	1.81	1.95	144	0
30.4	29.6	n/a	n/a	751.5	2.19	2.35	209	0
32.1	31.1	n/a	n/a	748.5	2.36	2.53	225	0
29.8	29.1	n/a	n/a	751.5	2.44	2.63	266	0
30.7	30.2	n/a	n/a	751.5	2.60	2.80	310	0
31.6	29.5	n/a	n/a	748.5	2.78	2.99	329	0
28.1	27.6	n/a	n/a	751.5	2.84	3.08	364	0
25	24	n/a	n/a	754	2.96	3.22	369	0
31.3	28.7	n/a	n/a	748.5	3.00	3.23	388	0
31.8	30.8	n/a	n/a	748.5	3.10	3.33	417	0
31	27.7	n/a	n/a	748.5	3.37	3.63	490	0
30.8	24.8	n/a	n/a	748.5	3.61	3.90	574	0
32	30.4	n/a	n/a	748.5	3.64	3.92	574	0

Table C.4 Experimental data for Flexipac 350Y HC, air/Kerosol 200 system

T1 [°C]	T2 [°C]	T3 [°C]	T4 [°C]	Pt [mmHg]	$u_{G,s}$ [m/s]	F [(Pa)$^{0.5}$]	dP/dz [Pa/m]	h_t [m^3/m^3]
$u_{L,s}$ = 35.6 [m^3/(m^2.hr)]								
n/a	n/a	30.9	30.7	n/a	0	0	0	0.117
28.4	29.8	30.6	30.2	751.5	0.82	0.88	88	0.114
29	30.1	30.8	30.6	752	1.12	1.21	141	0.118
28.7	30.6	30.7	30.6	752	1.34	1.44	252	0.124
30.2	30.4	31	30.5	751.5	1.55	1.67	346	0.128
27.5	30.2	30.8	30.1	751.5	1.65	1.78	421	0.131
27.8	30.4	30.8	30	751.5	1.82	1.96	610	0.141
27.7	30.2	30.5	30	751.5	1.91	2.06	818	0.152
30.8	31.1	31.7	31.2	751	1.94	2.09	912	n/a
$u_{L,s}$ = 28.8 [m^3/(m^2.hr)]								
n/a	n/a	31	30.9	n/a	0	0	0	0.103
28.5	29.5	30.8	30.4	751.5	0.82	0.88	82	0.103
29.4	30.2	30.9	30.6	752	1.13	1.21	126	0.105
29.5	30.6	31	30.9	752	1.37	1.48	201	0.107
30	30.7	31	30.8	751.5	1.63	1.75	289	0.110
27.2	30.2	30.9	30.1	753	1.76	1.90	384	0.112
26.7	30	30.8	29.8	753	1.91	2.06	516	0.116
26.2	29.9	30.8	29.6	753	2.01	2.18	654	0.122
26.3	30	30.8	29.5	753	2.08	2.25	818	0.136
26.3	29.7	30.7	29.5	753	2.13	2.31	1050	0.158
$u_{L,s}$ = 20.6 [m^3/(m^2.hr)]								
n/a	n/a	31.2	31	n/a	0	0	0	0.085
29.3	30	31	30.5	751.5	0.89	0.95	68	0.088
29.5	30.4	31	30.6	752	1.30	1.40	143	0.093
30.7	31	31.7	31.1	751	1.53	1.64	189	0.092
28.4	30	30.7	30	752.5	1.73	1.87	258	0.094
28.3	30.2	30.8	30	753	1.96	2.12	384	0.099
27.9	30.9	31.8	30.3	753	2.11	2.28	522	0.104
27.3	30.3	31.3	29.6	753	2.25	2.43	692	0.111
26.9	29.7	30.8	29.2	753	2.33	2.53	887	0.129
27	29.5	30.9	29.2	753	2.38	2.58	1132	0.153
$u_{L,s}$ = 12.7 [m^3/(m^2.hr)]								
n/a	n/a	31.3	31	n/a	0	0	0	0.068
29.4	30.4	31.4	30.5	751.5	0.97	1.05	69	0.072
29.8	30.8	31.8	30.7	751.5	1.31	1.42	127	0.074
29	30.2	30.9	29.7	752.5	1.89	2.04	270	0.079
28.5	30.3	30.9	29.5	752.5	2.18	2.35	396	0.082
28.2	30.4	31.1	29.3	752.5	2.39	2.58	535	0.087
28	29.9	30.7	29	752.5	2.51	2.72	673	0.093
28	30.2	30.8	29	752.5	2.62	2.83	799	0.101
31	32	32.3	31.4	751	2.77	2.98	987	0.115

Table C.4 Continued

T1 [°C]	T2 [°C]	T3 [°C]	T4 [°C]	Pt [mmHg]	$u_{G,s}$ [m/s]	F $[(Pa)^{0.5}]$	dP/dz [Pa/m]	h_t $[m^3/m^3]$
$u_{L,s}$ = 6.1 $[m^3/(m^2.hr)]$								
N/a	n/a	31.7	30.6	n/a	0	0	0	0.050
30	30.8	32.5	30	751.5	1.02	1.10	62	0.052
29.9	31.4	32.9	30	751.5	1.31	1.42	111	0.054
29.4	31.3	32.6	29.3	752	1.80	1.93	208	0.057
28.9	30.9	32.2	28.9	752	2.21	2.38	340	0.060
28.5	30.5	32.5	28.4	752.5	2.48	2.67	465	0.063
28.1	30.6	32.7	28.2	752.5	2.71	2.93	591	0.065
31	31.2	32	30.8	751	2.99	3.22	755	0.072
31	31	31.7	30.9	751	3.14	3.38	981	0.088

APPENDIX D

Experimental data on naphthalene sublimation

Table D.1 Experimental sublimation data, bottom half of packing coated (coating 1)

T1* [°C]	T2** [°C]	Pt [mmHg]	Mass loss [g]	ε	$u_{G,s}$ [m/s]	F [(Pa)$^{0.5}$]	$u_{G,e}$ [m/s]	$Re_{G,e}$	Sc_G	$k_G \times 10^2$ [m/s]
31.8	30.3	748	38.8	0.869	0.94	1.01	1.53	1031	2.37	1.81
30.3	28.5	748	23	0.858	0.94	1.01	1.55	1056	2.37	1.88
27.8	26.3	754.5	18.7	0.853	1.39	1.51	2.31	1619	2.34	2.47
27.4	26	755	24.2	0.856	1.39	1.52	2.30	1619	2.33	2.48
30.9	30.1	751	30.6	0.865	1.85	1.99	3.03	2057	2.36	2.88
30.5	29.6	751.5	39.9	0.855	1.85	1.99	3.06	2085	2.36	2.95
28.4	27.4	751	23.8	0.868	2.18	2.36	3.55	2454	2.36	3.42
28.1	27.2	753.5	26.5	0.862	2.19	2.37	3.60	2497	2.35	3.21
27.5	26.5	754	26.2	0.853	2.19	2.37	3.63	2531	2.35	3.40
30.6	30	750.5	38.3	0.874	2.64	2.84	4.27	2920	2.34	3.59
28.4	27.6	752.5	41	0.861	2.65	2.87	4.35	3020	2.34	3.55
27.8	27.2	749	28.9	0.864	3.10	3.35	5.08	3514	2.36	4.21
26.5	25.7	750	24.9	0.876	3.11	3.38	5.03	3514	2.36	4.11
19.7	19.1	754.5	23.8	0.89	4.13	4.54	6.56	4815	2.35	4.58
18.6	18	759.5	21.5	0.887	4.09	4.53	6.52	4850	2.34	4.63
19.5	19	759.5	20	0.889	4.87	5.38	7.75	5731	2.33	5.18
19.3	18.7	759.5	19.7	0.879	4.89	5.41	7.87	5835	2.33	5.24
18.2	17.7	756.5	24.6	0.88	5.30	5.85	8.52	6324	2.34	5.38
17.2	16.5	756.5	17.1	0.873	5.34	5.91	8.65	6466	2.34	5.63

* Temperature of air in
** Temperature of air out

Table D.2 Experimental sublimation data, top half of packing coated (coating 2)

T1* [°C]	T2** [°C]	Pt [mmHg]	Mass loss [g]	ε	$u_{G,s}$ [m/s]	F [(Pa)$^{0.5}$]	$u_{G,e}$ [m/s]	$Re_{G,e}$	Sc_G	$k_G \times 10^2$ [m/s]
27.1	25.1	754.5	15.4	0.871	0.93	1.01	1.51	1055	2.36	1.68
28.7	27	751.5	19.2	0.861	0.93	1.01	1.53	1057	2.36	1.80
27.5	26.2	758.5	17.9	0.866	1.39	1.52	2.27	1603	2.32	2.40
27.2	25.9	759	17.6	0.859	1.39	1.52	2.29	1622	2.32	2.43
25.9	24.5	754.5	17.1	0.871	1.83	1.99	2.98	2093	2.36	2.59
27.2	26	755	20	0.857	1.84	1.99	3.03	2116	2.35	2.67
28	27.1	751	20.8	0.864	2.20	2.37	3.59	2488	2.36	3.02
27.3	26.4	752.5	19.9	0.857	2.19	2.37	3.61	2518	2.35	3.10
27.3	26.5	755	22.9	0.865	2.62	2.85	4.28	3002	2.34	3.52
25.3	24.3	759.5	18.5	0.872	2.63	2.87	4.26	3044	2.33	3.45
28.2	27.7	749	27.3	0.874	3.09	3.34	5.00	3454	2.36	3.75
20.0	19.6	756.5	23.8	0.872	4.11	4.52	6.67	4892	2.34	4.37
19.5	19.1	756.5	23.4	0.872	4.12	4.54	6.69	4923	2.34	4.54
19	18.5	758	17.5	0.891	4.87	5.38	7.73	5725	2.34	4.72
16.7	16	758.5	14.5	0.877	4.87	5.41	7.86	5913	2.34	5.00
18.9	18.5	757	18	0.889	5.30	5.85	8.44	6243	2.34	4.85
18.4	18	757	17.5	0.883	5.30	5.85	8.49	6300	2.34	4.97

* Temperature of air in

** Temperature of air out

APPENDIX E

Table E.1 lists the equations used to estimate the physical properties of n-propanol and Table E.2 the equations used to estimate the properties of the monoethanolamine/n-propanol mixture. The viscosity of pure n-propanol is calculated from the correlation provided in (Reid and Prausnitz, 1986) and the density and surface tension from the correlations in the SIMSCI databank. The equations shown in Table E.2 were fitted on experimental data.

Table E.1 Physical properties of n-propanol

Property	Equation*	
ρ^o [kg/m^3]	$\rho^o = \left[\frac{8.10\times10^{-1}}{3.69^{1+\left(1-T/536.8\right)^{0.24}}}\frac{1}{Mr}\right]^{-1}$	(E1)
μ^o [cP]	$\ln\left(\mu^o\right) = -12.3 + \frac{2.67\times10^3}{T} + \left(2.01\times10^{-2}\right)T - \left(2.23\times10^{-5}\right)T^2$	(E2)
σ^o [N/m]	$\sigma^o = 3.43\times10^{-2} - \left(3.70\times10^{-5}\right)T$	(E3)

* Units of T is [K]

Table E.2 Physical properties of monoethanolamine/n-propanol

Property	Units	C_{MEA} [mol/dm^3]	Temp [K]	Equation*	
ρ	[kg/m^3]	0.2-1.0	288-303	$\rho^o + 14C_{MEA}$	(E4)
μ	[Pa.s]	0.2-1.0	288-303	$\mu^o.e^{0.18C_{MEA}}$	(E5)
σ	[N/m]	0.2-1.0	288-303	$\sigma^o + 7.31\times10^{-4}C_{MEA}$	(E6)

* Units of C_{MEA} is [mol/dm^3]

Table E.3 Rate of absorption of CO_2 into n-propanol/monoethanolamine solutions: Wetted-wall column experimental results

h_{column} [mm]	T_L [°C]	T_G [°C]	CO_2 in [vol%]	CO_2 out [vol%]	$P_{reactor}$ [kPa]	V_L [cm^3/s]	V_{air} [cm^3/s]	$n_{air}\times10^3$ [mol/s]	t_c [s]	$n_{CO2,in}\times10^5$ [mol/s]	$n_{CO2,out}\times10^5$ [mol/s]	$N_{CO2}\times10^4$ [mol/(m^2.s)]
C_{MEA} = 0.2 [mol/dm^3]												
60	15.1	14.2	1.2	1.08	100.08	1.52	43.7	1.83	0.55	2.22	1.99	4.74
90	15.2	14.3	1.23	1.05	100.15	1.52	43.7	1.83	0.83	2.27	1.94	4.74
90	15.1	14.4	0.9	0.77	100.15	1.52	43.7	1.83	0.83	1.66	1.42	3.40
90	15.1	14.4	0.57	0.48	100.15	1.52	43.7	1.83	0.83	1.05	0.88	2.34
90	15.4	14.4	1.23	1.05	100.22	0.99	43.3	1.81	1.10	2.25	1.92	4.70
90	15.4	14.3	0.9	0.775	100.22	0.99	43.3	1.81	1.10	1.64	1.41	3.24
90	15.3	14.3	0.58	0.495	100.22	0.99	43.3	1.81	1.10	1.06	0.90	2.19
90	29.8	30.2	1.25	1.08	100.23	1.52	43.7	1.73	0.74	2.19	1.89	4.25
90	29.9	30.2	0.92	0.795	100.23	1.52	43.7	1.73	0.74	1.61	1.39	3.10
90	29.9	30.2	0.61	0.52	100.23	1.52	43.7	1.73	0.74	1.06	0.90	2.22
90	29.8	30.2	1.24	1.08	100.23	0.99	43.7	1.73	0.98	2.17	1.89	4.00
90	29.8	30.2	0.8	0.69	100.23	0.99	43.7	1.73	0.98	1.40	1.20	2.72
90	29.8	30.2	0.61	0.52	100.23	0.99	43.7	1.73	0.98	1.06	0.90	2.22
C_{MEA} = 0.25 [mol/dm^3]												
60	15.4	14.6	1.28	1.07	100.24	1.52	30.2	1.26	0.55	1.64	1.37	5.75
60	15.4	14.6	0.83	0.7	100.24	1.52	30.8	1.29	0.55	1.08	0.91	3.59
60	15.5	14.6	0.57	0.47	100.24	1.52	30.2	1.26	0.55	0.72	0.60	2.70
90	15.3	14.6	1.22	1.01	100.39	1.52	39.8	1.67	0.83	2.06	1.70	5.05
90	15.4	14.6	0.8	0.65	100.39	1.52	40.8	1.71	0.83	1.38	1.12	3.67
90	15.2	14.6	0.48	0.385	100.39	1.52	39.2	1.64	0.83	0.79	0.63	2.22
90	15.5	14.6	0.8	0.65	100.39	0.99	40.8	1.71	1.10	1.38	1.12	3.67
90	15.2	14.6	0.48	0.385	100.39	0.99	39.2	1.64	1.10	0.79	0.63	2.22

Table E.3 Continued

h_{column} [mm]	T_L [°C]	T_G [°C]	CO_2 in [vol%]	CO_2 out [vol%]	$P_{reactor}$ [kPa]	V_L [cm^3/s]	V_{air} [cm^3/s]	$n_{air}\times10^3$ [mol/s]	t_c [s]	$n_{CO2,in}\times10^5$ [mol/s]	$n_{CO2,out}\times10^5$ [mol/s]	$N_{CO2}\times10^4$ [mol/(m^2.s)]
C_{MEA} = 0.25 [mol/dm^3]												
90	29.9	30.3	0.63	0.55	100.79	1.52	22.4	0.89	0.74	0.57	0.49	1.02
90	30.3	30.6	1.2	1.01	100.41	1.52	43.5	1.72	0.74	2.09	1.76	4.72
90	30.3	30.5	0.89	0.75	100.41	1.52	43.5	1.73	0.74	1.55	1.30	3.46
60	29.9	30.2	1.17	1.03	100.41	1.52	43.3	1.72	0.49	2.04	1.79	5.20
60	29.9	30.1	0.88	0.78	100.41	1.52	43.3	1.72	0.49	1.53	1.35	3.70
C_{MEA} = 0.3 [mol/dm^3]												
90	15.1	14.2	1.32	1.07	100.54	1.52	43.5	1.83	0.83	2.44	1.97	6.59
90	15.7	14.9	1.21	0.97	100.54	1.52	43.7	1.83	0.83	2.24	1.79	6.32
90	15.2	14.5	0.92	0.75	100.54	1.52	43.5	1.82	0.83	1.69	1.38	4.44
90	15.1	14.5	0.63	0.505	100.54	1.52	43.5	1.82	0.83	1.16	0.93	3.25
90	15.4	14.4	1.265	1.04	100.54	0.99	43.7	1.83	1.10	2.35	1.93	5.95
90	15.3	14.3	0.9	0.73	100.54	0.99	43.7	1.83	1.11	1.66	1.35	4.46
90	15.2	14.3	0.61	0.49	100.54	0.99	43.7	1.83	1.11	1.13	0.90	3.13
60	15.2	14.3	1.255	1.09	100.54	1.52	43.7	1.83	0.55	2.33	2.02	6.55
60	15.1	14.5	0.92	0.79	100.54	1.52	43.7	1.83	0.55	1.70	1.46	5.12
60	15	14.4	0.59	0.5	100.54	1.52	43.7	1.83	0.55	1.09	0.92	3.52
60	29.9	30.2	1.32	1.14	100.41	1.52	43.5	1.73	0.49	2.31	1.99	6.74
60	29.9	30.2	1.14	0.98	100.41	1.52	43.5	1.73	0.49	1.99	1.71	5.97
60	29.9	30.2	0.87	0.75	100.41	1.52	43.5	1.73	0.49	1.52	1.31	4.45
90	30.1	30.2	1.2	0.985	100.41	1.52	43.5	1.73	0.74	2.10	1.72	5.35
90	30.1	30.2	0.89	0.72	100.41	1.52	43.5	1.73	0.74	1.55	1.25	4.20
90	30.2	30.2	0.61	0.485	100.41	1.52	43.5	1.73	0.74	1.06	0.84	3.08

Table E.4 Experimental results for determination of effective surface area of Flexipac 350Y

T_{air}(in) [°C]	T_{air}(out) [°C]	T_{liq}(in) [°C]	T_{liq}(out) [°C]	P_{column} [kPa]	CO_2 in [vol%]	CO_2 out [vol%]	C_{MEA} [mol/dm^3]	$u_{G,s}$ [m^3/(m^{2}s)]	F_G [(Pa)$^{0.5}$]	n_{air} [mol/s]	uL,s [m^3/(m^{2}hr)]	$N_{CO2}\times10^4$ [mol/(m^{2}s)]	Area$\times10^4$ [m^2]	a_e [m^2/m^3]
$F_G \approx 1.1$ [(m/s).(kg/m^3)$^{0.5}$]														
24.2	24.5	23.4	26.8	99.79	1.05	0.96	0.247	1.07	1.15	1.35	6.1	4.52	3.59	110
24.2	23.7	23.2	25.9	99.79	1.05	0.9	0.247	1.06	1.15	1.34	13.6	4.50	3.57	182
24.3	23.9	23.6	25.6	99.79	1.05	0.88	0.247	1.06	1.15	1.34	17.8	4.50	3.57	207
23.5	24.4	23.5	25.3	99.79	1.03	0.84	0.247	1.06	1.14	1.34	24.7	4.42	3.51	235
$F_G \approx 1.4$ [(m/s).(kg/m^3)$^{0.5}$]														
23.3	22.5	19.3	24.7	100.66	1.08	1.01	0.280	1.32	1.44	1.72	6.1	5.37	4.26	92
21.3	23.3	22	22.6	100.59	1.04	0.9	0.270	1.30	1.42	1.67	13.6	4.89	3.88	196
20.2	20.6	20.4	21.8	100.99	1.05	0.9	0.276	1.31	1.44	1.71	17.8	5.13	4.07	204
19.6	20.8	20.4	21.4	100.99	1.05	0.88	0.276	1.31	1.43	1.70	24.7	5.14	4.08	230
$F_G \approx 2.0$ [(m/s).(kg/m^3)$^{0.5}$]														
19.6	22	21.9	20.8	100.99	1.03	0.97	0.276	1.93	2.11	2.47	6.1	5.03	3.99	121
19.7	22.2	21.5	21.2	100.99	1.05	0.95	0.276	1.91	2.09	2.45	13.6	5.16	4.10	194
19.5	21.5	20.8	21.4	100.99	1.05	0.94	0.276	1.89	2.07	2.43	17.8	5.21	4.14	209
20.6	22	22	22.4	100.59	1.04	0.91	0.270	1.86	2.03	2.39	24.7	5.02	3.99	252

APPENDIX F

Binary VLE for chlorobenzene/ethylbenzene test system

The recommended vapour pressure for chlorobenzene and ethylbenzene according to the IChemE (Onken, 1990) are:

Chlorobenzene(1): $$\log(P,[hPa]) = 7.040849 - \frac{1391.262}{T[C] + 213.024} \qquad (F1)$$

Ethylbenzene(2): $$\log(P,[hPa]) = 7.063282 - \frac{1412.676}{T[C] + 211.972} \qquad (F2)$$

Regression of the NRTL model (Abbott, 1994) on the experimental VLE data for chlorobenzene/ethylbenzene provided by the IChemE (Onken, 1990) yielded the following results:

a_{12} = -10.5556 [K]

a_{21} = 11.3096 [K]

alpha = 0.9 (F3)

Experimental data

The experimental data for Flexipac 350Y and Flexipac 350Y HC are given in Table F.1 and Table F.2. The data for Flexipac 500Y and Flexipac 500Y HC are given in Table F.3 and Table F.4.

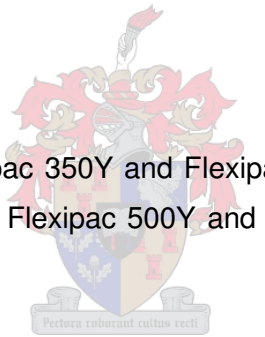

Table F.1 Total reflux distillation experimental results for Flexipac 350Y, chlorobenzene/ethylbenzene system

Run no	Conc. CLBZ [wt%]		Temperatures [°C]					P_{atm}	P_{top}	dP_{seg}	dP_{total}*	Q_{reb}	Q_{cond}	Q_{avg}
	Distillate	Bottoms	Reboiler	Sump	1	2	3	[kPa]	[kPa]	[mmH_2O]	[mmH_2O]	[kW]	[kW]	[kW]
1	80.53	46.41	135.8	135.3	134.9	134.3	134	101.26	101.26	7.5	34	24.9	19.3	22.1
2	79.69	44.16	136	135.5	135	134.4	134.2	101.13	101.13	12	60	34.0	28.1	31.1
3	78.91	42.09	136.2	135.7	135.3	134.6	134.2	101.13	101.13	18	87	40.0	34.4	37.2
4	78.54	40.51	136.5	135.8	135.4	134.6	134.2	101.13	101.13	23.5	110	44.1	38.1	41.1
5	78.09	39.7	136.6	135.8	135.5	134.6	134.2	101.19	101.19	28	130	45.3	39.8	42.5
6	78.17	37.32	136.8	136	135.6	134.6	134.2	100.99	100.99	50	O/R	50.6	44.9	47.8
7	78.45	42.01	135.9	135.4	135	134.5	134	100.66	100.66	13	65	34.1	29.7	31.9
8	77.96	38.85	136.6	135.8	135.4	134.8	134.2	100.59	100.59	32	O/R	46.3	42.2	44.2
9	82.48	45.36	116.9	116.3	115.7	115.2	114.5	100.86	60.22	9.5	46	25.1	21.4	23.3
10	81.21	41.37	118	117.4	116.6	115.6	115	100.79	61.00	20	103	35.8	32.5	34.1
11	80.96	39.79	117	116.3	115.4	114.7	113.8	100.06	58.58	28	138	37.9	34.7	36.3
12	80.61	48.74	116.9	116.4	115.2	114.5	113.8	100.19	57.86	40	O/R	40.1	35.6	37.9
13	80.27	37.17	117	116.2	115.4	114.5	113.8	100.19	57.86	48	O/R	41.1	36.0	38.6
14	80.76	36.68	117.2	117	115.7	114.8	114.2	100.13	57.80	62	O/R	42.6	38.2	40.4
15	84.85	44.67	94.8	94.4	93.1	92.6	91.9	99.66	29.39	10	50	19.9	16.2	18.1
16	83.94	41.38	96	95.7	94.3	93	92.6	99.53	30.10	20	110	27.9	25.3	26.6
17	84.09	39.95	96.3	95.7	94.2	93.3	92.6	99.53	29.26	29	145	30.3	26.2	28.3
18	83.5	38.2	97	96.6	94.8	94	93.1	99.59	29.32	41	O/R	31.5	28.1	29.8
19	83.03	36.8	97.2	96.6	95	94	93.1	99.66	29.39	52	O/R	32.7	28.8	30.8
20	83.21	35.76	98.2	97.6	96	94.8	93.6	99.86	29.59	61	O/R	34.8	31.7	33.3

* O/R: value outside measuring range

Table F.2 Total reflux distillation experimental results for Flexipac 350Y HC, chlorobenzene/ethylbenzene system

Run no	Conc. CLBZ [wt%]		Temperatures [°C]					P_{atm}	P_{top}	dP_{seg}	dP_{total}*	Q_{reb}	Q_{cond}	Q_{avg}
	Distillate	Bottoms	Reboiler	Sump	1	2	3	[kPa]	[kPa]	[mmH_2O]	[mmH_2O]	[kW]	[kW]	[kW]
1	77.89	48.39	135.5	135.1	135	134.5	134.3	100.99	100.99	6	26	22.2	16.7	19.4
2	78.12	39.55	136.5	136	135.8	134.5	134.4	100.93	100.93	33	147.5	49.3	43.9	46.6
3	78.74	45.20	135.8	135.4	135	134.6	134.2	100.99	100.99	9	45	27.8	24.0	25.9
4	77.99	42.37	136	135.6	135.3	134.9	134.2	100.79	100.79	16.5	82	37.8	33.3	35.6
5	77.42	40.53	136.2	135.9	135.4	134.9	134.4	100.73	100.73	21.5	106.5	43.2	37.4	40.3
6	76.74	38.16	136.4	136	135.7	135	134.3	100.79	100.79	28	141	46.8	42.3	44.6
7	79.31	39.13	136.7	136.3	135.8	134.9	134.2	100.53	100.53	48	O/R	51.8	49.3	50.5
8	80.75	48.32	116.4	115.8	115.2	114.8	114.2	100.73	59.24	5.5	26.5	18.6	15.2	16.9
9	82.38	46.21	116.5	116	115.4	114.6	114.2	100.66	59.18	10.5	52.5	25.6	22.7	24.2
10	81.96	43.79	116.7	116.2	115.5	115	114.2	100.66	59.18	16	85	32.4	28.5	30.5
11	81.79	42.46	117	116.3	115.5	114.9	114.3	100.79	59.31	21	105.5	35.9	32.2	34.1
12	81.22	40.65	117.8	117.2	116.2	115.6	114.7	100.93	59.44	29	145	39.6	36.8	38.2
13	80.33	39.01	118.1	117.5	116.6	115.8	115.1	100.66	60.02	36	O/R	43.3	40.0	41.7
14	80.11	37.41	117.8	117.3	116.4	115.6	114.7	100.66	59.18	43.5	O/R	45.1	41.3	43.2
15	79.64	35.60	118.2	118	116.6	115.7	115	100.66	59.18	62	O/R	47.1	43.2	45.1
16	85.07	46.42	95	94.6	93.7	93.2	92.2	100.26	29.99	10.5	56.5	20.6	17.7	19.1
17	85.39	43.08	96.3	95.8	94.6	94	93.1	100.06	29.79	21.5	117	27.8	25.2	26.5
18	84.60	41.28	97	96.3	95	94.2	93.1	100.06	29.79	30	153	31.8	30.0	30.9
19	83.65	39.53	97.8	97.3	95.7	94.8	93.6	100.13	29.86	40	O/R	35.4	32.1	33.8
20	83.97	38.57	97.9	97.3	95.8	94.6	93.4	99.86	29.59	50	O/R	37.7	33.8	35.7
21	83.71	36.71	98.8	98.2	96.4	95.4	94.2	99.73	29.46	60	O/R	38.5	35.7	37.1

* O/R: value outside measuring range